


This item was submitted to Loughborough University as a PhD thesis by the author and is made available in the Institutional Repository (<https://dspace.lboro.ac.uk/>) under the following Creative Commons Licence conditions.




CC creative commons
COMMONS DEED


Attribution-NonCommercial-NoDerivs 2.5


You are free:

- to copy, distribute, display, and perform the work

Under the following conditions:

 **Attribution.** You must attribute the work in the manner specified by the author or licensor.


 **Noncommercial.** You may not use this work for commercial purposes.

 **No Derivative Works.** You may not alter, transform, or build upon this work.

- For any reuse or distribution, you must make clear to others the license terms of this work.
- Any of these conditions can be waived if you get permission from the copyright holder.

Your fair use and other rights are in no way affected by the above.

This is a human-readable summary of the [Legal Code \(the full license\)](#).

[Disclaimer](#) 

For the full text of this licence, please go to:
<http://creativecommons.org/licenses/by-nc-nd/2.5/>

**Electrochemical Mechanisms
of the Impedance Spectrum in
Polymer Electrolyte Fuel Cells**

by

Samuel Cruz-Manzo

A Doctoral Thesis

Submitted in partial fulfillment of the requirements for the award of
Degree of Doctor of Philosophy of Loughborough University

May 2013

© by Samuel Cruz-Manzo 2013

Abstract

Electrochemical impedance spectroscopy (EIS) is a powerful technique that can be applied in-situ to deconvolute the various loss mechanisms in the polymer electrolyte fuel cell (PEFC) that occur at different rates. The frequency response of a PEFC that results from EIS is in essence characterised by energy dissipating and energy storing elements of the cell. It can be represented by an equivalent circuit that is composed of resistors and capacitors respectively. By understanding the arrangement and magnitude of the electrical components in the equivalent electrical circuit, it is possible to generate a deeper understanding of how and where the electrical energy that is generated due to the redox reaction is being dissipated and retained within the real physical system. Although the use of equivalent circuits is often an adequate approach, some electrochemical processes are not adequately described by electrical components. In which case, it is necessary to adopt a more rigorous approach of describing processes through the use of differential equations to describe the physics of the electrochemical system at the frequency domain.

Studies in the literature have attempted to construct mathematical models to describe the impedance response of the cathode catalyst layer (CCL) based on conservation equations describing the electrochemical and diffusion processes. However this has resulted in a complicated mathematical analysis which in turn results in complicated solutions. The resulting equations cannot be easily validated against real-world EIS measurements and only analytical results have been reported. In this thesis a mathematical model to describe the impedance response of the CCL has been developed. This model is derived from fundamental electrochemical theory describing the physics of the CCL. The mathematical treatment is simplified by taking into account some considerations based on the EIS theory. The resulting model can be easily applied to real-world EIS measurements of PEFCs and presents parameters commonly known in the electrochemical area. The scientific contribution of this doctoral thesis is mainly divided in two sections: Modelling and Application.

The first step of the modelling section develops an equation describing charge conservation in the CCL and together with Ohm's Law equation accounting for ionic conduction, predicts the impedance response of the CCL at low currents. The second step includes the change of oxygen concentration during the oxygen reduction reaction (ORR) into the equation accounting for CCL low current operation. The study of mass transport in the CCL is very complex; the literature has treated it with simplifications and approximations. The finite diffusion distance for oxygen to reach the reaction sites in the CCL forms a complicated network of multi-phase parallel and serial paths and can change in dimension at different operating conditions (flooding, drying). In the mathematical treatment of this doctoral thesis the finite diffusion distance and surface concentration of oxygen in the CCL are considered to be independent of the thickness of the CCL. EIS reflects only bulk measurements based on the total CCL thickness. Even though this results in an over-simplification for the oxygen diffusion in the total CCL, this approach simplifies the mathematical treatment to predict the impedance response of the CCL at high current operation, and as result it can be successfully validated against real-world EIS measurements.

In the application section the model is applied with real-world EIS measurements of PEFCs. First the model is applied with EIS measurements presenting inductive effects at high frequencies. The model reveals mechanisms masked at high frequencies of the impedance spectrum by inductance effects. The results demonstrate that the practice of using the real part of the Nyquist plot where the imaginary part is equal to zero to quantify the ohmic resistance in PEFCs can be subject to an erroneous interpretation due to inductive effects at high frequencies. Secondly the model is applied to cathode impedance data obtained through a three-electrode configuration in the measurement system and gives an insight into the mechanisms represented at low frequencies of the impedance complex-plot. The model predicts that the low frequency semicircle in PEFC measurements is attributed to low equilibrium oxygen concentration in the CCL-gas diffusion layer (GDL) interface and low diffusivity of oxygen through the CCL. In addition the model is applied with simultaneous EIS measurements in an Open-Cathode PEFC stack. The factors that limit the performance of the PEFC stack are evaluated with simultaneous EIS measurements and the model. The results show that the change in

impedance response of individual cells within the stack is attributed to oxygen limitations, degradation in membrane electrode assemblies (MEAs) and temperature distribution. This EIS knowledge enables an assessment of the state of health in operational fuel cell stacks. In the last section of the application section, the mathematical model translated in the time domain via reverse Laplace Transform predicts the current distribution through the CCL. This provides information to improve the performance of the CCL as well as determine the uptake of product water in the membrane.

Finally the conclusions and future work are presented. This doctoral thesis has established a backbone understanding of how the electrochemical and diffusion mechanisms relate to the electrochemical impedance spectra of PEFCs. The goal of a future work is to develop this EIS knowledge into a real-time EIS system for non-intrusive diagnostics of degradation in operational PEFCs. This implies a modification of the model to consider oxygen transport through the CCL thickness as part of a multi-species mixture using mass transport theory including concentrated solution theory to fuel cell engineering.

Acknowledgment

I would like to thank Professor Rui Chen for being my mentor and giving me the opportunity to undertake my doctoral studies at Loughborough University as well as Dr. Pratap Rama for his support, friendship and collaboration during my PhD studies.

I must also express my gratitude to Dr. Ulises Cano-Castillo from IIE, Mexico for recommending me to Loughborough University and facilitating communications between both parties.

To my friends Dr. James Poole, Dr. Paul Greenwood and Dr. Mehdi Mojtabi who helped me to establish myself in Loughborough, I would like thank you for your friendship through this time of transition.

Many thanks to my girlfriend Kathleen McLoughlin for her constant patience and support during the development of this doctoral thesis.

I would like to express my thanks to my family for believing in me and encouraging me to pursue my dream of studying a PhD abroad.

And finally I want to acknowledge the Mexican National Council for Science and Technology (CONACYT) for the sponsorship of my doctoral study at Loughborough University.

Contents

Chapter 1	1
Introduction	
1.1 Motivation	2
1.2 Objective	3
1.2.1 Particular Objectives	3
1.3 Knowledge Contribution	4
1.4 Outline of Thesis	5
1.5 References	7
Chapter 2	8
Fundamentals of Polymer Electrolyte Fuel Cells and Electrochemical Impedance Spectroscopy	
2.1 The Structure of the PEFC.....	8
2.2 The Voltage Output in the PEFC	10
2.2.1 Reversible Potential.....	10
2.2.2 Activation Overpotential	15
2.2.3 Ohmic Overpotential	17
2.2.4 Mass Transport Overpotential.....	18
2.2.5 Operating Voltage in a PEFC	20
2.3 The Catalyst Layer	21
2.3.1 The Charge Double Layer in the Catalyst Layer.....	22
2.3.2 AC Current in the Charge Double Layer of the Catalyst Layer	24
2.4 Fundamental Concepts of Electrochemical Impedance Spectroscopy	25
2.4.1 Experimental Methods for Impedance Measurements	26
2.4.2 Kramers-Kronig Relations.....	29
2.4.3 Representation of the Impedance in the Complex Plane	31
2.5 References	33

Chapter 3	34
A Literature Review on Electrochemical Impedance Spectroscopy in Polymer Electrolyte Fuel Cells	
3.1 In-situ EIS Measurements in PEFCs.....	35
3.2 Representation of the EIS through Equivalent Electrical Circuits.....	41
3.2.1 Randles Circuit.....	43
3.2.2 Transmission Line Circuit.....	48
3.3 Formula of de Levie to Characterise Porous Electrodes in PEFCs.....	52
3.4 Current Density Distribution through the Cathode Catalyst Layer.....	54
3.5 Conclusions.....	57
3.6 References.....	57
Chapter 4	61
Cathode Catalyst Layer Impedance Model for Low Current Operation	
4.1 Electrochemical Mechanisms of CCL.....	66
4.1.1 The Current in the Electrochemical Reaction.....	67
4.1.2 Ionic Resistance and Current Distribution in CCL.....	72
4.2 Cathode Catalyst Layer Impedance Model.....	73
4.2.1 Potential Distribution in Laplace Domain.....	74
4.2.2 Impedance Model of the Cathode Catalyst Layer in Frequency Domain.....	75
4.3 Impedance Model and Validation.....	76
4.3.1 The Impedance Model in the Frequency Domain.....	76
4.3.2 Experimental Set-up.....	77
4.3.3 Measured PEFC Impedance Response.....	77
4.3.4 Equivalent Circuit Model.....	79
4.3.5 Validation.....	79
4.4 Conclusions.....	81
4.5 References.....	81

Chapter 5	83
Cathode Catalyst Layer Impedance Model for High Current Operation	
5.1 Modelling Considerations.....	85
5.1.1 Oxygen Diffusion in the CCL.....	85
5.1.2 Considerations.....	86
5.2 CCL Mechanisms in Laplace Domain	87
5.2.1 Oxygen Transport during the ORR in Laplace Domain	88
5.2.2 Current Distribution in Laplace Domain	92
5.2.3 Potential Distribution in Laplace Domain	94
5.2.4 Impedance Model of CCL in Frequency Domain	94
5.2.5 Model Validation in Frequency Domain	95
5.3 Conclusions	97
5.4 References	98
Chapter 6	99
Inductive Effect on the Fuel Cell Cathode Impedance Spectrum at High Frequencies	
6.1 Inductive Effect on the Cathode Impedance Spectrum	100
6.1.1 Theoretical Analysis.....	101
6.1.1.1 Electrochemical Mechanisms in the Cathode Spectrum at High Frequency	106
6.1.2 Experimental Analysis.....	109
6.1.2.1 EIS Measurements.....	109
6.1.2.2 Kramers-Kronig Analysis on EIS Measurements	113
6.2 Validation of Inductance Effect on the Cathode Impedance Spectrum at High Frequency	115
6.3 Conclusions	118
6.4 References	119
Chapter 7	121
Low Frequency Electrochemical Mechanisms in the Fuel Cell Cathode Impedance Spectrum	
7.1 Experimental.....	122

7.2 Results	126
7.2.1 Cathode Impedance Validation	126
7.2.2 Estimation of Electrochemical and Diffusion Mechanisms	132
7.2.3 A Qualitative Analysis of Mass Transport Limitations	138
7.3 Discussion.....	140
7.4 Conclusions	140
7.5 References	141
Chapter 8.....	143
Analysis of the Performance of an Open-Cathode Polymer Electrolyte Fuel Cell Stack using Simultaneous EIS Measurements	
8.1 Experimental.....	145
8.1.1 Stack Measurements	147
8.1.2 Individual Cell Measurements	148
8.2 Results and Discussion.....	150
8.2.1 Electrochemical and Diffusion Mechanisms	150
8.2.2 Discussion.....	159
8.3 Conclusions	160
8.4 References	161
Chapter 9.....	163
Study of Current Distribution in the Fuel Cell Cathode Catalyst Layer through EIS	
9.1 CCL Low Current Distribution.....	164
9.1.1 Effect of Double-Layer Capacitance on CCL Low Current Distribution.....	166
9.1.2 Simulated Effect of Ionic Resistance on CCL Low Current Distribution	167
9.2 CCL High Current Distribution	169
9.2.1 Effect of Oxygen Diffusion Coefficient and Oxygen Bulk Concentration on CCL High Current Distribution	173
9.2.2 CCL performance at Different Current Density Operation	176
9.3 Discussion.....	178
9.4 Conclusions	181
9.5 References	183

Chapter 10	184
Conclusions and Future Work	
10.1 Conclusions.....	184
10.1.1 Modelling.....	185
10.1.2 Application.....	186
10.2 Future Work.....	191
10.3 References	193
Appendix A	194
Appendix B	198
Appendix C	204
Appendix D	205
Appendix E.....	207
Publications	211

List of Figures

Figure 2.1 Components of a single PEFC	10
Figure 2.2 Tafel slope	16
Figure 2.3 Polarisation curve of a PEFC.....	21
Figure 2.4 Catalyst layer structure.....	22
Figure 2.5 Charge double layer in the electrode-electrolyte interface	23
Figure 2.6 AC current and voltage waveforms.....	24
Figure 2.7 a) AC current and voltage superimposed into an electrochemical non-linear system, b) Lissajous plot in time domain	27
Figure 2.8 Impedance of a PEFC represented in the complex plane	31
Figure 3.1 Randles electrical circuit with Warburg element	43
Figure 3.2 Electrical circuit to model the anode impedance during CO poisoning	47
Figure 3.3 Transmission line circuit	48
Figure 3.4 A small section (dx) of the equivalent circuit of a pore, (e) potential, (i) current, (x) distance along pore axis, (R) electrolyte resistance per unit pore length, (Z) electrode impedance per unit pore length.....	52
Figure 4.1 Overall experimental and modelling structure.....	76
Figure 4.2 Experimental setup.....	77
Figure 4.3 Measured impedance response in a working PEFC under potentiostatic conditions of 0.8 V at 30, 40 and 60°C	78
Figure 4.4 Equivalent circuit model for the PEFC.....	79
Figure 4.5 Comparison of impedance between simulated (-) and measured (◆) data	80
Figure 5.1 Oxygen transport in the CCL.....	87
Figure 5.2 Electrical circuit for CCL characterisation at high currents.....	95
Figure 5.3 Comparison between simulated data using Eq. 5.24 (-) and measured data (◇) from Randles circuit.....	97

Figure 6.1 a) Simulated impedance spectrum from parameters in Tab. 6.1, b) Simulated high frequency region	104
Figure 6.2 a) Simulated impedance spectrum with different inductance values, b) Simulated high frequency region.....	105
Figure 6.3 a) Simulated impedance spectrum with inductance reduced in 3 orders of magnitude, b) Simulated high frequency region.....	106
Figure 6.4 Simulated current density distribution through the CCL thickness.....	108
Figure 6.5 Experimental setup.....	110
Figure 6.6 a) EIS measurements of the PEFC and cathode electrode, b) EIS measurements at high frequency.....	112
Figure 6.7 Residual in phase angle between K-K transformed and measured data for the PEFC and cathode impedances under the influence of inductance.....	114
Figure 6.8 a) Comparison between simulated and measured data, b) High frequency region	116
Figure 7.1 Experimental setup.....	123
Figure 7.2 a) PEFC and cathode measured data at 0.12, 0.2 and 0.32 A/cm ² , b) High frequency region	125
Figure 7.3 Anode impedance spectra.....	126
Figure 7.4 Overall modelling and experimental structure.....	129
Figure 7.5 a) Comparison between measured and simulated data, b) High frequency region	130
Figure 7.6 Comparison in Bode format (modulus) between measured and simulated data	130
Figure 7.7 Comparison in Bode format (phase) between measured and simulated data.	131
Figure 7.8 Measured data with 3ms time constant and simulated data with 0.3s time constant, a) 0.12 A/cm ² , b) 0.2 A/cm ² , c) 0.32 A/cm ²	136
Figure 7.9 Measured spectra with O ₂ diluted in He and N ₂	138
Figure 8.1 Open-cathode fuel cell stack for EIS measurements	145
Figure 8.2 Polarisation curve.....	146

Figure 8.3 Stack measured data at 0.1875, 0.3125 and 0.4375 A/cm ²	147
Figure 8.4 Measured data for different cells of the stack at 0.1875A/cm ²	149
Figure 8.5 Measured data for different cells of the stack at 0.3125 A/cm ²	149
Figure 8.6 Measured data for different cells of the stack at 0.4375 A/cm ²	150
Figure 8.7 Comparison between measured data and simulated data from Eq. 8.1	152
Figure 8.8 Equivalent electrical circuit for a faradaic process with adsorption.....	153
Figure 8.9 Comparisson between measured and simulated data from Eq. 8.2.....	154
Figure 8.10 High frequency EIS measurements for cell 1 \diamond , cell 3 Δ , cell 4 \circ ; a) 0.1875A/cm ² , b) 0.3125 A/cm ² , c) 0.4375 A/cm ²	157
Figure 8.11 Estimation of mass transport resistance in each individual cell.....	157
Figure 9.1 Simulated dynamic current response along the catalyst layer at (a) 30 °C and (b) 60 °C.....	165
Figure 9.2 Current density profiles in the catalyst layer; (a) steady-state current distribution at $t = \infty$; (b) dynamic response of current at a thickness fraction of 0.8.....	166
Figure 9.3 Effect of double-layer capacitance on CCL current profiles; (a) current distribution at steady-state; (b) dynamic response, $x = 0.8$ for different capacitances, 5.2, 2.6, 7.8 and 11.4 mF / cm^2	167
Figure 9.4 Effect of ionc resistance on CCL current profiles; (a) current distribution at steady-state; (b) dynamic response, $x=0.8$ for different proton resistances, 600, 300, 900 $m\Omega cm^2$	168
Figure 9.5 Simulated current distribution of the CCL in the time domain.....	172
Figure 9.6 Simulated transitory current distribution through the CCL	172
Figure 9.7 Simulated oxygen concentration distribution through the CCL.....	173
Figure 9.8 Effect of diffusion coefficient on the transient oxygen concentration distribution in the CCL, dashed increasing by one order of magnitude, thin represents the original value.	174
Figure 9.9 Effect of diffusion coefficient on the transient current density distribution in the CCL, dashed increasing by one order of magnitude, thin represents the original value.	175

Figure 9.10 Effect of bulk oxygen concentration on the transient concentration distribution in the CCL; (a) initial response; (b) response to steady-state, dashed increasing 500 %, thin represents the original value.....	175
Figure 9.11 Effect of bulk oxygen concentration on the transient current density distribution in the CCL; (a) initial response; (b) response to steady-state, dashed increasing 500 %, thin represents the original value.....	176
Figure 9.12 Simulated current distribution through the CCL thickness using parameters from table 7.1, Chapter 7.....	177
Figure 10.1 Frequency Response System Set-up.....	193
Figure A.1 Frequency domain integral contour for deriving K-K relations.....	194
Figure B.1 Effect of the potential change on the free energy of activation.....	198
Figure B.2 Relationship between the angle of intersection and the transfer coefficient .	199
Figure B.3 Nonlinear response	200
Figure D.1 Graphical User Interface for the Numerical Electrochemical Impedance Spectroscopy Modelling tool.....	206

List of Tables

Table 4.1 Kinetics, ohmic and capacitive parameters of the PEFC estimated by Zview and Corrview software.....	80
Table 5.1 Parameters of the CCL reported in the study of Malevich.....	96
Table 6.1 Parameters of the transmission line circuit accounting for the cathode electrode.....	103
Table 6.2 Parameters accounting for the cathode spectrum obtained through the GUI.....	117
Table 7.1 Parameters of the CCL estimated through Eq. 7.1.....	133
Table 8.1. Charge transfer resistance R_C , mass transport resistance R_W and adsorption resistance R_{Ad} calculated from Eq. 8.2.....	156

Nomenclature

A	active cell area (cm^2)
b	tafel slope (mV)
c_O	surface concentration of oxygen (mol/cm^3)
c_{OX}, c_{RE}	surface concentration of species (mol/cm^3)
c_O^*	oxygen bulk concentration (mol/cm^3)
c_{OX}^*, c_{RE}^*	concentration of species in equilibrium (mol/cm^3)
C_{dl}	capacitance between dissimilar materials (F/cm^2)
D	effective diffusion coefficient (cm^2/s)
E	potential in electrode far from equilibrium (V)
E^O	potential in electrode in equilibrium (V)
E_{Nernst}	reversible potential (V)
e	electron charge (1.602×10^{-19} coulombs / electron)
F	faraday constant (96485 C/mol)
f	frequency (Hz)
G	Gibbs free energy of activation (joules/mol)
H	heat of formation of the electrochemical reaction
i	imaginary component in impedance
j	current density (A/cm^2)
j_b, j_f	backward and forward current (A/cm^2)
j_o	exchange current density (A/cm^2)
j_L	limit current (A/cm^2)
j_m	maximum rate of ion transfer (A/cm^2)
j_n	internal current (A/cm^2)
\bar{j}	current distribution in catalyst layer (A/cm^2)
k_b, k_f	backward and forward reaction rate coefficient (cm/s^{-1})

N_A	number of molecules per mole (6.022×10^{23} molecule/mole)
P	parameter related to CPE (constant phase element)
P	pressure (Pa)
P_{H_2}	partial pressure of hydrogen (Pa)
P_{O_2}	partial pressure of oxygen (Pa)
R	ideal gas constant (8.3143 J/mol-K)
R_C	charge transfer resistance ($\Omega \cdot \text{cm}^2$)
R_M	mass transfer resistance ($\Omega \cdot \text{cm}^2$)
R_T	total ohmic resistance ($\Omega \cdot \text{cm}^2$)
R_P	ionic resistance in cathode catalyst layer ($\Omega \cdot \text{cm}^2$)
R_W	resistance for the diffusion process ($\Omega \cdot \text{cm}^2$)
S	entropy of the electrochemical reaction (J/mol-K)
T	temperature (K)
T_W	time constant for the diffusion process (s)
t	time (s)
V_{FC}	fuel cell voltage (V)
V_m	molar volume of the reactant gas
v	flux of oxygen ($\text{mol}/\text{cm}^2\text{s}$)
v_b, v_f	backward and forward reaction flux of the species ($\text{mol}/\text{cm}^2\text{s}$)
x	distance along the catalyst layer ($0 \leq x \leq 1$)
Y	parameter related to CPE ($\text{s}^P/\Omega \cdot \text{cm}^2$)
y	distance along the diffusive distance ($0 \leq x \leq \delta$)
Z	impedance of cathode catalyst layer ($\Omega \cdot \text{cm}^2$)
Z_W	Warburg impedance ($\Omega \cdot \text{cm}^2$)
z	electrons released or consumed
Z'	real part of impedance ($\Omega \cdot \text{cm}^2$)
Z''	imaginary part of impedance ($\Omega \cdot \text{cm}^2$)

Greek

α	charge transfer coefficient
δ	diffusive distance (cm)
η_{act}	activation overpotential (V)
η_{ohm}	ohmic overpotential (V)
η_{con}	concentration overpotential (V)
η	overpotential (V)
$\bar{\eta}$	potential distribution in catalyst layer (V)
η_{SS}	voltage in activation loss where the impedance measurement is taken (V)
ω	angular frequency (rad/s)

Abbreviations

AC	alternating current
ACL	anode catalyst layer
BPP	bipolar plate
CE	counter electrode
CL	catalyst layer
CO	carbon monoxide
CCL	cathode catalyst layer
CPE	constant phase element
EIS	electrochemical impedance spectroscopy
FRA	frequency response analyser
FEP	fluorinated ethylene propylene
GDE	gas diffusion electrode
GDL	gas diffusion layer
GUI	graphic user interface
HOR	hydrogen oxidation reaction
IHP	inner Helmholtz plane
K-K	kramers-kronig

LMA	levenberg marquadt algorithm
MEA	membrane electrode assembly
MPL	microporous layer
MRL	manufacturing readiness level
N/C	Nafion/carbon
OCP	open circuit potential
OHP	outer Helmholtz plane
ORR	oxygen reduction reaction
PEFC	polymer electrolyte fuel cell
PEM	polymer electrolyte membrane
PFSA	perfluorosulfonic acid
PFSI	perfluorosulfonate ionomer
PTFE	polytetrafluoroethylene
Pt	platinum
RE	reference electrode
RH	relative humidity
R-C	resistor-capacitor
SEM	scanning electron microscope
STP	standard temperature and pressure
TRL	technology readiness level
WE	working electrode

Chapter 1

Introduction

Polymer electrolyte fuel cells (PEFCs) are electrochemical devices that convert the chemical energy released from a hydrogen-oxidation and oxygen-reduction (redox) process into usable electrical energy and thermal energy. The redox process occurs electrochemically in the catalyst-based electrodes of the cell and forgoes any form of combustion; the PEFC is as such theoretically unbound by the Carnot limit. Research and development worldwide over the past two decades is resulting in the gradual commercialisation of the technology for civil and military markets. In order to maximise the impact that the PEFC can bring worldwide, there is a need to develop a robust and potentially cost-effective way of monitoring and optimising the performance, reliability and operating cost as a function of service life. While much is already known about the degradation mechanisms that affect PEFCs [1], thus far, this has not been matched by practical techniques that can be applied to operational PEFC stacks to systematically diagnose them. Standard techniques are usually based on macroscopic characterisation and do not necessarily reveal specific underlying degradation mechanisms.

Variations in operating modes and general cell design according to application means that performance degradation and failure mechanisms are also likely to change according to application [2]. Key technology indicators such as technology readiness level (TRL) and manufacturing readiness level (MRL) are intrinsically governed by failure and reliability. In the context of fuel cells, failure can occur as a consequence of gradual processes, in which certain operating conditions and operational routines cause a systematic degradation of structural and electro-kinetic properties of PEFC assemblies and culminate in the loss of performance below threshold values.

Electrochemical impedance spectroscopy (EIS) is an in-situ experimental technique that can unveil the electrochemical and diffusion process that occur at different rates within the PEFC. EIS has the potential to reveal the internal state and performance of a PEFC

without affecting its ability to perform as an energy conversion device. The resulting impedance is commonly represented in a complex plane and represents the electrochemical and diffusion mechanisms of the PEFC in the frequency domain. The conventional process of employing EIS for PEFC analysis involves the interrogation of a working cell using an alternating current (AC) signal, and using this to structure an equivalent electrical circuit based on its frequency response. EIS has become a primary tool in fuel cell research and development and as a result it is not only possible to reveal general changes in cell performance, but also the changes in fundamental internal electrochemical processes can also be diagnosed. EIS can be used to distinguish between different failures in a PEFC stack under load, for instance water management failures.

EIS translated into the time domain has not been used and reported in the literature. EIS measurements translated into the time domain could allow the evaluation of critical factors during PEFC operation. This technique could be more valuable for fuel cell research.

1.1 Motivation

EIS could have the potential to determine changes in critical operational factors in PEFCs such as reactant, liquid water and current distribution, catalytic poisoning, membrane conductivity and contact resistance. The measured results from EIS are widely interpreted through various equivalent electrical circuits. However, such interpretation cannot deliver the electrochemical mechanisms which are truly occurring in the PEFC. Some misconceptions and misunderstandings about how to relate the physical processes of a PEFC within the impedance response resulting from EIS have been reported in the literature. For instance, the ohmic resistance in a PEFC from EIS measurements has been reported to be where the impedance spectrum intercepts the real part of the complex plot at high frequencies neglecting intrusive effects from the measurement system. Low frequency EIS measurements have been commonly related to gas phase oxygen transport limitations in the gas diffusion layer (GDL) neglecting any mass transport limitations in the cathode catalyst layer (CCL).

When measuring EIS over an entire PEFC stack, only average properties of stack parameters can be determined. Thus, it is not possible to identify inhomogenities in a PEFC stack. Simultaneous EIS measurements in combination with fundamental electrochemical theory of PEFCs will provide reliable information about the factors that limit the PEFC stack performance.

There is a lack of understanding of how to interpret the frequency response of the EIS in relation to the spatio-temporal electrochemical mechanisms that occur within the PEFC. An impedance-based approach which allows a spatio-temporal current distribution analysis in the CCL has not been presented or validated in the fuel cell research to date.

1.2 Objective

The main objective of this doctoral thesis is to provide a backbone understanding about how the electrochemical mechanisms of the PEFC are represented at different frequencies in the EIS complex plot using a mathematical model derived from electrochemical theory. The mathematical model will be applied with real-world EIS measurements carried in any region of the polarisation curve. The mathematical model applied to simultaneous EIS measurements in a PEFC stack will allow an insight into the change in impedance response of individual cells. The mathematical model translated into the time domain will simulate the current distribution through the CCL.

1.2.1 Particular Objectives

- 1 To generate a numerical model to predict the impedance spectrum of the CCL at low currents based on fundamental electrode theory and the measurable properties of the CCL.
- 2 To extend the mathematical model devised in (1) to simulate the impedance spectrum in the frequency domain at high currents using diffusion theory and fundamental electrochemical theory.

- 3 To provide a clear understanding about how the electrochemical and diffusion mechanisms of a PEFC are related at different frequencies of the EIS complex plot using the theoretical treatment developed in (1), and (2).
- 4 To establish an insight into the change in impedance response of individual cells within a PEFC stack through the theoretical work developed in (1), (2), (3) and simultaneous EIS measurements.
- 5 To simulate the spatio-temporal current distribution in the CCL using the theoretical work developed in (1) and (2); and to apply the model to determine the characteristic transient and spatial charge in the CCL.

1.3 Knowledge Contribution

- 1 By coupling the fundamental electrochemical theory of the fuel cell with the measurement-based EIS analysis, it is possible to open a wider scope to generate a greater understanding of how the structure, material composition, and operating conditions of the CCL govern the cell performance.
- 2 This study has demonstrated the capability to predict the effect of the effective diffusion and equilibrium oxygen concentration of CCL on the cell performance based on the measured frequency response from EIS.
- 3 This study has demonstrated that intrusive effects, e.g. inductive effect in EIS measurements, can lead to an erroneous interpretation of the PEFC electrochemical mechanisms represented in complex-plots at high frequencies.
- 4 Mass transport limitations in PEFCs have been principally attributed to the gaseous oxygen transport limitations in the GDL neglecting any mass transport limitations in the CCL. This study has demonstrated that mass transport limitations in the CCL can be manifested in EIS measurements of PEFCs.

- 5 The combination of the theoretical treatment with simultaneous EIS measurements allows the identification and particularly the evaluation of the inhomogeneous performance along a PEFC stack.

1.4 Outline of Thesis

This doctoral thesis has been divided in four sections: Fundamentals (Chapter 2 and 3) Modelling (Chapters 4 and 5), Application (Chapters 6, 7, 8 and 9) and Conclusions (Chapter 10).

Chapter 1: Introduction

The first Chapter provides a brief introduction about EIS as a powerful tool for PEFC diagnosis and discusses the motivation, objectives and contributions.

Chapter 2: Fundamentals of Polymer Electrolyte Fuel Cells and Electrochemical Impedance Spectroscopy.

The second Chapter will discuss the equations that represent the losses in potential in a PEFC and fundamental concepts of EIS.

Chapter 3: Literature Review on Electrochemical Impedance Spectroscopy in Polymer Electrolyte Fuel Cells

The third Chapter will provide a literature review on EIS measurements in PEFCs.

Chapter 4: Cathode Catalyst Layer Impedance Model for Low Current Operation.

In the fourth Chapter, a numerical model to simulate the electrochemical impedance spectra of the CCL of PEFCs will be developed. The mathematical model will establish a backbone understanding of how the low current electrochemical mechanisms relate to the electrochemical impedance response of the CCL.

Chapter 5: Cathode Catalyst Layer Impedance Model for High Current Operation.

In the fifth Chapter, the mathematical model developed in Chapter 4 for CCL low current operation will be extended to simulate the electrochemical impedance spectrum in the frequency domain of the CCL operated at high currents.

Chapter 6: Inductive Effect on the Fuel Cell Cathode Impedance Spectrum at High Frequencies.

The sixth Chapter will discuss the high frequency electrochemical impedance measurements which are attributable to the inductance of the electrical cables of the measurement system using the theoretical treatment developed in Chapters 4 and 5. This Chapter will demonstrate that the common practice of calculating the ohmic resistance in PEFCs from EIS measurements can be subject to an erroneous interpretation due to the contribution of the inductance.

Chapter 7: Low Frequency Electrochemical Mechanisms in the Cathode Impedance Spectrum.

In Chapter seven an analysis of the mechanisms presented in the low frequency part of the PEFC cathode impedance spectrum has been carried out using EIS measurements and the theoretical treatment developed in Chapters 4 and 5. The results of this Chapter will provide an insight into how low frequency EIS measurements relate to mass transport limitations.

Chapter 8: Analysis of the Performance of an Open-Cathode Polymer Electrolyte Fuel Cell Stack using Simultaneous EIS Measurements.

In the eighth Chapter, an analysis of the change of impedance response of individual cells within a commercial Open-Cathode 4-cell stack is carried out using simultaneous EIS measurements and the theoretical treatment developed in Chapters 4, 5, 6 and 7. This Chapter will provide an insight into the factors that limit the performance of the PEFC stack.

Chapter 9: Study of Current Distribution in the Fuel Cell Cathode Catalyst Layer through EIS.

In the ninth Chapter, the model developed in Chapters 4 and 5 in the frequency domain will be transformed into the time domain by reverse Laplace Transform. The developed model in time domain can be applied to unveil the effect of kinetic, ohmic, and mass transport mechanisms on current distribution through the CCL from the measured impedance results.

Chapter 10: Conclusions and Future work.

The final Chapter will outline the contributions and conclusions of this doctoral thesis and will suggest the future work to be carried out.

1.5 References

-
- [1] Rama P., Chen R., and Andrews J., “A Review of Performance Degradation and Failure Modes for Hydrogen-Fuelled Polymer Electrolyte Fuel Cells”, *Proc. IMechE Part A: J. Power and Energy*, 222, (2008) pp. 421-441.
 - [2] Yu P.T., Gu W., Makharia R., Wagner F.T., and Gasteiger H. A., “The Impact of Carbon Stability on PEM Fuel Cell Startup and Shutdown Voltage Degradation, Durability – Fuel Starvation and Start/Stop Degradation”, *ECS Trans.*, 3 (2006), pp. 797-809.

Chapter 2

Fundamentals of Polymer Electrolyte Fuel Cells and Electrochemical Impedance Spectroscopy

In this Chapter, the fundamentals of the polymer electrolyte fuel cell (PEFC) and electrochemical impedance spectroscopy (EIS) are presented. The equations that describe the losses in the PEFC potential are derived from an electrochemical, thermodynamic and fluid mechanics analysis. The phenomenological processes that occur within the catalyst layer (CL) are also described.

EIS is a technique that can be applied in-situ to characterise the PEFC at a range of different frequencies. In this chapter the effect of the alternating current (AC) signal on the electrode-electrolyte interface i.e. carbon-Nafion interface in the CL is described. When an AC current is applied on the electrode-electrolyte interface an AC voltage output is obtained. Therefore the ratio between AC voltage output and AC input at a defined frequency is known as impedance.

2.1 The Structure of the PEFC

PEFCs are the best candidates to be considered as the future source of propulsion for automobiles because they are able to produce high power density at low temperature and are not bound by the Carnot cycle. A PEFC converts the chemical energy of a fuel such as hydrogen gas into electrical and thermal energies. Two electrodes (anode and cathode) separated by a polymer electrolyte membrane (PEM) are the main components in the PEFC. Each electrode consists of a gas diffusion layer (GDL) and a CL as a minimum.

The CL is a layer made of a matrix of carbon grains providing the electron conductivity, and Pt supported on carbon as the catalyst to drive the oxygen-reduction or hydrogen-oxidation processes. The GDL is a layer made of a porous carbon cloth and its main function is to distribute reactant gases to the active zones of the CL. The GDL typically contains a wetproofing agent such as polytetrafluoroethylene (PTFE) or fluorinated ethylene propylene (FEP) to facilitate the movement of liquid water through the cell. An additional layer that can be placed between the GDL and CL is the microporous layer (MPL), which is similar in composition to the GDL but treated to a higher level of wetproofing agent in order to force the flow of liquid water in certain directions within the cell. A primary hardware component of the PEFC is the bipolar plate (BPP), which provides structural rigidity to the cell and provides conductive pathways that enable the energy-carrying electrons that are lost in the anode catalyst layer (ACL) due to hydrogen oxidation reaction (HOR) to be gained in the cathode catalyst layer (CCL) for oxygen reduction reaction (ORR). Electrons are sent to the cathode electrode by an external circuit and travel through a load to produce an electrical potential difference.

The PEM is a quasi-porous proton-conducting material which serves to simultaneously transport the ions lost in the ACL through to the CCL. It is based on a PTFE backbone that is modified to hold sulfonic acid end groups and depends upon the presence of water for ionic conductivity. They are classified as perfluorosulfonic acid (PFSA) membranes. Nafion is a common commercial example of a PFSA membrane. Structurally reinforced PEMs consist of an inter matrix which is impregnated with PFSA electrolyte. These types of PEMs are resilient to dimensional change on water uptake and are mechanically durable. Modern fuel cells use multi-layer assemblies such as the membrane electrode assembly (MEA), which is a PEM sandwiched by ACL and CCL. The MEA is then employed with two GDLs on either side to make up a single cell. A gas diffusion electrode (GDE) is another type of assembly that consists of a GDL with a CL coating on one side. Two GDEs can be used to sandwich a PEM, thereby making up a single cell again.

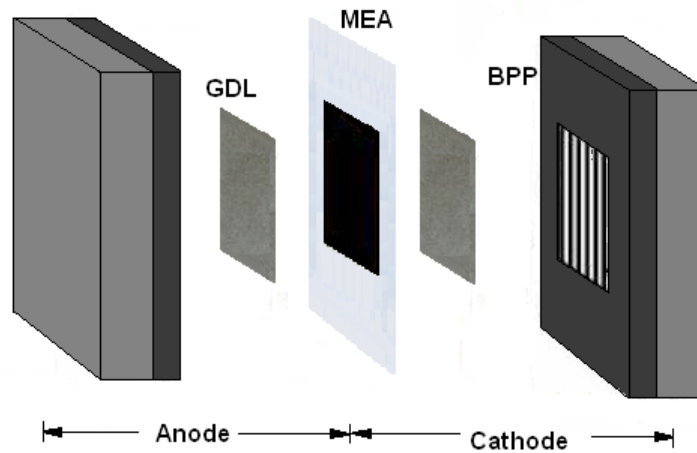


Figure 2.1 Components of a single PEFC

2.2 The Voltage Output in the PEFC

When an external circuit which allows the flow of electrons between the anode and cathode is not connected to the PEFC, an ideal voltage or reversible potential is present in the PEFC. This reversible potential is derived from thermodynamic principles and is also known as the Open Circuit Potential (OCP).

2.2.1 Reversible Potential

In an exothermal process such as the combustion of a fuel, the energy released is the heat of the chemical reaction or enthalpy. Enthalpy of a chemical reaction is the difference between heat of formation of products and reactants. Although combustion is not present in the PEFC, the enthalpy of the hydrogen combustion reaction is considered as a way to measure the energy input in a PEFC. Therefore the amount of reaction enthalpy that can be converted to electrical energy in a PEFC is known as Gibbs Free Energy (G).

For each hydrogen molecule consumed and each water molecule produced, two electrons travel through an external circuit connected between the anode and the cathode. For one mole of hydrogen consumed in the HOR, $2N_A$ electrons travel between the anode and

cathode, where N_A is Avogadro's number. The electrical charge that flows between the electrodes is represented as:

$$q = zN_A e = zF \quad (2.1)$$

where z is the number of electrons travelling between the electrodes, N_A is the number of molecules per mole = 6.022×10^{23} molecule/mol, e is the electron charge 1.602×10^{-19} coulombs / electron and F is the Faraday constant 96485 coulombs / electron-mole. The electrical work in the PEFC is defined as the product of the charge transferred in the fuel cell reaction and the potential:

$$-W_{el} = zFE \quad (2.2)$$

If the system is reversible, the electrical work is equal to the change in Gibbs Free Energy; therefore the potential in the PEFC is given by:

$$E = -\frac{\Delta G}{zF} \quad (2.3)$$

For standard temperature and pressure (STP, 298.15 °K and 1 bar), the potential is expressed as:

$$E^o = -\frac{\Delta G^o}{zF} \quad (2.4)$$

The potential of a PEFC at STP is 1.23 Volts. The Gibbs Free Energy changes at different temperature and pressure. The fuel cell potential at different temperature and pressure is obtained through a thermodynamic analysis [1].

For an isothermal process the change in Gibbs Free Energy is expressed as:

$$dG = V_m dp \quad (2.5)$$

where V_m is the molar volume of the reactant gas, and p is the pressure. Considering the reactant gas as a perfect gas ($pV_m = RT$) and substituting into Eq. 2.5 yields:

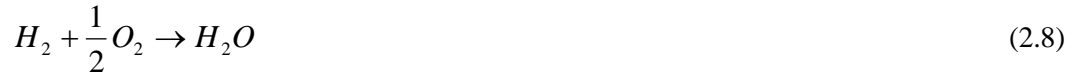
$$dG = RT \frac{dp}{p} \quad (2.6)$$

Integrating Eq. 2.6 and considering a change in pressure from the standard pressure p° to a partial pressure p with the reactant gas yields to:

$$G = G^\circ + RT \ln\left(\frac{p}{p^\circ}\right) \quad (2.7)$$

where G° and p° are the Gibbs Free Energy and pressure at standard conditions (1 bar).

For the general cell reaction:



The change in Gibbs Free Energy of the electrochemical reaction (change between products and reactants) expressed in Eq. 2.8 is given by:

$$\Delta G = G_{H_2O} - G_{H_2} - \frac{1}{2} G_{O_2} \quad (2.9)$$

Substituting Eq. 2.9 into Eq. 2.7 yields:

$$\Delta G = \Delta G^\circ + RT \ln \frac{\left[\frac{p_{H_2O}}{p^\circ}\right]^1}{\left[\frac{p_{H_2}}{p^\circ}\right]^1 \left[\frac{p_{O_2}}{p^\circ}\right]^{\frac{1}{2}}} \quad (2.10)$$

Substituting Eqs. 2.3, 2.4 into 2.10 yields:

$$E = E^o + \frac{RT}{zF} \ln \frac{\left[\frac{p_{H_2}}{P^o} \right]^1 \left[\frac{p_{O_2}}{P^o} \right]^{\frac{1}{2}}}{\left[\frac{p_{H_2O}}{P^o} \right]^1} \quad (2.11)$$

Eq. 2.11 is only valid for gaseous products and reactants. When liquid water is produced in the fuel cell the partial pressure of the products is equal to $p_{H_2O} = 1$. Also considering the reference pressure as $P^o = 1$, Eq. 2.11 can be represented as:

$$E = E^o + \frac{RT}{zF} \left[\ln(p_{H_2}) + \frac{1}{2} \ln(p_{O_2}) \right] \quad (2.12)$$

Eq. 2.12 represents the potential of the fuel cell for different partial pressures of the reactants. This potential can also change for different temperature; therefore Eq. 2.12 is modified as:

$$E = E^o + E_T^o + \frac{RT}{zF} \left[\ln(p_{H_2}) + \frac{1}{2} \ln(p_{O_2}) \right] \quad (2.13)$$

where E_T^o is the potential as a function of the temperature. From the thermodynamic theory, it is possible to represent the change in Gibbs free energy as:

$$\Delta G^o = \Delta H^o - T^o \Delta S^o \quad (2.14)$$

where ΔH^o is the heat of formation of the electrochemical reaction, T^o is the ambient temperature, and ΔS^o is the entropy of the electrochemical reaction at standard conditions. If the temperature is different from the standard temperature, the change in Gibbs free energy can be expressed as:

$$\Delta G_T = \Delta H_T - T \Delta S_T \quad (2.15)$$

According to Brady and Holum [2] the magnitudes of $\Delta H_T, \Delta S_T$ are insensitive for any change in temperature. This is because the heat of formation and entropy of both reactants and products increase equally with increasing temperature; therefore the difference between ΔH_T and ΔS_T is roughly the same. With an approximation given by:

$$\Delta G_T \approx \Delta H^o - T\Delta S^o \quad (2.16)$$

it is possible to consider that:

$$\Delta G_T^o = \Delta G^o - \Delta G_T \quad (2.17)$$

Substituting Eqs. 2.14, 2.16 into Eq. 2.17 yields:

$$\Delta G_T^o = \Delta S^o(T - T^o) \quad (2.18)$$

Substituting Eq. 2.18 into $-\Delta G_T^o = zFE_T^o$ which considers a reversible process gives:

$$E_T^o = \frac{-\Delta S^o(T - T^o)}{zF} \quad (2.19)$$

Finally substituting Eq. 2.19 into Eq. 2.13 gives the potential of the fuel cell at different temperature and pressure from standard conditions, as such:

$$E = E^o + \frac{-\Delta S^o(T - T^o)}{zF} + \frac{RT}{zF} \left[\ln(p_{H_2}) + \frac{1}{2} \ln(p_{O_2}) \right] \quad (2.20)$$

Eq. 2.20 is known as Nernst Equation and can be expressed as:

$$E_{Nernst} = 1.229 - 0.85 \times 10^{-3}(T - 298.15) + 4.31 \times 10^{-5} T \left[\ln(p_{H_2}) + \frac{1}{2} \ln(p_{O_2}) \right] \quad (2.21)$$

where E_{Nernst} is the reversible potential of the PEFC, T is the operating temperature, p_{H_2} is the partial pressure of hydrogen and p_{O_2} is the partial pressure of oxygen. When an external circuit with a load is connected between the anode and cathode to allow electrical current to flow, losses in the reversible potential occur due to the following factors:

- The kinetics of the electrochemical reactions due to the energy required to overcome the barrier changes in the electrode potential.
- Electronic and ionic resistances.
- Fuel Crossover through the membrane.
- Low reactant concentration in the electrodes due to mass transport limitations.

Commonly in the field of electrochemistry, the losses in the reversible potential are defined as overpotentials. This term has been coined because they are voltages superimposed over the reversible potential and in the fuel cell reduces the reversible potential.

2.2.2 Activation Overpotential

This overpotential is associated with the kinetics of the electrochemical reactions that take place on the electrode surface. The velocity of a chemical reaction is defined as the amount of substance in moles which is either electro-oxidized or electro-reduced by unit of time. This velocity is expressed as a function of the electrode area because the electrochemical reaction takes place between the electrode and the electrolyte interface, i.e. Nafion/Carbon interface. The rate of ORR for being the slowest reaction and the most complicated reaction sequence determines the velocity of the electrochemical reaction in the PEFC and therefore determines the activation overpotential. The activation overpotential can be expressed mathematically through the Tafel equation [1] as:

$$\eta_{act} = \frac{RT}{\alpha z F} \ln \left(\frac{j}{j_0} \right) \quad (2.22)$$

where R is the ideal gas constant, T is the operational temperature, z is the number of electrons released or consumed during the electrochemical reaction, F is the Faraday constant, α is the charge transfer coefficient and determines the magnitude of the non equilibrium between a par redox process to transfer electric charge between the electrode-electrolyte interface, j is the rate of electrical current density at which the electrochemical reactions are taking place, and j_0 is the exchange current density and relates the rate at which a reversible reaction takes place. This parameter can change in orders of magnitude for different electrochemical reactions and different electrode composition. In this case, if the exchange current is high, an increase in the activity of the electrode surface is expected. Eq. 2.22 is derived from a slope which relates the activation overpotential η_{act} as a function of the natural logarithm of the current j .

$$\eta_{act} = a + b \ln(j) \tag{2.23}$$

where:

$$a = -(RT / \alpha z F) \ln(j_0) \quad \text{and} \quad b = RT / \alpha z F$$

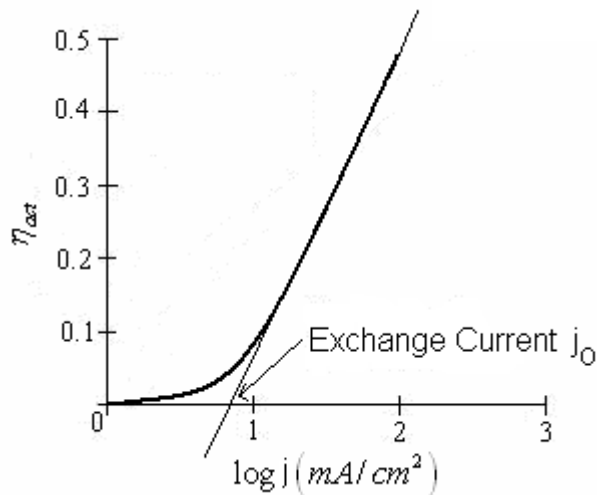


Figure 2.2 Tafel slope

Fig. 2.2 shows the Tafel slope to estimate the exchange current in the activation overpotential. The curve shown in Fig 2.2 represents the activation overpotential for an electrode (anode or cathode) and is obtained experimentally through a three electrode configuration in the PEFC. In the three electrode configuration, one electrode is the working electrode at which species undergo a redox reaction to give the analytical change in current or potential, a second electrode is called the counter electrode which carries the current (via a redox process). A third electrode called reference electrode is positioned close to the working electrode to minimize the effect of the PEM resistance on the activation polarisation curve.

To reduce the activation overpotential in the PEFC, the following factors have to be considered: raising the operating temperature to improve the kinetics of the electrochemical reaction, using more effective catalysts (this will increase the exchange current density), increasing reactant concentration (using pure oxygen instead of air), and increasing the operating pressure. This overpotential is dominant at low current densities and low temperature and occurs mainly at the cathode for being a much more complicated reaction sequence.

2.2.3 Ohmic Overpotential

Electronic resistance in the electrodes and bipolar plates and ionic resistance in the electrolyte of the CL and PEM are related to this type of overpotential. The drop in voltage due to the ohmic losses is proportional to the increase in current, as such:

$$\eta_{ohm} = jR_T \quad (2.24)$$

where j is the total current density and R_T is the total ohmic resistance to the flow of ions and electrons in the PEFC. To reduce the ohmic overpotential, electrodes and PEM with high electronic and ionic conductivity and also a good design and an appropriate selection of material for bipolar plates have to be considered.

2.2.4 Mass Transport Overpotential

The reactant gas after diffusing towards the electrode-electrolyte interface in the CL is consumed during the electrochemical reaction thereby a reactant concentration gradient is present. The gas concentration in the CL surface is less than the concentration present in the bulk of the GDL and bipolar plate. This drop in concentration affects the potential to produce the required electrical current. The gas reactant concentration in the CL will drastically be reduced if the gas reactant is consumed faster than it can reach the electrode-electrolyte interface. This phenomenon will lead to a limiting electrical current. Fick's first law relates the diffusive flux to the concentration field assuming that the flux occurs from the region of high concentration to the region of low concentration. The flux rate is a measure of the amount of substance that will flow through a defined area during a time interval.

$$v = \frac{D(c^* - c)}{\delta} \quad (2.25)$$

where v is the flux of the reactant gas through the electrode, D is the (effective) diffusion coefficient of the reactant gas and c^* is the bulk concentration, c is the reactant concentration at the surface of the CL, and δ is the diffusive distance. Substituting Faraday's law $v = j/zF$ into Eq. 2.25 yields a current density generated due to the difference in reactant concentration:

$$j = \frac{zFD(c^* - c)}{\delta} \quad (2.26)$$

where j is the current density, z is the number of electrons released or consumed, and F is the Faraday constant. A limiting current is present when there is no reactant gas in the CL surface $c = 0$, as such:

$$j_L = \frac{zFDc^*}{\delta} \quad (2.27)$$

If the partial pressure of one of the reactant gases (hydrogen or oxygen) changes from p_1 to p_2 and the other reactant is unchanged, Eq. 2.12 can be expressed as:

$$E_1 = E^o + \frac{RT}{zF} \ln(p_{1H_2,O_2}) \quad E_2 = E^o + \frac{RT}{zF} \ln(p_{2H_2,O_2}) \quad (2.28)$$

where z is the number of electrons released n or consumed $2n$ in the HOR and ORR respectively. Then the potential will change as:

$$\Delta E = E_2 - E_1 = \frac{RT}{zF} \ln(p_{2H_2,O_2}) - \frac{RT}{zF} \ln(p_{1H_2,O_2}) \quad (2.29)$$

Eq. 2.29 can be expressed as a function of the reactant concentrations, as such:

$$\Delta E = \frac{RT}{zF} \ln \left(\frac{c_{H_2,O_2}}{c_{H_2,O_2}^*} \right) \quad (2.30)$$

where c_{H_2,O_2}^* is the bulk concentration and is derived from the initial pressure supplied p_1 , and c_{H_2,O_2} is derived from p_2 and represents the surface concentration of the reactants in the CL for anode or cathode. The potential difference due to the change in concentration between the CL surface and the bulk supplied is called concentration overpotential. When the term inside the brackets of Eq. 2.30 is equal to 1 (low current range), mass transport overpotential becomes negligible. At high current density the term inside the brackets becomes less than 1, and Eq. 2.30 results in a negative expression for the concentration overpotential. Therefore the equation for the mass transport overpotential has to be considered with a negative sign. Substituting Eqs. 2.26, 2.27 into Eq. 2.30, yields the mass transport overpotential as a function of the current density:

$$\eta_{con} = -\frac{RT}{zF} \ln \left(\frac{j_L - j}{j_L} \right) \quad (2.31)$$

2.2.5 Operating Voltage in a PEFC

Combining the reversible potential defined in Eq. 2.21 with the Eqs. 2.22, 2.24, 2.31 that define each overpotential, it is possible to define a general equation for the operating voltage of a fuel cell at a current density j , as such:

$$V_{FC} = E_{nerst} - \eta_{act} - \eta_{ohm} - \eta_{con} \quad (2.32)$$

The PEM can conduct small amounts of electrons from the anode to the cathode. This effect is known as internal current in the PEFC. In the same way, there is hydrogen that crosses through the PEM. This amount of hydrogen passing from anode to cathode reacts with oxygen molecules due to the Pt catalyst, producing no flow of electrons through the external circuit. Hydrogen that migrates through the PEM is known as fuel crossover. This effect of fuel crossover is similar to the internal current because the crossover of one hydrogen molecule from anode to cathode wastes two electrons, and is the same as the two electrons crossing from anode to cathode internally, rather than from the external circuit. The magnitude of the internal current is in the order of 10^{-3} Amperes. Larminie and Dicks [1], and Balking, [3] have included this internal current in the irreversibilities defining the operating voltage of a fuel cell as:

$$V_{FC} = E_{nerst} - \frac{RT}{\alpha z F} \ln\left(\frac{j + j_n}{j_o}\right) - (j + j_n)R_T + \frac{RT}{zF} \ln\left(\frac{j_L - (j + j_n)}{j_L}\right) \quad (2.33)$$

The reversible potential calculated from Eq. 2.21, at ambient temperature and pressure is equal to 1.23 Volts, however in practical situations this reversible potential can drop to a value less than 1 Volt due to the internal current. This effect can be calculated in Eq. 2.33 at a zero current density j .

The voltage of a fuel cell can be represented through a Voltage-Current Density plot. In electrochemistry this plot is known as polarisation curve because this curve represents any change in the equilibrium potential of the electrochemical reactions due to the irreversibilities present in a PEFC. The voltage of a fuel cell as a function of the current density is shown in Fig. 2.3.

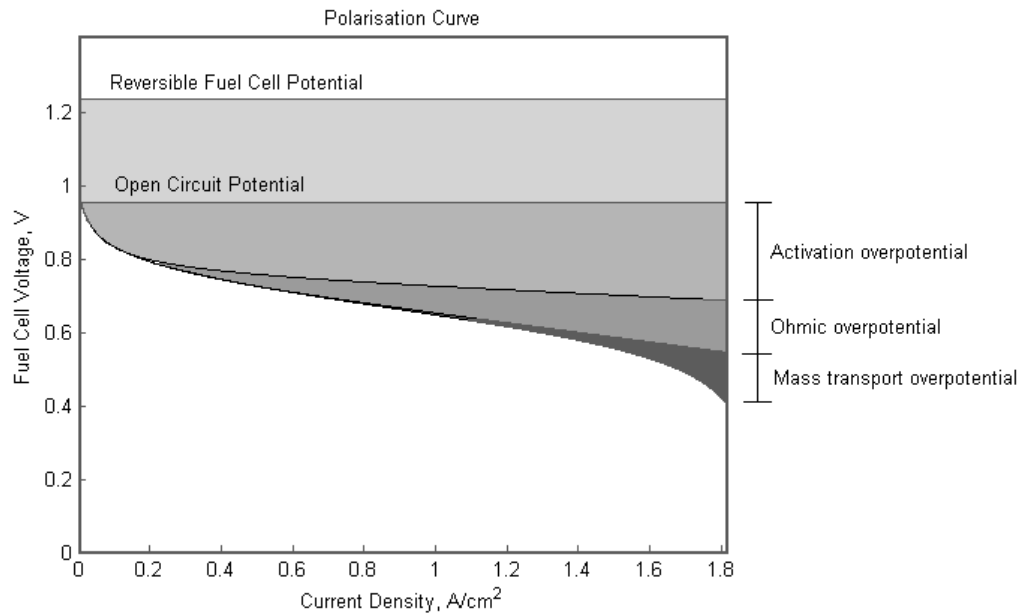


Figure 2.3 Polarisation curve of a PEFC

2.3 The Catalyst Layer

The CL is commonly formed by a composite structure of a matrix of carbon grains providing the electron conductivity, Pt supported on carbon as the catalyst, PTFE as a binder stabilizing the carbon matrix and as a hydrophobizing agent, and electrolyte network of perfluorosulfonate ionomer (PFSI) soaked with water. The carbon particles typically support noble metal or noble metal alloy deposits (i.e., platinum Pt, platinum-ruthenium PtRu) with sizes in the range of 2-5 nm on its surface to drive the electrochemical reactions forward at the operating temperatures of the PEFC. In addition, the CL contains a dispersion of polymer electrolyte to ensure continuity for ion conduction via the PEM.

The resulting matrix structure is porous in nature and characterised by tortuous pathways for reactant transport. The matrix of carbon grains forms agglomerate structures. The agglomerated structure of the CL presents a bi-functional pore distribution. Primary pores are the pores existing inside the agglomerates between the Pt/C particles. It has

been proposed that the molecules of the polymer electrolyte do not penetrate into the Pt/C particles [4]. Instead these molecules form a pathway of ion conduction attached to the surface of the agglomerated structure. Secondary pores constitute the void spaces between agglomerates. Electrochemical reactions in the PEFC rely upon the utilisation of Pt in the CL. Utilisation can be defined as the ratio of the electrocatalytic active surface area, which is accessible to the electrons and ions, to the total surface area of platinum. The literature suggests that it is possible to achieve a platinum utilisation of 86 – 87 % [5].

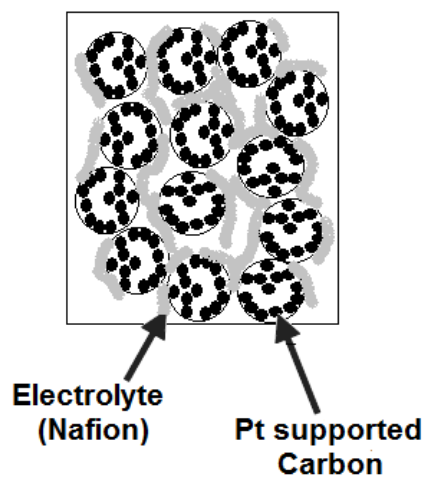


Figure 2.4 Catalyst layer structure

2.3.1 The Charge Double Layer in the Catalyst Layer

The CL is formed by a double layer structure for the interface between the electrode (Pt supported carbon) and electrolyte (Nafion) materials. At this interface electrons will be collected at the surface of the electrode and hydrogen ions H^+ will be attracted to the surface of the electrolyte. In the cathode electrode, electrons and ions, together with the oxygen supplied will take part in the ORR. A potential difference is present because of the charge distribution between electrons and ions at the electrode-electrolyte interface. This potential difference has a determinant role in the charge distribution within the reactants as well as in the position and orientation of the reactant to form the desired product. This potential difference is the sum of activation and mass transport overpotentials defined in section 2.2, hence an electrode-electrolyte interface in the CL

has to be presented during the HOR and ORR. The electrolytic phase consists of two interfaces. The interface closer to the electrode, known as inner interface, contains water molecules and sometimes other species such as ions which are specifically adsorbed. This layer is also known as Helmholtz or Stern Layer. The locus of the electrical centres of the ions is called the inner Helmholtz plane (IHP) which is at a distance x_1 from the electrode interface. The second interface presents solvated ions and can only approach the electrode at a distance x_2 , the locus centres of these solvated ions is called the outer Helmholtz plane (OHP). When the OHP has the same amount of charge as in the electrode surface, there are two layers charged. The interaction of the solvated ions with the electrode is assumed to be electrostatic in nature, so that interaction is independent of the chemical properties of the ions. Helmholtz considered that there is a potential drop confined just between the OHP in the solution and the electrode surface. This phenomenon is analogous to an electrical capacitor which has two plates of charge separated by a distance. Hence this phenomenon is called the double layer capacitance in the CL. However there are more factors to consider which can be in competition with the electrostatic interactions in this electrode-electrolyte interface such as diffusion/mixing in the solution. Under this factor, the ions are assumed to be able to move along the electrolyte. This region is called the diffusive layer which extends from the OHP into the bulk in the solution.

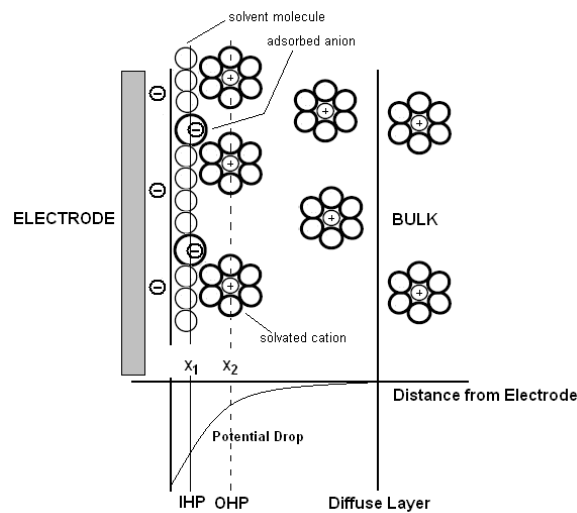


Figure 2.5 Charge double layer in the electrode-electrolyte interface

2.3.2 AC Current in the Charge Double Layer of the Catalyst Layer

When an alternating current passes through the CL, electrons are pushed and pulled away from the double layer, at the supply frequency. There is no net current flow. During the positive cycle of the AC current, conventional current flows to the double layer, and then electrons are formed in the electrode-electrolyte interface. This phenomenon attracts solvated ions from the diffuse layer. During the negative cycle of the AC current, a conventional current is drawn from the double layer interface and releases solvated ions towards the diffusive layer. The AC current makes the solvated ions oscillate to and from the diffuse layer at a defined frequency. It is possible to model the distribution of ions in the electrolyte in terms of capacitive elements. The AC current presents a 90° phase shift in relation to the AC voltage, as shown in Fig. 2.6.

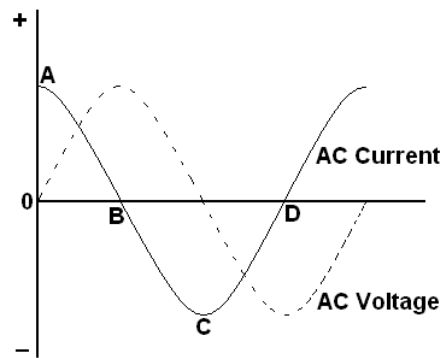


Figure 2.6 AC current and voltage waveforms

Fig. 2.6 shows that when the current has its maximum amplitude (A), the electrons flow back to the double layer and solvated ions from the diffusive layer are attracted to the electrode interface, at this point the potential difference is equal to zero. When the current is passing down through zero (B), the double layer is fully charged, the solvated ions from the diffusive layer are closer to the electrode interface and there is a maximum potential difference. When the AC current amplitude is at its minimum value (C), the electrons flow away from the double layer, and the attracted solvated ions are released back to the diffuse layer and the voltage goes to zero. The double layer is fully discharged when the voltage is at its minimum value (D).

2.4 Fundamental Concepts of Electrochemical Impedance Spectroscopy

EIS is an experimental technique to measure the opposition to the flow of an AC current within an electrochemical system which contains elements that dissipate energy and store energy. The opposition to the AC load, or impedance, can be measured over a range of frequencies thereby revealing the frequency response of the system. The term ‘frequency response’ corresponds to the steady-state response of the PEFC to a sinusoidal input. When the PEFC is subjected to a sinusoidal input (current), a sinusoidal output (voltage) will be produced at the same frequency as the input. However, the amplitude and phase of the output will be different from those of the input. To characterise the PEFC in the frequency domain, it is necessary to specify the amplitude ratio between the sinusoidal output (voltage) and the sinusoidal input (current), and the phase shift ratio between the sinusoidal output and the sinusoidal input as a function of the frequency.

A sinusoidal current signal of amplitude I_{AC} (amps) can be defined as:

$$I(t) = I_{AC} \sin(\omega t) \quad (2.34)$$

where t is time (seconds), $\omega = 2\pi f$ is the angular velocity in radians/seconds, f is the frequency (Hz). The output AC voltage signal obtained from the electrochemical system can be defined as:

$$V(t) = V_{AC} \sin(\omega t - \theta) \quad (2.35)$$

where V_{AC} is the amplitude of the output voltage (volts), and θ is the phase angle (radians). The phase angle is the difference between the phase of the sinusoidal voltage and sinusoidal current signals. A pure resistance can be calculated from Ohm’s law but in the case of an electrochemical system the resulting impedance is not purely resistive and is a function of the frequency of oscillation of the input signal. Ohm’s law for the AC case is expressed as:

$$Z = \frac{V_{AC} \sin(\omega t - \theta)}{I_{AC} \sin(\omega t)} \quad (2.36)$$

where Z is known as the impedance of the electrochemical system. Eq. 2.35 can be expressed with trigonometric relationships as:

$$V(t) = V_{AC}' \sin(\omega t) + V_{AC}'' \cos(\omega t) \quad (2.37)$$

where $V_{AC}' = V_{AC} \cos(\theta)$ and $V_{AC}'' = -V_{AC} \sin(\theta)$. The first term of Eq. 2.37 on the right hand side represents the voltage output component in phase with $I(t)$. The second one represents the output voltage component out of phase by $\pi/2$ with respect $I(t)$. The impedance in Eq. 2.36 can be expressed through a complex number and through the following relation:

$$Z = Z' + iZ'' \quad (2.38)$$

where $Z' = \frac{V_{AC}' \sin(\omega t)}{I_{AC} \sin(\omega t)}$ represents the real part and $Z'' = \frac{V_{AC}'' \cos(\omega t)}{I_{AC} \sin(\omega t)}$ the imaginary part of the complex number.

2.4.1 Experimental Methods for Impedance Measurements

One key advantage of the EIS technique is that it is non-invasive and can be applied *in-situ*. Another advantage is that the frequency response tests are simple to carry out and can be easily tuned for greater accuracy by using readily-available sinusoidal generators and precise measuring equipment. Impedance experiments involve the conversion of time-domain input and output signals into a complex quantity that is a function of frequency.

Lissajous Analysis

Prior to the use of frequency response analysers (FRAs), which convert time domain signals into frequency domain signals through a Fourier analysis, an analysis of Lissajous figures on oscilloscope screens was the accepted method for impedance measurements.

The amplitude of AC current and voltage superimposed into an electrochemical system response to estimate the impedance are represented in Fig. 2.7.

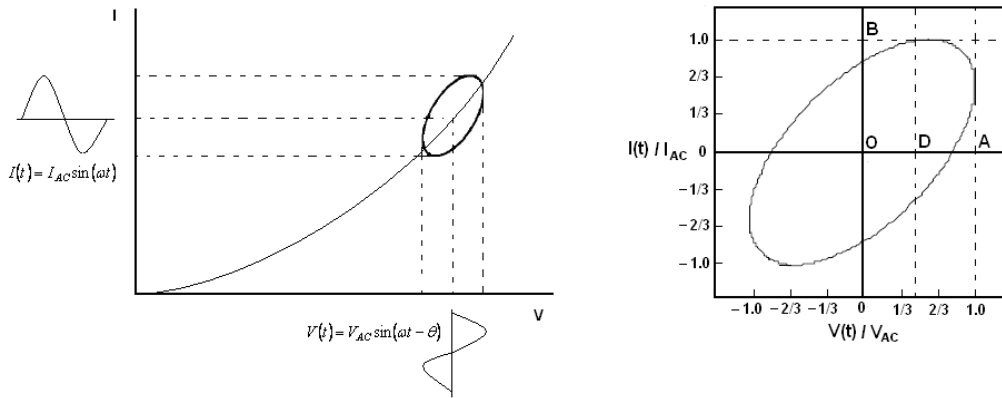


Figure 2.7 a) AC current and voltage superimposed into an electrochemical non-linear system, b) Lissajous plot in time domain

Fig. 2.7a) shows that for impedance analysis in non-linear systems, a small input amplitude signal has to be superimposed onto the Voltage-Current response. This small amplitude allows us to estimate the Voltage-Current response as a pseudo-linear system. For linear systems, high input amplitude can be superimposed. Fig. 2.7b represents a normalised value for the magnitudes of the time-domain signals. The shape of the ellipse provides information about the magnitude and phase angle of the impedance between output and input signals. The magnitude of the complex number expressed in Eq. 2.38 is obtained from Figure 2.7b) as:

$$|Z| = \frac{V_{AC}}{I_{AC}} = \frac{OA}{OB} \quad (2.39)$$

and the phase angle is represented as:

$$\vartheta = \sin^{-1}\left(-\frac{OD}{OA}\right) \quad (2.40)$$

The shape of the ellipse represented in the Lissajous plot of Fig 2.7 b) changes at different frequencies.

Frequency Fourier Analysis

Currently FRAs have replaced the Lissajous analysis through mathematical transformations by Fourier analysis. FRAs use an orthogonal system that involves sines and cosines to determine the complex impedance of a single-frequency input signal. A periodic function of time $f(t)$ that is integrated on $[-\pi, \pi]$ can be expressed as a Fourier series as:

$$f(t) = \frac{a_0}{2} + \sum_{n=1}^{\infty} [a_n \cos(n\omega t) + b_n \sin(n\omega t)] \tag{2.41}$$

where

$$a_0 = \frac{1}{\pi} \int_{-\pi}^{\pi} f(t) dt \quad a_n = \frac{1}{\pi} \int_{-\pi}^{\pi} f(t) \cos(n\omega t) dt \quad b_n = \frac{1}{\pi} \int_{-\pi}^{\pi} f(t) \sin(n\omega t) dt$$

are the Fourier coefficients of $f(t)$. Eq. 2.41 can be represented in terms of exponentials through Euler's formula, as such:

$$f(t) = \sum_{n=-\infty}^{\infty} [c_n e^{in\omega t}] \tag{2.42}$$

and the Fourier coefficients a_0, a_n, b_n are related to $c_n =$

$$\begin{matrix} (1/2)(a_n - ib_n) & n > 0 \\ (1/2)a_0 & n = 0 \\ (1/2)(a_{-n} + ib_{-n}) & n < 0 \end{matrix}$$

The coefficient c_n from Eq. 2.42 can be evaluated from:

$$c_n = \frac{1}{T} \int_0^T f(t) e^{-in\omega t} dt \tag{2.43}$$

where T is the period of the signal at frequency $\omega = 2\pi f$. Eq. 2.43 can be expressed in terms of Euler's formula:

$$c_n = \frac{1}{T} \int_0^T f(t) (\cos(n\omega t) - i \sin(n\omega t)) dt \tag{2.44}$$

The input AC current signal defined in Eq. 2.34 can be expressed in terms of exponential Fourier series Eq. 2.41 as:

$$I(\omega) = \frac{1}{T} \int_0^T I(t) (\cos(\omega t) - i \sin(\omega t)) dt \quad (2.45)$$

and the output AC voltage signal defined in Eq. 2.35 can be expressed as:

$$V(\omega) = \frac{1}{T} \int_0^T V(t) (\cos(\omega t) - i \sin(\omega t)) dt \quad (2.46)$$

The real parts of the current and voltage signals are defined as:

$$I_R(\omega) = \frac{1}{T} \int_0^T I(t) (\cos(\omega t)) dt \quad V_R(\omega) = \frac{1}{T} \int_0^T V(t) (\cos(\omega t)) dt \quad (2.47, 2.48)$$

The imaginary parts of the current and voltage signals are defined as:

$$I_i(\omega) = -\frac{1}{T} \int_0^T I(t) \sin(\omega t) dt \quad V_i(\omega) = -\frac{1}{T} \int_0^T V(t) \sin(\omega t) dt \quad (2.49, 2.50)$$

The impedance is the ratio between the complex numbers of the output signal and the input signal, as such:

$$Z = \frac{V_R(\omega) + iV_i(\omega)}{I_R(\omega) + iI_i(\omega)} \quad (2.51)$$

2.4.2 Kramers-Kronig Relations

The impedance resulting from the Fourier analysis has to be consistent with Kramers-Kronig (K-K) Relations. These relations are mathematical properties that relate the real and imaginary part of the frequency response resulting from the electrochemical system studied. K-K relations are applied to systems which are linear, causal and stable and have

been applied in electrochemical impedance data over the last 20 years [6,7,8]. In K-K the condition of stationarity implies that the causality condition is satisfied, and conversely causality condition implies stationarity of the corresponding electrochemical system. The derivation of these mathematical relations begins with an application of Cauchy's Integral Theorem [9] which defines the integral around a closed contour and evaluates the real part or imaginary part of the impedance at a particular frequency with a pole ω created in the real axis of the frequency domain. See Appendix A for derivations of these mathematical relations.

The Kramers-Kronig relation that defines the imaginary part Z'' from the real part Z' at a particular frequency ω is defined as:

$$Z''(\omega) = -\frac{2\omega}{\pi} \int_0^{\infty} \frac{Z'(x) - Z'(\omega)}{x^2 - \omega^2} dx \quad (2.52)$$

and the imaginary part obtained from the real part of the impedance is:

$$Z'(\omega) = Z'(\infty) + \frac{2}{\pi} \int_0^{\infty} \frac{xZ''(x) - \omega Z''(\omega)}{x^2 - \omega^2} dx \quad (2.53)$$

where x is an independent and continuous variable that represents the complex frequency. If the experimental imaginary part does not coincide with the transformed imaginary part (real to imaginary transformation), and the real imaginary part with the transformed real part; the data are not obtained under a causal system (the measured response is due only to the AC perturbation applied), linear system (for small AC perturbations) or stable system (the system returns to its original state after the perturbation is removed and does not change with time). The Kramers-Kronig relations cannot be used to determine if the measurements were corrupted by instrument artifacts.

2.4.3 Representation of the Impedance in the Complex Plane

Frequency response is often represented in a complex-impedance-plane or Nyquist format. The data are presented as a locus of points, where each data corresponds to a different measurement frequency. Complex-impedance-plane plots are very popular because the loci of the points yield an insight into the possible mechanisms of governing phenomena. A disadvantage of the Nyquist format is that frequency dependence and low impedance values are obscured. Characteristic frequencies should always be labelled to allow a better understanding of the time constant of the underlying phenomena.

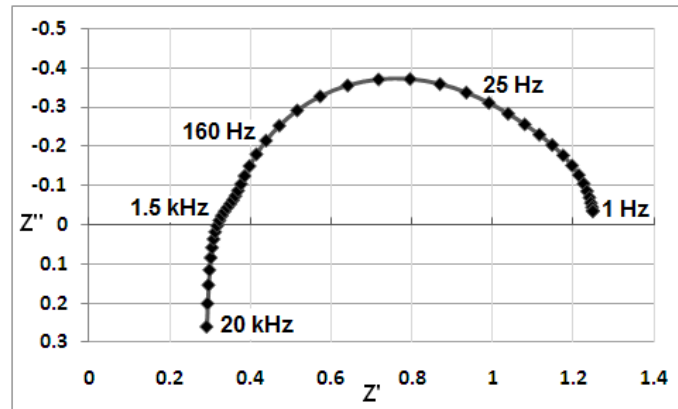


Figure 2.8 Impedance of a PEFC represented in the complex plane

Fig. 2.8 represents the impedance of a PEFC obtained through a FRA. In the literature [10,11], the values of the PEFC impedance at high frequencies with positive imaginary component in the complex-impedance plot have been attributed to the inductance of the electrical cables of the measurement system. This inductive effect could alter the shape of the Nyquist plot and lead to erroneous structure interpretations. Merida *et al.* [12] reported in his work that it is possible to minimise this inductive effect by maintaining equal lengths in the cables, twisting the leads, and polishing and clamping the metal contacts. In Fig. 2.8 the impedance value where the spectrum intercepts the real axis Z' (1.5 kHz) is related to the ohmic resistance in the PEFC [13,14]. At medium frequency (160 Hz-20 Hz) the spectrum features the charge transfer resistance during the ORR. This can provide information about the catalyst loading and catalyst utilization in the CL to drive the electrochemical reactions [15]. The impedance values at low frequencies (5 Hz -

1 Hz) feature mass transport limitations. These limitations account for the low diffusivity of oxygen to permeate into the active sites in the CL. The interpretation of the electrochemical and diffusion mechanisms in the PEFC impedance plot remains a challenge for fuel cell research. The use of equivalent electrical circuits with the experimental EIS technique is a well-established methodology to characterise processes in the PEFC. An electrical circuit can represent an identical impedance response to that obtained from the electrochemical system studied. Each electrical component in the electrical circuit describes a physical process that takes place in the electrochemical system. The most common electrical components to represent the impedance response in an electrochemical system are as follow:

Resistor, this component represents energy losses, electronic and ionic conductance in solid and aqueous medium. This element does not depend upon the frequency range applied.

Inductance, this component relates a magnetic field generated in electrical conductors of the measurement system and in the electrodes of an electrochemical system studied.

Capacitance, this component reflects the accumulation of electrostatic energy between two dissimilar materials.

Warburg, this element represents the opposition for diffusion of a chemical species in a finite or semi-infinite planar medium in the frequency domain.

Constant Phase Element (CPE), this element reflects the exponential distribution of time-constants in an electrode-electrolyte interface.

The next Chapter will describe the electrical circuits commonly reported in the literature to characterise the processes in the PEFC using EIS measurements.

2.5 References

- [1] Larminie J. and Dicks A., "Fuel Cell System Explained", Wiley, (2003) England.
- [2] Brady J.E. and Holm J.R., "Chemistry: The Study of Matter and Its Changes", John Wiley & Sons, Brisbane, (1996) Australia.
- [3] Balkin, A.R., "Modelling a 500W Polymer Electrolyte Membrane Fuel Cells", Thesis, Faculty of Engineering, University of Technology, Sydney, (2002), Australia.
- [4] Malek K., Eikerling M., Wang Q., Navessin T., and Liu Z., "Self-Organization in Catalyst Layers of Polymer Electrolyte Fuel Cells", *J. Phys. Chem. C*, 111, (2007), pp. 13627-13634.
- [5] Schmidt T.J., Gasteiger H.A., Stab G.D, Urban P.M, Kolb D.M, Behm R.J., "Characterization of High Surface Area Electrocatalysts using a Rotating Disk Electrode Configuration". *J. Electrochem. Soc.*, 145, (1998), pp. 2354-2358.
- [6] Macdonald D., and Urquidi-Macdonald M., "Application of Kramers-Kronig Transforms in the Analysis of Electrochemical Systems I. Polarization Resistance", *J. Electrochem. Soc.* 132, (1985), pp. 2316-2319.
- [7] Urquidi-Macdonald M., Real S., and Macdonald D., "Application of Kramers-Kronig Transforms in the Analysis of Electrochemical Impedance Data II. Transformations in the Complex Plane", *J. Electrochem. Soc.* 133, (1986), pp. 2018-2024
- [8] Urquidi-Macdonald M., Real S., Macdonald D., "Application of Kramers-Kronig Transforms in the Analysis of Electrochemical Impedance Data-III. Stability and Linearity", *Electrochim. Acta*, 35, (1990), pp. 1559-1566.
- [9] Orazem M., and Tribollet B., *Electrochemical Impedance Spectroscopy*, Wiley, New Jersey (2008).
- [10] Savova-Stoynov B., and Stoynov Z. B., "Analysis of the Inductance Influence on the Measured Electrochemical Impedance", *J. of Appl. Electrochem.*, 17, (1987), pp. 1150-1158.
- [11] Göhr H., Mirnik M. and Schiller C. A., "Distortions of High Frequency Electrode Impedance Their Causes and How to Avoid Them", *J. Electroanal. Chem.*, 180, (1984), pp. 273-285.
- [12] Mérida W., Harrington D. A., Le Canut J. M., and McLean G., "Characterisation of Proton Exchange Membrane Fuel Cell (PEMFC) Failures via Electrochemical Impedance Spectroscopy", *J. Power Sources.*, 161, (2006), pp. 264-274.
- [13] Ciureanu M., and Roberge R., "Electrochemical Impedance Study of PEM Fuel Cells. Experimental Diagnostics and Modeling of Air Cathodes", *J. Phys. Chem. B*, 105, (2001), pp. 3531-3539.
- [14] Liu F., Yi B., Xing D., Yu L., and Hou Z., "Development of Novel Self-Humidifying Composite Membranes for Fuel Cells", *J. Power Sources*, 124 (2003), pp. 81-89.
- [15] Paganin V. A., Oliveira C. L. F., Ticianelli E. A., Springer T. E., and Gonzalez E. R., "Modelistic Interpretation of the Impedance Response of a Polymer Electrolyte Fuel Cell", *Electrochim. Acta*, 43, (1998) pp. 3761-3766.

Chapter 3

A Literature Review on Electrochemical Impedance Spectroscopy in Polymer Electrolyte Fuel Cells

In this Chapter a literature review on electrochemical impedance spectroscopy (EIS) measurements in polymer electrolyte fuel cells (PEFCs) is presented. EIS measurements are commonly applied in-situ to characterise physical processes within an electrochemical system. Ex-situ EIS measurements provide information about physical properties of electrically conductive materials. EIS in-situ measurements allow the study of the electrochemical and diffusion mechanisms occurring during the PEFC operation; while ex-situ measurements allow the characterisation and the study of the physical properties in the different layers constituting the PEFC. The EIS technique measures the frequency dependence of the impedance of a PEFC. The objectives of EIS in PEFCs are mainly:

1. To obtain information of the electrochemical and diffusion mechanisms within the PEFC which can help to optimise and to select the most appropriate operating conditions.
2. To identify and differentiate the contribution of each component of the PEFC in the frequency domain such as, catalyst layer (CL), polymer electrolyte membrane (PEM), gas diffusion layer (GDL) which can assist to identify failures in the mode of operation during the PEFC performance.
3. To model the frequency response of the PEFC with an appropriate equivalent electrical circuit and consequently to interpret the electrochemical and diffusion mechanisms of the PEFC.

In this literature review, in-situ EIS measurements are only taken into consideration as the frequency response obtained during PEFC operation is related to the different operation modes, different gas fed modes, different operating conditions and the electrochemical and diffusion mechanisms within the PEFC.

3.1 In-situ EIS Measurements in PEFCs

EIS measurements have been carried out over the last 60 years [1,2], and have been applied to investigate the electrochemical processes in electrochemical systems as a function of the frequency. One of the earliest approaches for EIS measurements has been applied to characterise the electrochemical processes in electrodes of electrochemical fuel cells. de Levie [3] studied the electrochemical processes in porous and planar electrodes through EIS measurements. The conclusions of his work state that for a planar electrode the electrical current lines are normal to the electrode surface but for a porous electrode the current lines are effectively parallel to the electrode surface. The impedance of a planar electrode is the sum of the impedances of the components representing electrode processes but the impedance of a porous electrode is the geometric mean of those components. The method of ‘squaring’ described by de Levie [3] is a very simple way to graphically correlate the impedance of a porous electrode with that of a corresponding flat one. In this case, the phase angle is doubled and the absolute magnitude $|Z|$ is squared.

Ciureanu and Roberge [4] studied the impedance response of a H₂/air PEFC at room temperature, and its voltage dependence was examined as a function of humidification and air flow rate. The results showed that the EIS method has the potential to separate individual contributions of components to the overall impedance. The resistance of the membrane is calculated from the high frequency limit of the impedance spectrum. The cathode catalyst layer (CCL) is the main contributor of the loop at high frequency from the spectrum. The impedance of the GDL is responsible for the low frequency loop in the spectrum which increases at higher cathode overpotential. This low frequency loop appears when an excess of liquid water produced at the CCL starts to accumulate in the GDL, resulting in a limitation of the air transport to the GDL-CCL interface.

In the study reported by Merida *et al.* [5] two PEFC failure modes (dehydration and flooding) were investigated through EIS on a four-cell PEFC stack. These two extreme failure modes can be distinguished by impedance measurements in different frequency bands. Dehydration was simulated by switching the oxidant in one cell between saturated and dry air streams at the same temperature and maintaining constant humidification in the remaining cells. EIS spectra were measured as the cell potential decreases and the varying spectra were compared to the spectra obtained before switching the reactant. Flooding effect was simulated by altering the reactant stoichiometry of the oxidant flow downstream from an individual cell within the PEFC stack. The dehydration effects were measurable over the frequency range 0.5-100 kHz, while the flooding effects were measurable in the frequency range 0.5-100 Hz. Overall the work presents only impedance measurements of the whole PEFC stack and does not measure the impedance of single cells.

In the study of Yuan *et al.* [6] a diagnosis of a 500 W Ballard Mark V PEFC stack was evaluated through EIS. Three characteristic semicircles were presented in the spectra. A bigger loop from 1 kHz to 0.1 Hz was reported to reflect the behaviour of the stack cathode. This loop is known as kinetic loop and corresponds to the charge transfer process of the ORR. A smaller semicircle (high frequency loop, from 2 kHz to 1 kHz) has been associated to structural features of the membrane electrode assembly (MEA) [7] and distributed resistance effects in the electrolyte within the CL [8]. The high frequency intercept of the kinetic loop is related to the ohmic resistance of the stack. A third low frequency loop reflected the mass transport limitations in the gas phase of the cathode. In these EIS measurements the effects of temperature, flow rate and humidity on the stack performance were investigated. The diameter of the loop decreased with increasing the temperature. The temperature enhanced the kinetics of the oxygen reduction reaction (ORR). The third low frequency loop increases with increasing the current. At high current there is a higher liquid concentration produced by the ORR therefore a shortage of air is present. In the first study the temperature and current dependence of the ohmic resistance at high frequency was not reported. An extension from the previous work of Yuan *et al.* [9] to study the ohmic resistance of the 500 W Ballard Mark V PEFC stack represented at the high frequency end of the impedance spectra was presented. Two

methods (grounded mode and floating mode) were utilized for measuring the impedance of individual cells. In the grounded mode measurements, AC impedance spectra were measured in the order of one cell, two cells, three cells, etc until the impedance of the whole stack was measured. The floating mode method was able to measure the AC impedance spectra of each individual cell directly. The advantage of the floating method is that the data analysis is faster than the ground mode method. The results show that both methods are applicable to individual cells. The results also indicate a good agreement between the total Ohmic loss in the stack and the combined Ohmic losses of the individual cells. Some works have reported that the membrane resistance increases with increasing current density [10,11]. The Ohmic resistance extracted from EIS measurements in the study, shows a trend to decrease with increasing current density, which is contrary to previous studies [10,11]. This is attributed to the particular experimental condition used. AC impedance method is a sensitive technique for detection of the degree of membrane dehydration. Variations of ohmic resistances among the PEFC individual cells are high at low currents and low at high current.

An impedance analysis in a commercial PEFC stack (Ballard's 1.2 kW NexaTM) was carried out in the study of Dale *et al.* [12]. Impedance measurements were carried out in the fuel cell to study the performance of the whole stack and groups of cells under various loads. The study takes into account the effect of the fuel cell control system on the EIS results. High frequency artifacts were observed at the high frequency end of the impedance spectra due to fuel cell structure. Single cell EIS analysis was also carried out for individual cells placed at different locations in the stack. The authors did not draw a clear conclusion about the change in impedance for cells at different positions in the stack. The reason for change in Bode magnitude at low frequencies for the EIS measurements was not fully understood. The lowest ohmic resistance observed in the EIS measurements was for the cell nearest the air inlet side. The ohmic resistance increased from the air inlet to the hydrogen inlet side.

The limiting polarisation behaviour of a PEFC was studied using EIS measurements, in the work reported by Paganin *et al.* [13]. EIS impedance results were studied considering different potential losses caused by the kinetics of the ORR, the opposition to the flow of

ions in the electrolyte of the CCL and PEM, the oxygen diffusion in the gas phase in the CCL and GDL and the balance of water in the PEM. The EIS spectra show a small potential-independent arc at high frequency (20 kHz- 250 Hz) due to the presence of the distributed ionic resistance inside the CCL [14]. A potential-dependent arc presented at medium frequencies is related to the double layer capacitance between dissimilar materials combined with the charge transfer resistance of the ORR. At low overpotentials the radius of the impedance arc is dominated by charge transfer resistance of the ORR. At high current densities, characteristic processes relate to the oxygen diffusion appear in the impedance spectra. Therefore at high current densities the impedance semicircle presented at low current densities (low overpotentials) is split into two arcs [15,16]. The low frequency arc presented in the impedance measurements at high current is related to the water transport characteristic in the membrane. This process plays an important role in determining the limiting polarisation behaviour in PEFCs operated at high current only if pure oxygen is utilized as a reactant gas. When air is used instead, gas phase becomes the limiting factor.

Springer *et al.* [14] analysed PEFC cathode impedance spectra under various experimental conditions. The use of a reference electrode in the impedance measurements allowed the measure of the impedance accounting just for the cathode electrode. A negligible difference in response was seen when measuring cathode impedance relative to the anode or relative to a reference electrode placed on the side of the anode. Therefore, in the study it was assumed there is negligible voltage loss and negligible impedance at the anode at all currents measured. The resolution in the frequency domain of the overall change in cell impedance helps to resolve and to evaluate quantitatively individual contributions to PEFC losses. High catalyst utilization is achieved with thin-form catalyst layers made of ionomer/Pt/C composites. At medium current densities the ionic conductivity in the electrolyte of the CCL, and the finite oxygen permeability in this layer have a significant contribution in the impedance cathode spectrum. At high current densities the transport limitations in the gas phase in the GDL cathode features a second semicircle at low frequencies. This last feature is absent if the cathode is operated on pure oxygen where the gas-phase transport limitations are lifted.

The state of health of PEFC stacks during drying and flooding conditions has also been studied by Kurz *et al.* [17]. 6-cell PEFC stack impedance spectra were measured through a multichannel impedance analyzer. The study shows that the impedance measurements at two specific frequencies, one high (1 kHz) and one low frequency impedance (0.5 Hz) are a good indicator to predict voltage drops caused by drying and flooding. A Proportional Integral Derivative (PID) control strategy, which has the voltage drop as input variable and the required air flux for the stack to overcome the two failure modes as the output variable, operated the stack fully autonomously and was able to prevent all voltage drops caused by flooding.

Localized EIS measurements can assist in the design of flow channels as the local conditions in a PEFC can change due to a manufacturing inconsistency during cell design. However, the main challenge of the localized EIS technique remains in the redesign of a fuel cell to carry out spatially resolved measurements. Localized EIS measurements along a single channel of a PEFC were carried out for the first time by Brett *et al.* [18]. A single channel machined out of a printed circuit board that has 10 segmented current collectors running adjacent and along the channel was used. The EIS results showed that the diameter of the impedance spectra increased with distance along the channel from the gas inlet. The increase in diameter was attributed to oxygen diffusion limitation in the electrode diffuser. Then reactant starvation occurs along the flow channel. The results show how conventional EIS measurements on the bulk fuel cell are not representative and not sufficient to properly characterise the operation of a PEFC.

A spatially resolved in-situ diagnostic method for PEFCs using EIS measurements was carried out in the study reported by Schneider *et al.* [19]. This method pinpointed inhomogeneities in the current distribution. The combination of locally resolved current density measurements and local EIS allows the identification of local inhomogeneities in the performance of a PEFC. A segmented PEFC 29.2 cm² was used for the tests in which the anode and cathode flow field plates are segmented into 11 electrically isolated segments. The GDL of the MEA is not segmented, so lateral currents across the GDL are allowed to occur as it happens in nonsegmented PEFCs as well. A multichannel frequency response analyser for both data acquisition and frequency response analysis

was built up. The analyser consists of ten voltage and ten current channels and can carry out impedance measurements for up to nine segments in the flow field plates and the entire cell in parallel. The results show differences in the local cell impedance spectra. For low humidity for H₂/O₂ PEFC operation, the locally resolved impedance spectra show that the performance loss along the flow field plate channels can be attributed to drying effects. For H₂/air operation an increasing size of the low frequency loop on the local impedance spectra along the gas channels from the air inlet to the outlet is observed. This effect can be related to the cumulative flooding on the GDL and a decreasing molar fraction of oxygen in the cathode gas stream along the channels.

The contributions of different process effects on the complex plane in PEFCs are discussed by Romero-Castanon *et al.* [7]. EIS experiments were carried out in a 5 cm² single cell operated with a back pressure of 20 kPa in the cathode side and 62 kPa for the anode and the temperature was kept at room temperature (30 °C). The EIS results show that the high frequency region in the impedance spectra was not associated with any faradaic process nor with mass transport limitations on the cathode electrode side. The MEA structural features could be responsible for this behaviour. To explore the dependence of the ORR in the cathode on the potential, the charge transfer resistance and capacitance values were estimated. The charge transfer resistance decreases exponentially when the potential is decreased far away from activation control up to a value determined by transport limitations. The formation of the cathode capacitance was achieved after the polarisation of about 200 mV from open circuit after which the cathode capacitance reached a value that remained constant for large currents. The work concludes that the faradaic contribution is shown to exist at the low-medium frequency range measured and the MEA structural component in the absence of reaction at the high frequency range. The magnitude of the capacitance corresponds to porous electrodes.

A review of EIS technique in PEFC diagnosis was reported by Yuan *et al.* [20]. In-situ experimental methods such as Galvonastatic mode, Potentistatic mode, Gas feeding mode, and Reference electrode for measuring the impedance of a PEFC are examined. Also typical impedance spectra in several common scenarios are presented. In addition to the traditional impedance technique, the applications of EIS in fuel cell research tend

towards the local-resolved and the multi-channel impedance measurements. To date, in current fuel cell research an impedance approach involving the time-domain technique has not been validated in fuel cell research. EIS measurements in time domain could make this technique more valuable for fuel cell research [21]. The review discussed in the work reported by Yuan, only EIS measurements in the frequency domain are reported. The time domain technique, which applies frequency signal to a cell and measures the PEFC response as a function of time, is not often used. It is known that the time of the AC impedance measurement based on frequency domain depends on the range and number of frequencies contained in the spectra and the number of cycles measured per frequency. Time domain measurements of impedance based on Fourier Transformation have been applied to electrochemical systems [22]. This area needs further work in order to apply this technology to fuel cell research.

Overall, the works mentioned so far have identified through a visual inspection of the EIS measurements, the electrochemical mechanisms during the ORR and diffusion mechanisms in the PEFC for a range of different frequencies. However, this approach does not give a clear understanding about the limitations in mass transport represented at low frequencies of the EIS spectrum. Other authors as mentioned in the next section have defined and applied equivalent electrical circuits within the EIS technique to accurately estimate the factors that influence the nature of polarisation curves from EIS measurements.

3.2 Representation of the EIS through Equivalent Electrical Circuits

The use of equivalent electrical circuits with the experimental EIS technique is a well-established methodology to characterise processes in the PEFC. The frequency response of a PEFC that results from EIS is in essence characterised by energy dissipating and energy storing elements of the cell. It can be represented by an equivalent electrical circuit model that is composed of resistors and capacitors respectively [23,24,25,26]. By understanding the arrangement and magnitude of the resistive and capacitive elements in the equivalent circuit, it is possible to generate a deeper understanding of how and where

the chemical energy that is released from the redox reaction is being dissipated and retained within the real physical system.

Inductance is caused by the magnetic field generated by electric currents. Some works in the literature have identified inductive effect which is represented in EIS measurements with positive imaginary component on the complex plot at high frequencies. Ciureanu and Roberge [4] reported in their work that PEFC experimental impedance spectra in the high frequency range showed an inductive behaviour characteristic to the experimental set up. To avoid complications resulting from such inductive characteristics, they limited the high frequency range to 1 kHz. Fouquet *et al.* [26] reported that inductive behaviour from the wires in EIS measurements was predominant above 1 kHz. Merida *et al.* [5] reported in their work that it is possible to minimise the inductive effect by maintaining equal lengths in the cables, twisting the large current leads to the electronic load, and polishing and clamping the metal contacts. Hampson *et al.* [27] concluded in their work, that the presence of porosity on electrodes may lead to the impedance becoming inductive at high frequencies. To date there is no work published that reveals the high frequency inductive effect on PEFC EIS measurements.

Equivalent electrical circuits to interpret the mechanisms related to the impedance response of an electrochemical system have been used for over thirty years [27]. Different arrangements of electrical circuits from simple components [28,24,4,26] to more complicated transmission line representations [29,30,31,32,33,34] have been reported in the literature to model and characterise different processes in a PEFC. Each equivalent electrical circuit can represent a specific physical process occurring in a PEFC. However the circuits are limited to a certain range of operating currents.

Other different arrangements of the electrical components have been reported in the literature to model and characterise other phenomenological processes in the PEFC. For instance, an electrical circuit proposed by Wagner and Gülzow [28] represents the PEFC during normal operation and during CO poisoning in the anode. Ciureanu and Wang [35] proposed an electrical circuit to study the performance of the anode of an H₂/H₂ fed Fuel Cell, this circuit also models the effect of CO poisoning and adsorbed species in the CL.

3.2.1 Randles Circuit

The most common electrical circuit configuration to characterise the PEFC is based on Randles circuits which are connected in series with a resistance [36]. This electrical circuit consists of a resistance R_e accounting for the opposition to flow of ions and electrons in the PEM, GDL, CCL connected in series with a resistance R_c accounting for the charge transfer between the electrode-electrolyte interface during the ORR and connected in parallel with a capacitor for the double layer capacitance for the interface between dissimilar materials i.e., Nafion/Carbon (N/C). To include mass transport effect in the Randles circuit, a Warburg component W_s which models finite diffusion of oxygen in the electrode is connected in series with the charge transfer resistance of the ORR.

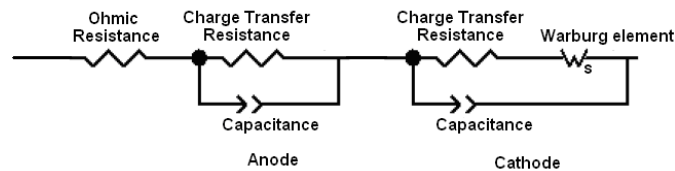


Figure 3.1 Randles electrical circuit with Warburg element

The Randles with Warburg element circuit is reported in the study of Orazem *et al.* [25] to demonstrate a graphic representation of the Nyquist and Bode plot for reactive electrodes. EIS data are commonly represented through a complex-impedance-plane, where each data point corresponds to a different measurement frequency. The impedance of the Randles circuit is represented in the complex-plane where the asymptotic limit of the real part at high frequency corresponds to Ohmic Resistance R_e and at low frequency corresponds to the sum of Ohmic resistance and resistance of ORR $R_e + R_c$. A depressed semicircle indicates that a more detailed model is required and multiple loops provide a clear indication that more than one time constant are required to describe the process. Graphical interpretations of Nyquist and Bode plots provide guidance for the development of appropriate physical models. A visual inspection of the complex-plane does not allow the interpretation of the electrochemical mechanisms in the frequency domain. Analysis of the Bode plot for EIS measurements can provide both qualitative and quantitative evaluation of electrochemical impedance data.

Transfer resistance of ORR and Mass transport resistance in PEFCs with microporous layers (MPLs) using EIS were investigated in the study reported by Malevich *et al.* [24]. The impedance spectra were fit to the Randles circuit with Warburg element as shown in Fig. 3.1. The medium and high frequency response loops from the EIS measurements are attributed to the cathode charge transfer and mass transport processes and are represented by a resistor R_c and Warburg impedance W_s connected in series. In this circuit, a constant phase element (CPE) which models the non-homogeneity in the charge distribution between the electrode-electrolyte interfaces in the CCL [37] is applied instead of a capacitor and is connected in parallel to R_c and W_s to represent the double-layer capacitance for the cathode. The ohmic resistance accounting for ionic resistances of the membrane and the catalyst layers, electronic resistances of the flow field plates, GDLs and all interfacial contact resistances is represented by R_e . The results show that the charge transfer resistance decreases, while the mass transport resistance increases with increasing current density for cells with and without MPL. The charge transfer resistance for cells with a MPL is lower than that for cells without MPL. Cells with MPL demonstrate lower mass transport resistance compared with cells without MPL. In the study mass-transport resistance is most likely due to the gas transport in the GDL. The presence of MPL helps to reduce the water saturation in GDL, thereby improving the oxygen transport to the CCL.

Fouquet *et al.* [26] monitored the flooding and drying out of a PEFC stack using the Randles model with EIS measurements. Parameters of the Randles circuit were fitted to the EIS data. In order to improve the quality of the fit, the standard capacitor was changed by a CPE in the electrical circuit. The EIS measurements show a full depressed semicircle at high frequencies followed by a smaller semicircle at low frequencies. In the case of a flooded PEFC, both real and imaginary parts of the impedance grow larger, and the two semicircles are no longer visually resolvable. With a dry PEFC, the whole spectrum is shifted toward the positive side of the real axis. The process of flooding is characterised by the modification of the low frequency part of the PEFC stack's impedance which, in turn, is associated with the diffusion process through the GDL. In the case of a drying membrane, the impedance spectra progressively shift toward the positive part of the real axis, while the low frequency loop grows to a comparable size as

the high frequency one. The variations of the Randles parameters while the membrane is drying are less dramatic than in the case of flooding. Robust and reliable PEFC's state of hydration monitoring was demonstrated using the parameters defining the Randles circuit.

Characterisation of MEA in PEFCs through electrical circuits and EIS measurements was conducted in the study of Wagner [23]. Impedance spectra were measured at open circuit potential with symmetrical gas supply (H_2/H_2 and O_2/O_2), without using a reference electrode and at normal operating condition H_2/O_2 . To evaluate the measured impedance, the reaction steps are translated into a Randles electrical circuit which contains various electrical elements representing the reaction steps. The impedance results in the low frequency range are much higher when operated symmetrically with oxygen than the impedance when the PEFC is operated symmetrically with hydrogen. The impedance of a PEFC at open circuit potential is mainly determined by the charge transfer resistance of the cathode. EIS measured on the PEFC operated with H_2/O_2 at low current show an exponential potential dependency due to the high activation energy of the ORR in the low frequency range. EIS measurements at frequencies higher than 10 kHz are related to the membrane resistance. With further increasing current density, an increase in the PEFC impedance is observed. A second time constant in the lowest frequency region appears at high current and is related to mass transport. To identify the oxygen diffusion process the impedance has to be measured over a wide frequency range, down to 10 mHz.

A measurement model based on the Voight circuit to interpret EIS data in PEFCs is shown in the study of Agarwal and Orazem [38]. A Voight circuit consists of Randles electrical circuits connected in series and then repeated a finite number of times. By including a sufficient number of terms in the Voight circuit it is possible to fit impedance data for typical stationary electrochemical systems such as PEFCs. Lack of complete agreement between the data and the measurement model could be attributed to the error structure (or noise) of the experimental data or nonstationary processes. The measurement model based on the Voight circuit can be used to identify the frequency-dependent error structure of impedance spectra. The error structure can be used to weight the data during regression and to provide a means of deciding whether a given regression provided a

good fit [39,40]. The Voigt circuit can be used to check the consistency of electrochemical impedance data to the Kramers-Kronig relations because the model itself satisfies the Kramer-Kronig relations and provides a statistically adequate fit to electrochemical impedance data. The measurement model allows correct identification of the number of physical processes that can be discerned from the impedance response of systems that are unaffected by mass transport or by the frequency dependence associated with nonuniform current/potential distributions.

A modification of the Randles circuit to study the effect of CO (carbon monoxide) in the anode when testing the PEFC with H_2+CO/H_2 in anode and cathode respectively is presented in the study of Jiang *et al.* [41]. This equivalent electrical circuit includes a resistance and constant phase element $R_{ad}-CPE_{ad}$ accounting for H_2 adsorption connected in series with an $R_{ox}-CPE_{ox}$ to account for lowering of the H_2 adsorption due to CO oxidation and also connected in series with the charge transfer resistance R_{CT} of the electrode/electrolyte interface, as shown in Fig. 3.2. This electrical circuit has also been used by Ciureanu *et al.* [42,35,43] and Venkataraman *et al.* [44] to study the influence of CO poisoning of the platinum gas diffusion electrodes. The behaviour of the poisoned anode is studied in which the gas is switched to different CO content (10, 50, 100 and 550 ppm). The EIS complex plots present a pseudoinductive semicircle loop at low frequencies which is attributed to CO electro-oxidation and removal by oxygenated species (OH_{ads}) on the electrode surface. Bai and Conway [45], have demonstrated that an inductive loop behaviour in systems with adsorbed species is related to a change in the sign of the coverage dependence on potential. CO poisoning is reduced at high temperature due to CO's exothermal adsorption reaction mechanisms, therefore more vacant active surface sites are available for hydrogen chemisorption at low frequency. If the bias potential is increased the hydrogen adsorption impedance curve (inductive loop) is reduced because more electrode active surface becomes available for hydrogen adsorption as the CO is oxidized.

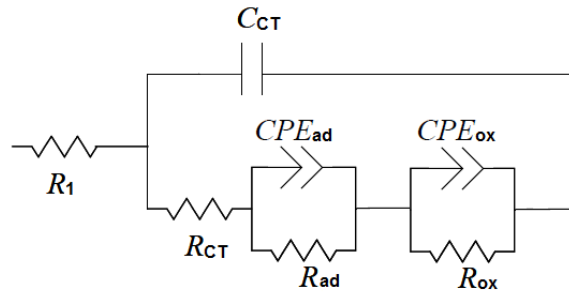


Figure 3.2 Electrical circuit to model the anode impedance during CO poisoning

EIS measurements have limitations and present disadvantages as the low impedance values are obscured for low frequencies and some effects are not visible due to a masking effect in the impedance complex plot [13]. Yuan *et al.* [9] attempted to separate both processes, charge transfer and diffusional effects, in impedance spectra that account for a H_2 /air PEFC stack operated at high current densities and feature a single loop through a Randles electrical circuit. The results showed that the Randles equivalent circuit model cannot account for the exact electrode process at high current densities because the charge transfer resistance of the ORR increased with increasing current density. Similar results have been reported by Springer *et al.* [14].

Equivalent electrical circuits combined with EIS measurements can deliver information about the opposition for the charge transfer during the ORR and the opposition for the ion and electron to conduct through the PEFC. However the interpretation of frequency dependent mechanisms related to oxygen transport limitations in PEFC is still a subject to debate, as this has been principally attributed to the gaseous oxygen transport limitations in the GDL neglecting any mass transport limitations in the CCL [46,47,48]. However, it is suspected that the CCL becomes flooded before the GDL because water is generated in the CCL and transported into the GDL, and the CCL has lower porosity and smaller pore size, and tends to have higher flooding levels than the GDL [49].

3.2.2 Transmission Line Circuit

Eikerling and Kornyshev [29] proposed an electrical circuit using a transmission line to represent the impedance and to characterise the porous CL of PEFCs. This equivalent circuit consists of an upper rail to account for the ionic conduction, and a lower rail to represent the electron access in the CL. In the upper rail distributed resistances to account for the ionic resistance in the CL electrolyte are considered. Usually the distributed electron resistances are neglected to simplify the mathematical analysis because the resistance to ion transfer in the electrolyte of the CL is much greater than the resistance to the electron transfer in the carbon of the CL by several orders of magnitude. Between the upper rail and lower rail, parallel distributed resistances and capacitances to account for the charge transfer process and the capacitance effect between the Nafion/carbon interface are considered. These three elements are then repeated a finite number of times as shown in Fig. 3.3. The transmission line circuit reported by Eikerling and Kornyshev to characterise the CCL operated at high currents cannot be used because it does not account for oxygen transport limitations in the CCL. At low currents, this phenomenon does not occur because the rate of water production is low and so does not appear as an equivalent electrical component in the transmission line. The transmission line is connected in series with an ohmic resistance and an inductor component. The inductor component represents the inductance presented in the electrical cables of the measurement system while the ohmic resistance corresponds mainly to the PEM, GDL, and Plate.

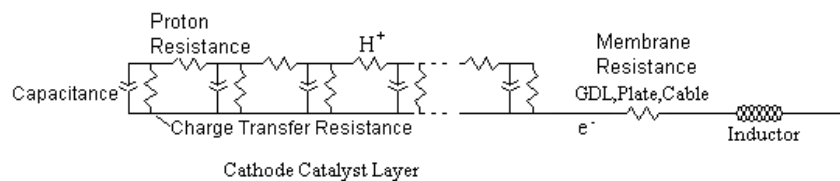


Figure 3.3 Transmission line circuit

Measurements of CCL electrolyte resistance in PEFCs using EIS were carried out in the study of Makharia *et al.* [30]. EIS measurements were carried out in a 5 cm² PEFC (H₂-O₂) with MEA 0.8 and 0.4 Nafion/Carbon ratio. EIS data were fitted to a PEFC model in which the CL physics are accurately represented by a transmission line model. Extracted parameters include cell ohmic resistance, CL electrolyte resistance, and double layer

capacitance. This author considered that no anode catalyst layer electrolyte loss is expected because the hydrogen oxidation reaction (HOR) in the anode is so facile that any electrolyte resistance would have the impact of shifting the anode current distribution close to the membrane, without requiring significant anode overpotential to do so. Parameters were extracted from each impedance curve at various current densities by fitting the experimental data to the transmission line equivalent circuit using commercial software Zview (Transmission Line-Open Circuit Terminus, DX-Type 6, Scribner Associates, Inc., version 2.3). The measured CL electrolyte resistance increased with decreasing ionomer concentration in the CCL. This author concluded that the practice of using a single frequency in the EIS measurements to estimate the ohmic resistance of the PEFC is subjected to large errors (10-50%) due to contributions from the catalyst layer resistance. The size of the errors depends on the frequency used, the size of the ohmic and catalyst layer resistances, and the size of the inductance of the measurements cables.

The finite transmission line equivalent circuit describing the impedance behaviour of a PEFC electrode was used by Lefebvre *et al.* [31]. In this study experimental EIS plots for carbon-supported Pt electrodes with and without Nafion impregnation were obtained. Before EIS measurements were carried out, the cell was operated with H_2/O_2 at 0.5 V until the steady state was obtained. EIS measurements were obtained with nitrogen flowing over the cathode and hydrogen flowing over the anode. Diffusion and kinetic impedances associated with the faradaic process are negligible because the electrodes were purged with nitrogen prior to, and during, the impedance measurements. Fitting of simulated data to the experimental data using the finite transmission line equivalent circuit provides a profile of the variation of the catalyst layer's ionic conductivity with distance from the membrane. The simulated curves using the finite transmission line equivalent circuit shows a 45° region at high frequency due to ionic resistance profile in the catalyst layer. The specific capacitance in the Nafion/carbon interface may also decrease with distance into the cathode catalyst layer due to decreasing electrolyte penetration and wetting. Overall this study demonstrates that the Nafion-containing electrode is shown to have a much higher ionic conductivity, and consequently, has a larger active catalyst area and provides better fuel cell performance.

Suzuki *et al.* [32] demonstrated diagnostic techniques to evaluate ionic conductivity and gas diffusivity in the CL. The ionic conductivity using EIS measurements showed notable dependence on Nafion loading. The ionic conductivity is estimated on the basis of a 1-D homogeneous model of the electrode which consists of the finite transmission line equivalent circuit. The ionic conductivity increases with increasing volume fraction of Nafion. This indicates that CLs with a higher volume fraction have a thicker Nafion layer covering the Pt/C particle and/or a larger number of ionic channels. The gas diffusivity measurements using helium gain revealed the contribution of Knudsen diffusion in the CL. The results in this study show that the ionic conductivity increases if the Nafion content is increased. Thus ionic transport in the catalyst layers does not appear to bring about significant loss. However, oxygen transport is found to be limited significantly in the CL. Improving gas diffusivity in the CL by changing the material or preparation process could reduce mass transport losses and lead to a high-power MEA.

The impedance response of the PEFC is described by the finite transmission line equivalent circuit as reported by Hou *et al.* [33]. In this study the ionic resistance of the CL is measured at different current densities after the PEFC suffered subfreezing temperatures. Compared with those of the CL before being frozen, the ionic resistances unexpectedly decreased a little, which matched well with the polarisation results. Considering that the frequency-dependent penetration depth was small in the high frequency region, a semi-quantitative method based on the finite transmission line equivalent circuit was followed to investigate the ionic resistance profile across the whole CL. The results showed the ionic resistance decreased with increasing current density and became smaller within the frequency-dependent (10 kHz to 200 Hz) penetration depth of the CL after the cell suffered freezing temperatures. This was consistent with the improved cell performance at low current densities. The change of the ionic resistance profile induced by ice formation was not equal across the whole CL. The ionic resistance close to the interface between the membrane and CL decreased, while the ionic resistances farther away from the interface increased. The change of the ionic resistance profile was not uniform across the CL after the cell experienced freeze/thaw cycles, which was more evident at the higher current densities.

Li and Pickup [34] studied the effect of Nafion loading in the CCL of PEFC electrodes by EIS measurements. Experimental impedance data were simulated based on the finite transmission-line equivalent circuit describing the impedance behaviour of a PEFC electrode. In this work the use of EIS provide a clear understanding of the influence of nafion loading on the properties and performances of PEFC cathodes. The impedance results show that the ionic conductivity of the cathode increased greatly with increasing nafion loading, and this is the main factor responsible for the increase in performance up to 30% Nafion. The loss of performance at higher nafion loading must have been due to an increasing oxygen transport resistance, because the electrode resistance did not increase significantly. In fact the highest electronic resistances were observed at low nafion loadings, indicating that Nafion played a significant role as a binder. Loss of electronic conductivity in the catalyst layer is not an issue at high nafion loadings, but a resistance between the CL and the carbon paper support appears to be a problem if insufficient Nafion is used. This work concludes that EIS provides strong evidence that accurate conductivity profiles can be determined for PEFC CLs. The results obtained follow the expected trends with other observations, and are qualitative reasonable. There is good evidence that results obtained under an inert atmosphere are representative of conductivity profiles in operating fuel cells.

In the study of Cano-Castillo *et al.* [50], the gradual flooding of a single PEFC was produced and EIS measurements were carried out in order to follow changes of the PEFC impedance parameters. The PEFC was tested at room temperature and without humidification in both gases and under dead-end configuration. EIS measurements were carried out at different degrees of flooding. These changes in flooding were followed by using two equivalent circuit models: one simple model of the Randles type accounting for cathode and anode interfaces and a more complex model based on a transmission line, more suitable for porous electrodes in order to include ionic resistance of the catalyst layers. Measurements at open circuit potential show that the overall impedance decreases as the water excess increases. This decreasing in tendency was attributed to a smaller charge transfer resistance of the cathode, favoured by the water present in the cell. Both models give reasonable description of experimental data, therefore charge transfer resistance from Randles model could be used as a seed value in the transmission line

model. The anode and cathode capacitance seem constant but the ionic resistance (from the transmission line model) in the anode decreases its value while the cathodic ionic resistance stays very low for all cases of water content.

The transmission line equivalent circuit has been broadly applied to characterise the ionic resistance in the CCL electrolyte for PEFCs operated at low currents. At high currents, the product water that is formed in the CCL can begin to saturate the tortuous pathways of the porous network, which then acts as a resistance to the mass transport of oxygen from the interface with the GDL to the catalyst sites. At low currents, this phenomenon does not occur because the rate of water production is low and so does not appear as an equivalent electrical component in the transmission line given in Fig. 3.3.

3.3 Formula of de Levie to Characterise Porous Electrodes in PEFCs

Porous electrodes are used in PEFCs because they have the advantage of an increased effective active area. A porous electrode may have the same structure as a porous layer; however, the pore walls are electroactive for a porous electrode, while the pore walls are inert for a porous layer. The porous electrode is usually represented by a simplified single pore-model. The impedance of the pore can be represented by the transmission line presented in Fig. 3.4.

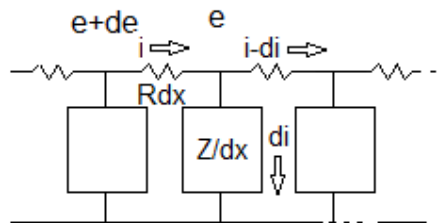


Figure 3.4 A small section (dx) of the equivalent circuit of a pore, (e) potential, (i) current, (x) distance along pore axis, (R) electrolyte resistance per unit pore length, (Z) electrode impedance per unit pore length

The general solution of a pore can be obtained only by a numerical calculation of the corresponding transmission line. de Levie [3] calculated analytically the impedance of one pore using the transmission line circuit:

$$Z_{deLevie} = (RZ)^{1/2} \coth\left(\ell\sqrt{\frac{R}{Z}}\right) \quad (3.1)$$

$$\text{With } Z = \frac{R_K}{1+i\omega R_K C} \quad (3.2)$$

where R is the electrolyte resistance for one-unit length pore with units of $\Omega\cdot\text{cm}^{-1}$ and Z is the interfacial impedance for a unit length pore, with units of $\Omega\cdot\text{cm}$, and ℓ is the length of the pore. R_K is the charge transfer resistance of the electrolyte-electrode interface taken per unit pore length.

Eikerling and Kornyshev [29] derived a similar formula as the one presented by de Levie in Eq. 3.1 to represent the complex impedance of the CCL at low overpotentials. This study considered the CCL as an agglomerate structure of carbon particles bounded together by polytetrafluoroethylene (PTFE) which serves, in addition, as a hydrophobizing agent in order to ensure good gas porosity of the layer. The voids between the agglomerates are penetrated by the polymer electrolyte, which forms the proton conducting pathways. Similar to the analysis derived by de Levie, the CCL structure was represented by a transmission line equivalent circuit where the parameters as electrolyte resistance and electrode/electrolyte interface impedance are assumed to depend only on the coordinate x (thickness). The effect of oxygen depletion is neglected as this is not represented in the transmission line equivalent circuit of Fig. 3.3. The results show that ionic transport limitations in the CCL can be represented by a straight line feature in the impedance spectra at high frequencies. This straight line in the high frequency domain can provide information about the localisation and distribution of the catalyst and electrolyte in the CCL.

Eq. 3.1 can be only used to characterise CCL in H_2/O_2 PEFCs. If a PEFC is operated with H_2/N_2 , there is no faradaic reaction and therefore the kinetic resistance R_K in Eq. 3.2 becomes infinite. Then Eq. 3.2 can be expressed as $Z = 1/i\omega C$. Gazzarri *et al.* [51] estimated the local relative humidity (RH) in the CCL of a PEFC as a function of its effective ionic resistance. In the study, the term effective ionic resistance denotes the

ionic resistance averaged over the CCL thickness, which depends on the distribution and self-organized structure of the ionomer in the CCL and the degree of liquid saturation. Impedance measurements were carried out in H_2/N_2 under conditions of equal relative humidity on anode and cathode. Two distinct regions in the impedance spectra were apparent; a 45° straight line with respect to the real axis to represent ionic transport in the CCL, and a vertical line at low frequency typical of capacitive behaviour. The resulting impedances were modelled using Eq. 3.1 and considering the kinetic resistance R_K as an infinite value $Z = 1/i\omega C$. The CCL ionic resistance decreased with increasing inlet RH on both sides (anode and cathode). More remarkably, ionic resistance at the cathode also decreased with increasing anode inlet RH and a constant 30% humidity set at the cathode. The latter observation is an indication of a very effective water transport process through the membrane and the cathode.

The ionic resistance in the cathode with various ionomer/carbon (I/C) weight ratios was characterised in a H_2/N_2 PEFC using EIS under various operating conditions in the study of Liu *et al* [52]. AC impedance data were analysed by fitting the impedance equation derived by Eikerling [29] that describes the impedance of the CCL. The 45° line at high frequency end of the spectrum under such operating conditions was presented. The results show that the ionic conductivity starts to drop at I/C ratios of approximately $< 0.6/1$ or an ionomer volume fraction of $\sim 13\%$ in the catalyst layer. High electrode I/C ratios ($I/C \geq 0.6/1$) are necessary for cells operating at low relative humidity to avoid significant losses from high electrode ionic resistances.

3.4 Current Density Distribution through the Cathode Catalyst Layer

Voltage losses from ionic conduction, ORR kinetics, and mass transport limit the performance of PEFCs. To improve the fuel cell performance, it is necessary to determine to what extent each process is responsible for limiting cell voltage. In some studies [53,54,55], the ORR kinetics have been related to the amount of platinum surface area available in the CCL. Also these studies assume a 100% catalyst utilization thereby neglecting any potential drop across the CCL. This assumption will not always be correct, because the ionic resistance and the ORR kinetic resistance in the CCL change as a

function of fuel cell operating conditions. Ions migrating through the ionomer phase of the CCL may react closer to the membrane if ionic resistance is increased or in the case where ions react through the entire CCL if ionic resistance is reduced. The ORR current distribution is further influenced by the mass transport resistance of oxygen reactant diffusion into the CCL and/or of oxygen permeation through the thin layer of ionomer covering the Pt catalyst sites. These mass transport effects would also have an effect on the current distribution through the CCL. This emphasizes the need to estimate internal current distribution measurements on PEFCs.

To date, different experimental techniques to measure the current distribution through the PEFC have been developed such as the printed circuit developed by Brown [56] and Cleghorn [57], the partial MEA/subcell and passive current mapping technique by Stumper [58], the magnetic loop current sensor by Wiser [59], the segmented cell resistor network by Noponen [60] and the segmented cell / multipotentiostatic by Mench *et al.* [61, 62, 63]. Brett *et al.* [64], developed a method to measure current distribution in a PEFC at high resolution, in real time and in a non-intrusive way. The system consisted of a printed circuit board attached to the flow channels to construct an array of current collector electrodes. The results showed that there is a dramatic variation in current density along the channel depending on operating conditions. This spatial variation is influenced by reactant composition and humidity, operating temperature and pressure, pore flooding hardware issues such as bipolar plate design, and moisture content of the membrane. Measurements of current distribution were carried out by Yang *et al.* [65] using a segmented PEFC. Twelve segmented subcells in conjunction with a multichannel potentiostat were used to measure the current distribution. Stainless steel ribs along with teflon inserts and a sheet of gaskets form the serpentine gas flow field. Experiments were carried out using a commercially available MEA (50 cm²) and carbon paper as GDL. The cell temperature was set at 80° C and a relative humidity of 100% for the hydrogen inlet and 50% and 25% for the air inlet. The results showed the highest local current density near the dry cathode inlet, thus suggesting that membrane dehydration in the inlet region is absent under these operating conditions. GDL and MPL in the cathode diffuse the water back to the anode side to protect the membrane from losing water.

Other works have focused on the estimation of the current distribution through the CCL thickness using mathematical models. Neyerlin *et al.* [66] defined a mathematical relation in which the current distribution through the CCL thickness in the absence of oxygen mass transport resistances is determined by the ratio of the ionic resistance and an effective kinetic resistance described by the Tafel slope. The higher this dimensionless ratio is, the more the current distribution will be skewed toward the membrane interface, while low values of this ratio predict a homogeneous current distribution. If the ORR current distribution is skewed toward the membrane interface, the local current density must increase compared to an ideal uniform current distribution, because the same average current must be provided by fewer catalyst sites (poor utilization). This increased local current density near the membrane results in greater kinetic losses. Overall this model predicts electrode potential loss and catalyst utilization in the absence of gas transport resistances. So it is possible to estimate from the ratio of ohmic to kinetic losses, the catalyst utilization and the ohmic drop in the CCL.

Thompson *et al.* [67] studied the general behaviour of water uptake by the membrane and ice storage in the porous electrodes during isothermal, galvanostatic operation of PEFCs and under conditions of initial water content and current density at -20°C . This author affirmed that the development of cold-start models that include the physics of membrane uptake of product water and filling of electrode pores with water (ice), needs a solid knowledge of how the ORR current is distributed through the CCL thickness. The study investigated the voltage loss sources, current distribution and ice formation within the CCL through experiments based on Cryo-scanning electron microscope (SEM) images of electrodes following voltage failures to assess ice filling of the cathode void volume [68] and using the model reported by Neyerlin [66]. CCL ohmic losses were measured and found to be significant at subfreezing temperatures, therefore the ohmic losses account for as much as the ORR kinetic losses. Current distribution modelling with the CCL thickness indicates that ORR favours the electrode membrane interface at moderate current densities. Cryo-SEM images confirmed this prediction, which indicates that filling the electrode with ice occurs from the membrane outward towards the diffusion medium. At lower currents, where the model predicts a more uniform current distribution, more even ice filling of the electrode appears from cryo-SEM images.

A structure-based mathematical model of the CCL in PEFCs is presented in the study of Liu [69]. The model incorporates full spatial coupling of porous composite structure, liquid water saturation, transport of reactants and products, and electrochemical conversion in ORR. The solution allows correlating effects observed in global current-voltage relations to spatial distributions of liquid water, reactants, and reaction rates. The results show that if the accumulation of liquid water is increased in the pores of the CCL, the depletion of oxygen concentration is exacerbated, and thus renders the reaction rate distribution more non-uniform. In order to generate the same integral current, the rates of current generation per effectively utilized catalyst surface have to increase, which in turn leads to the increase of the electrode overpotential.

3.5 Conclusions

Overall the literature review has demonstrated that there is still a lack of understanding about how to relate the physical processes of a PEFC within the impedance response resulting from EIS. For instance, the ohmic resistance in a PEFC from EIS measurements has been reported to be where the impedance spectrum intercepts the real part of the complex plot at high frequencies neglecting inductive effects from the measurement system. Low frequency EIS measurements have been commonly related to gas-phase oxygen transport limitations in the GDL neglecting any mass transport limitations in the CCL. The available electrical circuits cannot account for the exact electrode processes at high currents.

3.6 References

- [1] Ershler B. V., "Investigation of Electrode Reactions by the Method of Charging-Curves and with the Aid of Alternating Currents", *Disc. Faraday Soc.*, 1, (1947), pp. 269-267
- [2] Randles J. E. B., "Kinetics of Rapid Electrode Reactions", *Disc. Faraday Soc.*, 1, (1947), pp. 11-19
- [3] R. de Levie, 'Electrochem. Eng.', Vol. 6, (edited by Delahay and Tobias) p. 329.
- [4] Ciureanu M., and Roberge R., "Electrochemical Impedance Study of PEM Fuel Cells. Experimental Diagnostics and Modeling of Air Cathodes", *J. Phys. Chem. B*, 105, (2001), pp. 3531-3539.
- [5] Mérida W., Harrington D. A., Le Canut J. M., and McLean G., "Characterisation of Proton Exchange Membrane Fuel Cell (PEMFC) Failures via Electrochemical Impedance Spectroscopy", *J. Power Sources*, 161, (2006), pp. 264-274.
- [6] Yuan X., Sun J. C., Blanco M., Wang H., Zhang J., and Wilkinson D. P., "AC Impedance Diagnosis of a 500W PEM Fuel Cell Stack, Part I: Stack impedance", *J. Power Sources*, 161, (2006), pp. 920-928

- [7] Romero-Castañón T., Arriaga L.G, and Cano-Castillo U., “Impedance Spectroscopy as a Tool in the Evaluation of MEA’s”, *J. Power Sources*, 118, (2003), pp. 179-182.
- [8] Freire T. J. P., and Gonzalez E. R., “Effect of Membrane Characteristics and Humidification Conditions on the Impedance Response of Polymer Electrolyte Fuel Cells”, *J. Electroanal. Chem.*, 503, (2001), pp. 57-68
- [9] Yuan X., Sun J. C., Wang H., and Zhang J., “AC Impedance Diagnosis of a 500W PEM Fuel Cell Stack Part II: Individual Cell Impedance”, *J. Power Sources*, 161, (2006), pp. 929-937
- [10] Slade S., Campbell S. A., Ralph T. R., and Walsh F. C., “Ionic Conductivity of an Extruded Nafion 1100 EW Series of Membranes”, *J. Electrochem. Soc.*, 149, (2002), pp. A1556-A1564
- [11] Andraus B., and Sherer G. G., “Proton-Conducting Polymer Membranes in Fuel Cells—Humidification Aspects” *Solid State Ionics*, 168, (2004), pp. 311-320
- [12] Dale N. V., Mann M. D., Salehfar H., Dhirde A. M., and Han T., “ac Impedance Study of a Proton Exchange Membrane Fuel Cell Stack Under Various Loading Conditions”, *J. Fuel Cell Sci. Technol.*, 7, (2010), pp. 031010
- [13] Paganin V. A., Oliveira C. L. F., Ticianelli E. A., Springer T. E., and Gonzalez E. R., “Modelistic Interpretation of the Impedance Response of a Polymer Electrolyte Fuel Cell”, *Electrochim. Acta*, 43, (1998), pp. 3761-3766.
- [14] Springer T. E., Zawodzinski T. A., Wilson M. S. and Gottesfeld S., “Characterization of Polymer Electrolyte Fuel Cells Using AC Impedance Spectroscopy”, *J. Electrochem. Soc.*, 143, (1996), pp. 587-599
- [15] Springer T. E., and Raistrick I. D., “Electrical Impedance of a Pore Wall for the Flooded-Agglomerate Model of Porous Gas-Diffusion Electrodes”, *J. Electrochem. Soc.*, 136, (1989), pp. 1594-1603.
- [16] Raistrick I. D., “Impedance Studies of Porous Electrodes”, *Electrochim. Acta*, 35, (1990), pp. 1579-1586.
- [17] Kurz T., Hakenjos A., Kramer J., Zedda M., and Argert C., “An Impedance-Based Predictive Control Strategy for the State-of-Health of PEM Fuel Cell Stacks” *J. Power Sources*, 180, (2008), pp. 742-747.
- [18] Brett D. J. L., Atkins S., Brandon N. P., Vesovic V., Vasileiadis N., and Kucernak A., “Localized Impedance Measurements along a Single Channel of a Solid Polymer Fuel Cell”, *Electrochem. Solid-State Lett.*, 6, (2003), pp. A63-A66.
- [19] Schneider I. A., Kuhn H., Wokaun A., and Scherer G. G., “Fast Locally Resolved Electrochemical Impedance Spectroscopy in Polymer Electrolyte Fuel Cells”, *J. Electrochem. Soc.*, 152, (2005), pp. A2092-A2103.
- [20] Yuan X., Wang H., Sun J. C., and Zhang J., “AC Impedance Technique in PEM Fuel Cell Diagnosis—A Review”, *Int. J. Hydrogen Energy.*, 32, (2007), pp. 4365-4380.
- [21] Bard A. J. and Faulkner L. R. ., *Electrochemical Methods, Fundamentals and Applications*, New York: Wiley Interscience; 1980 pp. 368-415
- [22] Popkurov G.S., and Schindler R. N., “Effect of Sample Nonlinearity on the Performance of Time Domain Electrochemical Impedance Spectroscopy”, *Electrochim. Acta*, 40, (1995), pp. 2511-2517.
- [23] Wagner N., “Characterization of Membrane Electrode Assemblies in Polymer Electrolyte Fuel Cells Using A.C. Impedance Spectroscopy”, *J. Appl. Electrochem.*, 32, (2002), pp. 859-863.
- [24] Malevich D., Halliop E., Peppley B. A., Pharoah J. G. and Karan K., “Investigation of Charge-Transfer and Mass-Transport Resistances in PEMFCs with Microporous Layer Using Electrochemical Impedance Spectroscopy”, *J. Electrochem. Soc.*, 156, (2009), B216-B224.
- [25] Orazem M. E., Pebere N., and Tribollet B., “Enhanced Graphical Representation of Electrochemical Impedance Data”, *J. Electrochem. Soc.*, 153, (2006), pp. B129-B136.
- [26] Fouquet N., Doulet C., Nouillant C., Dauphin-Tanguy G., and Ould-Bouamama B., “Model Based PEM Fuel Cell State-of-Health Monitoring via AC Impedance Measurements”, *J. Power Sources*, 159, (2006), pp. 905–913.
- [27] Hampson N. A., Karunathilaka S. A. G. R., and Leek R., “The Impedance of Electrical Storage Cells”, *J. Appl. Electrochem.*, 10, (1980), pp. 3-11.
- [28] Wagner, N., and Gülzow E., “Change of Electrochemical Impedance Spectra (EIS) with Time during CO-Poisoning of the Pt-Anode in a Membrane Fuel Cell”, *J. Power Sources*, 127, (2004), pp. 341–347
- [29] Eikerling M., and Kornyshev A. A., “Electrochemical Impedance of the Cathode Catalyst Layer in Polymer Electrolyte Fuel Cells”, *J. Electroanal. Chem.*, 475, (1999) pp. 107-123.
- [30] Makharia R., Mathias M. F. and Baker D. R., “Measurement of Catalyst Layer Electrolyte Resistance in PEFCs Using Electrochemical Impedance Spectroscopy”, *J. Electrochem. Soc.*, 152, (2005), pp. A970-A977.

- [31] Lefebvre M. C., Martin R. B., and Pickup P. G., "Characterization of Ionic Conductivity Profiles within Proton Exchange Membrane Fuel Cell Gas Diffusion Electrodes by Impedance Spectroscopy", *Electrochem. Solid-State Lett.*, 2, (1999), pp. 259-261.
- [32] Suzuki T., Murata H., Hatanaka T., and Morimoto Y., "Analysis of the Catalyst Layer of Polymer Electrolyte Fuel Cells", *R&D Review of Toyota*, Toyota Central R&D Labs, Inc., 39, (2003), pp. 33-38.
- [33] Hou J., Song W., Yu H., Fu Y., Hao L., Shao Z., and Yi B., "Ionic Resistance of the Catalyst Layer after the PEM Fuel Cell Suffered Freeze", *J. Power Sources*, 176, (2008), pp. 118-121.
- [34] Li G., and Pickup P. G., "Ionic Conductivity of PEMFC Electrodes", *J. Electrochem. Soc.*, 150, (2003), pp. C745-C752.
- [35] Ciureanu M., and Wang H., "Electrochemical Impedance Study of Anode CO-Poisoning in PEM Fuel Cells", *J. New Mat. Electrochem. Systems*, 3, (2000), pp. 107-119.
- [36] Boillot M., Bonnet C., Didierjean S., and Lapicque F., "Investigation of the Response of Separate Electrodes in a Polymer Electrolyte Membrane Fuel Cell without Reference electrode", *J. Appl. Electrochem.*, 37, (2007), pp. 103-110.
- [37] Hsu C. H., and Mansfeld F., "Concerning the Conversion of the Constant Phase Element Parameter Y_0 into a Capacitance", *Corrosion*, 57, (2001), pp. 747-748.
- [38] Agarwal P., and Orazem M. E., "Measurement Models for Electrochemical Impedance Spectroscopy I. Demonstration of Applicability", *J. Electrochem. Soc.*, 139, (1992), pp. 1917-1927.
- [39] Agarwal P., Orazem M. E., and García-Rubio L. H., "Application of the Kramers Kronig Relations to Electrochemical Impedance Spectroscopy," presented at the ASTM International Symposium on Electrochemical Impedance: Analysis and Interpretation, San Diego, California, November 4-5, (1991).
- [40] Agarwal P., Orazem M. E., and Hiser A., "Application of Electrochemical Impedance Spectroscopy to Metal Hydrides," presented at the 180th Meeting of the Electrochemical Society, Phoenix, Arizona, October 13-18, 1991.
- [41] Jiang R., Kunz H. R., and Fenton J. M., "Electrochemical Oxidation of H_2 and H_2/CO Mixtures in Higher Temperature ($T_{cell} > 100^\circ C$) Proton Exchange Membrane Fuel Cells: Electrochemical Impedance Spectroscopy", *J. Electrochem. Soc.*, 152, (2005), pp. A1329-A1340.
- [42] Ciureanu M., and Wang H., "Electrochemical Impedance Study of Electrode-Membrane Assemblies in PEM Fuel Cells I. Electro-oxidation of H_2 and H_2/CO Mixtures on Pt-Based Gas-Diffusion Electrodes", *J. Electrochem. Soc.*, 146, (1999), pp. 4031-4040.
- [43] Ciureanu M., Mikhaillen S. D., and Kaliaguine S., "PEM Fuel Cells as Membrane Reactors: Kinetic Analysis by Impedance Spectroscopy", *Catalysis Today*, 82, (2003), pp. 195-206.
- [44] Venkataraman R., Kunz H. R., and Fenton J. M., "Development of New CO Tolerant Ternary Anode Catalysts for Proton Exchange Membrane Fuel Cells", *J. Electrochem. Soc.*, 150, (2003), pp. A278-A284.
- [45] Bai L., and Conway B. E., "Complex Behavior of Al Dissolution in Non-Aqueous Medium as Revealed by Impedance Spectroscopy", *J. Electrochem. Soc.*, 137, (1990), pp. 3737-3747.
- [46] Perry M. L., Newman J., Cairns J. E., "Mass Transport in Gas-Diffusion Electrodes: A Diagnostic Tool for Fuel-Cell Cathodes", *J. Electrochem. Soc.*, 145, (1998), pp. 5-15.
- [47] Tsai C. R., Chen F., Ruo A.C., Chang M.-H., Chu H.-S., Soong C. Y., Yan W. M., and Cheng C. H., "An Analytical Solution for Transport of Oxygen in Cathode Gas Diffusion Layer of PEMFC", *J. Power Sources*, 160, (2006), pp. 50-56.
- [48] Bultel Y., Wiezell K., Jaouen F., Ozil P. and Lindbergh G., "Investigation of Mass Transport in Gas Diffusion Layer at the Air Cathode of a PEMFC", *Electrochim. Acta*, 51, (2005), pp. 474-488.
- [49] Lin G., He W., and Nguyen T. V., "Modeling Liquid Water Effects in the Gas Diffusion and Catalyst Layers of the Cathode of a PEM Fuel Cell", *J. Electrochem Soc.*, 151, (2004), pp. A1999-A2006.
- [50] Cano-Castillo U., Ortiz A., Manzo S., Arriaga L. G. and Orozco G., "Parameter Changes During Gradual Flooding of a PEM Fuel Cell Through EIS Studies", *ECS Trans.*, 3, (2006), pp. 931-939.
- [51] Gazzarri J., Eikerling M., Wang Q., and Liu Z., "Estimation of Local Relative Humidity in Cathode Catalyst Layers of PEFC", *Electrochem. Solid-State Lett.*, 13, (2010), pp. B58-B62.
- [52] Liu Y., Murphy M. W., Baker D. R., Gu W., Ji C., Jorne J., and Gasteiger H. A., "Proton Conduction and Oxygen Reduction Kinetics in PEM Fuel Cell Cathodes: Effects of Ionomer-to-Carbon Ratio and Relative Humidity", *J. Electrochem. Soc.*, 156, (2009), B970-B980.
- [53] Neyerlin K.C., Gu W., Jorne J., and Gasteiger H. A., "Determination of Catalyst Unique Parameters for the Oxygen Reduction Reaction in a PEMFC", *J. Electrochem. Soc.*, 153, (2006), pp. A1955-A1963.
- [54] Kocha S. S., in *Handbook of Fuel Cells: Fundamentals, Technology, and Application*, Vol. 3, W. Vielstich, A. Lamm, and H. A. Gasteiger, Editor, p. 538, Wiley, New York (2003).

- [55] H. A. Gasteiger, W. Gu, R. Makharia, M.F. Mathias, and B. Sompalli, in *Handbook of Fuel Cells: Fundamentals, Technology, and Applications*, Vol. 3, W. Vielstich, A. Lamm, and H.A. Gasteiger, Editors, p. 593, Wiley, New York (2003).
- [56] Brown C. J., Pletcher D., Walsh F. C., Hammond J. K., and Robinson D., "Local Mass Transport Effects in the FMO1 Laboratory Electrolyser", *J. Appl. Electrochem.*, 22, (1992), pp. 613-619.
- [57] Cleghorn S. J. C., Derouin C. R., Wilson M. S., and Gottesfeld S., "A printed Circuit Board Approach to Measuring Current Distribution in a Fuel Cell", *J. Appl. Electrochem.*, 28, (1998), pp. 663-672.
- [58] Stumper J., Campbell S. A., Wilkinson D. P., Johnson M. C., and Davis M., "In-situ Methods for the Determination of Current Distributions in PEM Fuel Cells", *Electrochim. Acta*, 43, (1998), pp. 3773-3783.
- [59] Wieser Ch., Helmbold A., and Gulzow E., "A New Technique for Two-Dimensional Current Distribution Measurements in Electrochemical Cells", *J. Appl. Electrochem.*, 30, (2000), pp. 803-807.
- [60] Noponen M., Mennola T., Mikkola M., Hottinen T., and Lund P., "Measurement of Current Distribution in a Free-Breathing PEMFC", *J. Power Sources*, 106, (2002), pp. 304-312.
- [61] Mench M.M., Wang C. Y., and Ishikawa M., "In Situ Current Distribution Measurements in Polymer Electrolyte Fuel Cells", *J. Electrochem. Soc.*, 150, (2003), pp. A1052-A1059.
- [62] Mench M. M. and Wang C. Y., "An In Situ Method for Determination of Current Distribution in PEM Fuel Cells Applied to a Direct Methanol Fuel Cell", *J. Electrochem. Soc.*, 150, (2003), pp. A79-A85.
- [63] Mench M. M., Dong Q. L. and Wang C. Y., "In Situ Water Distribution Measurements in a Polymer Electrolyte Fuel Cell", *J. Power Sources*, 124, (2003), pp. 90-98.
- [64] Brett D. J. L., Atkins S., Brandon N. P., Vesovic V., Vasileiadis N., and Kucernak A. R., "Measurement of the Current Distribution along a Single Flow Channel of a Solid Polymer Fuel Cell", *Electrochem. Commun.*, 3, (2001), pp. 628-632.
- [65] Yang X. G., Burke N., Wang C. Y., Tajiri K., and Shinohara K., "Simultaneous Measurements of Species and Current Distributions in a PEFC under Low-Humidity Operation", *J. Electrochem. Soc.*, 152, (2005), pp. A759-A766.
- [66] Neyerlin K. C., Gu W., Jorne J., Clark A. Jr., and Gasteiger H. A., "Cathode Catalyst Utilization for the ORR in a PEMFC Analytical Model and Experimental Validation", *J. Electrochem. Soc.*, 154, (2007), pp. B279-B287.
- [67] Thompson E. L., Jorne J., Gu W., and Gasteiger H. A., "PEM Fuel Cell Operation at -20°C. II. Ice Formation Dynamics, Current Distribution, and Voltage Losses within Electrodes", *J. Electrochem. Soc.*, 155, (2008), pp. B887-B896.
- [68] Thompson E. L., Jorne J., Gu W., and Gasteiger H. A., "PEM Fuel Cell Operation at -20°C. I. Electrode and Membrane Water (Charge) Storage", *J. Electrochem. Soc.*, 155, (2008), pp. B625-B634.
- [69] Liu J. and Eikerling M., "Model of Cathode Catalyst Layers for Polymer Electrolyte Fuel Cells: The Role of Porous Structure and Water Accumulation", *Electrochim. Acta*, 53, (2008), pp. 4435-4446.

Chapter 4

Cathode Catalyst Layer Impedance Model for Low Current Operation

In this Chapter, a numerical model based on the fundamental electrode theory and the impedance experimental study has been developed to simulate the low current distribution in the time domain and the electrochemical impedance spectra of the cathode catalyst layer (CCL) of polymer electrolyte fuel cells (PEFCs). The model development consists of two stages, to establish the fundamental equations for the low current distribution in the CCL in the time domain, and to resolve the fundamental theory in the frequency domain. It was validated by comparing the simulated impedance of the CCL directly against the impedance data measured from an operational test cell. The simulated frequency response agrees well with the experimental data. The results showed that the model has established a backbone understanding of how the low current electrochemical mechanisms relate to the electrochemical impedance spectra of the CCL. It established a wider scope to relate the electrochemical impedance data to the fundamental theory of PEFCs.

Electrochemical reactions in the PEFC rely upon the utilisation of Pt in the catalyst layer (CL). One of the most important challenges is to obtain the highest electrochemically active surface area with the minimum amount of the catalyst. It has been proven that a simultaneous increase of electrochemical activity and rate of species transport cannot be obtained with a single homogeneous phase [1]. Furthermore, improving one property of the CL can adversely affect another. For instance, by increasing the amount of the electrolyte between agglomerates the ionic conductivity can be enhanced, but will also close void spaces for reactant transport. Developing CLs with smaller agglomerated structures can increase the electrode-electrolyte interface but can compromise secondary pores. An optimal CL structure is thus difficult to achieve.

To enhance the understanding of the factors governing the performance of CL structures and therefore how to engineer optimal CL structures, it is necessary to harness capabilities from both modelling and experimental techniques in a complementary manner. As discussed previously in Chapter 3, electrochemical impedance spectroscopy (EIS) is a non-invasive experimental technique which measures the opposition to the flow of an alternating current (AC) within a system which contains elements that dissipate energy and store energy. When subjecting a PEFC to a sinusoidal input (voltage), a sinusoidal output (current) is generated at the same frequency as the input but with a different amplitude and phase. The PEFC can be characterised in the frequency domain by measuring both the amplitude ratio of the input sinusoid (voltage) to the output sinusoid (current) and the phase shift as functions of the frequency. The energy dissipating and energy storing elements of the cell that result in the observed frequency response can be represented by an equivalent circuit model that is composed of resistors and capacitors respectively. The equivalent circuit model is fitted to the frequency response of the PEFC, to recreate the same spectrum.

The literature demonstrates that the EIS technique has been widely applied to characterise and evaluate electrochemical systems, particularly PEFCs. To date, the most rudimentary but pertinent application has been based on altering the operating conditions of the cell and determining its influence on the overall impedance response of the cell by considering both the measured frequency response and the simulated response from an equivalent circuit model. Romero *et al.* [2] applied this approach to demonstrate that the main characteristics in fuel cell impedance spectra are determined by the cathode. A classical circuit considering pore impedance coupled to a faradaic impedance component was proposed. The dependence of the cathode reaction characteristics on the potential was explored and values of the charge transfer resistance and cathode double layer capacitance were calculated and plotted. The results showed that the formation of the cathode capacitance was achieved after polarisation of about 200 mV from open circuit after which the cathode capacitance reached a value that remained constant for large currents. Furthermore, the charge transfer resistance diminished as overpotential increased.

Wagner [3] proved that it is possible to separate the overall cell impedance into impedance contributions from the electrode and the electrolytic resistance by simulating the measured EIS with an equivalent circuit. This treatment consisted of two resistor-capacitor (RC) parallel circuits each corresponding to the anode and cathode (charge transfer resistance and electrode capacitance), both in series with an ohmic resistance representing mainly the membrane. The results showed that the electrode impedances can be separated to represent the impedance of different reaction steps. Furthermore, integrating the impedance elements in the current density domain enabled the calculation of the individual overpotentials in the cell.

The use of EIS technique and the equivalent circuit method have also been used in the work of Jiang *et al.* [4]. This study compared impedance spectra at various CO concentrations mixed with hydrogen. An electric circuit was then used to fit the experimental impedance spectrum, similar to that applied by Wagner [3]. Modifications to the circuit were made in the anode circuit by introducing a $R_{ox} - C_{ox}$ parallel combination in series to a $R_{ad} - C_{ad}$ parallel couple for hydrogen adsorption to account for the lowering of the hydrogen adsorption impedance due to CO oxidation. Several sets of parameters obtained with the equivalent circuit were presented. The results showed a pseudo-inductive curve in the fourth quadrant of the complex-impedance-plane that accounts for the higher CO concentrations in the anode. Anode impedance shows that higher CO concentrations induced larger overpotentials for hydrogen oxidation by reducing the active surface of the anode. Andreaus *et al.* [5] used a simple model to fit the fuel cell impedance, varying the membrane thickness and the humidification of the reactants in the PEFC. The study was based on a simple Randles circuit using finite diffusion (Warburg) impedance in series with the charge transfer resistance of the cathode circuit to account for the limited oxygen supply due to cathode flooding. The results demonstrated that the impedance of the anode increased with membrane thickness. This could be attributed to a decrease in the net flux of water from cathode towards the anode. Wagner and Gülzow [6], included an inductive element in the electrode circuit to represent a surface relaxation process due to the competitive oxidation of H₂ and CO at the anode. In other studies [7,8] although the impact of such an element during fitting is small, the literature suggests that these inductive elements can be related to the flooding

of the electrodes. Other techniques have been developed using the same electrical circuits mentioned above with the aim of analysing the performance of the PEFC by impedance measurements considering the various effects influencing PEFC output, such as mass transport, charge transfer and ohmic overpotentials [9,10].

The literature demonstrates that the EIS technique has been increasingly applied to characterise the PEFC CL. Makharia *et al.* [11] applied the transmission line circuit model to interpret EIS data for cathodes with two different Nafion-to-carbon (N/C) weight ratios. The results demonstrated that the resistance of the CL electrolytic network increased with decreasing N/C concentration in the electrode. The work presented by Li and Pickup [12] also used the EIS technique and the finite transmission-line circuit to describe the effect of Nafion loading in the CCL. The impedance results provided strong evidence that the ionic conductivity of the CL increased with increasing Nafion content. Lefebvre *et al.* [13] demonstrated that EIS can be applied to extract detailed information about ion transport in the CL. Data for CLs with and without impregnated ionomer were compared. The Nafion-containing electrode was shown to have a much higher ionic conductivity, and, consequently, had a larger active area and provided better fuel cell performance.

Cano-Castillo *et al.* [7] analysed general flooding characteristics of the PEFC cathode using EIS measurements and the transmission line circuit model. As expected, the ionic resistance in the anode catalyst layer (ACL) decreased as the content of water in the cell increased. This could be explained by the back-diffusion of water from the cathode to anode, driven by a gradient in its concentration across the separating polymer electrolyte membrane (PEM). As the cathode is the source of water, it is not expected to have high ionic resistance but can be subject to flooding, thereby inducing a mass transport effect. Eikerling and Kornyshev [14] constructed impedance models for PEFCs and derived analytical solutions for several cases. This author also pointed out that there are two different ways to approach modelling: (i) using a system of differential equations to describe the physics and electrochemistry, or (ii) using an equivalent electric circuit of resistors and capacitors. In this approach the effects of reaction kinetic, double layer capacitance and ion conductivity in the CL were studied. The results help to distinguish

the contribution of the CL from the contribution of other fuel cell components and characterise it quantitatively. Suzuki *et al.* [15] demonstrated diagnostic techniques for evaluating ion conductivity and gas diffusivity in the CL. The ion conductivity measurements using the AC impedance method showed a reasonable dependence on Nafion loading. The gas diffusivity measurement using helium gain revealed the contribution of Knudsen diffusion in the CL. From these measurements, gas diffusion in the CL appears to limit the cell performance. Devan *et al.* [16] presented a macrohomogeneous model for a porous electrode that includes coupled potential and concentration gradients with linear kinetics. The equations are solved to obtain an analytical expression of a porous electrode. The results showed that concentration gradients become significant at very high exchange current densities.

It is noteworthy that the frequency response of a PEFC obtained from EIS reflects the response of the entire cell, including the internal layers and the phenomenological processes occurring within them. When an equivalent circuit is fitted to the frequency response of the entire PEFC, it is possible to selectively subtract some of the electrical components from that circuit in order to obtain the transmission line circuit which corresponds solely to one specific CL, as demonstrated by the literature. The frequency response of this CL alone can then be reproduced using the obtained transmission line circuit and previously-measured electrochemical properties of the CL. In this simulated frequency response, a 45° straight-line appears at the high frequency end of the spectra. When, for example, a parallel resistor-capacitor (R-C) circuit is used instead of the transmission line circuit, this straight-line does not appear. The literature demonstrates that this linear region can be associated to the ion transport in the CL [11,13] and that its value can be calculated from the projection of this section onto the real axis.

The purpose of this Chapter is to establish the relationship between the fundamental theory of the phenomenological process that occur within the CCL at low currents to the frequency response of a working PEFC and its equivalent circuit, i.e., the transmission line model. The objective of this Chapter is to generate a numerical model to predict the impedance spectrum of the CCL at low currents based on fundamental electrode theory and measurable properties of the CCL.

The study begins by stating the electrochemical reaction rates on a thickness basis to define the total current as a function of the CL thickness. Ionic resistance is subsequently considered in the expression of total current. The theoretical treatment in the time domain is then translated into the frequency domain which leads towards a mathematical expression to simulate the impedance spectrum of the CL, taking into account key parameters such as the Tafel slope, the exchange current, the ionic resistance and the charge capacitance.

The simulated frequency response from the numerical model is then validated at three operating temperatures. The physics of the CL (double layer capacitance, charge transfer resistance across the electrode-electrolyte interface and ion resistance in the electrolytic network) are obtained from experimental impedance curves for a PEFC by fitting the experimental curve to a transmission line circuit for the CCL using ZView software (Scribner Associates Inc. version 2.3). This is a standard software technique based on the Levenberg-Marquadt Algorithm (LMA) [17].

4.1 Electrochemical Mechanisms of CCL

The theoretical treatment of the electrochemistry of the CCL in this study is considered in six steps. The first step focuses on the fundamentals of reaction kinetics for the CCL and the definition of the forward and backward rate constants for the oxidation and reduction reactions. This is then modified to incorporate the dependence of reaction rates on temperature. The third step establishes the basic expression for total current in the CL. This is subsequently modified to include capacitance effects in the CCL, and the resulting equation is then linearised. The fifth step introduces ion resistance, which leads to an expression in the time domain that can be solved to determine spatial and temporal current distributions in the CCL. Finally, the key expression in the time domain is translated into the frequency domain to predict the frequency response of the CCL.

The main assumptions and considerations for the current theoretical treatment of the CCL are as follow:

- the mathematical analysis is considered for a PEFC under isobaric and isothermal conditions;
- only effects in the CCL are considered;
- oxygen diffusion limitations in the CCL are negligible at low currents;
- spatial gradients are only considered through the thickness of the CCL, and therefore the model is mathematically one-dimensional;
- the resistance to ion transfer in the electrolyte of the CL is much greater than the resistance to electron transfer in the carbon of the CL by several orders of magnitude [11]. Therefore electronic Ohmic loss in CCL can be regarded as being negligible. The literature suggests that this is a reasonable assumption when using a high-frequency resistance meter to estimate the resistivity of the catalyst layer [15];
- the metal alloy deposits supported on carbon and the dispersion of polymer electrolyte are spread homogenously in the CCL;

4.1.1 The Current in the Electrochemical Reaction

The electrochemical reaction occurring at the electrode takes the following form:



where Ox is the oxidized form of the chemical species (reactants), and Re is the reduced form of the chemical species (products). In equilibrium both reactions take place simultaneously, and the reactant rate (i.e., the amount of a reactant utilised or the amount of a product formed per unit time) is proportional to the surface concentration. However, the chemical reaction proceeds at different rates. The factors that affect reaction rates are; the surface area of a catalyst site; temperature; the phase of the reactants (i.e., gas or liquid) and the catalyst loading. A change in one or more of these factors may alter the rate of a reaction. When a catalyst is used (platinum in fuel cells) the reaction rate can be stated on a catalyst weight or surface area basis. In this analysis thickness basis was considered.

For reaction 4.1, the forward reaction flux of the chemical species considering thickness of catalyst layer is given by:

$$\frac{dv_f}{dx} = k_f c_O \quad (4.2)$$

and the backward reaction is given by:

$$\frac{dv_b}{dx} = k_b c_R \quad (4.3)$$

where $v_{f,b}$ is the flux of the species, $k_{f,b}$ is the reaction rate coefficient and $c_{O,R}$ is the surface concentration of the chemical species. Substituting Faraday's law $v = j/zF$ into the forward reaction flux yields an expression for the forward current:

$$\frac{\vec{dj}_f}{dx} = zFk_f c_O \quad (4.4)$$

and into the backward reaction flux yields the backward current:

$$\frac{\leftarrow{dj}_b}{dx} = zFk_b c_R \quad (4.5)$$

where z is the number of electrons released or consumed and F is the Faraday constant. Another factor altering the rate of the reaction is temperature. This can be expressed by Arrhenius equation:

$$k_{f,b} = A_a \exp\left(\frac{-G_{f,b}}{RT}\right) \quad (4.6)$$

where k is the reaction rate coefficient, G is Gibbs free energy of activation, R is the ideal gas constant, T is the temperature and A_a is called frequency factor. If the potential in the equilibrium of the chemical reaction is changed to a new value the Gibbs free energy will change as well, as detailed in the Appendix B.1. The forward reaction rate coefficient can be expressed as:

$$k_f = k^0 \exp\left(\frac{\alpha z F (E^o - E)}{RT}\right) \quad (4.7)$$

and the backward reaction rate coefficient as:

$$k_b = k^0 \exp\left(\frac{-(1-\alpha)zF(E^o - E)}{RT}\right) \quad (4.8)$$

where α is the charge transfer coefficient, E is the potential away from equilibrium and k^0 is called the standard rate constant¹. Substituting into the forward and backward current, Eqs. 4.4, 4.5 yields:

$$\frac{\vec{d}j_f}{dx} = zFc_o k^0 \exp\left(\frac{\alpha z F (E^o - E)}{RT}\right) \quad (4.9)$$

$$\frac{\overleftarrow{d}j_b}{dx} = zFc_R k^0 \exp\left(\frac{-(1-\alpha)zF(E^o - E)}{RT}\right) \quad (4.10)$$

Under equilibrium conditions, the reaction in Eq. 4.1 proceeds in both directions simultaneously at the same rate. Therefore the potential in equilibrium is equal to the potential of the electrode, $E^o = E$. In addition, the concentration (denominated as bulk concentration under this state) are the same for the chemical species, $c_{O,R}^*$. The rate at which the forward and backward transfer of charge occurs at equilibrium is known as the exchange current, j_0 . As such:

$$j_0 = zFc_o^* k^0 = zFc_R^* k^0 \quad (4.11)$$

When an external load is connected to a PEFC a current flows through the electrodes. The

¹ In the electrochemical literature, sometimes it is also called the intrinsic rate constant.

total current is the difference between the forward and backward currents and can be expressed as:

$$\frac{dj}{dx} = zFc_o k^0 \exp\left(\frac{\alpha zF(E^o - E)}{RT}\right) - zFc_R k^0 \exp\left(\frac{-(1-\alpha)zF(E^o - E)}{RT}\right) \quad (4.12)$$

A relationship between the potential far from equilibrium with regard to the equilibrium potential can be expressed as:

$$\eta = E_o - E \quad (4.13)$$

where η is a deviation from both potentials (overpotential). Substituting Eq. 4.13 into the expression of total current gives:

$$\frac{dj}{dx} = zFc_o k^0 \exp\left(\frac{\alpha zF\eta}{RT}\right) - zFc_R k^0 \exp\left(\frac{-(1-\alpha)zF\eta}{RT}\right) \quad (4.14)$$

Multiplying both terms in Eq. 4.14 by the bulk concentration $c_{O,R}^*$, and substituting the exchange current j_o defined in Eq. 4.11, gives:

$$\frac{dj}{dx} = \frac{c_o}{c_o^*} j_o \exp\left(\frac{\alpha zF\eta}{RT}\right) - \frac{c_R}{c_R^*} j_o \exp\left(\frac{-(1-\alpha)zF\eta}{RT}\right) \quad (4.15)$$

At low currents there are limited mass transportation effects therefore it is considered that there is no effect on the concentration of chemical species through the CCL. It can be assumed that $c = c^*$ for both reduction and oxidation processes. In addition when the overpotential increases, the contribution of the second term on the right-hand side of Eq. 4.15 becomes small, and therefore it can be neglected. The final equation rate of the current generation across the CL is:

$$\frac{dj}{dx} = j_o \exp\left(\frac{\alpha zF\eta}{RT}\right) \quad (4.16)$$

The CL is formed by a double layer structure for the interface between the dissimilar materials, i.e., the electrode-electrolyte interface. The electrode represents the electron-conducting network of carbon-supported platinum agglomerates while the electrolyte represents the ion-conducting dispersion of Nafion. At this interface an electric field is presented and has a determinant role in the charge distribution within the reactants as well as in the position and orientation of the reactant to form the desired products. This double layer can behave like a capacitor C_{dl} that is in parallel with the electrode reactions, the current passing from the electrode to the electrolyte either can take part in the charge transfer reactions or can contribute to the charge in the capacitive effect. As shown in Eq. 4.17.

$$\frac{dj}{dx} = j_0 \exp\left(\frac{\alpha z F \eta}{RT}\right) + C_{dl} \frac{d\eta}{dt} \quad (4.17)$$

The PEFC demonstrates a nonlinear current-voltage behaviour, as the current has an exponential dependence on potential. This can be seen in the polarisation curve representing the performance on the PEFC. Therefore, Eq. 4.17 is inherently nonlinear. Eq. 4.17 considers an input variable j , and an output variable η ; however it is necessary to approximate the response of this nonlinear system to that represented by a linear system around one point η_{ss} which represents the steady state of the nonlinear system.

Linearity in electrochemical systems is controlled by potential. The use of a low-amplitude voltage in the EIS technique allows application of a linear model in order to interpret the impedance spectra. For systems presenting a linear current-voltage relationship, a very large amplitude can be used. For systems presenting nonlinear current-voltage relationship, a much smaller amplitude is needed.

An electrochemical system that follows the Tafel law is polarized at a potential η_{ss} on the polarisation curve. If a potential is superimposed by EIS, the current response can be calculated using the Taylor series expansion. As such, a linear equation to represent the

current after superimposing a potential can be obtained by applying the mathematical treatment described in Appendix B.2 to Eq. 4.17 as such:

$$\frac{d\bar{j}}{dx} = \frac{\bar{\eta}}{R_C} + C_{dl} \frac{d\bar{\eta}}{dt} \quad (4.18)$$

where R_C represents the charge transfer resistance presented in the ORR and is defined as

$$R_C = \frac{b}{j_0 \exp(\eta_{SS} / b)} \quad (4.19)$$

$b = RT/\alpha zF$ is known as the Tafel slope.

4.1.2 Ionic Resistance and Current Distribution in CCL

The current passing through the electrode-electrolyte interface presents a capacitive behaviour due to an electrical field and consequently a potential difference between the dissimilar materials. The potential difference is represented as:

$$\bar{\eta} = \eta_{ELECTROLYTE} - \eta_{ELECTRODE} \quad (4.20)$$

Substituting Eq. 4.20 into Eq. 4.18 gives:

$$\frac{d\bar{j}}{dx} = \frac{\eta_{ELECTROLYTE} - \eta_{ELECTRODE}}{R_C} + C_{dl} \frac{d(\eta_{ELECTROLYTE} - \eta_{ELECTRODE})}{dt} \quad (4.21)$$

Furthermore ion conduction in the CCL depends upon the electrolytic dispersion and the state of hydration within the CCL. In addition, by neglecting the electronic resistance in the CCL [11,14,15] as a first approximation the mathematic analysis can be simplified. The potential in the electrolyte network can be expressed by Ohms law:

$$\frac{d\eta_{ELECTROLYTE}}{dx} = \bar{j} R_p \quad (4.22)$$

If Eq. 4.21 is substituted into Eq. 4.22 and neglecting the potential of the electrode $\eta_{ELECTRODE} = 0$, and considering η_{SS} in R_C as a constant due to $R_p/R_C \ll 1$ [11], see Appendix B.3, gives:

$$\frac{d^2 \bar{j}}{dx^2} = R_p \left[\frac{\bar{j}}{R_C} + C_{dl} \frac{d \bar{j}}{dt} \right] \quad (4.23)$$

Eq. 4.23 is a second-order partial differential equation and represents the low current distribution through the thickness of the CCL in the time domain taking into account, electrode kinetics, charge capacitance and ionic resistance in the CCL.

4.2 Cathode Catalyst Layer Impedance Model

The electrochemical reaction in a PEFC results in an inhomogeneous distribution of charge in the CL. As a result, a non-ideal capacitive behaviour has to be considered in the theoretical treatment. In order to correct for this inhomogeneity, a constant phase element (CPE) Y_S^P is used in the Laplace transform s of Eq. 4.23 to replace the capacitor C_{dl} in the electrochemical mechanisms of the CCL [18], as such:

$$\frac{d^2 \bar{j}(s)}{dx^2} = R_p \left[\frac{\bar{j}(s)}{R_C} + Y_S^P \bar{j}(s) \right] \quad (4.24)$$

where Y represents a parameter related to CPE and superscript P represents a parameter to correct the inhomogeneity in the distribution of charge. Eq. 4.24 gives the distribution of current in the CCL in the Laplace domain and can take the form of a homogeneous equation which can be solved through the method of n^{th} -order homogeneous equations with constant coefficients, as described in the Appendix B.4, which gives:

$$\bar{j}(s) = A \exp(\lambda_1 x) + B \exp(\lambda_2 x) \quad (4.25)$$

where $\lambda_{1,2} = \pm \sqrt{R_p \left[\frac{1}{R_c} + Ys^p \right]}$ represents the distinct roots of the characteristic equation represented.

Evaluating boundary conditions in Eq. 4.25, at the GDL-CCL $x=0$ and $\bar{j}(s)=0$, while at the CCL-PEM interface $x=1$ and $\bar{j}(s)=j_m(s)$, where $j_m(s)$ represents the maximum current as a function of the ion conduction via the PEM in the Laplace domain, gives:

$$0 = A + B \quad (4.26)$$

$$j_m(s) = A \exp(\lambda_1) + B \exp(\lambda_2) \quad (4.27)$$

Evaluating Eqs. 4.26 and 4.27 to determine A and B yields:

$$A = -\frac{j_m(s)}{\exp(\lambda_2) - \exp(\lambda_1)} \quad B = \frac{j_m(s)}{\exp(\lambda_2) - \exp(\lambda_1)} \quad (4.28)$$

Substituting Eq. 4.28 into Eq. 4.25 with the trigonometric identities yields the current distribution in the Laplace domain:

$$\bar{j}(s) = j_m(s) \frac{\sinh \lambda_1 x}{\sinh \lambda_1} \quad (4.29)$$

4.2.1 Potential Distribution in Laplace Domain

The potential in the Laplace domain can be obtained by transforming in the Laplace domain s , rearranging and replacing the capacitor C_{dl} by the CPE in Eq. 4.18 as such:

$$\bar{\eta}(s) = \frac{R_C}{1 + Ys^p R_C} \frac{d\bar{j}(s)}{dx} \quad (4.30)$$

Differentiating Eq. 4.29 with respect to x and substituting into Eq. 4.30 gives the potential in the Laplace domain:

$$\bar{\eta}(s) = \frac{R_C j_m(s) \lambda_1 \cosh(\lambda_1 x)}{[1 + Ys^p R_C] \sinh(\lambda_1)} \quad (4.31)$$

4.2.2 Impedance Model of the Cathode Catalyst Layer in Frequency Domain

The impedance of the CCL is defined as the ratio between the potential, Eq. 4.31, and the current Eq. 4.29 at the frequency domain with $s = i\omega$; where ω is the angular frequency, i is the imaginary component,

$$Z = \frac{\bar{\eta}(i\omega)}{\bar{j}(i\omega)} = \frac{R_C \lambda_1 \coth(\lambda_1 x)}{1 + Y(i\omega)^p R_C} \quad (4.32)$$

With $\lambda_1 = \sqrt{R_p \left[\frac{1}{R_C} + Y(i\omega)^p \right]}$

Eq. 4.32 represents the opposition to the flow of an alternating current within the CCL which contains physical processes that dissipate energy and store energy. The solution of Eq. 4.32 over a range of frequencies will contain real and imaginary components, which can be presented on a Nyquist plot.

4.3 Impedance Model and Validation

4.3.1 The Impedance Model in the Frequency Domain

The overall experimental and modelling framework developed for the current study is illustrated in Fig. 4.1. There are in essence two elements of the experimental work; the first element provides the frequency response of a working cell for validation purposes while the second element provides the requisite kinetic parameters of the CCL from electrical test to supplement the theoretical treatment. The modelling work involves two sequential stages; initially, a mechanistic description in the time domain followed by a translation into the frequency domain. Once validated in the frequency domain, results are obtained from the time domain in order to deduce spatial and temporal current gradients. This will be discussed in the next Chapter 9.

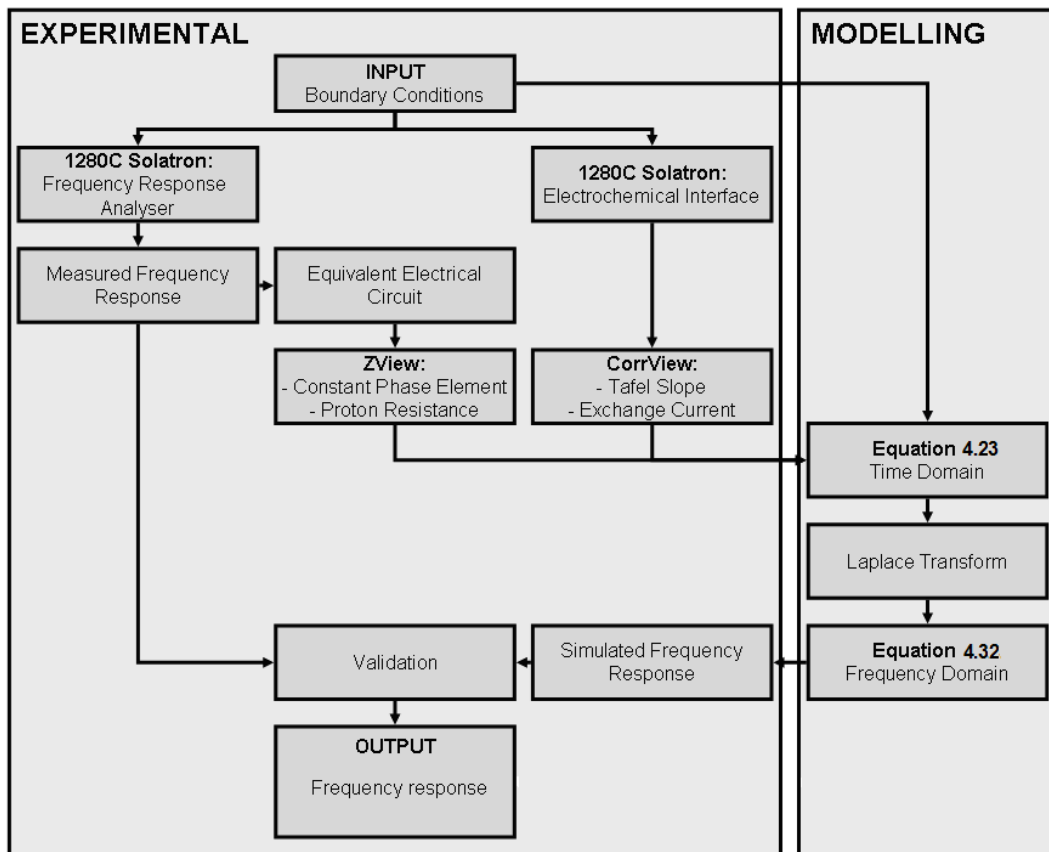


Figure 4.1 Overall experimental and modelling structure

4.3.2 Experimental Set-up

A commercial (Electrochem®) 5cm² single cell with carbon-supported 0.5 mgPt/cm² was used for the electrical tests. The cell was supplied with neat hydrogen and oxygen and operated with a dead-ended anode and cathode (stoichiometric ratio of 1) both at a gas pressure of 1 atm. The operating temperature of the cell was adjusted to 30, 40 and 60 °C. Both gases were fed dry. EIS measurements were taken at one current of the voltage-current curve in the activation zone for the three temperatures with a two-electrode configuration. The tests were performed using a Solartron 1280C electrochemical interface and a Solartron 1280C frequency response analyzer. The frequency scan was performed from 100 kHz down to 0.1 Hz, with an alternating voltage signal and 10mv amplitude. To estimate the kinetic parameters, the fuel cell was tested in a three-electrode configuration using CorrWare software. A reference electrode made of a platinum wire was in direct contact with the PEM of the cathode side. The 1280C unit measured the difference in potential between the working electrode (WE) and the reference electrode (RE).

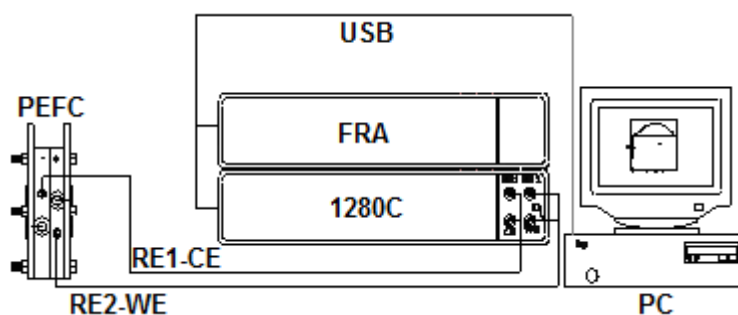


Figure 4.2 Experimental setup

4.3.3 Measured PEFC Impedance Response

Fig. 4.3 shows the measured impedance response of the whole PEFC when operating at 30, 40 and 60 °C. The results show that the diameter of the impedance spectra reduces with increasing operating temperature. The results also show that for 30 and 40 °C the high-frequency end of the impedance spectra intercepts the x -axis at a higher value than for 60 °C. The vertical segment at the high frequency end reflects the inductance in the

electrical cables of the measurement system. This vertical segment does not change in length and therefore demonstrates no significant change with temperature. Therefore, the main differences lie in the arc diameters and the x -intercept.

The arc of an impedance spectrum for an entire cell depends upon the kinetics of both electrodes. The reduction in arc diameter with respect to operating temperature occurs because the higher operating temperature fundamentally improves the electrode kinetics. The x -intercept reflects the resistance of the PEM; the lower the value of the x -axis intercepts, the lower the resistance of the PEM. In the current work, the impedance spectra are measured under potentiostatic conditions of 0.8 V. The improved kinetics with temperature allow a greater current to be drawn at this cell potential. At 30, 40 and 60°C, the current drawn is 19, 19.6 and 20 mA/ cm² respectively. It is possible that the resistance of the cell at 60°C could be lower than for the other two temperatures because the amount of water generated within the cell, which increases with current density and which is also due to residual water in the cell as the three tests are conducted sequentially with increasing temperature.

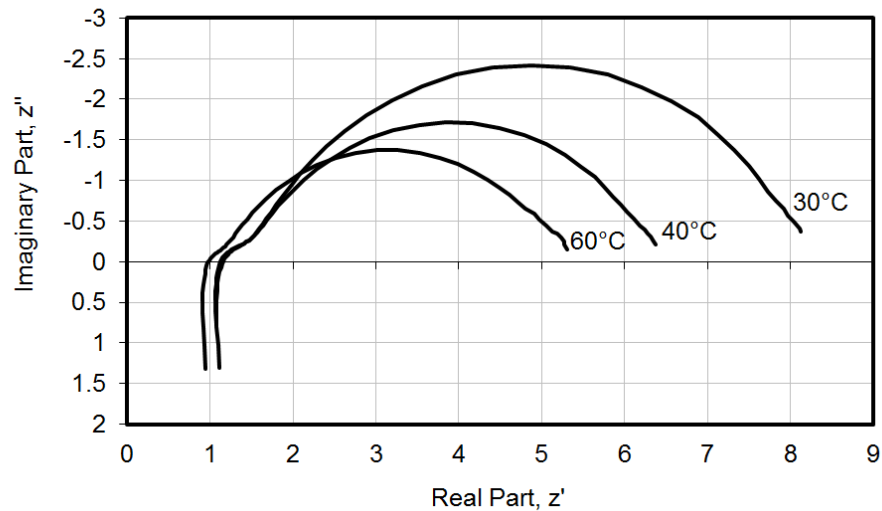


Figure 4.3 Measured impedance response in a working PEFC under potentiostatic conditions of 0.8 V at 30, 40 and 60°C

4.3.4 Equivalent Circuit Model

In order to obtain the parameters of the CCL for the mathematical analysis such as ionic resistance and CPE, the EIS was analysed by adjusting experimental data using a commonly-used equivalent circuit model where each electrode was represented by a transmission line. In this work the Ohmic resistance due to the supporting material in the electrode is neglected. The transmission line of each electrode is connected in series with an inductor element and a resistor. The inductor element accounts for the inductance of the cables used in the test equipment and the Ohmic resistance represents the resistance to ion flow across the PEM.

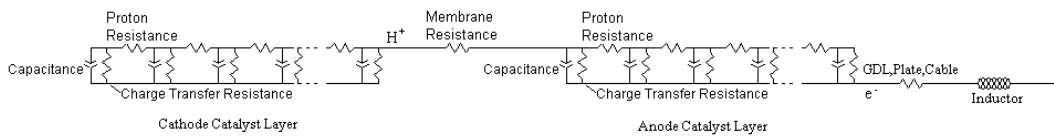


Figure 4.4 Equivalent circuit model for the PEFC

As discussed in the literature review, once an equivalent circuit model is fitted to the measured impedance spectrum of the entire cell, the transmission line of the anode catalyst layer, the Ohmic resistor for the PEM and the inductor element are all removed to leave the transmission line of the cathode catalyst layer. This can then be used to generate the AC impedance response of just the CCL in isolation, which is otherwise masked in the measured impedance spectrum of the entire cell.

4.3.5 Validation

In order to validate the theoretical treatment developed in this work, it is necessary to determine the kinetic parameters of the CCL, the ionic resistance of the CCL and the capacitive effect of the CCL for Eq. 4.32. The kinetic parameters are measured using the three-electrode configuration and CorrView software. The reported values for exchange current density j_0 for the ORR vary in literature from 10^{-4} to 10^{-7} A/cm² [19,20] depending on the morphology of the Pt catalysts. The ionic resistance and the capacitive elements are generated by the ZView software based on the measured impedance spectrum and the

transmission line accounting for the CCL as part of the entire equivalent circuit of the PEFC. Tab. 4.1 shows the parameters estimated by CorrView and ZView for the current configuration and test cases.

T °C	R _p Ω.cm ²	j ₀ x 10 ⁻⁵ A/cm ²	b x 10 ⁻³ V	Y x10 ⁻³ s ^p / Ω.cm ²	P	η _{ss} V
30	0.9	6.5	66.88	12	0.806	0.34
40	0.88	6.9	62.45	12.5	0.775	0.33
60	0.6	7.3	59.28	11.4	0.787	0.32

Table 4.1 Kinetics, ohmic and capacitive parameters of the PEFC estimated by Zview and Corrview software

The simulated impedance response based on the theoretical treatment is validated against the isolated impedance response of the CCL which is regenerated from the transmission line model of the CCL, as described in section of Equivalent Circuit Model. Fig. 4.5 shows the comparison between simulated and measured data at 30, 40 and 60°C. The simulated results were obtained from Eq. 4.32, and the measured data were from the transmission line equivalent electric circuit accounting from CCL. Overall, Fig. 4.5 shows that with the parameters given in Tab. 4.1, the theoretical model is capable of simulating the frequency response of the CCL with high accuracy. As with Fig. 4.3, Fig. 4.5 demonstrates that the frequency response is highly dependent upon operating temperature due to the effect on electrode kinetics.

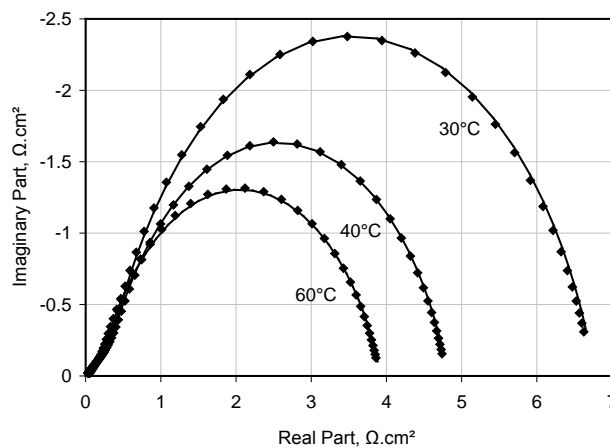


Figure 4.5 Comparison of impedance between simulated (-) and measured (♦) data

4.4 Conclusions

This Chapter has demonstrated that while EIS serves an important role in terms of PEFC diagnostics through in-situ impedance spectra and equivalent circuit modelling, a deeper understanding of internal fuel cell processes can be generated by coupling the experimental technique to underlying fundamental theory. The current Chapter demonstrates that the theory of electrode kinetics can be applied in order to simulate the frequency response of a PEFC CCL at low current densities. The theoretical formulation in the spatial domain is translated into the frequency domain using Laplace transforms. The predicted frequency response of the CCL is validated against that obtained from the measured electrochemical impedance spectra of a 5 cm² active area PEFC. The frequency response of the CCL is obtained by fitting the measured frequency response of the entire cell to an equivalent electrical circuit model, and reproducing the response of the CCL by extracting a transmission line to represent the CCL in isolation. The model is validated at three operating temperatures; 30, 40 and 60 °C. The results demonstrate excellent agreement between the simulated frequency response of the CCL and that obtained from measurements. The validation therefore confirms the theoretical treatment for low current operation.

4.5 References

- [1] Zhang J., PEM Fuel Cell Electrocatalysts and Catalysts Layers, Springer, New York (2008).
- [2] Romero-Castañón T., Arriaga L.G, and Cano-Castillo U., "Impedance Spectroscopy as a Tool in the Evaluation of MEA's", *J. Power Sources*, 118, (2003), pp. 179-182.
- [3] Wagner N., "Characterization of Membrane Electrode Assemblies in Polymer Electrolyte Fuel Cells using A.C. Impedance Spectroscopy", *J. Appl. Electrochem.*, 32, (2002), pp. 859-863.
- [4] Jiang R., Kunz H. R., and Fenton J. M., "Electrochemical Oxidation of H₂ and H₂/CO Mixtures in Higher Temperature (T_{cell} > 100°C) Proton Exchange Membrane Fuel Cells: Electrochemical Impedance Spectroscopy", *J. Electrochem. Soc.*, 152, (2005), pp. A1329-A1340.
- [5] Andreas B., McEvoy A. J., and Sherer G. G., "Analysis of Performance Losses in Polymer Electrolyte Fuel Cells at High Current Densities by Impedance Spectroscopy", *Electrochim. Acta*, 47, (2002), pp. 2223-2229.
- [6] Wagner, N., and Gülzow E., "Change of Electrochemical Impedance Spectra (EIS) with Time during CO-Poisoning of the Pt-Anode in a Membrane Fuel Cell", *J. Power Sources*, 127, (2004), pp. 341-347.
- [7] Cruz-Manzo S., and Cano-Castillo U., "Study of phenomena in a PEM fuel cell during increasing operating temperature using EIS", *Hydrogen Forum HYPOTHESIS VII*, Merida, Mexico, March 2007, ISBN: 968-6114-21-1.
- [8] Cano-Castillo U., Ortiz A., Manzo S., Arriaga L. G. and Orozco G., "Parameter Changes During Gradual Flooding of a PEM Fuel Cell Through EIS Studies", *ECS Trans.*, 3, (2006), pp. 931-939.

- [9] Schiller, C. A., Richter F., Gulzow E., and Wagner N., "Relaxation Impedance as a Model for the Deactivation Mechanism of Fuel Cells due to Carbon Monoxide Poisoning", *Phys. Chem. Chem. Phys.*, 3, (2001), pp. 2113-2116.
- [10] Baschuk, J. J., and Li X., "Modelling of Polymer Electrolyte Membrane Fuel Cells with Variable Degrees of Water Flooding", *J. Power Sources*, 86, (2000), pp. 181-196.
- [11] Makharia R., Mathias M. F. and Baker D. R., "Measurement of Catalyst Layer Electrolyte Resistance in PEFCs Using Electrochemical Impedance Spectroscopy", *J. Electrochem. Soc.*, 152, (2005), pp. A970-A977.
- [12] Li G., and Pickup P. G., "Ionic Conductivity of PEMFC Electrodes", *J. Electrochem. Soc.*, 150, (2003), pp. C745-C752.
- [13] Lefebvre M. C., Martin R. B., and Pickup P. G., "Characterization of Ionic Conductivity Profiles within Proton Exchange Membrane Fuel Cell Gas Diffusion Electrodes by Impedance Spectroscopy", *Electrochem. Solid-State Lett.*, 2, (1999), pp. 259-261.
- [14] Eikerling M., and Kornyshev A. A., "Electrochemical Impedance of the Cathode Catalyst Layer in Polymer Electrolyte Fuel Cells", *J Electroanal. Chem.*, 475, (1999), pp. 107-123.
- [15] Suzuki T., Murata H., Hatanaka T., and Morimoto Y., "Analysis of the Catalyst Layer of Polymer Electrolyte Fuel Cells", R&D Review of Toyota, Toyota Central R&D Labs, Inc., 39, (2003), pp. 33-38.
- [16] Devan S., Subramanian V. R., and White R. E., "Analytical Solution for the Impedance of a Porous Electrode", *J. Electrochemical Soc.*, 151, (2004), A905-A913
- [17] Scribner Associates Inc., "ZView Version: 2.1b," 150E, NC 28387, USA, 1984
- [18] Hsu C. H., and Mansfeld F., "Concerning the Conversion of the Constant Phase Element Parameter Y0 into a Capacitance", *Corrosion*, 57, (2001), pp. 747-748
- [19] Parthasarathy A., Srinivasan S., and Appleby A., J., Temperature Dependence of the Electrode Kinetics of Oxygen Reduction at the Platinum/Nation Interface-A Microelectrode Investigation, *J. Electrochem. Soc.*, 139, (1992), pp. 2530-2537.
- [20] Srinivasan S., *Fuel Cells From Fundamentals to Applications*, Springer, New York (2008).

Chapter 5

Cathode Catalyst Layer Impedance Model for High Current Operation

In this Chapter, a mathematical model to simulate the electrochemical impedance spectrum in the frequency domain of a polymer electrolyte fuel cell (PEFC) cathode catalyst layer (CCL) operated at high currents has been developed. The model is based on diffusion theory and the fundamental theories of electrochemistry. The general theory of experimental controlled-current methods to account for the change of oxygen concentration during the oxygen reduction reaction (ORR) will be taken into account. This method allows the derivation of the Warburg impedance that accounts for the diffusional impedance semicircle at low frequencies in experimental EIS measurements. Change of oxygen concentration due to ORR and ionic conductivity are related to the current distribution equation reported in Chapter 4 for low current operation of the CCL. The results from the mathematical model are compared against the frequency response of an experimental spectrum for a working PEFC reported in the literature.

The performance of a PEFC depends on the concentration of the reactants supplied to the catalyst layer (CL). A concentration gradient is therefore established which affects the electrochemical reaction. The study of the mass transport in the CCL is complex, yet has been treated in the literature with certain simplifications and approximations. Berger *et al.* [1,2,3,4,5] considers that diffusion occurs perpendicularly to the surface of the electrochemical reaction. Under this condition it is possible to assume that the drop of the reactant concentration is linear. There are two different methods of describing species diffusion in electrochemical systems when a thin film of finite diffusion is involved, such as in the CCL. Finite diffusion in the CCL describes the slow diffusion of the oxygen through a coating or a passive film. Semi-infinite diffusion is another method and can occur in batteries or super capacitors [6]. This method relies on a fixed amount of electro-active material; once it is consumed, it cannot be replaced.

As mentioned in the previous Chapters of this doctoral thesis, electrochemical impedance spectroscopy (EIS) is a technique that can be applied in-situ to separate the effects of physical processes in the PEFC that occur at different rates and to characterise mass transport effects. The frequency response that results from the EIS technique can be represented by an equivalent electrical circuit that is composed of resistors and capacitors. Each component represents a physical phenomenon occurring inside the PEFC. The diffusional impedance semicircle represented in experimental EIS measurements at high currents has been accurately reproduced through a mathematical expression derived from the Butler-Volmer equation and Fick's Second Law. This mathematical expression is known as the Warburg impedance. The literature demonstrates that the Warburg element in an equivalent electrical circuit of the PEFC can account for diffusive oxygen transport in the CCL, while the use of the Warburg element to model semi-infinite and finite diffusion in electrochemical systems has also been demonstrated. Malevich *et al.* [7] used the EIS technique and applied the Warburg element for finite diffusion in the equivalent circuit of a PEFC to study the influence of mass transport in the microporous layers (MPLs) of the cathode. The results showed that mass transport resistance increases with high current density for cells with and without the MPL. However, cells with a MPL demonstrated a lower mass-transport resistance compared to cells without a MPL. Skale *et al.* [8] proposed an alternative model for fitting electrochemical impedance spectra of protective coatings. EIS measurements were applied to characterise the coating degradation which is important to reduce the corrosion rate of metals. In this work the Warburg element for a semi-infinite diffusion in combination with EIS data were used to analyze the ion diffusion through micropores in the coating. That work concluded that the use of the Warburg element presents a better fit for these types of measurements than by models employing the constant phase element (CPE). The use of the semi-infinite Warburg impedance has also been used by Onda *et al.* [6] to approximate the response of nickel/metal-hydride and lithium-ion batteries. EIS measurements with the pulse current method and the equivalent circuit could provide a good estimate of the overpotential resistance that describes the thermal behaviour of batteries. Ciureanu *et al.* [9] applied EIS measurements with an equivalent electrical circuit which contains the semi-infinite Warburg impedance to measure the ionic conductivity of hydrated membranes of the PEFC. The EIS spectra showed a straight line with a 45° slope for the pure diffusion case.

At high temperatures the diffusion component of the spectra decreased, which can be attributed to dehydration. Fouquet *et al.* [10] monitored flooding and drying of a PEFC using a Randles electrical circuit coupled with a Warburg finite-length diffusion element in combination with AC impedance measurements. These results showed that the electrical model allowed parameters exhibiting high sensitivity to either flooding or drying out of the membrane electrode assembly (MEA) to be identified.

The objective of this Chapter is to develop a mathematical model to simulate the high current impedance spectrum in the frequency domain of the CCL using diffusion theory and the fundamental theories of electrochemistry. It is possible as such to establish a wider scope to relate the AC electrochemical impedance technique to the fundamental theory of PEFCs.

5.1 Modelling Considerations

Studies in the literature [11,12] have attempted to construct impedance models of the CCL based on conservation equations. A recent study by Kulikovsky [13] reported a system of differential equations based on charge conservation in the CCL, Ohm's Law relating ionic conductivity, and oxygen mass conservation equation to develop a mathematical model for the CCL impedance. The oxygen mass conservation equation considered Fick's second Law with oxygen effective diffusion coefficient in the CCL and oxygen consumption as a function of the CCL thickness. The solution of the system of differential equations resulted in complicated mathematical equations and only approximate analytical solutions were reported. No attempts were made to validate the model with real-world EIS measurements.

5.1.1 Oxygen Diffusion in the CCL

- There are three modes of transport of oxygen in the CCL which can have an effect on mass transport limitations: gas-diffusion in the electrode-pore, dissolved oxygen diffusion in the liquid water surrounding the agglomerate, and dissolved oxygen in the ionomer phase.

- The finite diffusion distance for oxygen to reach the reaction sites in the CCL forms a complicated network of multi-phase parallel and serial paths.
- The finite diffusion distance could change in dimension for different CCL composition (e.g. Nafion loading, porosity, tortuosity) and at different fuel cell operating conditions (current density, temperature, relative humidity, etc.)
- The study of mass transport in the CCL is very complex; the literature has treated it with some simplifications and approximations.
- A modelling approach to consider oxygen transport through the CCL thickness as part of a multi-species mixture using mass transport theory with concentrated solution theory could give a detailed characterisation of oxygen transport limitations through the thickness of the CCL; nevertheless the validation of the resulting equations with real-world EIS measurements could become a challenge.

5.1.2 Considerations

- EIS only measures bulk parameters in the total CCL thickness and reflects a total mass transport resistance and a total effective diffusion coefficient for the three modes of oxygen transport in the CCL.
- In the mathematical treatment of this Chapter, the finite diffusion distance y for oxygen to diffuse through the CCL will be considered to be independent from the thickness x of the CCL, as shown in Fig. 5.1, to simulate the CCL impedance spectrum at high currents.
- The change in oxygen concentration in the CCL during the ORR will be considered from the CCL-gas diffusion layer (GDL) interface c_o^* at $y=0$ to the CCL-polymer electrolyte membrane (PEM) interface c_o' at $y=\delta$, as shown in Fig. 5.1.

- Even though this mathematical treatment results in an over-simplification for the oxygen diffusion in the total CCL; this will simplify the mathematical analysis, and will allow the derivation of a model with parameters commonly known in the electrochemical area such as the Warburg impedance which simulates the low frequency semicircle of EIS measurements in PEFCs operated at high currents.

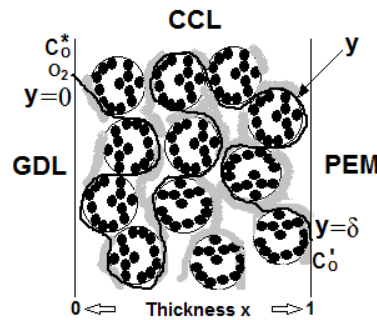


Figure 5.1 Oxygen transport in the CCL

5.2 CCL Mechanisms in Laplace Domain

The CL is formed by a double layer structure between the electrode and electrolyte interface. This double layer can behave like a capacitor that is in parallel with the electrode reactions. Therefore the current across the thickness of the CCL can take part in the charge transfer due to the ORR or contribute to the charge in the capacitive effect. This phenomenon was discussed and developed previously in Chapter 4. The electrochemical reaction in the PEFC results in an inhomogeneous distribution of charge in the catalyst layer. To correct for this inhomogeneity, a CPE Y_S^P has to be used in the Laplace transform s of the low current equation, (Eq. 4.18, Chapter 4) to replace the capacitor C_{dl} . In Chapter 4, it was considered that there is no change in oxygen concentration in the CCL at low currents. In this Chapter the ratio between oxygen concentrations at the CCL-PEM interface and GDL-CCL interface $c_o'(s)/c_o^*(s)$ defined in the modelling considerations from previous section 5.1.2 is taken into account at medium and high currents at the Laplace domain. This ratio between oxygen concentrations is

considered from the fact that the EIS technique only measures the change in oxygen concentration in the total CCL thickness.

$$\frac{d\bar{j}(s)}{dx} = \frac{c_o(s)}{c_o^*(s)} \frac{\bar{\eta}(s)}{R_C} + Ys^P \bar{\eta}(s) \quad (5.1)$$

Eq. 5.1 represents the current passing from electrode-electrolyte in the Laplace domain. The first term represents the rate of charge transfer due to the distribution of oxygen and the kinetics of the ORR in the CCL. The second term represents the rate of charge transfer due to the capacitive effect in the Laplace domain, $\bar{j}(s)$ is the current across the thickness of the CCL in the Laplace domain, $\bar{\eta}(s)$ is the potential difference between the electrode and electrolyte interface in the Laplace domain, $c_o(s)$ is the oxygen concentration at the CCL-PEM interface, $c_o^*(s)$ is the equilibrium oxygen concentration at the GDL-CCL interface in the Laplace domain, Y represents a parameter related to capacitance, superscript P represents a parameter to correct the inhomogeneity in the distribution of charge, R_C represents the charge transfer resistance presented in the ORR defined in Eq. 4.19, x represents the thickness (dimensionless) of the CCL from $x=0$ CCL-GDL interface to $x=1$ CCL-PEM interface. The change in oxygen concentration is estimated through the theory of controlled-current methods.

5.2.1 Oxygen Transport during the ORR in Laplace Domain

The concentration profile of chemical species during a simple electron-transfer reaction $Ox + e^- \xleftrightarrow{K} Re$ can be derived from the general theory of controlled-current methods [14]. This theory solves Fick's Second Law of diffusion and relates its solution with the flux of chemical species and Faraday's Law to account for the change in concentration of chemical species during an electrochemical reaction at a fixed current. The same procedure will be taken into account for the derivation of the change of oxygen concentration during the ORR in the CCL.

Step 1. Solution of Fick's Second Law in Laplace domain

Fick's Second Law is considered to model the effect of diffusion on the distribution of oxygen concentration in the CCL with respect to time, as such:

$$D \frac{\partial^2 c_o(y,t)}{\partial y^2} = \frac{\partial c_o(y,t)}{\partial t} \quad (5.2)$$

EIS measurements are carried out in PEFCs operated at steady state. At steady state the oxygen concentration is independent of time; hence Fick's Second Law can be expressed in Laplace domain s . D is the effective diffusion coefficient of oxygen. The solution of Eq. 5.2 in the Laplace domain requires an initial condition in $t=0$ as $c_o(y,0)=c_o^*$. This solution in the Laplace domain through the method of *undetermined coefficients for a nonhomogeneous linear differential equation* (see Appendix C) takes the form of:

$$c_o(y,s) - c_o^*(s) = A \exp(\beta_1 y) + B \exp(\beta_2 y) \quad (5.3)$$

The characteristic equation represented in the homogeneous part of Eq. C.2 Appendix C has two distinct roots $\beta_{1,2} = \pm \sqrt{s/D}$, y is the distance for oxygen to diffuse in the CCL from CCL-GDL interface $y=0$ to CCL-PEM interface $y=\delta$, as shown in Fig. 5.1. Evaluating boundary conditions in Eq. 5.3 at the CCL-GDL interface $c_o(0,s)=c_o^*(s)$ while at the CCL-PEM interface $c_o(\delta,s)=c'_o(s)$, gives:

$$A = \frac{c_o^*(s) - c'_o(s)}{\exp(\beta_2 \delta) - \exp(\beta_1 \delta)} \quad B = \frac{c'_o(s) - c_o^*(s)}{\exp(\beta_2 \delta) - \exp(\beta_1 \delta)} \quad (5.4)$$

Substituting Eq. 5.4 back into Eq. 5.3 gives:

$$c_o(y,s) - c_o^*(s) = \frac{[c_o^*(s) - c'_o(s)] \exp(\beta_1 y)}{\exp(\beta_2 \delta) - \exp(\beta_1 \delta)} + \frac{[c'_o(s) - c_o^*(s)] \exp(\beta_2 y)}{\exp(\beta_2 \delta) - \exp(\beta_1 \delta)} \quad (5.5)$$

Step 2. Change in oxygen concentration during the ORR

The first term on the right-hand side of Eq. 5.1 represents the current at which oxygen is consumed during the ORR in the Laplace domain:

$$\frac{d\bar{j}_1(s)}{dx} = \frac{c_o'(s)\bar{\eta}_1(s)}{c_o^*(s)R_c} \quad (5.6)$$

From Faraday's Law it is possible to establish that the current density in the CCL in the Laplace domain is proportional to the charge transferred and the consumption of reactant:

$$\frac{d\bar{j}_1(s)}{dx} = zFv(s) \quad (5.7)$$

where $v(s)$ is the flux of reactant, z is the number of electrons consumed during the ORR, and F is the Faraday constant.

From Fick's First Law it is possible to establish that the flux of reactant is proportional to concentration gradient

$$v(s) = -D \frac{dc_o(y,s)}{dy} \Big|_{y=\delta} \quad (5.8)$$

where D is the effective diffusion coefficient of oxygen and y is the distance for oxygen to diffuse in the CCL, as shown in Fig. 5.1.

In steady state the current at which the oxygen is consumed in the ORR from Faraday's Law is equal to the diffusion flux from Fick's First Law. Combining Eqs. 5.6, 5.7 and 5.8 yields:

$$\frac{c_o'(s)\bar{\eta}_1(s)}{c_o^*(s)zFR_c} = -D \frac{dc_o(y,s)}{dy} \Big|_{y=\delta} \quad (5.9)$$

Differentiating Eq. 5.5 with respect to the finite diffusion distance y yields:

$$\frac{dc_o(y,s)}{dy} = \frac{[c_o^*(s) - c_o(s)]\exp(\beta_1 y)}{\exp(\beta_2 \delta) - \exp(\beta_1 \delta)} \beta_1 + \frac{[c_o(s) - c_o^*(s)]\exp(\beta_2 y)}{\exp(\beta_2 \delta) - \exp(\beta_1 \delta)} \beta_2 \quad (5.10)$$

Rearranging Eq. 5.10 considering trigonometric identities and considering $\beta_2 = -\beta_1$ yields:

$$\frac{dc_o(y,s)}{dy} = \frac{\beta_1 [c_o(s) - c_o^*(s)] \cosh(\beta_1 y)}{\sinh(\beta_1 \delta)} \quad (5.11)$$

Substituting Eq. 5.11 into Eq. 5.9 with the boundary of CCL-PEM interface $y=\delta$ yields:

$$\frac{c_o(s)}{c_o^*(s)} \frac{\bar{\eta}_1(s)}{zFR_c} = -D\beta_1 \frac{c_o(s) - c_o^*(s)}{\tanh(\beta_1 \delta)} \quad (5.12)$$

Rearranging Eq. 5.12 yields:

$$\frac{c_o(s)}{c_o^*(s)} = \left[1 + \frac{\bar{\eta}_1(s) \tanh(\beta_1 \delta)}{R_c zFD\beta_1 c_o^*(s)} \right]^{-1} \quad (5.13)$$

The use of a small amplitude sinusoidal perturbation through the EIS technique allows the use of a linear model to represent the impedance of the CCL. The ratio between oxygen concentration at the CCL-PEM interface and CCL-GDL interface can be expressed as a function of mass transport resistance in the Laplace domain and charge transfer resistance. Considering the Laplace form $\bar{\eta}_1(s) = \bar{\eta}_1/s$ and $c_o^*(s) = c_o^*/s$ in the term on the right-hand side of Eq. 5.13 and replacing $\bar{\eta}_1$ by $\bar{\eta}_1 = RT/zF$ which represents a linearized relation of the overpotential [14], where R is the ideal gas constant, T is the operating temperature, and $\beta_1 = \sqrt{s/D}$ yields:

$$\frac{c_o'(s)}{c_o^*(s)} = \frac{R_C}{R_C + Z_W} \quad (5.14)$$

where:

$$Z_W = R_W \frac{\tanh(sT_W)^{0.5}}{(sT_W)^{0.5}} \quad (5.15)$$

is known as the Warburg Impedance [7,10] and represents the mass transport resistance in the Laplace domain and simulates the low frequency semicircle in EIS measurements of PEFCs,

with

$$R_W = \frac{RT\delta}{z^2 F^2 c_o^* D} \quad (5.16)$$

defined as resistance for the diffusion process and

$$T_W = \frac{\delta^2}{D} \quad (5.17)$$

defined as the time constant to diffuse oxygen through the CCL.

5.2.2 Current Distribution in Laplace Domain

Substituting Eq. 5.14 into Eq. 5.1 yields:

$$\frac{d\bar{j}(s)}{dx} = \frac{\bar{\eta}(s)}{R_C + Z_W} + Ys^P \bar{\eta}(s) \quad (5.18)$$

The literature identifies that ionic resistance in the electrolytic phase (i.e., polymer electrolyte) is higher than electron resistance presented in the electrode network of the CCL (i.e., typically carbon-supported catalyst) [15]. Furthermore ionic conduction in the CCL depends upon the electrolytic dispersion and the state of hydration within the CCL. In addition, by neglecting electron conduction in the CCL as a first approximation the mathematic analysis can be simplified. The potential in the electrolyte network can then be expressed by Ohms law $d\bar{\eta}(s)/dx = \bar{j}(s)R_p$, where R_p is the resistance to the flow of ions in the electrolytic phase of the CCL. This phenomenon was discussed previously in section 4.1.2, Chapter 4. If Eq. 5.18 is substituted into the potential in the electrolyte network and neglecting the potential of the electrode and considering η_{ss} in R_C as a constant due to $R_p/R_C \ll 1$ [15], see Appendix B.3, yields:

$$\frac{d^2 \bar{j}(s)}{dx^2} = R_p \left[\frac{\bar{j}(s)}{R_C + Z_w} + Y_{S^p} \bar{j}(s) \right] \quad (5.19)$$

Eq. 5.19 is a 2nd order homogeneous equation and represents the current distribution through the thickness of the CCL in the Laplace domain taking into oxygen distribution, electrode kinetics, charge capacitance and ionic resistance in the CCL. Its solution can be obtained by applying the method of *the nth-order homogeneous equation with constant coefficients*:

$$\bar{j}(s) = A \exp(\gamma_1 x) + B \exp(\gamma_2 x) \quad (5.20)$$

where $\gamma_{1,2} = \pm \sqrt{R_p \left[\frac{1}{R_C + Z_w} + Y_{S^p} \right]}$ represents the distinct roots of the characteristic equation presented.

Evaluating boundary conditions in Eq. 5.20, at the GDL-CCL $x=0$ and $\bar{j}(s)=0$, while at the CCL-PEM interface $x=1$ and $\bar{j}(s)=j_m(s)$, where $j_m(s)$ represents the current density of the cell, gives the current distribution in the Laplace domain,

$$\bar{j}(s) = j_m(s) \frac{\sinh(\gamma_1 x)}{\sinh(\gamma_1)} \quad (5.21)$$

5.2.3 Potential Distribution in Laplace Domain

The potential in the Laplace domain can be obtained by arranging Eq. 5.18 as:

$$\bar{\eta}(s) = \frac{R_c + Z_w}{1 + Ys^p(R_c + Z_w)} \frac{d\bar{j}(s)}{dx} \quad (5.22)$$

Differentiating Eq. 5.21 with respect to x and substituting into Eq. 5.22 gives the potential in the Laplace domain

$$\bar{\eta}(s) = \frac{[R_c + Z_w] j_m(s) \gamma_1 \cosh(\gamma_1 x)}{[1 + Ys^p(R_c + Z_w)] \sinh(\gamma_1)} \quad (5.23)$$

5.2.4 Impedance Model of CCL in Frequency Domain

The impedance of the CCL is defined as the ratio between the potential, Eq. 5.23, and the current, Eq. 5.21 in the frequency domain with $s = i\omega$; where ω is the angular frequency, i is the imaginary component,

$$Z_{CCL} = \frac{\bar{\eta}(i\omega)}{\bar{j}(i\omega)} = \frac{[R_c + Z_w] \gamma_1 \coth(\gamma_1 x)}{1 + Y(i\omega)^p [R_c + Z_w]} \quad (5.24)$$

$$\text{With } \gamma_1 = \sqrt{R_p \left[\frac{1}{R_c + Z_w} + Y(i\omega)^p \right]}$$

Eq. 5.24 represents the opposition to the flow of an alternating current AC within the CCL which contains physical processes that dissipate energy and store energy. The opposition to the AC load, or impedance, can be measured over a range of frequencies,

thereby revealing the frequency response of the CCL. By understanding the magnitude of the electrochemical and oxygen transport mechanisms represented in Eq. 5.24, it is possible to generate a deeper understanding of how and where the chemical energy that is released from the redox reaction is being dissipated and retained within the CCL. For the specific case where Z_w is considered to be negligible either due to a high diffusion coefficient or high bulk oxygen concentration, Eq. 5.24 will represent the current distribution in the CCL with equilibrium boundary conditions in terms of oxygen concentration. These conditions can occur for low current operation and as such, Eq. 5.24 reduces to Eq. 4.32 provided in Chapter 4 for low current characterisation. The solution of Eq. 5.24 over a range of frequencies will contain real and imaginary components, which can be presented on a Nyquist plot. Eq. 5.24 can be represented through the impedance of the electrical circuit shown in Fig. 5.2. The four elements represented in Fig. 5.2 are represented k_N a finite number of times, where k represents a collection of carbon-supported catalytic agglomerates coated by a thin layer of polymer electrolyte. Eq. 5.24 represents the impedance of the circuit shown in Fig. 5.2 considering k_N parameters.

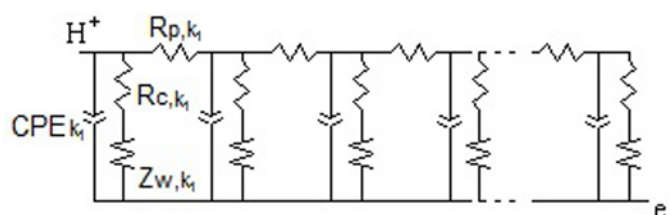


Figure 5.2 Electrical circuit for CCL characterisation at high currents

5.2.5 Model Validation in Frequency Domain

The modelling predictions of the mechanistic treatment of Eq. 5.24 can be compared against an experimental impedance spectrum reported in the literature of a hydrogen-air PEFC (H_2/Air) operated at 700 mA/cm^2 and $60 \text{ }^\circ\text{C}$ [7]. Requisite parameters defining the kinetics of the ORR, the double charge capacitance, the bulk concentration and the (effective) diffusion coefficient of oxygen were determined directly from the published experimental data. The validation process is described here.

An experimental impedance curve measured at high current of the polarisation curve was reported by Malevich *et al.* [7] and was considered in this study to validate the impedance model of the CCL. This author used a Randles equivalent circuit, as shown in Fig. 3.1, to estimate the charge transfer resistance, double layer capacitance and the Warburg impedance of the CCL.

The parameters of the Randles electrical circuit such as capacitance, charge transfer resistance and the Warburg element are estimated using ZView 2.9 software (Scribner Associates, Inc). As discussed in the literature [16], once an equivalent circuit model is fitted to the measured impedance spectrum of the entire cell, the electrical circuit of the anode catalyst layer and the Ohmic resistor for the PEM are all removed in order to reveal the equivalent circuit of the CCL. This can then be used to generate the AC impedance response of just the CCL in isolation, which is otherwise masked in the measured impedance spectrum of the entire cell.

The parameters of the Randles electrical circuit reported by Malevich *et al.* [7] are shown in Tab 5.1. These parameters were used to directly compare the model prediction from Eq. 5.24 to the impedance response generated from the Randles circuit. The Randles circuit does not take into account the ionic resistance R_p in the CCL electrolyte. The value of ionic resistance R_p in Eq. 5.24 was considered with a small order of magnitude 10^{-9} to be regarded as being negligible.

j mA/ cm ²	R_{ohm} Ω cm ²	R_C Ω cm ²	R_W Ω cm ²	T_W s	δ cm
700	0.017	0.173	0.136	0.110	0.0035

Table 5.1 Parameters of the CCL reported in the study of Malevich *et al.* [7]

Fig. 5.3 shows the comparison between the simulated spectrum from Eq. 5.24 and the spectrum generated from the Randles circuit.

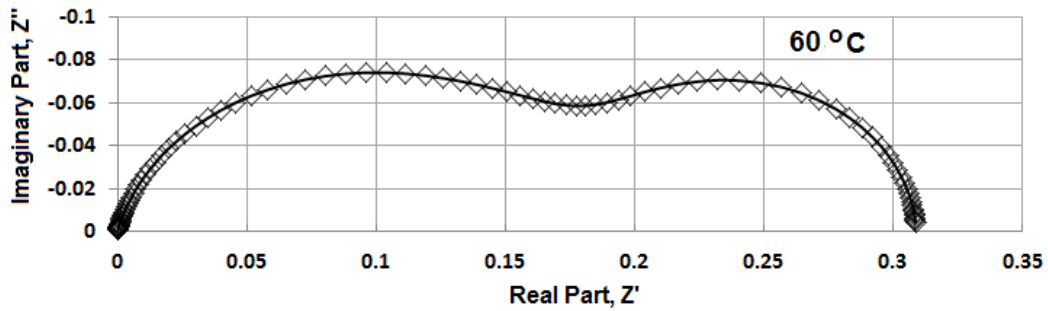


Figure 5.3 Comparison between simulated data using Eq. 5.24 (-) and measured data (\diamond) from Randles circuit

The results exhibit good agreement between the simulated and the measured data from the Randles circuit. The first arc of the impedance spectra reflects the capacitive effect due to the double layer interface between dissimilar materials and the kinetics of the ORR in the CCL. The second arc reflects the oxygen diffusion process within the CCL and is presented at low frequencies of the impedance spectrum.

5.3 Conclusions

The study began by solving the non-stationary diffusion equation expressed by Fick's second law with Faraday's Law to define the rate of oxygen distribution during the ORR in the CCL. By coupling the rate of oxygen concentration and ionic conductivity with the equation derived in Chapter 4 for low current operation of the CCL in the frequency domain it was possible to establish the impedance response of the CCL taking into account oxygen transport limitations Z_w , electrode kinetics R_c , charge distribution $Y(i\omega)^p$ and ionic resistance R_p in the CCL.

The mathematical treatment is validated against an impedance spectrum reported in the literature for a PEFC operated at 700 mA/cm^2 and $60 \text{ }^\circ\text{C}$. The physical processes in the CCL such as charge-transfer resistance, double-layer capacitance, ionic resistance in the electrolyte network and mass transport resistance in the frequency domain are taken from published experimental data [7]. The mathematical model agreed well with the frequency response of the CCL reported in the literature.

5.4 References

- [1] Berger C., Handbook of Fuel Cell Technology, Prentice-Hall, Inc. / Englewood Cliffs, N.J., New York, (1968).
- [2] Amphlett, J. C., Baumert, R. M., Mann, R. F., Peppley, B. A., and Roberge, P. R., "Performance Modeling of the Ballard Mark IV Solid Polymer Electrolyte Fuel Cell I. Mechanistic Model Development", *J. Electrochem. Soc.*, 142, (1995), pp. 1-8.
- [3] Larminie, J.E., Dicks, A., Fuel cell Systems Explained, John Wiley & Sons, LTD, Chichester, England, 2000.
- [4] Balkin, A. R., Modelling a 500 Watt Polymer Electrolyte Membrane Fuel Cells, Thesis, Faculty of Engineering, University of Technology, Sidney, Australia, 2002.
- [5] Correa J. M., Farret F. A., Canha L. N., "An analysis of the Dynamic Performance of Proton Exchange Membrane Fuel Cells Using an Electrochemical Model", *Industrial Electronics Society Annual Conference*, 1, (2001), pp.141-146.
- [6] Onda K., Nakayama M., Fukuda K., Wakahara K., Araki T., "Cell Impedance Measurement by Laplace Transformation of Charge or Discharge Current–Voltage", *J. Electrochem. Soc.*, 153, (2006), pp. A1012-A1018.
- [7] Malevich D., Halliop E., Peppley B. A., Pharoah J. G., Karan K., "Investigation of Charge-Transfer and Mass-Transport Resistances in PEMFCs with Microporous Layer Using Electrochemical Impedance Spectroscopy", *J. Electrochem. Soc.*, 156, (2009), pp. B216-B224.
- [8] Skale S., Dolecek V., Slemnik M., "Substitution of the Constant Phase Element by Warburg Impedance for Protective Coatings", *Corrosion Science*, 49, (2007), 1045-1055.
- [9] Ciureanu M., Mikhailenko S. D., and Kaliaguine S., "PEM Fuel Cells as Membrane Reactors: Kinetic Analysis by Impedance Spectroscopy", *Catalysis Today*, 82, (2003), pp. 195–206.
- [10] Fouquet N., Doulet C., Nouillant C., Dauphin-Tanguy, D., and Ould-Bouamama, B., "Model Based PEM Fuel Cell State-of-Health Monitoring via AC Impedance Measurements", *J. Power Sources*, 159, (2006), pp. 905-913.
- [11] Eikerling M., and Kornyshev A. A., "Electrochemical Impedance of the Cathode Catalyst Layer in Polymer Electrolyte Fuel Cells", *J Electroanal. Chem.*, 475, (1999) pp. 107-123.
- [12] Perry M. L., Newman J., Cairns J. E., "Mass Transport in Gas-Diffusion Electrodes: A Diagnostic Tool for Fuel-Cell Cathodes", *J. Electrochem. Soc.*, 145, (1998), pp. 5-15.
- [13] Kulikovskiy A.A., "A Physical Model for Catalyst Layer Impedance", *J. Electroanal. Chem*, 669, (2012), pp. 28-34.
- [14] Bard A. J., and Faulkner L. R, Electrochemical Methods, John Wiley & Sons, Inc., New York, (2001).
- [15] Makharia R., Mathias M. F. and Baker D. R., "Measurement of Catalyst Layer Electrolyte Resistance in PEFCs Using Electrochemical Impedance Spectroscopy", *J. Electrochem. Soc.*, 152, (2005), pp. A970-A977.
- [16] Cano-Castillo U., Ortiz A., Manzo S., Arriaga L. G. and Orozco G., "Parameter Changes During Gradual Flooding of a PEM Fuel Cell Through EIS Studies", *ECS Trans.*, 3, (2006), pp. 931-939.

Chapter 6

Inductive Effect on the Fuel Cell Cathode Impedance Spectrum at High Frequencies

Little attention has been considered on the inductance effect of the measurement system on impedance measured data. This Chapter demonstrates that the inductive effect of the electrical cables of the measurement system deforms the high frequency region of the cathode impedance spectrum and as such leads to an erroneous interpretation of the electrochemical mechanisms in the cathode catalyst layer (CCL). The Chapter demonstrates that a realistic understanding of factors governing electrochemical impedance spectroscopy (EIS) measurements can only be gained by applying fundamental modelling which accounts for underlying electrochemical phenomena and experimentation in a complementary manner.

The EIS measurements with positive imaginary components at the high frequency end of the polymer electrolyte fuel cell (PEFC) spectrum have been attributed to the inductance of the electrical cables of the measurement system. According to Ampere's law, inductance is caused by the magnetic field generated by electric currents. Inductance is commonly related to inductors formed by a wire wound in a coil; however a small straight piece of wire can present some self-inductance. The effect of inductance is often seen at the highest frequencies. The impedance of an inductor increases with increasing frequency and its effect can be noticed in low impedance systems < 1 ohm such as the PEFC. The inductive effect of the electrical cables in the EIS measurement system deforms the high frequency region and leads to an erroneous structural interpretation on the impedance spectrum [1,2]. Special care with the electrical connections must be taken during impedance measurements, as this could lead to irrelevant information normally represented as inductance and can lead to an incorrect interpretation at high frequencies of the impedance complex-plane. Ciureanu and Roberge [3] reported in their work that PEFC experimental impedance spectra in the high frequency range showed an inductive

behaviour characteristic to the experimental set up. To avoid complications resulting from such inductive characteristics, they limited the high frequency range to 1 kHz. Fouquet *et al.* [4] reported that inductive behaviour from the wires in EIS measurements was predominant above 1 kHz. Makharia *et al.* [5] concluded that the practice of using a specific high frequency value to estimate the ohmic resistance of the PEFC is subject to large errors (10-50%). The sizes of these errors depend on the frequency used and the size of the inductance. Merida *et al.* [6] reported in their work that it is possible to minimise the inductive effect by maintaining equal lengths in the cables, twisting the large current leads to the electronic load, and polishing and clamping the metal contacts. Other studies have reported that it is necessary to optimise the cables of the measurement system to reduce interference signals. In the study of Asghari *et al.* [7] an inductive characteristic at high frequencies in the EIS spectrum resulted from a non-uniform contact (assembly) pressure in a PEFC. The inductive characteristic was diminished gradually as the level of uniformity of the assembly pressure increased (uniform tightening of the supportive tie rods in the PEFC).

The objective of this Chapter is to reveal the inductive effect on the high frequency region of the complex-plot for the cathodic side of a PEFC. The validated model that accounts for the impedance spectrum of the CCL derived previously in Chapter 5 is applied with experimental impedance data reported in the literature. A further validation of the inductive effect is carried out by comparing the mathematical model with cathode experimental impedance data obtained with a three-electrode configuration and the use of conventional electrical cables (power flexible cable) and special low inductive cables (Low inductive cable with fusion Lug Technology, TDI POWER).

6.1 Inductive Effect on the Cathode Impedance Spectrum

In this Chapter the analysis of the inductive effect on the cathode impedance spectrum is divided into a theoretical analysis and experimental analysis. The theoretical analysis studies the effect of inductance on EIS measurements reported in the literature using the impedance model derived in Chapter 5 that accounts for the cathodic side of the PEFC. In the experimental analysis, an analysis of the Kramers-Kronig (K-K) consistency for

linear, steady and causal electrochemical systems was evaluated to analyse the inductive effect on the experimental impedance results.

6.1.1 Theoretical Analysis

In the previous Chapters 4 and 5, a model was developed based on fundamental electrochemical and diffusion theory to simulate the impedance spectrum of the CCL of a PEFC operated in any zone of the polarisation curve. The use of equivalent electrical circuits with the experimental EIS technique is a well-established methodology to characterise processes in the PEFC [8]. The electrical circuit that models the cathode impedance spectrum generated from EIS analysis and obtained through a reference electrode contains an inductor element that accounts for the inductance of the cables used in the test equipment connected in series with a resistance that accounts for the polymer electrolyte membrane (PEM), gas diffusion layer (GDL) and bipolar plate and connected in series with a circuit accounting for the CCL, in which for this specific case is the CCL impedance equation 5.24 reported previously in Chapter 5:

$$Z_C = L(i\omega) + R_e + \frac{(R_C + Z_W)\gamma \coth(\gamma x)}{1 + Y(i\omega)^p (R_C + Z_W)} \quad (6.1)$$

where $\gamma = \sqrt{R_p \left[\frac{1}{R_C + Z_W} + Y(i\omega)^p \right]}$

R_p is the resistance to the flow of ions in the electrolytic phase of the CCL,

R_C represents the charge transfer resistance presented in the oxygen reduction reaction (ORR) defined as $R_C = b / j_0 \exp(\eta_{SS} / b)$, where b is the Tafel slope, η_{SS} represents a value of voltage in activation overpotential, and j_0 is the exchange current,

Z_W is defined as the Warburg impedance and describes diffusion across a finite dimension in the frequency domain [4] $Z_W = R_W \tanh(i\omega T_W)^{0.5} / (i\omega T_W)^{0.5}$, with

$R_w = RT\delta / (z^2 F^2 c_o^* D)$ defined as resistance for the diffusion process and $T_w = \delta^2 / D$ defined as the time constant to diffuse oxygen through the CCL,

$Y(i\omega)^p$ Y represents a parameter related to constant phase element (CPE), superscript P represents a parameter to correct the inhomogeneity in the distribution of charge,

ω is the angular frequency,

i is the imaginary component in impedance,

L represents the inductance in the electrical cables of the measurement system,

R_e represents the total ohmic resistance to flow of electrons and ions in the bipolar plate, GDL, and PEM.

x represents the thickness of the CCL (dimensionless) and for EIS measurements is equal to 1.

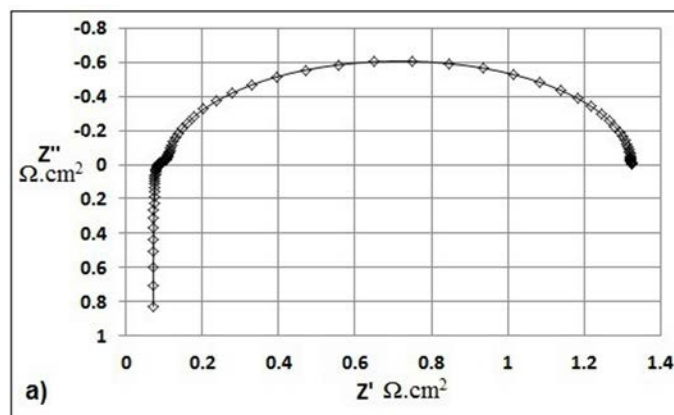
Makharia *et al.* [5] estimated the ionic resistance in the CCL for a 5 cm² PEFC (H₂-O₂) using membrane electrode assemblies (MEAs) with 0.8 and 0.4 Nafion/Carbon (N/C) ratios through impedance measurements. The impedance measurements were tested from 100 kHz to 0.01 Hz through a Zahner IM6e potentiostat. The authors considered that no losses across the electrolyte in the anode catalyst layer were expected because the hydrogen oxidation reaction (HOR) in the anode is so facile that any ionic electrolyte resistance would have the impact of shifting the anode current distribution close to the membrane, without requiring significant anode overpotential to do so. Therefore the PEFC impedance spectrum only accounts for the cathode electrode. In these published data the lack of a reference electrode could add an uncertainty to the interpretation of the data. In this theoretical analysis the published data are considered to represent the cathode impedance spectrum obtained through a reference electrode. The experimental analysis in the next section will consider a reference electrode to separate the cathode impedance

spectrum from the PEFC impedance spectrum. In the work of Makharia *et al.*, the ionic resistance of the CCL was estimated by fitting the experimental PEFC spectrum to the equivalent electrical circuit type transmission line using Zview software (Transmission Line-Open Circuit Terminus, DX-Type 6, Scribner Associates, Inc., version 2.3). The parameters of the equivalent circuit extracted from the experimental data of a MEA with 0.8 N/C ratio operated at 0.03 A/cm² are shown in Tab. 6.1.

j (A/cm ²)	L (H) Inductance	R_e Ω.cm ² Ohmic Resistance	R_p Ω.cm ² Ionic Resistance	Capacitance mF.cm ²	R_C Ω.cm ² Charge Transfer Resistance
0.03	1.32×10^{-6}	0.0687	0.122	19.67	1.215

Table 6.1 Parameters of the transmission line circuit accounting for the cathode electrode

The parameters in Tab. 6.1 were substituted into Eq. 6.1 to simulate the experimental impedance spectrum with no mass transport effect $z_w = 0$ as reported by Makharia and as shown in Fig. 6.1a. The resistive parameters from Tab. 6.1 should be reflected in the real component Z' (Ω.cm²) at Z'' (Ω.cm²) = 0 of the simulated impedance spectrum obtained from the mathematical model.



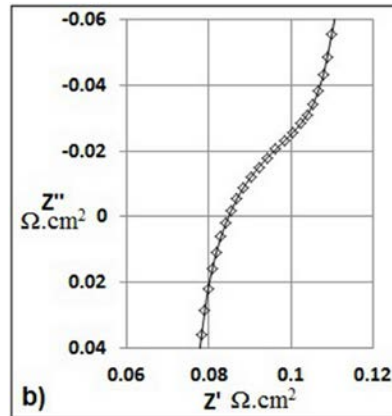


Figure 6.1 a) Simulated impedance spectrum from parameters in Tab. 6.1, b) Simulated high frequency region

In the literature, the real component $Z' \Omega \cdot \text{cm}^2$ at high frequency where the imaginary component $Z'' \Omega \cdot \text{cm}^2$ of the impedance spectrum is equal to zero has been reported as the ohmic resistance for the PEM, GDL and plate [3,9,10], which in this study corresponds to R_e from Tab. 6.1. A 45° region representing the ionic resistance in the CCL at high frequency when the PEFC is tested for H_2/N_2 operation has been also reported in the literature [11,12] and has been estimated by projecting the 45° region onto the real part Z' and calculated as $R_p/3$. The simulated impedance spectrum at high frequency represented in Fig. 6.1b reflects a value of $Z' = 0.084 \Omega \cdot \text{cm}^2$ at $Z'' = 0 \Omega \cdot \text{cm}^2$, which is different from R_e in Tab. 6.1, and the 45° region accounting for $R_p/3$ is difficult to estimate from Fig. 6.1b. This difference between R_e in Tab. 6.1 and the real component $Z' = 0.084 \Omega \cdot \text{cm}^2$ at $Z'' = 0 \Omega \cdot \text{cm}^2$ high frequency of the simulated impedance spectrum is attributed to the inductive effect L present in the impedance measurements.

The inductance L given in Tab. 6.1 was increased by one order of magnitude and decreased by one, two and three orders of magnitude in Eq. 6.1 to demonstrate its effect on the high frequency region of the complex plot, as shown in Figs. 6.2a, 6.2b.

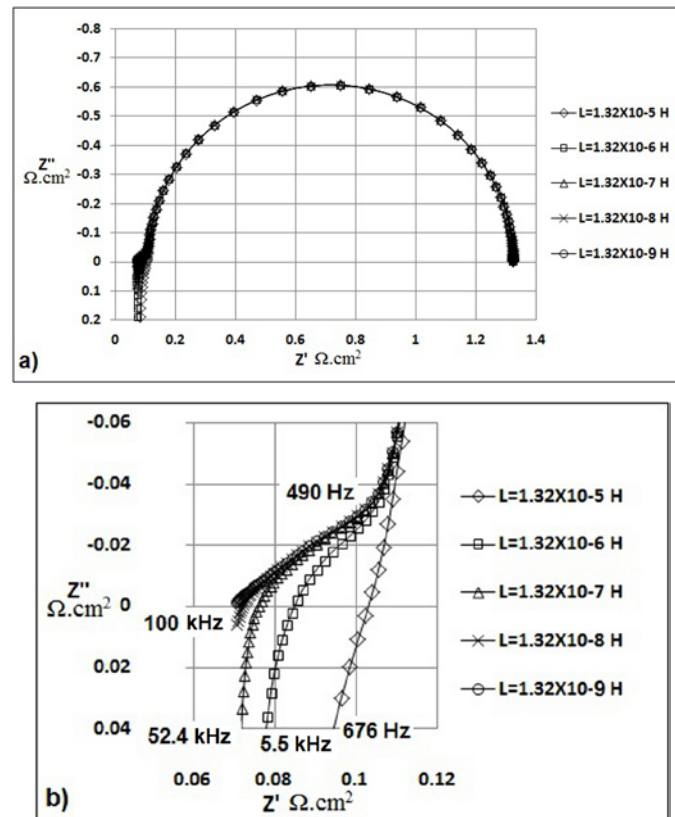


Figure 6.2 a) Simulated impedance spectrum with different inductance values, b) Simulated high frequency region

Fig. 6.2b shows that the real part Z' of the simulated data at high frequency where the imaginary part Z'' is zero in the complex plot changes for different inductance values. Inductance has been attributed to the external measurement system. Fig. 6.2b demonstrates that the spectra with different inductance values lead to an incorrect interpretation of the cathode mechanisms at high frequencies. Inductance of the measurement system does not have an effect on low frequencies where the mass transport effect is manifested; however, this inductance can misrepresent the high frequency mechanisms such as the ionic (and electro) conductivity in the real part of the complex plot Z' at $Z''=0$. Kurz *et al.* [13] predicted the voltage drop for dehydration in different PEFC stack impedance spectra through a specific high frequency value (1 kHz). This methodology reported by Kurz *et al.* to compare impedance data at high frequency through one high frequency value taken as a reference would seem a reasonable method, as for different inductance present in the system, the real component Z' will be kept

constant and just the imaginary component Z'' will be changed. Nevertheless this procedure would not correctly interpret the PEFC mechanisms present for such frequency.

6.1.1.1 Electrochemical Mechanisms in the Cathode Spectrum at High Frequency

This study demonstrates that if the inductive component L represented in Tab. 6.1 is reduced by 3 orders of magnitude in Eq. 6.1, the 45° line which has been reported in the literature [11,12] as the ionic resistance in the CCL is revealed in the cathode spectrum, as shown in Figs. 6.3a, 6.3b.

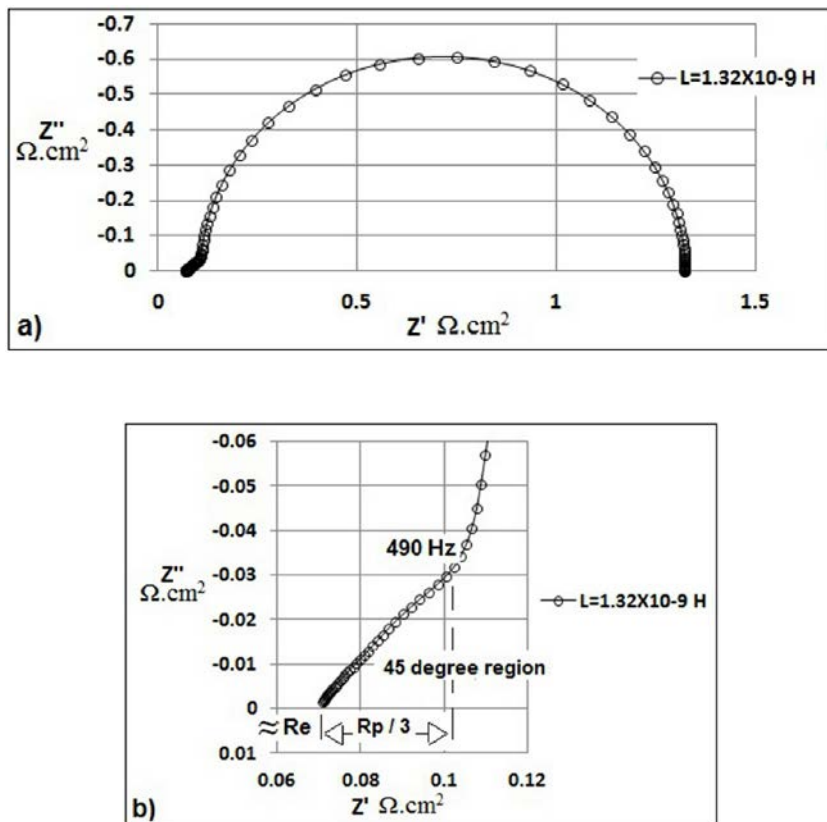


Figure 6.3 a) Simulated impedance spectrum with inductance reduced in 3 orders of magnitude, b) Simulated high frequency region

Fig. 6.3b shows that at the high-frequency end of the spectrum (100 kHz) the real impedance data Z' approximately reflects the value R_e reported in Tab. 6.1 and the ionic resistance is estimated by projecting the 45° region onto the real part $Z'\Omega.cm^2$. This projection between 100 kHz and 490 Hz is approximately $R_p/3$, and the difference between $R_e + R_p/3$ and the real impedance data Z' at a frequency of 0.01 Hz reflects the charge transfer resistance R_C of Tab. 6.1. The resistive parameters Z' at $Z'' = 0 \Omega.cm^2$ presented in the simulated impedance spectrum yield a 2% error compared with the parameters reported in Tab. 6.1. This error is attributed to the capacitor C_{dl} in Tab. 6.1. Instead a CPE, $Y(i\omega)^p$ should have been used in Eq. 6.1 which is not reported in the published data and appears in the transmission line equivalent circuit in Zview software to correct the inhomogeneity of the charge distribution between the electrode-electrolyte interfaces in the CCL [14]. This study demonstrates that the cathodic mathematical model represented by Eq. 6.1 is reliable in correctly estimating the inductance effect and the electrochemical mechanisms of the CCL.

An impedance-based approach which allows a spatio-temporal interpretation of internal fuel cell processes has not been presented or validated in fuel cell research to date. For example, as reported by Thompson *et al.* [15] by knowing exactly how the current for ORR is distributed through the CCL, it would be possible to develop cold start models that include the physics of product water uptake in the membrane and the filling of electrode pores with water (ice). Previously in Chapter 4, the low current distribution through the CCL thickness in the time that considers electrode kinetics, charge capacitance and ionic resistance in the CCL was defined as follows:

$$\frac{d^2 \bar{j}}{dx^2} = R_p \left[\frac{\bar{j}}{R_C} + C_{dl} \frac{d\bar{j}}{dt} \right] \quad (6.2)$$

where R_p represents the resistance to the flow of ions in the electrolytic phase of the CCL, R_C is the charge transfer resistance presented in the ORR, and C_{dl} is the charge capacitance between the electrode-electrolyte interface. The first term on the right-hand side of Eq. 6.2 defines the current distribution by the ratio of the ionic resistance to the

charge transfer resistance. Neyerlin *et al.* [16] defined a similar relationship, where the higher the non-dimensional ratio is, the more the current distribution will be skewed toward the membrane interface, while low values of this ratio predict a homogeneous current distribution. If the ratio between ionic resistance and charge transfer resistance increases, as expressed in Eq. 6.2, the ions may react closer to the membrane. However, in the case where the ratio between ionic resistance and charge transfer resistance is reduced, the ions will react through the entire CCL thickness leading to a uniform current distribution.

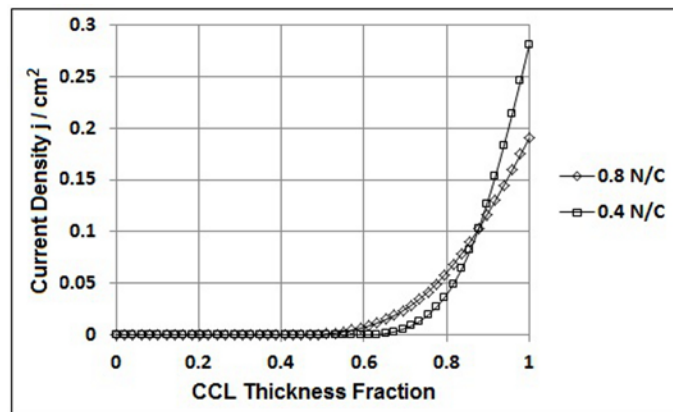


Figure 6.4 Simulated current density distribution through the CCL thickness

The parameters from Tab. 6.1 that represent the electrochemical mechanisms of a MEA with 0.8 N/C ratio and for a MEA with 0.4 N/C ratio reported in Makharia's study operated at 0.03 A/cm^2 were substituted into Eq. 6.2 to simulate the current distribution through the CCL thickness. Fig. 6.4 shows the current distribution through the CCL thickness. The current distribution increases from the $x=0$ thickness fraction (GDL-CCL interface) to the $x=1$ thickness fraction (CCL-PEM interface). This reflects the transfer of ions from the PEM and the anode catalyst layer, which results in maximum current at the interface between the CCL and the PEM and a minimum current at the interface between the CCL and GDL as ions are consumed due to the ORR through the thickness of the CCL. A high ionic resistance (0.4 N/C) within the CCL electrolyte tends to skew the current distribution towards the membrane interface. Therefore, as reported by Thompson *et al.* [15], the same average current has to be provided by fewer catalyst sites near the membrane. The increase in ionic resistance results in kinetic losses because the ORR

current distribution expressed in Eq. 6.2 is a function of the Tafel slope, exchange current density and ionic resistance. The ionic resistance in the CCL related to the magnitude of the 45° region ($R_p/3$) in the cathode impedance spectrum at high frequency can bias the ORR current density distribution towards the membrane interface, as shown in Fig. 6.4. Overall this study demonstrates that it is necessary to take extra care in the hardware of the measurement system in order to quantify the cathode mechanisms revealed at high frequencies.

6.1.2 Experimental Analysis

The contributions of the anode and cathode in the PEFC impedance spectrum using a two-electrode configuration in the EIS measurements are difficult to interpret, as this information is masked in the PEFC impedance spectrum. A three-electrode configuration for EIS allows the measurement of half-cell impedance (anode or cathode) to be carried out. Some studies [17,18] have applied the three-electrode configuration in EIS measurements. Under such conditions, the signals are measured between the working electrode (WE) and the reference electrode (RE), and the current induced is collected by the counter electrode (CE).

6.1.2.1 EIS Measurements

A 25 cm^2 commercially-available fuel cell and test rig acquired from Baltic Fuel Cells were used for the experimental tests. The MEA was DuPont Nafion-115 with a platinum loading of 0.4 mg/cm^2 on both electrodes. The operational temperature was 50°C and the back gas pressure was held to 0.9 bar(g) for both anode and cathode. Flow rates were constant during all the experiments, hydrogen in the anode with a stoichiometry of 2.5 and air in the cathode with a stoichiometry of 3. The PEFC was operated with 100% hydrogen relative humidity (RH) in the anode; the air supplied in the cathode was dry. In terms of optimal performance of operational PEFCs, the effect of RH in the reactant gases is not definite. For instance, Yan *et al.* [19] reported that optimal performance in a PEFC can occur at low air relative humidity and high hydrogen relative humidity.

EIS measurements were carried out through a multichannel frequency response analyser FRA (Z#106 WonATech Co). The multichannel FRA consists of five channels and simultaneously measures five impedance spectra through one induced DC current value. The multichannel system is connected with a RBL488 Dynaload load bank. The multichannel FRA superimposes a small AC sinusoidal perturbation onto the bias current induced by the RBL488 Dynaload unit and measures the AC voltage signals resulting from the PEFC. The impedance measurements were carried out in a galvanostatic mode with 5% AC amplitude of the DC current [20,21,22] to obtain a linear answer from the system and at frequencies from 10 kHz to 0.2 Hz, the high frequency in the EIS measurements was limited due to the bandwidth of the electronic load. The low frequency is not relevant in the inductive effect of the measurement cables. To separate the impedance spectrum of the cathode from the impedance spectrum of the cell, a reference electrode made of a platinum wire was inserted such that it was in direct contact with the PEM of the cathode side. Two channels from the Z#106 FRA were used to simultaneously measure the impedance of the PEFC and the impedance solely accounting for the cathode electrode.

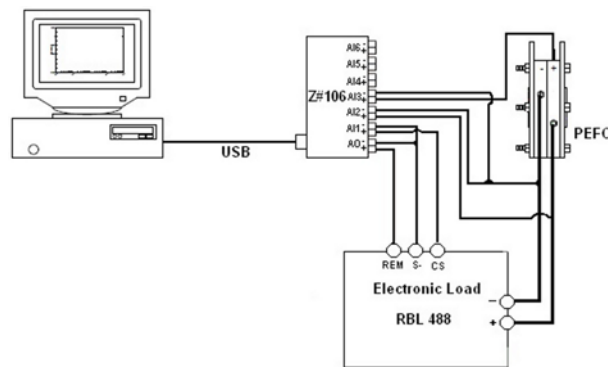


Figure 6.5 Experimental setup

Based on the results from the theoretical analysis in section 6.1.1, EIS measurements were carried out at 0.2 A/cm^2 using two different electrical cables, a conventional electrical cable (power flexible cable) and a special electrical cable (Low inductive cable with fusion Lug Technology, TDI POWER) connected between the PEFC and the RBL488 Load, as shown in Fig. 6.5. A reference electrode and the use of the multichannel FRA allowed the separation of the cathode impedance spectrum from the

impedance spectrum of the entire cell. For this study high inductance spectra are dominant when the conventional electrical cable was used, and low inductance spectra when the special low inductive cable referred to above was used in the EIS measurements.

It has been proposed that the PEFC impedance spectrum largely represents the electrochemical processes in the cathode, and as discussed because the electrochemical mechanisms in the anode are fast and facile are not expected to have a contribution [3,4]. Fig. 6.6a shows a difference between the spectrum of the cell and the spectrum of the cathode. Fig. 6.6b shows that the real part Z' that accounts for the cathode at high frequency when $Z''=0$ is smaller than that for the cell. The semi-circular part of cathode spectrum presents roughly the same features as the PEFC spectrum and a shift over the real part Z' . This difference is expected as the cathode is hydrated by the water produced by the ORR and due to electro-osmotic drag from the anode. This difference in the real part Z' between the cell and cathode could be attributed to the electro-osmotic effect in the anode. The transport of water from the anode to the cathode by electro-osmotic drag can play a role in dehydrating the membrane and inducing performance degradation [23]. The magnitude of the inductive effect (EIS measurements with positive imaginary component Z'') on the spectrum of the cell was higher than that of the cathode using the conventional cable (high inductance spectra). The sensing cables from the FRA to measure the cell impedance spectrum were connected to the hardware of the cell where electrical cables lie. The reference electrode allowed the reduction of the inductive effect on the EIS measurements for the cathode by placing the sensing cables from the FRA as far apart as possible from the inductive source (electrical cables).

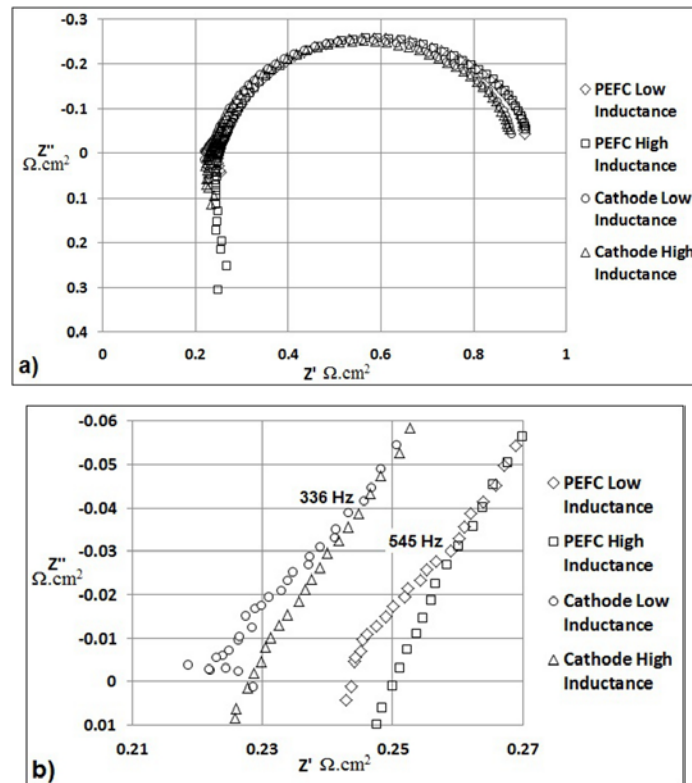


Figure 6.6 a) EIS measurements of the PEFC and cathode electrode, b) EIS measurements at high frequency

Fig. 6.6b shows the high frequency region of the experimental impedance spectra. As expected from the theoretical analysis in section 6.1.1 low inductance in the measurement system reveals the 45° region at a frequency of 336 Hz in the cathode spectrum which accounts for the CCL ionic resistance and plays an important role in the ORR current density distribution through the CCL thickness, as discussed in the previous section. The PEFC spectrum with low inductance in Fig. 6.6b also presents a 45° region at 545 Hz which is slightly different from that of the cathode. This spectrum of the entire cell not only accounts for the ionic resistance in the CCL electrolyte but also the mechanisms present in the anode.

6.1.2.2 Kramers-Kronig Analysis on EIS Measurements

One key advantage of the EIS technique is that it is non-invasive and can be applied in-situ. Another advantage is that the frequency response tests are simple to carry out and can be easily tuned for greater accuracy by using readily-available sinusoidal generators and precise measuring equipment. Impedance experiments involve the conversion of time-domain input and output signals into a complex quantity that is a function of frequency. The resulting experimental impedance has to be consistent with K-K relations. These relations are mathematical properties that relate the real and imaginary part of the frequency response resulting from the electrochemical system studied. The derivation of the K-K mathematical relations begins with an application of Cauchy's Integral Theorem which defines the integral around a closed contour and evaluates the real part or imaginary part of the impedance at a particular frequency with poles created at $-\omega$ and ω in the real axis of the frequency domain. K-K relations are applied to systems which are linear, causal and stable and have been applied in electrochemical impedance data over the last 20 years [24,25,26]. If the experimental imaginary component of the PEFC impedance does not coincide with the transformed imaginary component (real to imaginary transformation), nor the experimental real component with the transformed real component then the experimental data are not obtained under either a causal system (the measured impedance response is due only to the AC perturbation applied), linear system (for small AC perturbations) or stable system (the system returns to its original state after the perturbation is removed and does not change with time) [25]. The K-K relations cannot be used to determine if the impedance measurements were corrupted by instrument artifacts. In the work reported by Macdonald *et al.* [26] different amplitudes of the AC sinusoidal perturbation with a potentiostatic mode were changed from 5 mV to 150 mV to test the linearity condition of data for a rapidly corroding aluminium alloy through the K-K relations. The results showed a successful K-K transformation of the impedance data, in spite of a clear violation of linearity when the amplitude was increased. This success in the K-K transformation was an artifact of the experimental equipment used for the impedance measurements. The authors concluded that some commercial frequency response analysers are narrow band devices that reject inputs at frequencies other than that designated; in other words some frequency response analysers can reject harmonic components of the current response that manifest nonlinearity.

An analysis of the K-K consistency for linear, steady and causal systems was evaluated to analyse the inductive effect on the experimental impedance results of this study. The K-K consistency was evaluated through ZMAN software [27] in which the K-K transformed data are calculated by Maclaurin's series method. The difference or residual in phase angle between the K-K transformed data and the measured impedance data $\Delta Phase = \varphi Z_{KK} - \varphi Z_{EXP}$ provides excellent sensitivity to discrepancies in the experimental values; this also can indicate a need to remove experimental data that are not consistent with the K-K relations [28].

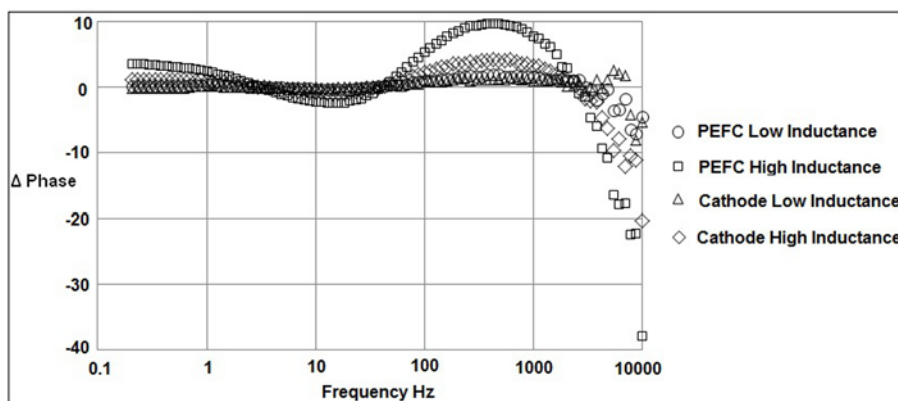


Figure 6.7 Residual in phase angle between K-K transformed and measured data for the PEFC and cathode impedances under the influence of inductance

The residual phase in Fig. 6.7 is presented because one or more of the conditions to satisfy the K-K relations such as causality, linearity and stability are not fulfilled. Since the PEFC polarisation curve is a nonlinear response, the use of a low AC amplitude in the impedance measurements allows the evaluation of the PEFC polarisation curve as a pseudo-linear response. A high AC amplitude would not be consistent with the K-K condition for linear systems [26]. The PEFC under study was steady, thereby the EIS measurements were repetitive. The causality condition is not satisfied in the EIS measurements with inductance. Hence the measured impedance response is not only due to the AC perturbation but also to the external inductance of the measurement cables. The condition of stationarity is implicit in the requirement of causality and vice versa [28]. The statement mentioned before can be demonstrated in the EIS data presenting high inductance where the difference in phase is present at high frequencies (not causal) and

low frequencies (not steady), as shown in Fig. 6.7. The K-K relations, based on the property of causality, demonstrate a useful method for data validation [29].

The residual phase in Fig. 6.7 is reduced for the data with low inductance. The cathode presents a minor difference in the residual phase compared to the PEFC because the reference electrode allows the reduction of the inductive effect on the EIS measurements because the sensing cables from the FRA are located away from the inductive source. The 45° high frequency region in the cathode low inductance impedance spectrum was revealed at a frequency of 336 Hz and for the PEFC was revealed at a frequency of 545 Hz, as shown in Fig. 6.6b. In Fig. 6.7 the residual phase of the EIS data presenting low inductance is less at frequencies of 336 Hz and 545 Hz for the cathode and the PEFC respectively than for EIS data with high inductance. The measured EIS data at frequencies where the residual phase is different to zero do not reflect the physics and chemistry of the electrochemical system studied. If the external inductance of the experimental system could be eliminated and the remaining inductance would be due to any intrinsic inductance presented in the porous media of the electrode, the K-K transformation would be satisfactorily achieved as this inductance would be a physical property of the system studied. K-K transforms represent a convenient means of evaluating the validity of experimental impedance data.

6.2 Validation of Inductance Effect on the Cathode Impedance Spectrum at High Frequency

In these experimental results, the use of a reference electrode ensures that the data accounting for the processes in the CCL are captured for analysis and interpretation. To validate the experimental results, the mathematical model devised in Eq. 6.1 was compared with the cathode experimental spectra obtained using a graphical user interface (GUI) developed in Matlab®, see Appendix D. The GUI allows the fitting of the parameters from Eq. 6.1 to achieve a good agreement between the experimental and simulated data. The least squares fitting method was used in order to find the best-fit between the model and the measured data. A good quality fit is obtained when the sum of the deviations squared (least square error) between the simulated and measured

impedance data has a minimum value, for instance < 0.1 . Figs. 6.8a, 6.8b show the comparison between the simulated data and the measured data.

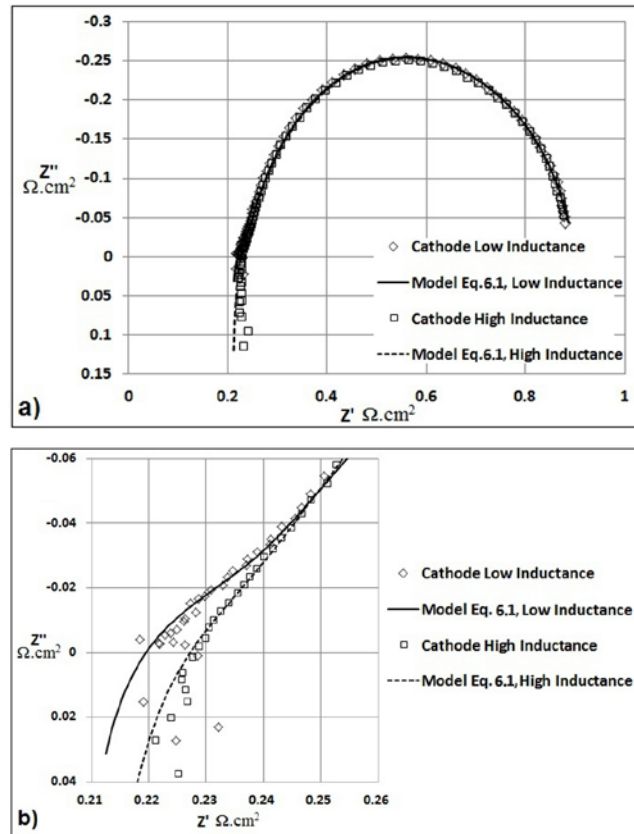


Figure 6.8 a) Comparison between simulated and measured data, b) High frequency region

Scattered data at high frequencies were present for both experimental cathode spectra, as shown in Fig. 6.8b, and were more noticeable for the low inductance spectrum. This behaviour could be attributed to external noise at high frequency during the EIS tests. The noise disappeared when the magnitude of the inductance was increased, for instance in the high inductance PEFC spectrum the shape of inductive effect presented a straight line, as shown in Fig. 6.6a. To quantify the inductive effect on the experimental data, the biggest value of the data presented in the positive imaginary component Z'' of the spectrum was taken as a reference.

Eq. 6.1 was first fitted to the experimental cathode spectrum for low inductance using the GUI developed in Matlab® (Appendix D) and the results are shown in Tab. 6.2. Mass transport effects at low frequencies were apparent during the EIS measurements, as shown in the parameters from Tab. 6.2 defining Z_w in Eq. 6.1. This effect is not relevant in the inductive effect at high frequencies.

j (A/cm ²)	L (H)	R_e Ω.cm ²	R_p Ω.cm ²	Y CPE x10 ⁻³ s ^p /Ω.cm ²	P	R_C Ω.cm ²	R_w Ω.cm ²	T_w sec
0.2	6.77x10 ⁻⁷	0.195	0.12	38.2	0.8282	0.41	0.26	0.003

Table 6.2 Parameters accounting for the cathode spectrum obtained through the GUI

Once defined, the inductive component which simulates the low inductance cathode spectrum was increased from $L = 6.77 \times 10^{-7} H$ to $L = 2.07 \times 10^{-6} H$ and the remaining parameters from Tab. 6.2 were kept constant. This allowed the simulation of the cathode spectrum with high inductance as shown in Fig. 6.8b. It is noticed that the calculated inductance of the curve with high inductance presents the same order of magnitude as the inductance from the data taken from the literature [5] shown in Tab. 6.1 of the theoretical analysis in section 6.1.1 of this study. Therefore, taking these values as a base, an inductance of the order of $10^{-9} H$ and using a sinusoidal generator and precise measuring equipment allowing the increase of the frequency up to 100 kHz would clearly show the 45° region that extends from the real component Z' and whose projection onto the real part Z' represents the ionic resistance of the electrolyte in the CCL. The inductance that remains present in the data for the low inductive cathode spectrum can be attributed to the hardware of the PEFC or any intrinsic inductance presented in the porous media of the CCL. Hampson *et al.* [30] concluded on their work, that the presence of porosity on electrodes may lead to the impedance becoming inductive at high frequencies.

This experimental study complements the theoretical analysis presented in section 6.1.1, by separating the cathode impedance spectrum from the PEFC and comparing the same system under the influence of the inductance on the measurement impedance. The inductance of the electrical cables of the measurement system and hardware of the PEFC

or for a special case an intrinsic inductance due to the nature of the porous media in the electrode can mask the ionic conductivity, which plays an important role in the ORR current distribution through the CCL in the high frequency region of the cathode impedance spectrum.

6.3 Conclusions

This Chapter has identified and demonstrated a key technical problem of PEFC impedance measurements. The inductance in the electrical cables deforms the high frequency region and leads to an incorrect interpretation of the PEFC impedance spectrum in the high frequency range. This study is divided in two sections. The first section simulates the effect of inductance on cathode impedance measurements reported in the literature and reveals the mechanisms in the CCL masked by the inductive effect through the mathematical model derived in Chapter 5. Secondly an experimental analysis is presented to validate the theory established in the theoretical analysis. This Chapter demonstrates that the cathode mathematical model represented in Eq. 6.1 and derived in Chapter 5 can be applied reliably in order to correctly estimate the inductance effect and the electrochemical mechanisms of the CCL at high frequencies of the complex-plot. This study demonstrates that the practice of using the real part Z' of the complex plot where the imaginary part Z'' is equal to zero, or through a single frequency as a reference to quantify the ohmic resistance in PEFC can be subject to an erroneous interpretation due to the contribution of the size of the inductance. The K-K mathematical relations were applied to the experimental data presenting inductance and demonstrated that the measured data at high frequencies do not represent the physics and chemistry of the PEFC and cathode. The experimental analysis through the multichannel FRA has demonstrated that there is a difference between impedance spectra of the PEFC and cathode which contrasts the theory in which there is no anodic contribution in the PEFC measured impedance. Future work is expected to fill the gap that exists between impedance in a PEFC and the cathode to accurately estimate the factors that influence the nature of polarisation curves such as kinetic losses, ohmic losses and mass transport losses from experimental EIS measurements.

6.4 References

- [1] Savova-Stoynov B., and Stoynov Z. B., "Analysis of the Inductance Influence on the Measured Electrochemical Impedance", *J. Appl. Electrochem.*, 17, (1987), pp. 1150-1158.
- [2] Göhr H., Mirnik M. and Schiller C. A., "Distortions of High Frequency Electrode Impedance Their Causes and How to Avoid Them", *J. Electroanal. Chem.*, 180, (1984), pp. 273-285.
- [3] Ciureanu M., and Roberge R., "Electrochemical Impedance Study of PEM Fuel Cells. Experimental Diagnostics and Modeling of Air Cathodes", *J. Phys. Chem. B*, 105, (2001), pp. 3531-3539.
- [4] Fouquet N., Doulet C., Nouillant C., Dauphin-Tanguy, D., and Ould-Bouamama, B., "Model Based PEM Fuel Cell State-of-Health Monitoring via AC Impedance Measurements", *J. Power Sources*, 159, (2006), pp. 905-913.
- [5] Makharia R., Mathias M. F. and Baker D. R., "Measurement of Catalyst Layer Electrolyte Resistance in PEFCs Using Electrochemical Impedance Spectroscopy", *J. Electrochem. Soc.*, 152, (2005), pp. A970-A977.
- [6] Mérida W., Harrington D. A., Le Canut J. M., and McLean G., "Characterisation of Proton Exchange Membrane Fuel Cell (PEMFC) Failures via Electrochemical Impedance Spectroscopy", *J. Power Sources*, 161, (2006), pp. 264-274.
- [7] Asghari S., Mokmeli A., Samavati M., "Study of PEM Fuel Cell Performance by Electrochemical Impedance Spectroscopy", *Int. J. Hydrogen Energy*, 35, (2010), pp. 9283-9290.
- [8] Orazem M. E., Pebere N., and Tribollet B., "Enhanced Graphical Representation of Electrochemical Impedance Data", *J. Electrochem. Soc.*, 153, (2006), pp. B129-B136.
- [9] Liu F., Yi B., Xing D., Yu J., Hou Z., and Fu Y., "Development of Novel Self-Humidifying Composite Membranes for Fuel Cells", *J. Power Sources*, 124, (2003), pp. 81-89.
- [10] Li G., and Pickup P. G., "Ionic Conductivity of PEMFC Electrodes", *J. Electrochem. Soc.*, 150, (2003), pp. C745-C752.
- [11] Lefebvre M. C., Martin R. B., and Pickup P. G., "Characterization of Ionic Conductivity Profiles within Proton Exchange Membrane Fuel Cell Gas Diffusion Electrodes by Impedance Spectroscopy", *Electrochem. Solid-State Lett.*, 2, (1999), pp. 259-261.
- [12] Gazzarri J., Eikerling M., Wang Q., and Liu Z., "Estimation of Local Relative Humidity in Cathode Catalyst Layers of PEFC", *Electrochem. Solid-State Lett.*, 13, (2010), pp. B58-B62.
- [13] Kurz T., Hakenjos A., Kramer J., Zedda M., and Argert C., "An Impedance-Based Predictive Control Strategy for the State-of-Health of PEM Fuel Cell Stacks" *J. Power Sources*, 180, (2008), pp. 742-747
- [14] Hsu C. H., and Mansfeld F., "Concerning the Conversion of the Constant Phase Element Parameter Y0 into a Capacitance", *Corrosion*, 57, (2001), pp. 747-748.
- [15] Thompson E. L., Jorne J., Gu W., and Gasteiger H. A., "PEM Fuel Cell Operation at -20°C. II. Ice Formation Dynamics, Current Distribution, and Voltage Losses within Electrodes", *J. Electrochem. Soc.*, 155, (2008), pp. B887-B896.
- [16] Neyerlin K. C., Gu W., Jorne J., Clark A. Jr., and Gasteiger H. A., "Cathode Catalyst Utilization for the ORR in a PEMFC Analytical Model and Experimental Validation", *J. Electrochem. Soc.*, 154, (2007), pp. B279-B287.
- [17] Chan S. H., Chen X. J., and Khor K. A., "Reliability and Accuracy of Measured Overpotential in a Three-Electrode Fuel Cell System", *J. Appl. Electrochem.*, 31, (2001), pp. 1163-1170.
- [18] Dolle M., Orsini F., Gozdz A. S., Tarascon J. M., "Development of Reliable Three-Electrode Impedance Measurements in Plastic Li-Ion Batteries", *J. Electrochem. Soc.* 148, (2001), pp. A851-A857.
- [19] Yan Q., Toghiani H., and Causey H., "Steady State and Dynamic Performance of Proton Exchange Membrane Fuel Cells (PEMFCs) under Various Operating Conditions and Load Changes", *J. Power Sources*, 161, (2006), pp. 492-502.
- [20] Yuan X., Sun J. C., Wang H., and Zhang J., "AC Impedance Diagnosis of a 500W PEM Fuel Cell Stack Part II: Individual Cell Impedance", *J. Power Sources*, 161, (2006), pp. 929-937.
- [21] Gode P., Jaouen F., Lindbergh G., Lundblad A., and Sundholm G., "Influence of the Composition on the Structure and Electrochemical Characteristics of the PEFC Cathode", *Electrochim. Acta*, 48, (2003), pp. 4175-4187.
- [22] Jaouen F., Lindbergh G., and Wiezell K., "Transient Techniques for Investigating Mass-Transport Limitations in Gas Diffusion Electrodes II. Experimental Characterization of the PEFC Cathode", *J. Electrochem. Soc.* 150, (2003), pp. A1711-A1717.
- [23] Nguyen T.V., and White R.E., "A Water and Heat Management Model for Proton-Exchange-Membrane Fuel Cells", *J. Electrochem. Soc.*, 140, (1993), pp. 2178-2186.

- [24] Macdonald D. D., and Urquidi-Macdonald M., “Application of Kramers-Kronig Transforms in the Analysis of Electrochemical Systems I. Polarization Resistance”, *J. Electrochem. Soc.*, 132, (1985), pp. 2316-2319.
- [25] Urquidi-Macdonald M., and Real S., and Macdonald D. D., “Application of Kramers-Kronig Transforms in the Analysis of Electrochemical Impedance Data II. Transformations in the Complex Plane”, *J. Electrochem. Soc.*, 133, (1986), pp. 2018-2024.
- [26] Urquidi-Macdonald M., Real S., and Macdonald D. D., “Applications of Kramers-Kronig Transforms in the Analysis of Electrochemical Impedance Data-III. Stability and Linearity”, *Electrochim. Acta*, 35, (1990), pp. 1559-1566.
- [27] ZMAN 2.2, 2005, WonATech Co., Seoul, Korea.
- [28] Orazem M., and Tribollet B., *Electrochemical Impedance Spectroscopy*, Wiley, New Jersey (2008).
- [29] Boukamp B. A., “Electrochemical Impedance Spectroscopy in Solid State Ionics: Recent Advances”, *Solid State Ionics*, 169, (2004), pp. 65-73.
- [30] Hampson N. A., Karunathilaka S. A. G. R., and Leek R., “The Impedance of Electrical Storage Cells”, *J. Appl. Electrochem.*, 10, (1980), pp. 3-11.

Chapter 7

Low Frequency Electrochemical Mechanisms in the Fuel Cell Cathode Impedance Spectrum

In this Chapter, a study of the mechanisms presented in the low frequency part of the polymer electrolyte fuel cell (PEFC) cathode impedance spectrum has been carried out using electrochemical impedance spectroscopy (EIS) measurements and the model developed in previous Chapters. In many EIS studies the presence of two loops in the complex plot of EIS measurements for a H₂/air PEFC have been observed. The high frequency loop has been related to the charge transfer process during the oxygen reduction reaction (ORR) and the low frequency loop has been related to gas phase oxygen transport limitations in the cathode [1]. Other studies have related the low frequency loop to back diffusion of water in the polymer electrolyte membrane (PEM) and diffusion of water in the catalyst layer (CL) [2]. Freire and Gonzalez [3] reported that the loop at low frequencies in EIS measurements has two contributions: the effect of liquid water formed at the cathode, which affects the transport of oxygen, and the hydration effects that limit water transport in the membrane. In some cases [4,5], there is no distinct separation of the two loops in impedance measurements. This makes the detailed analysis more difficult and little information has been provided on the relative contribution of the charge transfer and diffusional effects under such conditions.

EIS measurements have limitations and present disadvantages as the low impedance values are obscured for low frequencies and some effects are not visible due to a masking effect in the impedance plot [6]. Yuan *et al.* [7] attempted to separate both charge transfer and diffusional processes in the impedance spectra that account for a H₂/air PEFC stack and feature a single loop at high current densities through a Randles electrical circuit. The results showed that the Randles equivalent circuit model cannot account for the exact electrode process at high current densities because the charge transfer resistance of the ORR increased with increasing current density. Similar results have been reported by Springer *et al.* [1]. Mass transport effects in EIS measurements due to oxygen transport

limitations are still a subject of debate as this has been principally attributed to the gaseous oxygen transport limitations in the gas diffusion layer (GDL) neglecting any mass transport limitations in the cathode catalyst layer (CCL) [8,9,10]. However, it is suspected that the CCL becomes flooded before the GDL because water is generated in the CCL and transported into the GDL, and has a lower porosity and smaller pore size, and tends to have higher flooding levels than the GDL [11].

The objective of this Chapter is to give an insight about the electrochemical mechanisms represented at low frequencies of the PEFC impedance spectrum commonly accounted to mass transport limitations. To validate this study, the simulated data from the model derived in Chapter 5 that accounts for the cathode impedance spectrum were compared with cathode EIS measurements in Bode format (modulus and phase) and impedance format (real, imaginary) obtained in a three-electrode configuration in the measurement system.

7.1 Experimental

EIS is commonly applied as a single channel through a two-electrode configuration. A two-electrode configuration makes it difficult to identify, to separate and to reveal the process related to each electrode (anode, cathode) in the impedance spectrum of a cell. A three-electrode configuration in EIS allows the measurement of half-cell impedance (anode or cathode) to be carried out. Some studies [12,13] have applied the three-electrode configuration in EIS measurements. Under such conditions, the signals are measured between the working electrode (WE) and the reference electrode (RE), and the current induced is collected by the counter electrode (CE).

A 25 cm² commercially-available fuel cell and test rig acquired from Baltic Fuel Cells were used for the experimental tests. The membrane electrode assembly (MEA) consisted of a catalyst coated membrane (DuPont Nafion-115) with a platinum loading of 0.4mg/cm² and carbon black for the electrodes. The thickness of the CCL was 12µm. The contact pressure on the active cell area was adjusted through a pneumatic air cylinder from the Baltic Fuel Cell compression unit. The contact pressure on the active area was

fixed to 1.4 N/mm^2 . The operational temperature was 50°C and the gauge back gas pressure was held at 0.9 bar for both the anode and cathode. Flow rates were held constant during all the experiments, hydrogen to the anode was supplied at a stoichiometry of 2.5 and air to the cathode supplied at a stoichiometry of 3. The PEFC was operated with 100% hydrogen relative humidity (RH) in the anode; the air supplied in the cathode was dry. In terms of optimal performance of operational PEFCs, the effect of RH in the reactant gases is not definite. For instance, Qiang Yan *et al.* [14] reported that optimal performance in a PEFC can occur at low air relative humidity and high hydrogen relative humidity.

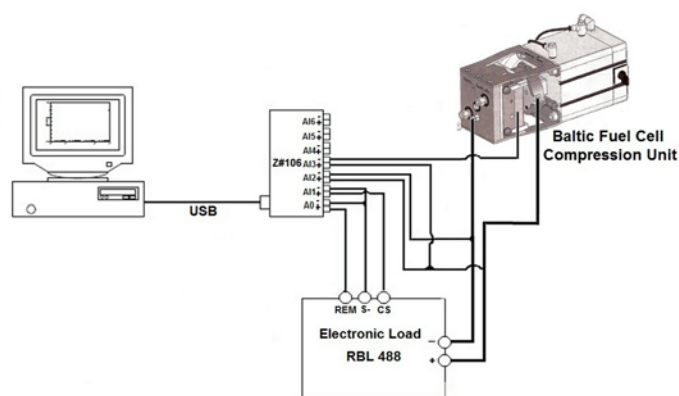


Figure 7.1 Experimental setup

EIS measurements were carried out through a multichannel frequency response analyser (FRA) (Z#106 WonATech Co). The multichannel FRA consists of five channels and simultaneously measures five impedance spectra through a DC current value induced. EIS measurements were carried out at three different current densities 0.12 , 0.2 and 0.32 A/cm^2 . The multichannel system is connected with a RBL488 Dynaload, as shown in Fig. 7.1. The multichannel FRA superimposes an AC sinusoidal perturbation onto the bias current induced by the RBL488 Dynaload unit and measures the AC voltage signals resulting from the PEFC. The impedance measurements were carried out in a galvanostatic mode to control the current through the cell with a 5% AC amplitude of the DC current [7,15,16] to obtain a linear response from the system and at frequencies from 10 kHz to 0.3 Hz. The high frequency in the EIS measurements was limited due to the bandwidth of the electronic load. Scattered data in the EIS measurements were manifested at high current densities and at frequencies lower than 0.3 Hz. The air gas

reactant supplied in the cathode was dry and the water produced by the ORR ensured an optimal hydrated state in the CCL and PEM. However at low frequencies < 0.3 Hz during the EIS measurements the high water concentration in the cathode lead to instability in the PEFC. Previously in Chapter 6, it was demonstrated that the inductance of the electrical cables of the measurement system deforms the high frequency region of the PEFC spectrum and as such leads to an incorrect interpretation of the electrochemical mechanisms at high frequencies. In this study, special electrical cables (Low inductive cable with fusion Lug Technology, TDI POWER) connected between the PEFC and the RBL488 Load were used to reduce inductive effects on the EIS measurements. To separate the impedance spectrum of the cathode from the impedance spectrum of the cell, a reference electrode made of a platinum wire was inserted such that it was in direct contact with the PEM of the cathode side. It has been demonstrated that misalignment in the electrodes of the MEA can significantly shift reference electrode signal [17]. The signal of a reference electrode can be shifted towards the electrode that protrudes whether the reference electrode is inserted in the anode or cathode side. In these experimental results, the reference electrode was in direct contact with the PEM closer to the bigger electrode (cathode). Two channels from the Z#106 FRA were used to simultaneously measure the impedance of the PEFC and the impedance solely accounting for the cathode electrode.

The resulting impedance is commonly shown in a complex plane and represents the electrochemical and diffusion mechanisms of the PEFC in the frequency domain. It has been proposed that the PEFC impedance spectrum largely represents the electrochemical processes in the cathode, and because the electrochemical mechanisms in the anode are fast and less complicated sequences, therefore they are not expected to have a contribution and can be regarded as negligible [18,19]. This theory will not always be valid as the transport of water from the anode to the cathode by electro-osmotic drag can play a role in dehydrating the membrane and inducing performance degradation [20].

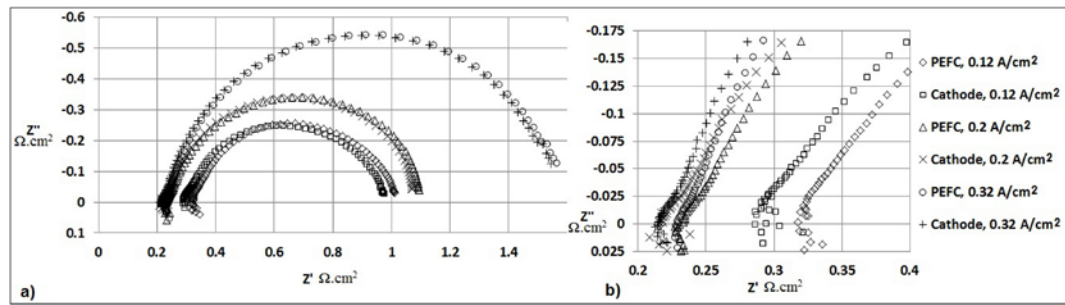


Figure 7.2 a) PEFC and cathode measured data at 0.12, 0.2 and 0.32 A/cm², b) High frequency region

The diameters of the spectra accounting for PEFC and cathode increase with increasing current density, as shown in Fig. 7.2a. When the kinetics of the ORR dominates the cell performance such as in the low current density range of the polarisation curve, the impedance spectrum mainly represents the charge transfer effect during the ORR and its diameter decreases with increasing current density [6]. In Fig. 7.2a, the increase in diameter of the spectra with increasing current density can be attributed to an increase in oxygen transport limitations. One of the disadvantages of the EIS technique is that multiple energy controlled processes during the electrochemical reaction can be masked in the impedance plot. The impedance results of Fig. 7.2a reflect the overlapping of two semicircles. One is related to the charge transfer of the ORR effect which decreases with increasing current density and the other is related to mass transport effect which increases with increasing current density. The semi-circular part of the cathode spectra presents roughly the same features as the PEFC spectra and a shift over the real part $Z'\Omega.cm^2$. This effect is expected as the cathode is hydrated by the water produced by the ORR and due to electro-osmotic drag from the anode. The difference between the PEFC and cathode spectra can be attributed to the electro-osmotic effect from the anode. The cathode and PEFC spectra at current densities of 0.2 and 0.32 A/cm² intercept the real component $Z'\Omega.cm^2$ at almost the same position, as shown in Fig 7.2b; this suggests that the PEM and CCL are fully hydrated at 0.2 A/cm² so an increase in current density leads to an increase in oxygen transport limitations.

The PEFC impedance response is considered the sum of the individual impedance responses of each individual electrode. Then the difference between the PEFC and

cathode impedance response represented in Fig. 7.2 gives the anode impedance response as shown in Fig. 7.3.

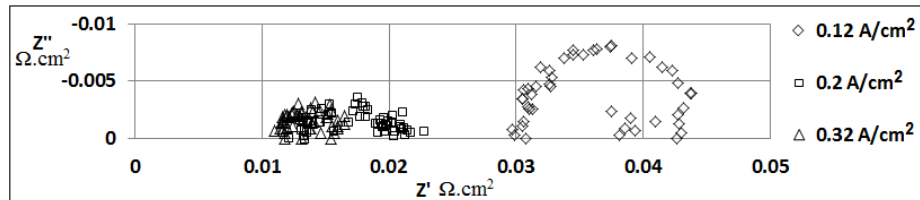


Figure 7.3 Anode impedance spectra

In Fig. 7.3, the semi-circle of the anode spectrum is related to the charge transfer of the electrochemical reaction that takes place in the anode, and its magnitude decreases with increasing current density. This demonstrates that the hydrogen oxidation reaction (HOR) taking place in the anode is a faster and a less complicated reaction sequence than the ORR in the cathode with increasing current density. The impedance data at high frequency presented over the real part Z' $\Omega.cm^2$ of the complex plot in Fig. 7.3 represent the ionic resistance in the anode catalyst layer (ACL). This ionic resistance in the anode decreases due to the higher water concentration presented in the cathode in which water is transported to the anode side to hydrate the entire system. The anode contribution in the PEFC impedance spectrum neglecting any contaminant in the hydrogen supplied such as CO which can affect the PEFC performance [21] can be considered negligible at higher current densities.

7.2 Results

7.2.1 Cathode Impedance Validation

The electrical circuit that models the cathode impedance spectrum generated from EIS analysis and obtained through a reference electrode contains an inductor element that accounts for the inductance of the cables used in the test equipment connected in series with a resistance that accounts for the PEM, GDL and bipolar plate. They are connected in series with a circuit that accounts for the CCL, in which for this specific case is the CCL impedance equation derived in Chapter 5,

$$Z_C = L(i\omega) + R_e + \frac{(R_C + Z_W)\gamma \coth(\gamma x)}{1 + Y(i\omega)^P (R_C + Z_W)} \quad (7.1)$$

where
$$\gamma = \sqrt{R_p \left[\frac{1}{R_C + Z_W} + Y(i\omega)^P \right]}$$

R_p is the resistance to the flow of ions in the electrolytic phase of the CCL,

R_C represents the charge transfer resistance presented in the oxygen reduction reaction (ORR) defined as $R_C = b / j_0 \exp(\eta_{SS} / b)$, where b is the Tafel slope, η_{SS} represents a value of voltage in activation overpotential, and j_0 is the exchange current,

Z_W is defined as the Warburg impedance and describes diffusion across a finite dimension in the frequency domain [18] $Z_W = R_W \tanh(i\omega T_W)^{0.5} / (i\omega T_W)^{0.5}$, with $R_W = RT\delta / (z^2 F^2 c_o^* D)$ defined as resistance for the diffusion process and $T_W = \delta^2 / D$ defined as the time constant to diffuse oxygen through the CCL,

$Y(i\omega)^P$ Y represents a parameter related to constant phase element (CPE), superscript P represents a parameter to correct the inhomogeneity in the distribution of charge,

ω is the angular frequency,

i is the imaginary component in impedance,

L represents the inductance in the electrical cables of the measurement system,

R_e represents the total ohmic resistance to the flow of electrons and ions in the bipolar plate, GDL, and PEM.

In these experimental results the use of a reference electrode in the measurement system ensures that the data accounting for the processes in the cathode are captured for analysis and interpretation. The overall modelling and experimental framework developed for the current study is illustrated in Fig. 7.4. The modelling work involves the simulation of the cathode impedance through Eq. 7.1 and using a graphic user interface (GUI) developed in Matlab®. In Eq. 7.1 there are some parameters that can be estimated through a graphical interpretation of the complex plot. This allowed the reduction of the number of parameters to be fitted in the measured EIS spectra. The high frequency limit of the real part Z' of the impedance spectrum is given by a resistance R_e accounting for ohmic losses in the PEM, GDL, and bipolar plate [22]. In Chapter 6, it was demonstrated that if the inductance of the measurement cables is reduced, the ionic resistance R_p in the CCL electrolyte can be represented in the cathode impedance spectrum by a 45° straight line at the high frequency end of the spectrum and its value over the real part of the impedance spectrum is calculated as $R_p/3$. Ciureanu and Roberge [19] reported that the double layer capacitance is calculated as: $C_{dl} = Y/(R_e^{-1} + R_c^{-1})^{1-p}$, and Hsu [23] defined the capacitance as: $C_{dl} = Y(2\pi f_c)^{p-1}$, noting that f_c is the characteristic frequency at which the negative imaginary part of the impedance reaches its maximum value. The CCL oxygen diffusion time constant T_w was fixed at 3ms as reported by Springer *et al.* [1] to avoid inclusion of another fitting variable. The charge transfer resistance R_c and mass transport resistance R_w whose contributions are at medium and low frequencies respectively were the only parameters used in the fitting process. This provides assurance that the parameters in Eq. 7.1 correctly relate to the physics and chemistry that are occurring. The experimental work provides the measured frequency response of the cathode for validation purposes. The least squares fitting method was used in order to find the best-fit between the model and the measured data. A good quality fit is obtained when the sum of the deviations squared (least square error) between the simulated and measured impedance data has a minimum value, for instance < 0.1 .

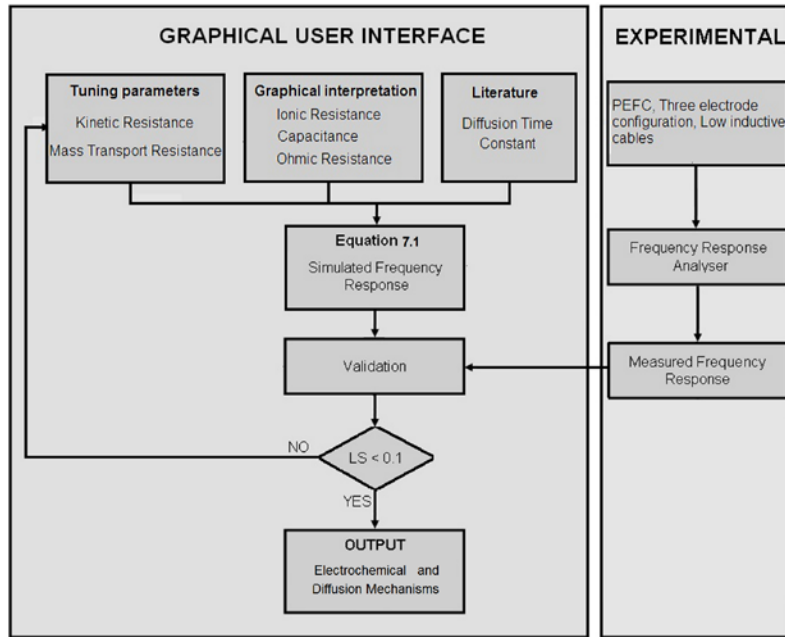


Figure 7.4 Overall modelling and experimental structure

In Fig. 7.5, the results show a good agreement between the measured and simulated data in the complex-plot with an exception at the highest frequencies (> 7 kHz) where the measured data exhibit a scatter due to high frequency noise present during the EIS test and due to external inductance of the measurement system. In Chapter 6, it was demonstrated that the property of causality in the Kramers-Kronig (K-K) mathematical relations for EIS measurements is violated by the external inductance of the measurement cables and external noise during EIS. Thereby the measured data at the highest frequencies (scattered data) in Fig. 7.5 do not represent the physics and chemistry of the cathode. The model of Eq. 7.1 is based on differential equations describing the detail of the physical processes in the cathode, as shown in Chapters 4 and 5; therefore the comparison between measured and simulated data provides a good validation of the measured data, rather than evaluating the data to an analysis of K-K consistency.

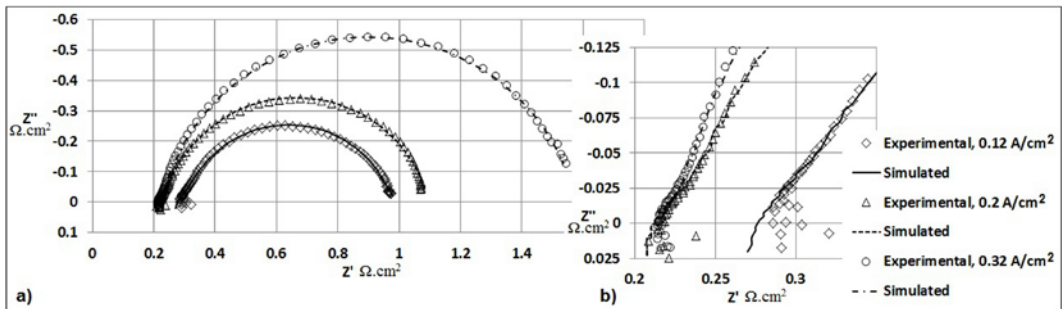


Figure 7.5 a) Comparison between measured and simulated data, b) High frequency region

A further validation of the mathematical model against the modulus and phase angle of the frequency response of the measured data was carried out. Sensitivity to discrepancies between model and experimental data can be assessed by comparing the experimental data with the simulated data in a Bode format (modulus and phase). Orazem and Tribollet [24] reported in their study that the Bode modulus and real part component of the impedance plots are relatively insensitive to the quality of the fit of a model to impedance data. The imaginary component of the impedance and Bode phase angle plots are modestly sensitive to fit quality.

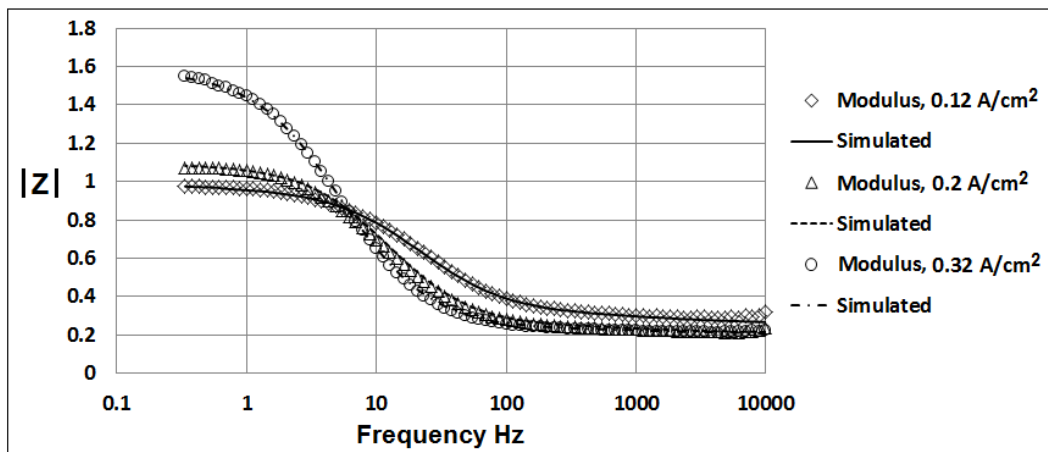


Figure 7.6 Comparison in Bode format (modulus) between measured and simulated data

Figs. 7.6, 7.7 show the comparison between measured and simulated data in Bode format. Fig. 7.6 shows that the model is able to reproduce accurately the Bode modulus for all the frequencies. Fig. 7.7 shows a discrepancy in the phase angle between measured and

simulated data at the highest frequencies (> 7 kHz). The model cannot reproduce the measured phase angle in the frequency range of 7 kHz to 10 kHz because the measured data over this frequency range do not represent the physics and chemistry of the electrochemical system, as discussed previously. Fig. 7.6 shows that the modulus at 0.2 and 0.32 A/cm² show a similar tendency from 10 kHz down to ~ 6 Hz. The modulus from 10 kHz to 6 Hz can be related to the hydrated state of the CCL and PEM which indicates that CCL and PEM at 0.2 and 0.32 A/cm² are fully hydrated due to the water produced by the ORR. The asymptotic value at high frequency (10 kHz) provides a qualitative value of the ionic resistance in the PEM and CCL which decreases at current densities of 0.2 and 0.32 A/cm². The asymptotic value of the modulus at a low frequency of 0.3 Hz provides a qualitative value of the mass transport resistance which increases with increasing current density.

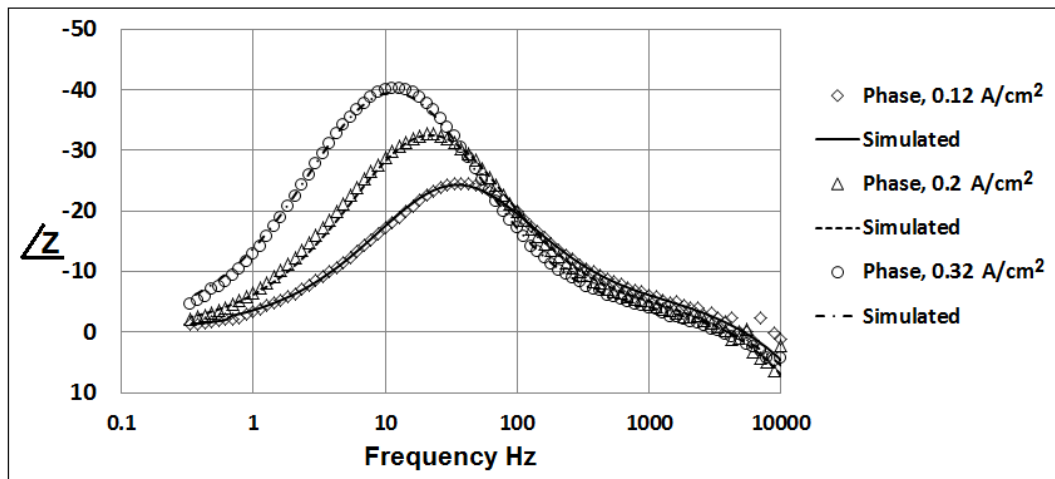


Figure 7.7 Comparison in Bode format (phase) between measured and simulated data

In Fig. 7.7 the phase angle for the three current densities presents the same tendency from 10 kHz down to ~ 120 Hz. The phase angle tends toward zero with decreasing frequency < 0.3 Hz for the three cases, indicating that the current and potential come into phase as the frequency approaches zero. An out of phase shift for the three cases is clearly shown in Fig. 7.7. The single peak in the phase angle plot suggests that a single time constant describes the electrochemical process; multiple peaks would provide a clear indication that more than one time constant is required to describe the electrochemical process

during the ORR [24]. In Fig. 7.7, the frequency, where the phase angle reaches its minimum value, decreases with increasing current density. This reduction in frequency suggests that the process required to control the ORR becomes slower with increasing current density. Overall, the simulated data demonstrates that the mathematical model shown in Eq. 7.1 can be reliably applied in order to reproduce the measured data obtained at the three different current densities.

7.2.2 Estimation of Electrochemical and Diffusion Mechanisms

The mathematical model represented by Eq. 7.1 allows the estimation of the ionic resistance R_P of the CCL electrolyte, charge transfer resistance R_C of the ORR and mass transport resistance R_W due to oxygen limitations in the cathode from EIS measurements. The ionic resistance in the CCL electrolyte decreases with increasing current density, as shown in Tab. 7.1. This effect is attributed to the water produced during the ORR and the water transported from anode to cathode by electro-osmotic drag. The charge transfer resistance, whose dependence on electrode potential is given by the Tafel equation and reflects the increase in the driving force for the interfacial oxygen reduction process, decreases with increasing current density. The mass transport resistance, due to gaseous oxygen transport limitations and as a function of the gaseous oxygen equilibrium concentration c_o^* in the CCL-GDL interface, increases with increasing current density, as shown in Tab.7.1. Mass transport resistance is a minimum at 0.12 A/cm^2 due to the low water concentration produced during the ORR, which improves the ability of oxygen to permeate to the active sites of the CCL; nevertheless low water concentration increases the ionic resistance in the CCL. At a current density of 0.2 A/cm^2 , both charge transfer and mass transport resistances have roughly the same magnitude therefore under such a current density the balance between the electrochemical and diffusion processes is achieved. At a current density of 0.32 A/cm^2 , the mass transport effect dominates the performance of the PEFC.

Current	$R_p \Omega.cm^2$	$R_c \Omega.cm^2$	$R_w \Omega.cm^2$	$T_w s$
0.12 A/cm ²	0.16	0.5675	0.1125	0.003
0.2 A/cm ²	0.1125	0.41	0.445	0.003
0.32 A/cm ²	0.09	0.3125	1.02	0.003

Table 7.1 Parameters of the CCL estimated through Eq. 7.1

Mass transport limitations have been principally attributed to the gaseous oxygen transport limitations in the GDL neglecting any mass transport limitations in the CCL [8,9,10]. However, it is suspected that the CCL becomes flooded before the GDL. Mass transport limitations represented in the complex plot of EIS measurements have been a subject to debate.

Oxygen Permeability Through CCL - The CL is commonly formed by a composite structure of a matrix of carbon grains providing the electron conductivity, Pt supported on carbon as the catalyst, Teflon (PTFE) as a binder that stabilizes the carbon matrix and as a hydrophobizing agent, and electrolyte network of perfluorosulfonate ionomer (PFSI) soaked with water. The matrix of carbon grains forms agglomerate structures. Primary pores are those that exist inside the agglomerates between the carbon grains. Secondary pores constitute the void spaces between agglomerates. There are mainly three principal modes of transport of O₂ in the CCL: gas-phase diffusion in the CCL pore (primary, secondary), diffusion in the liquid-water film surrounding the catalytic agglomerate, and diffusion in the ionomer of the agglomerate. The analysis of this study assumes that the catalyst agglomerate is covered by a film of liquid water and Nafion is homogeneously spread through the thickness of the CCL. Springer *et al.* [25] defined and estimated the permeability of oxygen in the CCL through EIS measurements. The permeability of oxygen in the CCL Dc_o^* was defined by the product of the effective diffusion coefficient of oxygen and the equilibrium oxygen concentration in the CL. Their EIS results showed oxygen permeabilities of the order of magnitude 10^{-10} for a CL with 5 μ m thickness of a 5cm² H₂/air PEFC. This author concluded that a low value for the oxygen permeability is required to generate the break in the cell polarisation curve. The thickness of the CL used

in the EIS measurements in this study is $12\mu\text{m}$ and the oxygen permeability in the CCL calculated from EIS measurements and through Eq. 7.1 are $Dc_o^* = 1.92 \times 10^{-10}, 4.86 \times 10^{-11}, 2.23 \times 10^{-11} \text{ mol/cm.s}$ for 0.12, 0.2 and 0.32 A/cm^2 respectively. The decrease of the oxygen permeability reflects a limitation in transport routes for oxygen in the CCL.

Time Constant of Oxygen Diffusion Through CCL - The single peak in the phase angle of EIS measurements shown in Fig. 7.7 reflects the fact that a single energy process controls the ORR. The single loop of the EIS measurements shown in Fig. 7.5 reflects the same assumption. However, this may not always be the case as the capacitance related to the charge transfer process of the ORR and the oxygen diffusion effect are normally represented together in EIS measurements. One of the disadvantages of the EIS technique is that the frequency dependency is obscured because multiple energy controlled processes of an electrochemical system can be masked in the frequency plot. Based on the results from Fig. 7.5, the mass transport effect was overlapped with the charge transfer effect in the EIS measurements. Similar results were reported by Yuan *et al.* [7] when a 280 cm^2 PEFC stack was operated with a hydrogen stoichiometry of 2, and an air flow stoichiometry of 2.5. In the study carried out by Yuan *et al.*, the separation between the charge transfer process and mass transport effect in EIS measurements was apparent when the PEFC stack was operated with a hydrogen stoichiometry of 2 and a fixed air flow rate of $20 \text{ standard L min}^{-1}$ (low air flow stoichiometry). Ciureanu and Roberge [19] carried out EIS measurements in a 25 cm^2 PEFC with flow rates at stoichiometry of 1.2 hydrogen and 2 air. The results show the additional loop at low frequencies that accounts for oxygen transport limitations in the cathode. Other studies have reported the presence of two loops in the EIS measurements where, at low frequencies, reflects the oxygen transport limitations in the gas phase because of the shortage of the air supply operated at a fixed air flow rate. Within the fuel cell there is a competition mainly between back-transport of water from cathode to anode and electro-osmotic drag of water by ions from anode to cathode. If no other source or sink of water is considered, the ideal operating point needs to be where both fluxes are equal. If the H_2/air PEFC is operated with a low air flow rate the semicircle that represents the mass transport limitations at low frequencies is visualized in the EIS measurements. In Chapter 5, it was demonstrated that

the mathematical model represented in Eq. 5.24 is able to reproduce EIS measurements resulting in the low frequency loop attributed to gaseous oxygen transport limitations in the cathode.

The time constant to diffuse oxygen through the CCL expressed in Eq. 7.1, is defined by $T_w = \delta^2 / D$ where δ represents the characteristic length scale of the diffusive process in the CCL, in which for this specific case is considered to be the thickness of the CCL and D represents the effective diffusion coefficient for oxygen transport in the CCL. Springer *et al.* [1] reported time constants to diffuse oxygen through the CCL not larger than 3 ms using a mathematical model fitted with EIS measurements for a 5cm² H₂/air PEFC. The time constant in their study was fixed at 3 ms for all EIS measurements to avoid inclusion of another fitting variable. The time constant for the validation in this study was fixed a constant value of 3 ms, as reported by Springer, for the three EIS measurements, as shown in Tab. 7.1. The oxygen diffusion coefficients calculated from EIS measurements have been reported [26] to be the “effective” oxygen diffusion coefficients for oxygen transport through multiphase material in the cathode. The effective diffusion and equilibrium oxygen concentration estimated from Eq. 7.1 were $D = 4.8 \times 10^{-4} \text{ cm}^2/\text{s}$ and $c_o^* = 4.008 \times 10^{-7}, 1.013 \times 10^{-7}, 4.651 \times 10^{-8} \text{ mol/cm}^3$ for 0.12, 0.2 and 0.32 A/cm² respectively. The time constant $T_w = 3 \text{ ms}$ from Tab. 7.1 was increased by two orders of magnitude in Eq. 7.1 by decreasing the effective diffusion coefficient by two orders of magnitude as $D = 4.8 \times 10^{-6} \text{ cm}^2/\text{s}$ to simulate its effect on the EIS measurements. The remaining parameters from Eq. 7.1 were kept constant.

The semicircles that represent the charge transfer of the ORR and mass transport effects are overlapped in the experimental cathode spectra, as shown in Fig. 7.5. The results in Fig. 7.8 show that if the time constant $T_w = 3 \text{ ms}$ from Tab. 7.1 is increased by two orders of magnitude in Eq. 7.1, it is possible to separate at 3.33 Hz the semicircles that represent charge transfer effect and oxygen transport limitations in the cathode spectra and whose diameters reflect roughly the same value as the R_c and R_w from Tab. 7.1. Springer *et al.* [1] concluded that it is not possible to visualize the charge transfer effect and mass transport effect in PEFC EIS measurements with time constants of 10^{-4} , 10^{-3} , 10^{-2} orders of magnitude, and with either air or oxygen as a gas reactant.

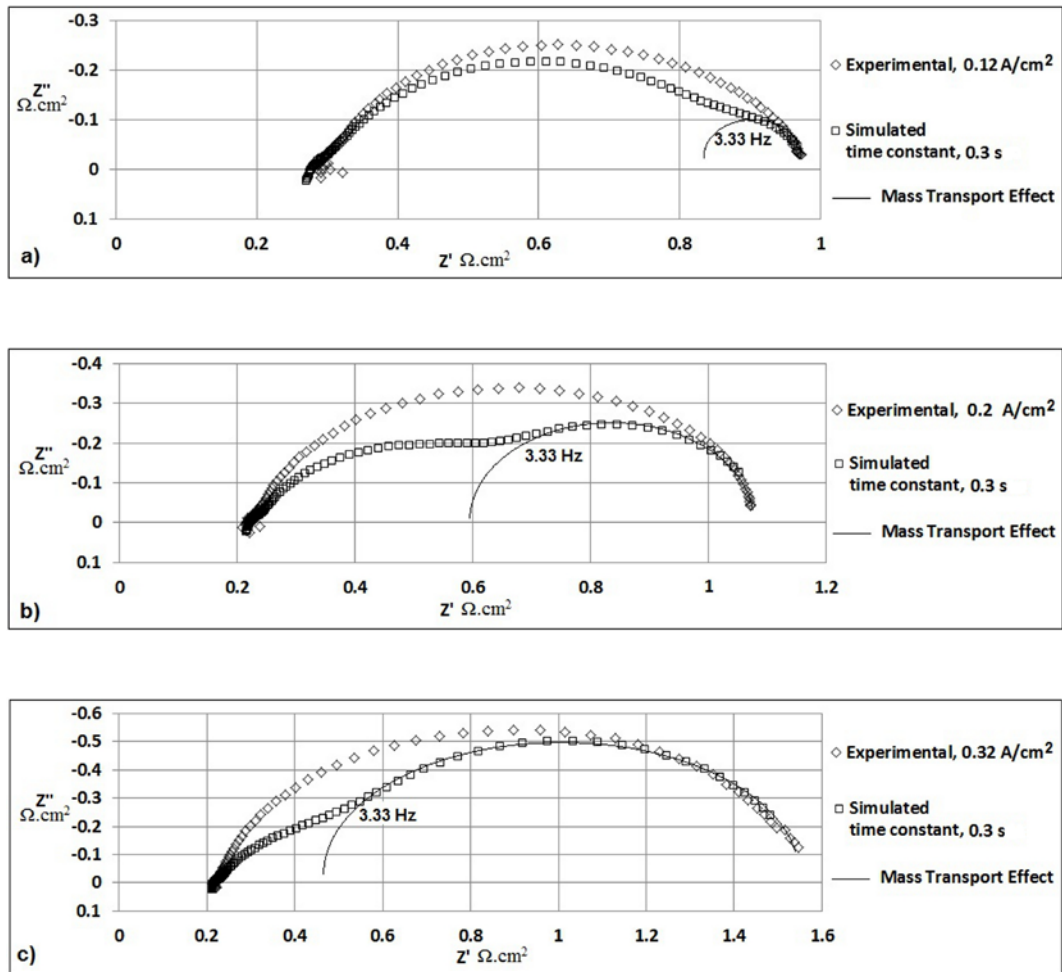


Figure 7.8 Measured data with 3 ms time constant and simulated data with 0.3 s time constant, a) 0.12 A/cm², b) 0.2 A/cm², c) 0.32 A/cm²

Malevich *et al.* [26] reported in their study the effective diffusivity of oxygen in gas phase and ionomer phase of the CCL to be $2.68 \times 10^{-4} \text{ cm}^2/\text{s}$ and $2.83 \times 10^{-6} \text{ cm}^2/\text{s}$, respectively. These values have the same order of magnitude as the CCL oxygen diffusion estimated for time constants 0.003 and 0.3 s in this study. It can be concluded from the EIS cathode measurements of Fig. 7.5 with time constants of 0.003 s and CCL oxygen diffusion constant of $4.8 \times 10^{-4} \text{ cm}^2/\text{s}$ that the main contribution to oxygen transport is through the porous media of the CCL. The simulated cathode spectra in Fig. 7.8 with a time constant of 0.3 s and a diffusion of $4.8 \times 10^{-6} \text{ cm}^2/\text{s}$ suggest that the main

contribution to oxygen transport is through the ionomer surrounding the agglomerate in the CCL.

Because this is a macroscopic modelling approach, it is not possible to separate transport mechanism contributions due to small pores between agglomerates in which the Knudsen flow would be expected to be the prevailing mechanism and due to macropores in the void space between the agglomerates where a molecular diffusion would be the dominant transport mechanism. Water saturation in the CCL is expected when the PEFC is fed at low flow rates. Low flow rates result in the decrease of the effective porosity in the CCL due to the accumulation of water. Under such conditions an increase in the CCL diffusion time constant is expected. Malevich *et al.* also reported diffusive time constants with a magnitude in the order of 10^{-1} s in EIS measurements of a PEFC stack with microporous layers (MPLs) adjacent to the GDLs. The EIS measurements clearly showed the mass transport loop at low frequencies but with a diameter that is relatively smaller than the charge transfer loop. The MPL can reduce water saturation in the GDL and promote the water back to the CCL. Under this condition a saturation of liquid water in the CCL is expected. The mass transport resistance R_w , shown in Tab. 7.1, is a function of the gaseous oxygen equilibrium concentration c_o^* in the CCL-GDL interface; a MPL enhances the gaseous oxygen transport through the GDL and therefore increases the equilibrium oxygen concentration at the CCL-GDL interface. Hence EIS measurements carried out in a PEFC with MPLs present lower mass transport resistance than for cells without MPLs. However under this condition, an increase in the time constant for the diffusion process of oxygen in the CCL is expected because the diffusivity of gaseous oxygen transport in the CCL is reduced due to the higher water concentration.

In cells without MPLs as the case of this study, an increase in amount of water due to the ORR is expected in the GDL with increasing current density. It can be concluded that the increase of mass transport resistance as shown in Tab. 7.1 and represented by the diameter of the EIS loop at low frequencies is related to the low equilibrium oxygen concentration in the CCL-GDL interface as water is blocking the path for oxygen to permeate through the GDL, and the time constant for the diffusion process in EIS

measurements is related to the oxygen transport through the composite structure in the CCL.

7.2.3 A Qualitative Analysis of Mass Transport Limitations

It is not straightforward to determine the role of the effective diffusion coefficient D of oxygen in the CCL for different operating conditions, because this parameter is related to the different modes of transport through the multiphase material in the CCL. The aim of this section is to identify the mass transport effect of the CCL in EIS measurements when the cathode is fed with O_2 diluted in He and N_2 . EIS measurements were provided by Johnson Matthey Fuel Cells. A 6 cm^2 PEFC was operated at 500 mA/cm^2 , $80\text{ }^\circ\text{C}$, 20 psig anode and cathode inlet pressures, 100% RH for the anode and 30% RH for the cathode. The flow rates were kept constant throughout the experiment at 125.5 sccm on the anode and 313 sccm on the cathode. The cell was allowed to sit at the required current on pure oxygen for 5 minutes. The gas was then switched to 40% O_2 in helium, held for a few minutes and then switched to 40% O_2 in nitrogen. EIS measurements from 65 kHz to 1 Hz in a two electrode configuration were measured for each experimental condition. The MEA was a developmental sample from Johnson Matthey Fuel Cells with 0.4 mg Pt/cm^2 on both anode and cathode. The membrane was a commercial $30\mu\text{m}$ perfluorinated sulphonic acid membrane. The gas diffusion layers were based on wetproofed Toray TGP-H-060.

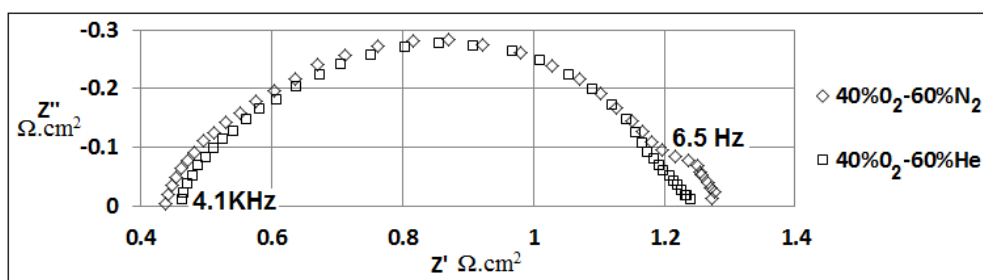


Figure 7.9 Measured spectra with O_2 diluted in He and N_2

Fig. 7.9 represents the EIS measurements of the PEFC (anode and cathode) where anode contribution has a minimum effect at high frequencies and does not contribute in the mass transport mechanisms at low frequencies, as discussed in section 7.1. The EIS results

presented high inductance values in the positive part of the complex plot at frequencies from 63 kHz to 4.1 kHz; these values are not shown in Fig. 7.9 to clearly visualize the mass transport effect at low frequencies. In Chapter 6, it was demonstrated that the inductance presented during the EIS measurements deforms the high frequency region; therefore in Fig. 7.9 it is not possible to draw a conclusion about the difference between spectra at 4.1 kHz. The oxygen concentration in the CCL may be considered similar for the two cases (O_2/He and O_2/N_2). Thus, concentration-related effects, e.g., the variation in charge transfer ORR resistance due to different concentrations, are expected to be minimal. This can be demonstrated in Fig. 7.9 in which both semicircles present similar characteristics from frequencies of 4.1 kHz to 6.5 Hz.

The diffusivity of O_2 diluted in N_2 at $80^\circ C$ has been reported [27] to be $2.8 \times 10^{-5} m^2/s$ and the diffusion coefficient of water vapour in N_2 is $3.9 \times 10^{-5} m^2/s$ at the same conditions; the oxygen diffusivity in He is $1.13 \times 10^{-4} m^2/s$ and the diffusion coefficient of water vapour in He is $3.14 \times 10^{-4} m^2/s$. Gas phase diffusion of oxygen in Heliox (O_2/He) is considerably faster than in O_2/N_2 due to the difference in diffusion coefficients of oxygen in nitrogen and in helium. So when the background gas in the cathode is switched to N_2 from He, a difference in impedance measurements is expected, as shown in Fig. 7.9. The loop presented from 6.5 Hz to 1 Hz for the O_2/N_2 case may be attributed to processes related primarily to the gas-phase oxygen limitations in the GDL which increases oxygen limitations at the CCL-GDL interface and low diffusivity of oxygen through the CCL. The He dissolved in O_2 increased the equilibrium oxygen concentration at the GDL-CCL interface. Suzuki *et al.* [28] carried out experimental measurements using helium-oxygen mixture and air. They concluded that Knudsen diffusion in the small pores of the CCL limits the performance of the PEFC.

In this study, the PEFC was operated using O_2 diluted in N_2 and He as background gases. The diffusivity of O_2 and vapour water diluted in He is higher than if N_2 is used as a background gas. For practical applications, air (21% O_2 , 79% N_2) is used as reactant gas in the cathode side, and the impedance plot under these operating conditions would count for mass transport limitations due to low equilibrium oxygen concentration at the CCL-GDL interface and low oxygen diffusion through the CCL, as discussed in section 7.2.2.

7.3 Discussion

The oxygen diffusion coefficient in the CCL can be adversely affected by CCL structure, composition and operating conditions. It is clearly known that by reducing the void space between agglomerates due to the accumulation of water the ability of oxygen to permeate into the active sites of the CCL will be affected. There are two more modes of transport of oxygen in the CCL which can have an effect on the ORR: dissolved oxygen diffusion in the liquid water surrounding the agglomerate, and dissolved oxygen in the ionomer phase. To date, the effect of the oxygen diffusion on every single phase of the CCL material through impedance measurements has not been studied, and the literature mainly considers the gas phase diffusion as the crucial factor of the mass transport limitations.

One of the challenges in the impedance technique is to separate the mass transport limitations between the CCL and the GDL. Equivalent electrical circuits with Warburg electrical component have been broadly used in PEFC impedance measurements to estimate the mass transport limitations. However it has not been clear how to relate the effect of oxygen transport limitations in the CCL and GDL. As for a higher water content in the CCL the mass transport limitations in the GDL would be reduced and vice-versa. Mass transport in PEFC impedance measurements have been commonly attributed to oxygen transport limitations in the GDL neglecting any mass transport effect in the CCL. This study has demonstrated that mass transport limitations represented in EIS measurements are related to the equilibrium oxygen concentration at the GDL-CCL interface and the diffusivity of oxygen through the composite structure in the CCL.

7.4 Conclusions

EIS measurements that account for the cathodic side of the PEFC were compared with simulated data obtained through the cathode Impedance model developed in the previous Chapters. A validation in the complex-plot and bode format was carried out to account for the exact electrode process in the cathode EIS measurements. The results showed that the low frequency loop in PEFC impedance measurements that commonly attributed to mass transport limitations is attributed to the oxygen equilibrium concentration in the CCL-

GDL interface and the diffusivity of oxygen through the CCL. It was possible to generate a deeper understanding of the internal phenomenological process in the CCL by coupling the experimental EIS technique to the fundamental theory.

7.5 References

- [1] Springer T. E., Zawodzinski T. A., Wilson M. S. and Gottesfeld S., "Characterization of Polymer Electrolyte Fuel Cells Using AC Impedance Spectroscopy", *J. Electrochem. Soc.*, 143, (1996), pp. 587-599
- [2] Wagner N., Schnurnberger W., Muller B., and Lang M., "Electrochemical Impedance Spectra of Solid Oxide Fuel Cells and Polymer Membrane Fuel Cells", *Electrochim. Acta*, 43, (1998), pp. 3785-3793.
- [3] Freire T. J. P., and Gonzalez E. R., "Effect of Membrane Characteristics and Humidification Conditions on the Impedance Response of Polymer Electrolyte Fuel Cells", *J. Electroanal. Chem.*, 503, (2001), pp. 57-68.
- [4] da Silva, S. L. A., and Ticianelli, E. A., "Studies of the Limiting Polarization Behavior of Gas Diffusion Electrodes with Different Platinum Distributions and Hydrophobic Properties", *J. Electroanal. Chem.*, 391 (1995), pp. 101-109.
- [5] Lee S. J., Mukerjee S., McBreen J., Rho Y. W., Kho Y. T., and Lee T. H., "Effects of Nafion Impregnation on Performances of PEMFC Electrodes", *Electrochim. Acta*, 43, (1998), pp. 3693-3701.
- [6] Paganin V. A., Oliveira C. L. F., Ticianelli E. A., Springer T. E., and Gonzalez E. R., "Modelistic Interpretation of the Impedance Response of a Polymer Electrolyte Fuel Cell", *Electrochim. Acta*, 43, (1998), pp. 3761-3766.
- [7] Yuan X., Sun J. C., Wang H. and Zhang J., "AC Impedance Diagnosis of a 500W PEM Fuel Cell Stack Part II: Individual Cell Impedance", *J. Power Sources*, 161, (2006), pp. 929-937.
- [8] Perry M. L., Newman J., Cairns J. E., "Mass Transport in Gas-Diffusion Electrodes: A Diagnostic Tool for Fuel-Cell Cathodes", *J. Electrochem. Soc.*, 145, (1998), pp. 5-15.
- [9] Tsai C. R., Chen F., Ruo A.C., Chang M.-H., Chu H.-S., Soong C. Y., Yan W. M., and Cheng C. H., "An Analytical Solution for Transport of Oxygen in Cathode Gas Diffusion Layer of PEMFC", *J. Power Sources*, 160, (2006), pp. 50-56.
- [10] Bultel Y., Wiezell K., Jaouen F., Ozil P. and Lindbergh G., "Investigation of Mass Transport in Gas Diffusion Layer at the Air Cathode of a PEMFC", *Electrochim. Acta*, 51, (2005), pp. 474-488.
- [11] Lin G., He W., and Nguyen T. V., "Modeling Liquid Water Effects in the Gas Diffusion and Catalyst Layers of the Cathode of a PEM Fuel Cell", *J. Electrochem. Soc.* 151, (2004), pp. A1999-A2006.
- [12] Chan S. H., Chen X. J., and Khor K. A., "Reliability and Accuracy of Measured Overpotential in a Three-Electrode Fuel Cell System", *J. Appl. Electrochem.*, 31, (2001), pp. 1163-1170.
- [13] Dolle M., Orsini F., Gozdz A. S., Tarascon J. M., "Development of Reliable Three-Electrode Impedance Measurements in Plastic Li-Ion Batteries", *J. Electrochem. Soc.* 148, (2001), pp. A851-A857.
- [14] Yan Q., Toghiani H., and Causey H., "Steady State and Dynamic Performance of Proton Exchange Membrane Fuel Cells (PEMFCs) under Various Operating Conditions and Load Changes", *J. Power Sources*, 161, (2006), pp. 492-502.
- [15] Gode P., Jaouen F., Lindbergh G., Lundblad A., and Sundholm G., "Influence of the Composition on the Structure and Electrochemical Characteristics of the PEFC Cathode", *Electrochim. Acta*, 48, (2003), pp. 4175-4187.
- [16] Jaouen F., Lindbergh G., and Wiezell K., "Transient Techniques for Investigating Mass-Transport Limitations in Gas Diffusion Electrodes II. Experimental Characterization of the PEFC Cathode", *J. Electrochem. Soc.* 150, (2003), pp. A1711-A1717.
- [17] He W., and Nguyen V. T., "Edge Effects on Reference Electrode Measurements in PEM Fuel Cells", *J. Electrochem. Soc.* 151 (2004), pp. A185-A195.
- [18] Fouquet N., Doulet C., Nouillant C., Dauphin-Tanguy, D., and Ould-Bouamama, B., "Model Based PEM Fuel Cell State-of-Health Monitoring via AC Impedance Measurements", *J. Power Sources*, 159, (2006), pp. 905-913.

- [19] Ciureanu M., and Roberge R., "Electrochemical Impedance Study of PEM Fuel Cells. Experimental Diagnostics and Modeling of Air Cathodes", *J. Phys. Chem. B*, 105, (2001), pp. 3531-3539.
- [20] Nguyen T.V., and White R.E., "A Water and Heat Management Model for Proton-Exchange-Membrane Fuel Cells", *J. Electrochem. Soc.*, 140, (1993), pp. 2178-2186.
- [21] Wagner, N., and Gülzow E., "Change of Electrochemical Impedance Spectra (EIS) with Time during CO-Poisoning of the Pt-Anode in a Membrane Fuel Cell", *J. Power Sources*, 127, (2004), pp. 341-347
- [22] Liu F., Yi B., Xing D., Yu J., Hou Z., and Fu Y., "Development of Novel Self-Humidifying Composite Membranes for Fuel Cells", *J. Power Sources*, 124, (2003), pp. 81-89.
- [23] Hsu C. H., and Mansfeld F., "Concerning the Conversion of the Constant Phase Element Parameter Y0 into a Capacitance", *Corrosion*, 57, (2001), pp. 747-748.
- [24] Orazem M., and Tribollet B., *Electrochemical Impedance Spectroscopy*, Wiley, New Jersey (2008).
- [25] Springer T. E., Wilson M. S., and Gottesfeld S., "Modeling and Experimental Diagnostics in Polymer Electrolyte Fuel Cells", *J. Electrochem Soc.*, 140, (1993), pp. 3513-3526.
- [26] Malevich D., Halliop E., Peppley B. A., Pharoah J. G., Karan K., "Investigation of Charge-Transfer and Mass-Transport Resistances in PEMFCs with Microporous Layer Using Electrochemical Impedance Spectroscopy", *J. Electrochem. Soc.*, 156, (2009), pp. B216-B224.
- [27] Fu R. S., Zhang X., and Pasaogullari U., "Heat and Mass Transfer in Polymer Electrolyte Fuel Cells in Ultra-Low Humidity Operation", *ECS trans.*, 25, (2009), pp. 323-332.
- [28] Suzuki T., Murata H., Hatanaka T., and Morimoto Y., "Analysis of the Catalyst Layer of Polymer Electrolyte Fuel Cells", R&D Review of Toyota, Toyota Central R&D Labs, Inc., 39, (2003), pp. 33-38.

Chapter 8

Analysis of the Performance of an Open-Cathode Polymer Electrolyte Fuel Cell Stack using Simultaneous EIS Measurements

In this Chapter, the factors that limit the performance in a commercial Open-Cathode polymer electrolyte fuel cell (PEFC) stack are assessed using simultaneous electrochemical impedance spectroscopy (EIS) measurements. Open-Cathode PEFCs have to survive under a range of operational environments varying from, for example, a winter low of sub-zero air temperatures to a summer high relative humidity. They also have to survive under a range of atmospheric compositions which can include sulphur dioxide, nitrous oxides and ionic contamination, as well as fuel impurities that can all potentially cause irreversible damage to the PEFC [1]. The list of critical contaminants is much longer if we also consider the effects of battlefield gases for military application [2]. As such, the fuel cell industry requires a fast-performing, non-intrusive and affordable diagnostics system which can determine changes in critical operational factors such as reactant, liquid water and current distribution, catalytic poisoning, membrane conductivity and contact resistance.

EIS is a powerful technique that can be applied in-situ for diagnosis of the PEFC performance. Much of the work conducted in fuel cell research has limited the EIS technique to a single cell due to the requirement of setting up of a high cost power source and limitations in the experimental set-up, for example most commercial load banks operating at high currents do not have good frequency response. Few studies [3,4,5] have applied EIS measurements in PEFC stacks for different operating conditions and under various loading conditions. Commercial PEFC stacks are equipped with a control system for safe operation and optimal performance. Some works [3] have suggested that the effect of all system components on the PEFC stack must be taken into consideration

during EIS measurements. The disadvantage of this method is that inaccurate quantitative data at high frequencies can be obtained by intrusive signals from the system components. Cimenti [6] *et al.* reported that if a shunt resistor is connected with a PEFC stack to measure the current, a capacitive arc at high frequencies (> 1 kHz) in EIS measurements is observed. They concluded that the high frequency arc is likely an experimental artefact caused by neglecting the frequency dependence of the shunt resistor. Some works have limited the EIS study to 1 kHz to avoid complications from such high frequency external artefacts [7]. Previously in Chapter 6, it was demonstrated that the inductive effect of the measurement system deforms the high frequency region of the PEFC impedance spectrum and gives a wrong interpretation of the electrochemical mechanisms at high frequency.

The impedance response of the whole stack does not provide information about the factors that limit the performance within the stack. Little work has been done in the study of the impedance response of individual cells within a large PEFC stack, and the results have clearly shown that the impedance response of the cells changes at different locations in the stack. The change in impedance of individual cells within the stack could be attributed to the non-uniform distribution of current density along the stack. Therefore in order to improve the performance of a PEFC stack, it is important to know and to optimise the current distribution within each cell. No accurate information has been given in relation to the change in impedance of individual cells within the stack. Dale *et al.* [3] provided no clear argument about the change of the Bode magnitude at low frequencies for cells at different positions in the stack. The authors concluded that the deviation of bode magnitude at low frequencies was attributed to the capacitance effect between the electrode-electrolyte interface. In the previous chapter, Chapter 7, EIS measurements were carried out in a single PEFC at three different current densities. The results were compared with simulated data from the validated impedance model derived in Chapter 5. It was concluded that the asymptotic value of the bode magnitude at low frequencies provided a qualitative value of the mass transport resistance which increases with increasing current density. In this study an analysis of the performance of an Open-Cathode PEFC stack using simultaneous EIS measurements has been carried out.

The objective of this Chapter is to provide an insight into the change in impedance of individual cells within a commercial Open-Cathode 4-cell stack. The electrochemical and diffusion mechanisms in each cell are calculated through the theoretical treatment derived in Chapter 5; therefore it is possible to have an insight into the factors that limit the performance of the PEFC stack.

8.1 Experimental

A commercial Open-Cathode 4-cell stack with a 16 cm² area was used for the experimental tests as shown in Fig. 8.1. The membrane electrode assemblies (MEAs) were made of Nafion 211 with platinum loadings of 0.4mg/cm² and carbon black for the electrodes. The gas diffusion layers (GDLs) were made of carbon felt with 200µm width. The 4-cell stack consists of open cathodes with two 5V DC fans for oxidant supply (as air) and cooling. The stack consists of bipolar plates made of FU4369 HT material with a thickness of 5 mm. High purity hydrogen (99.999 %) was used during the tests to reduce fuel impurities which can limit the performance of the PEFC. Open-Cathode fuel cells are commonly operated with a dead-ended hydrogen outlet; however under such a configuration a non-steady response is expected at medium and high currents due to build-up of water. In this study the fuel cell stack was run in a through flow mode at the anode. Flow rate of hydrogen in the anode was kept constant during all the experiments with a stoichiometry of 2. The hydrogen supplied was dry. The PEFC stack was operated at ambient temperature 22 °C and the hydrogen back pressure was held at 0.4 bar(g). Polarisation curves were recorded prior to impedance measurements as shown in Fig. 8.2.

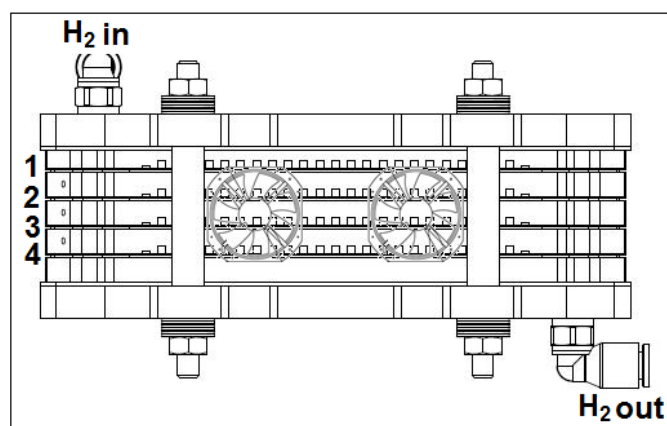


Figure 8.1 Open-cathode fuel cell stack for EIS measurements

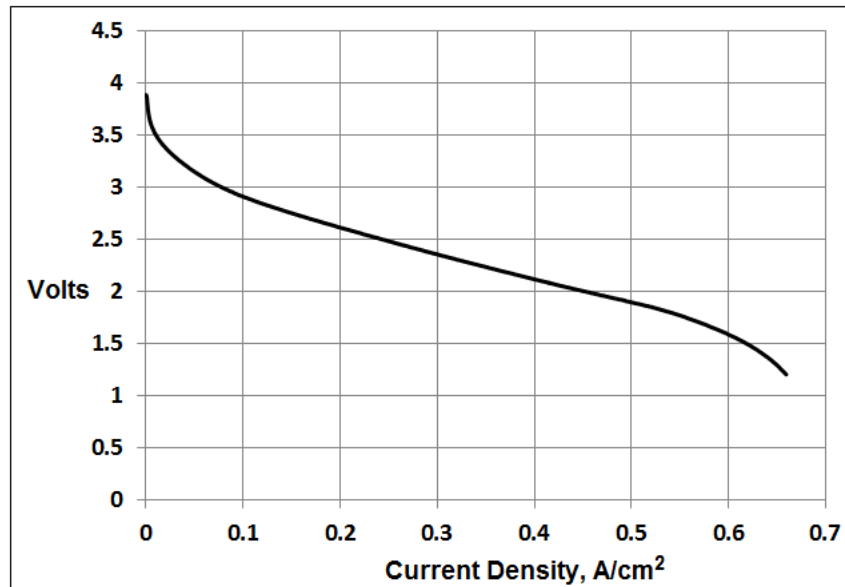


Figure 8.2 Polarisation curve

EIS measurements were carried out through a multichannel frequency response analyzer FRA (Z#106 WonATech Co). The multichannel FRA consists of five channels and simultaneously measures five impedance spectra through a single induced DC current value. The multichannel system is connected with a RBL488 Dynaload. The multichannel FRA superimposes a small AC sinusoidal perturbation onto the bias current induced by the RBL488 Dynaload unit and measures the AC voltage signals resulting from the PEFC. The impedance measurements were carried out in a galvanostatic mode with a 5% AC amplitude of the DC current [5,8,9] to obtain a linear response from the system at frequencies from 10 kHz to 0.1Hz. Special electrical cables (Low inductive cable with Fusion Lug Technology, TDI POWER) connected between the PEFC and the RBL488 Load were used to reduce high frequency inductive effects on the EIS measurements. Five channels from the Z#106 FRA were used to simultaneously measure the impedance of the PEFC stack and the impedance solely for each cell.

EIS measurements were carried out at three different current densities 0.1875, 0.3125, and 0.4375 A/cm² of the polarisation curve, as shown in Fig. 8.2. The PEFC stack was run over 60 minutes at the required current with no variation in the voltage to ensure a steady state for EIS measurements. EIS measurements for current densities

$<0.1875\text{A/cm}^2$ were not possible, as the low AC amplitude superimposed onto the DC current made it difficult for the FRA to distinguish between noise and response. At high current densities $>0.4365\text{ A/cm}^2$ the fuel cell stack was not steady for a long period of time due to the high water concentration produced by oxygen reduction reaction (ORR).

8.1.1 Stack Measurements

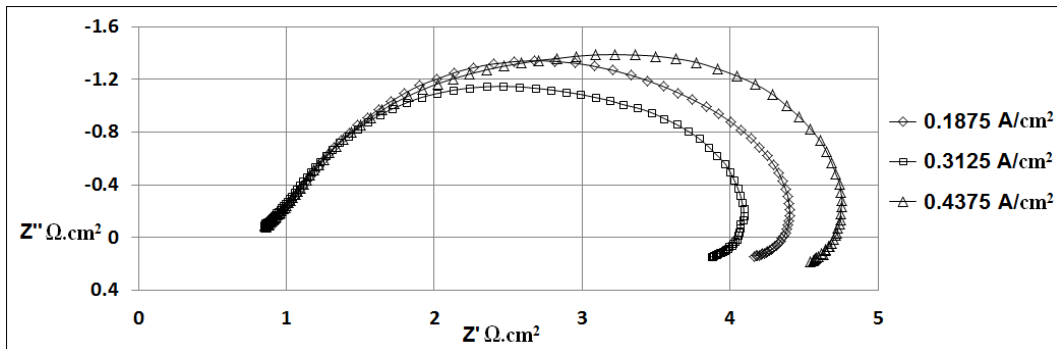


Figure 8.3 Stack measured data at 0.1875, 0.3125 and 0.4375 A/cm²

The resulting stack impedance is shown in a complex plane and represents the electrochemical and diffusion mechanisms in the frequency domain. The diameter of the spectrum decreases from a current density of 0.1875 A/cm² to 0.3125 A/cm² and increases from a current density of 0.3125 A/cm² to 0.4375 A/cm², as shown in Fig. 8.3. EIS measurements have limitations and present disadvantages as the low impedance values are obscured for low frequencies and some effects are not visible due to a masking effect in the impedance plot [10]. Therefore the impedance results of Fig. 8.3 reflect the overlapping of two semicircles. One is related to the charge transfer resistance during the ORR which decreases with increasing current density and the other is related to oxygen transport limitations which increases with increasing current density. At high frequencies there is no inductive effect (EIS measurements with positive imaginary component) of the measurement cables which deforms the high frequency region of the impedance spectra, as demonstrated in Chapter 6. The sensing cables of the FRA which measure the voltage levels in each cell were directly connected to the bipolar plates of the PEFC stack. This allowed the reduction of inductive effects on the EIS measurements at high frequency by placing the sensing cables from the FRA as far apart as possible from the inductive

source (current cables). At high frequencies (Fig. 8.3) it is clearly shown that the 45° straight line represents the ionic resistance of the catalyst layer as previously demonstrated in Chapter 6. At low frequencies inductive effects on the EIS results were apparent for the three current densities. Makharia *et al.* [11] suggested that the possible reason for this inductive effect at low frequencies are the side reaction and intermediates involved in fuel cell reactions. Antoine *et al.* [12] showed that the adsorption step involved in the ORR of the fuel cell gives rise to this inductive behaviour. Roy *et al.* [13] developed an impedance model to account for the reaction mechanisms that may be responsible for the inductive response at low frequencies, the model proposes the formation of hydrogen peroxide (H_2O_2) as an intermediate in a two step ORR. It has been reported [14] that crossover of hydrogen to the cathode facilitates the reaction of oxygen and hydrogen at the cathode, generating hydroxyl and hydroperoxyl radicals which react further to produce H_2O_2 at the cathode. The hypothesis that H_2O_2 may be formed at the cathode of a fuel cell is supported by the results of Inaba *et al.* [15].

8.1.2 Individual Cell Measurements

The use of the multichannel FRA allows the measurement of the impedance response of each cell of the PEFC stack simultaneously. The cells were numbered from the hydrogen inlet side starting from 1, as shown in Fig. 8.1. Fig. 8.4 shows the impedance plot for the four cells at $0.1875 A/cm^2$. The four cells show the inductive effect at low frequencies. There is little difference observed in this inductive effect at low frequencies for the cells at different positions in the stack. The cell located closer to the hydrogen inlet (cell 1) results in a smaller impedance spectrum than the other cells, as shown in Fig. 8.4. The second cell shows the highest impedance spectrum which could be related to the structural features of the MEA. The measured data from 10 kHz to 100 Hz are similar for cells 1, 3 and 4. The difference in impedance response at low frequencies in cells 1, 3 and 4 could be related to limitations in oxygen transport through the GDL and cathode catalyst layer (CCL).

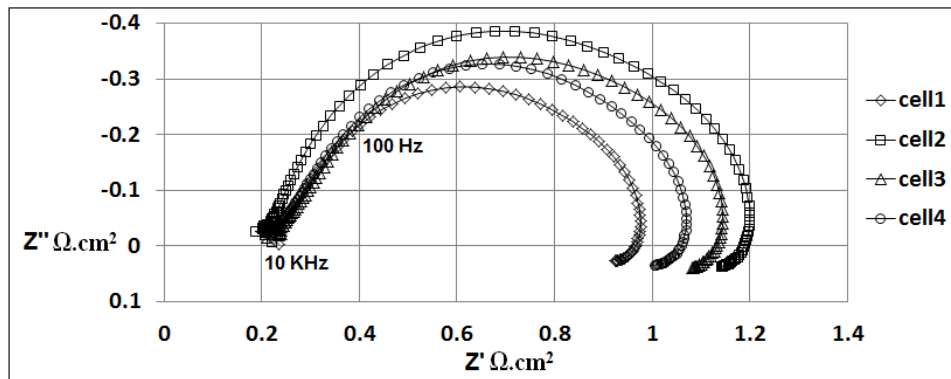


Figure 8.4 Measured data for different cells of the stack at 0.1875 A/cm^2

Fig. 8.5 shows the impedance results of the four cells at a current density of 0.3125 A/cm^2 . The diameters of the spectra decrease with increasing current density from 0.1875 A/cm^2 to 0.3125 A/cm^2 . When the kinetics of the ORR dominate the cell performance such as in the low current density range of the polarisation curve, the impedance spectrum mainly represents the charge transfer resistance during the ORR and its diameter decreases with increasing current density [10]. At a current density of 0.3125 A/cm^2 there is an increase in the driving force for the interfacial oxygen reduction process. The impedance response of cell 3 at low frequencies is higher than cells 1 and 4. Cell 2 shows the biggest impedance spectrum.

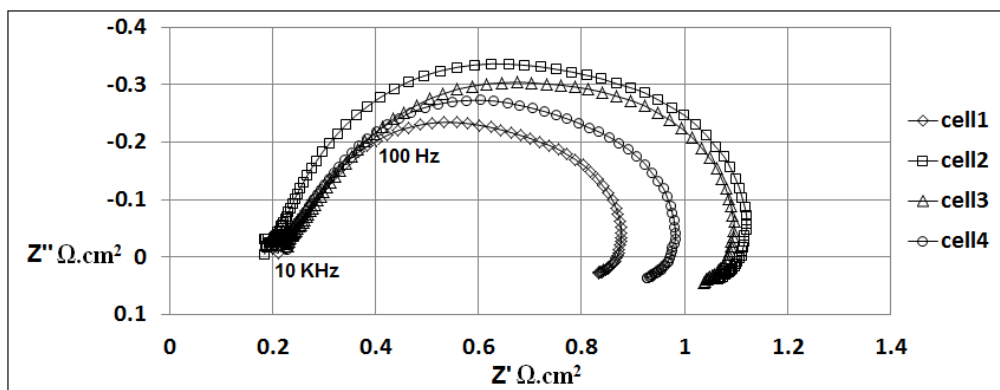


Figure 8.5 Measured data for different cells of the stack at 0.3125 A/cm^2

Fig. 8.6 shows the impedance results at a current density of 0.4375 A/cm^2 . One of the disadvantages of the EIS technique is that multiple energy controlled processes during the

electrochemical reaction can be masked in the impedance plot. Therefore the semicircles that represent the charge transfer of the ORR and mass transport effects are overlapped in the experimental impedance spectra. Similar results were reported by Yuan *et al.* [5] when EIS measurements were carried out in a H₂/air PEFC stack. Their results show that EIS measured data feature a single semicircle at high current densities. The increase in diameter of the spectra with increasing current density from 0.3125 A/cm² to 0.4375 A/cm² as shown in Fig. 8.6 is attributed to an increase in oxygen transport limitations.

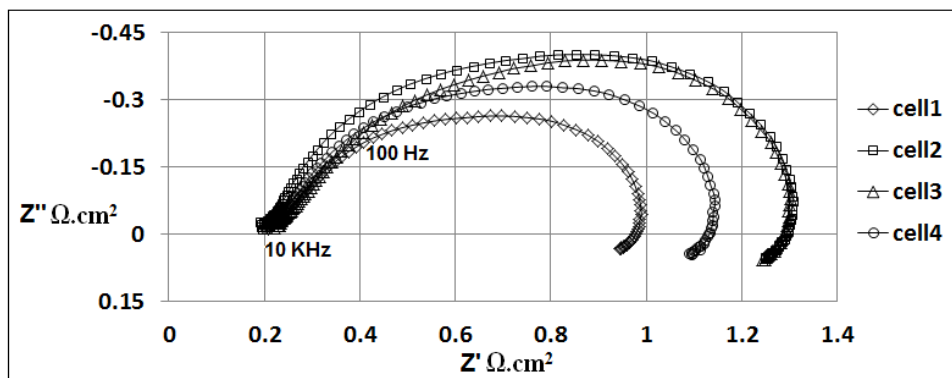


Figure 8.6 Measured data for different cells of the stack at 0.4375 A/cm²

8.2 Results and Discussion

In this study the factors that limit the performance in the Open-Cathode PEFC stack are assessed through EIS measurements and the details of the impedance model derived in Chapter 5. It is possible to generate a deeper understanding of the internal phenomenological processes by coupling the experimental EIS technique to the fundamental electrochemical and diffusion theories.

8.2.1 Electrochemical and Diffusion Mechanisms

The use of equivalent circuits with the experimental EIS technique is a well-established methodology to characterise processes in the PEFC. The electrical circuit that models the PEFC spectrum neglecting anode contribution contains a resistance that accounts for the polymer electrolyte membrane (PEM), GDL and bipolar plate connected in series with a

circuit accounting for the CCL, in which for this specific case is the CCL impedance equation derived in Chapter 5,

$$Z_{FC} = R_e + \frac{(R_c + Z_w) \gamma \coth(\gamma x)}{1 + Y(i\omega)^p (R_c + Z_w)} \quad (8.1)$$

With
$$\gamma = \sqrt{R_p \left[\frac{1}{R_c + Z_w} + Y(i\omega)^p \right]}$$

- R_p Resistance to the flow of ions in the electrolytic phase of the CCL.

- R_c Charge transfer resistance presented in the ORR defined as $R_c = b / j_0 \exp(\eta_{ss} / b)$, where b is the Tafel slope, η_{ss} represents a value of voltage in activation overpotential, and j_0 is the exchange current.

- Z_w Warburg impedance [16] and describes resistance for oxygen diffusion across CCL in the frequency domain $Z_w = R_w \tanh(i\omega T_w)^{0.5} / (i\omega T_w)^{0.5}$, with $R_w = RT\delta / (z^2 F^2 c_o^* D)$ defined as resistance for the diffusion process and $T_w = \delta^2 / D$ defined as the time constant to diffuse oxygen through the CCL.

- $Y(i\omega)^p$ Y represents a parameter related to constant phase element (CPE), superscript P represents a parameter to correct the inhomogeneity in the distribution of charge.

- ω Angular frequency.

- i Imaginary component in impedance.

- R_e Total ohmic resistance to the flow of electrons and ions in the bipolar plate, GDL and PEM.

Fouquet *et al.* [16] monitored the performance of a H₂/air six-cell PEFC stack under drying and flooding conditions through EIS measurements. The Randles circuit with Warburg element that represents the cathode electrochemical mechanisms was applied to the cell impedance data at high currents. The authors made the assumption that the rate limiting reaction in the cell is the ORR at the cathode; therefore anode contribution to the cell impedance data was considered negligible. In the previous chapter, Chapter 7, it was demonstrated that a reference electrode inserted in a PEFC operated with 100% relative humidity in the anode and the use of a multichannel FRA allowed the separation of the impedance response of the cell and cathode. The results showed that the difference between cell and cathode impedance responses attributed to anode contribution (hydrogen oxidation reaction) become negligible at medium and high currents. In this study anode contribution can be considered negligible for the EIS measurements at medium and high currents.

The simulated data from Eq. 8.1 were compared with the measured EIS data using a Graphic User Interface (GUI) developed in Matlab[®], see Appendix D. The use of the GUI with Eq. 8.1 for EIS analysis has already been demonstrated in Chapters 6 and 7. The GUI allows the fitting of the parameters from Eq. 8.1 to achieve a good agreement between the experimental and simulated data. The least squares fitting method was used in order to find the best-fit between the model and the measured data. A good quality fit is obtained when the sum of the deviations squared (least square error) between the simulated and measured impedance data has a minimum value, for instance < 0.1. The results show that Eq. 8.1 cannot reproduce EIS measurements in the positive imaginary part of the complex impedance plane at low frequencies as shown in Fig. 8.7.

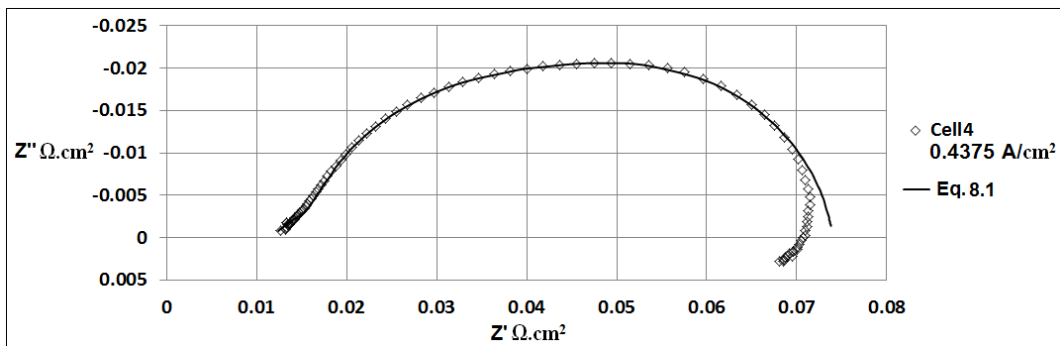


Figure 8.7 Comparison between measured data and simulated data from Eq. 8.1

Adsorbed intermediate species - EIS measurements in the positive imaginary part of the complex impedance plane at low frequencies are commonly recognised as an inductive loop. This inductive loop has been considered a characteristic of systems containing consecutive heterogeneous reactions with potential-dependent adsorbed intermediate species [17]. Roy *et al.* [13] developed two different impedance models to predict low frequency inductive loops in EIS measurements of PEFCs. The models accounted for the additional reaction formation of H_2O_2 and formation of platinum oxide (PtO) with subsequent dissolution of Pt on the CCL. Ambrosi and Sarli [18] reported that electrochemical reactions that take place within the electrolyte can be governed by both the rate constants and the intermediate species adsorbed on the electrode. The authors reported an electrical circuit for a faradaic process with adsorption, as shown in Fig. 8.8.

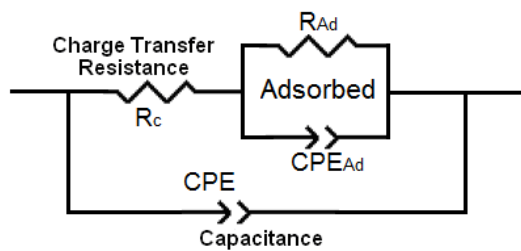


Figure 8.8 Equivalent electrical circuit for a faradaic process with adsorption

Fig. 8.8 shows that if intermediate species are involved in the ORR, an additional equivalent network formed by a pseudo-capacitance CPE_{Ad} in parallel with a pseudo-resistance R_{Ad} should be added in series with the former R_C in the R_C - CPE combination that represents simple reaction kinetics. As the adsorption only covers a fraction of the total electrode area, such a fraction fluctuates at the same frequency of the potential but differs in phase with it. Ciureanu and Wang [19] reported the same electrical circuit shown in Fig. 8.8 to account for an electrode with adsorbed intermediate species at the interface between dissimilar materials i.e. Nafion-carbon.

The second term on the right-hand side of Eq. 8.1 was derived in Chapters 4 and 5 by considering simple reaction kinetics $Ox + e^- \xleftrightarrow{K} Re$ and does not consider adsorbed intermediate species during the ORR which can limit the performance of the PEFC. In Eq. 8.1 the term expressed as $(R_C + Z_W)$ represents the total process resistance during the

ORR, charge transfer resistance R_C in series with mass transport resistance Z_W due to oxygen transport limitations. Bard and Faulkner [20] reported that the overpotential during an electrochemical reaction can be considered the sum of terms associated with the different reaction steps: mass transport overpotential, charge transfer overpotential and overpotential associated with a preceding reaction. Therefore the electrode reaction can be represented by a resistance composed of a series of resistances representing the various steps during the electrochemical reaction. If the term representing the process associated with the adsorbed intermediate species during the ORR $Z_{Ad} = R_{Ad} / (1 + Y_{Ad}(i\omega)^{p_{Ad}} R_{Ad})$ derived from Fig. 8.8 is put in series with $(R_C + Z_W)$ in Eq. 8.1 to consider the total process resistance during the ORR as reported by Bard and Faulkner [20]. An approximate representation for the impedance response of the PEFC considering adsorbed intermediate species can be expressed as,

$$Z_{FC} = R_e + \frac{(R_C + Z_W + Z_{Ad})\gamma \coth(\gamma x)}{1 + Y(i\omega)^p (R_C + Z_W + Z_{Ad})} \quad (8.2)$$

where
$$\gamma = \sqrt{R_p \left[\frac{1}{R_C + Z_W + Z_{Ad}} + Y(i\omega)^p \right]}$$

The resulting Eq. 8.2 needs further detailed study to analyse how adsorbed intermediate species Z_{Ad} could affect the ORR current distribution through the CCL in the spatio-temporal domain. If the parameters represented in Eq. 8.2 are fitted to the measured EIS data using the GUI in Matlab® and considering the least square error < 0.1, it is possible to reproduce the inductive loop at low frequencies as shown in Fig. 8.9.

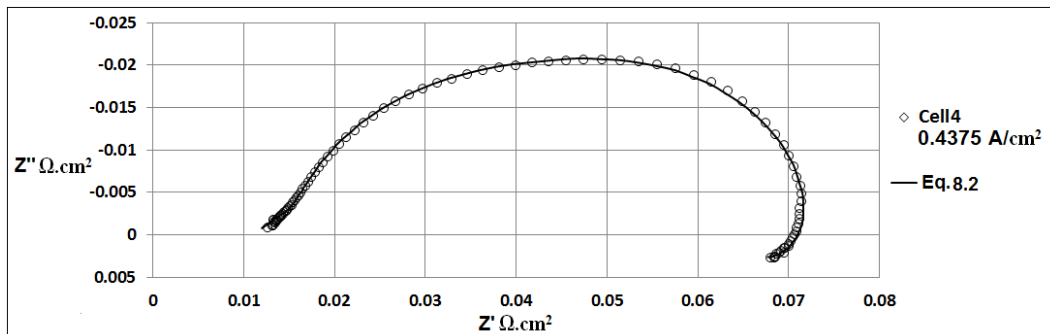


Figure 8.9 Comparison between measured and simulated data from Eq. 8.2

The results show that Eq. 8.2 is able to reproduce the low frequency loop which is related to adsorbed intermediate species in the ORR. The electrochemical and diffusion mechanisms of the measured data were calculated through Eq. 8.2 and the results are shown in Tab. 8.1. The parameters of R_{Ad} and $Y_{Ad}(i\omega)^P$ that represent Z_{Ad} to account for the adsorbed intermediate species during the ORR resulted in negative numbers. Bai and Conway [21] demonstrated in their work that EIS measurements with positive imaginary components (inductive loop) at low frequencies in electrochemical systems with adsorbed intermediate species are related to a change in the sign of the coverage φ dependence on potential ($d\varphi/dE$). Ciureanu and Wang [19] reported EIS measurements in a H_2/H_2+CO PEFC. EIS measurements showed the inductive loop at low frequencies with increasing bias potential. In their study the electrical circuit shown in Fig. 8.8 was applied with EIS measurements and this resulted in negative values for R_{Ad} and CPE_{ad} . They concluded that the negative parameters in Z_{Ad} which cause the inductive loop are a result of the decrease of CO coverage on the electrode with increasing bias potential due to oxidation of CO by oxygenated species on the electrode-electrolyte interface. In this study Y_{Ad} was found constant for all the measured data ($-5.1375 \text{ s}^p/\Omega\text{cm}^2$ with $P_{ad}=0.8$) and R_{Ad} is shown in Tab. 8.1. Overall R_{Ad} becomes more negative with increasing current density for all cells. At this point it is not clear what adsorbed intermediate species are interfering with the ORR and limiting the PEFC stack performance. In this particular stack an air filter in the fan should have been considered to remove any particulate matter that might contaminate the CCL. The process responsible for the inductive characteristic at low frequencies could also be attributed to hydrogen crossover through the PEM or bipolar plates to form H_2O_2 during the ORR as reported by Roy *et al.* [13]. A further study to consider crossover of hydrogen through bipolar plates made of FU4369 HT material should be investigated.

Charge Transfer Resistance - The measured data from 10 kHz to 100 Hz are similar for cells 1, 3 and 4, as shown in Figs. 8.4, 8.5 and 8.6. The temperature distribution through this particular stack is not very significant in the kinetics of the electrochemical reaction as the measured data in the frequency range of 10 kHz - 100 Hz presented the same trend at the same current density with an exception for cell 2. The parameter charge transfer resistance R_C calculated from EIS measurements and Eq. 8.2 is shown in Tab. 8.1. The

charge transfer resistance R_C , whose dependence on electrode potential is given by the Tafel equation and reflects the increase in the driving force during the ORR, remains constant for cells 1, 3 and 4 at the same current density. R_C is a function of the exchange current density j_0 , as such $R_C = b / j_0 \exp(\eta_{ss} / b)$. A decrease in j_0 results in an increase of R_C and thus a decrease in the activity of the electrode surface is produced. Cell 2 shows a higher R_C than the rest of the cells at the same current density which can be attributed to low electrocatalytic activity in cell 2. Therefore the activation overpotential in the PEFC stack is dominated by the charge transfer resistance of cell 2. As expected R_C decreases in the four cells with increasing current density.

	$R_C \Omega.cm^2$	$R_w \Omega.cm^2$	$R_{Ad} \Omega.cm^2$
0.1875A/cm²			
Cell1	0.7712	0.0128	-0.128
Cell2	0.9312	0.1216	-0.192
Cell3	0.7712	0.1584	-0.176
Cell4	0.7712	0.0736	-0.16
0.3125 A/cm²			
Cell1	0.6544	0.064	-0.136
Cell2	0.8144	0.176	-0.184
Cell3	0.6544	0.2304	-0.2
Cell4	0.6544	0.152	-0.184
0.4375 A/cm²			
Cell1	0.6336	0.1952	-0.184
Cell2	0.7568	0.4272	-0.232
Cell3	0.6336	0.504	-0.328
Cell4	0.6336	0.3552	-0.248

Table 8.1 Charge transfer resistance R_C , mass transport resistance R_w and adsorption resistance R_{Ad} calculated from Eq. 8.2

Ohmic Resistance - Fig. 8.10 shows the high frequency region of the EIS measurements at the three different current densities. The measured data of cell 2 are not shown in Fig. 8.10 as the data of this cell from 10 kHz to 100 Hz showed a different trend compared to the rest of the cells as shown in Figs. 8.4, 8.5 and 8.6. Cell 3 shows a slightly higher ohmic resistance than cell 1 and 4 at the three current densities, this effect can be noticeable in the real part Z' at 10 kHz of the spectra, as shown in Fig. 8.10. The increase in ohmic resistance could be attributed to dehydration in the PEM which may have been caused by an increase in reaction generated heat in cell 3. Ohmic resistance seems to be

more sensitive than charge transfer resistance to the temperature distribution through the stack.

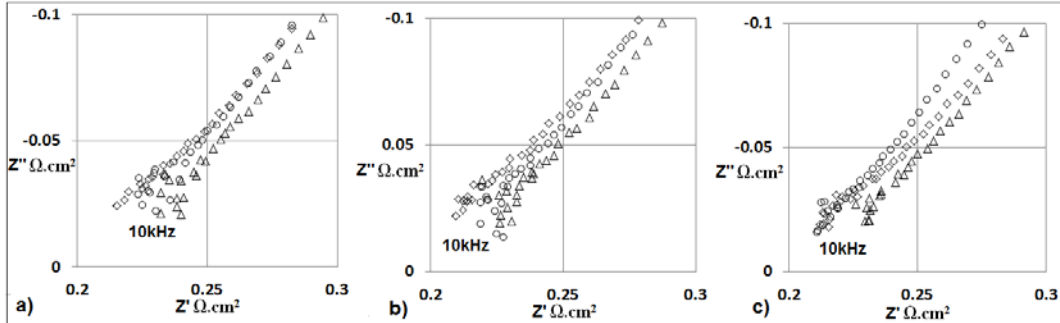


Figure 8.10 High frequency EIS measurements for cell 1 \diamond , cell 3 Δ , cell 4 \circ ; a) 0.1875 A/cm^2 , b) 0.3125 A/cm^2 , c) 0.4375 A/cm^2

Oxygen Transport limitations - The mass transport resistance R_w , due to gaseous oxygen transport limitations and as a function of the gaseous oxygen equilibrium concentration c_o^* in the CCL-GDL interface, increases with increasing current density for all cells, as shown in Tab. 8.1. Cells 2 and 3 show higher mass transport resistance than cell 1 and 4. Cell 3 shows the highest mass transport resistance as shown in Fig. 8.11. The increase in mass transport resistance of cell 3 could be attributed to a high water concentration produced by the ORR which affects the transport of oxygen to reach the reaction sites in the CCL; however, the increase in ohmic resistance in cell 3 (PEM dehydration), shown in Fig. 8.10, demonstrates a contrasting case.

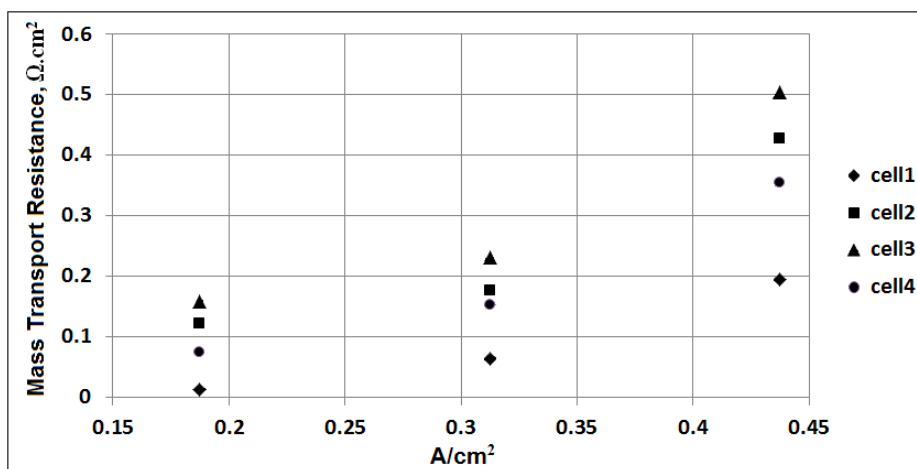


Figure 8.11 Estimation of mass transport resistance in each individual cell

Santa Rosa *et al.* [22] studied the effect of critical conditions on an Open-Cathode 8-cell stack operated at ambient temperature and pressure. Three different fans for oxidant supply and cooling were used to investigate how the air flow rate affects the stack performance. A 5 V DC fan was found to be the best option because it ensures enough stack cooling and oxidant supply. The authors concluded that a fan with lower voltage affects the stack performance at medium-high currents because lower air fan flow rate cannot expel excessive reaction generated heat which in turns leads to dehydration in the PEM (high ohmic resistance).

In this study, EIS measurements demonstrate that inhomogeneity of air flow rate in an open-cathode PEFC stack not only leads to an increase in ohmic resistance but also leads to an increase in mass transport limitations in the cells. Limitations in air flow rate decrease the gaseous oxygen equilibrium concentration in the GDL-CCL interface and increase mass transport resistance. The position and distance of the fans with respect to the open cathodes in this particular stack played an important role for mass transport limitations. Two 5V DC axial fans were centred 1cm over the open cathode of cell 3 as shown in Fig. 8.1. Air enters the fan evenly as it follows the physics of moving from a high pressure area into a low pressure area. The air then spreads outwards as it leaves the fan due to a centrifugal force. This results in a vacuum area absent of air flow in the center of the fan and therefore the majority of the airflow is around the sides of the fan. This could explain the increase in oxygen transport limitations in cell 3 for the three currents, as shown in Fig. 8.11. A fan characteristic curve (FCC) presents three typical regions for axial fans: a stalling, an unstable and an optimal operating region [23]. Sasmito *et al.* [24] reported that the interception between the operating point of an Open-Cathode fuel cell stack and a FCC should be located in the optimal operating region and be sufficiently far away from any unstable and stalling region. With most fans there is no air flow right in the center of the fan. The majority of the airflow is around the sides of the fan; this effect limits the pressure within the open cathode in cell 3 and thus the operating point of cell 3 corresponds to the stalling point in the FCC. This effect could explain the increase in oxygen transport limitations and the increase in reaction generated heat in cell 3 which increases the ohmic resistance.

The results for the oxygen diffusion time constant in the CCL, represented by $T_w = \delta^2 / D$, where δ represents the characteristic length of the diffusive path in the CCL and D represents the effective diffusion coefficient for oxygen transport in the CCL, are not shown in Tab. 8.1. Three diffusion processes exist in the CCL: diffusion through the porous media, water film and electrolyte film covering the catalyst agglomerate. It is not straightforward to determine the role of the effective diffusion coefficient D in the time constant T_w calculated from the measured data of this study because this parameter is related to the modes of transport through the multiphase material in the CCL. At this point it is not clear which one of these diffusion processes is the limiting one. In the literature [25], it has been proposed that the effective diffusion in the diffusion time constant of impedance measurements is related to the diffusion of oxygen through the GDL. This is not the case for the measured data of this study, as the diffusion time constant did not follow the same trend as the mass transport resistance R_w shown in Tab 8.1 and Fig. 8.11.

8.2.2 Discussion

The inhomogeneous performance along a PEFC stack can be monitored with the use of simultaneous EIS measurements. Some works in the literature have used simultaneous EIS measurements during PEFC operation to diagnosis the factors that limit the stack performance. However some misconceptions and misunderstandings about how to relate the physical processes of a PEFC stack with the change in impedance response have been reported. One of the disadvantages of the EIS technique is that multiple energy controlled processes during the electrochemical reaction can be masked in the impedance measurements. The interpretation of the electrochemical and diffusion mechanisms which are truly happening in a PEFC stack can be unveiled by relating the electrochemical impedance data to the fundamental theory of PEFCs. This level of understanding is critical to industry to drive the development, optimisation and running of PEFCs as reliable commercial products. In this study the factors that limit the performance in an Open-Cathode PEFC stack are assessed through simultaneous EIS measurements and the use of the impedance model derived in previous Chapters 4 and 5. It is possible to diagnose degradation in MEAs which yield low electrochemical activity in the electrodes

through experimental EIS and modelling. Oxygen transport limitations due to flooding can be diagnosed at low frequencies of EIS measurements. The selection of fans based on power rating, type, stack length, bipolar plate channel dimensions requires careful consideration for the operating point and resulting stack performance. The performance of a fan with respect to an Open-Cathode fuel cell stack is measured experimentally and estimated from various engineering correlations or computational fluid dynamics (CFD) analyses. EIS measurements can provide a direct correlation about variations in air flow through the open cathodes in an open-cathode PEFC. Finally another common effect limiting the stack performance is the presence of adsorbed intermediate species during the ORR. This effect has been identified in EIS measurements as an inductive loop at low frequencies. Open-Cathode PEFC stacks are exposed to a range of atmospheric compositions which can include sulphur dioxide, nitrous oxides, ionic contamination, carbon monoxide, etc. A further investigation to include poisoning effects on Open-Cathode PEFCs which is normally present in the positive imaginary part of the complex impedance plane at low frequencies will be researched in future work.

8.3 Conclusions

This study has demonstrated that EIS is a powerful tool for in-situ diagnosis of a PEFC stack. EIS measurements that account for each cell in an Open-Cathode PEFC stack were compared with simulated data from the model derived previously in Chapter 5. The results showed that EIS measurements in the positive imaginary part of the complex impedance plane that account for adsorbed intermediate species during the ORR cannot be reproduced through the model derived in Chapters 4 and 5. The model was modified to include adsorbed intermediate species mechanisms during the ORR and the results showed a good agreement between measured data and simulated data. Electrochemical and diffusion mechanisms for each cell in the PEFC stack were calculated through EIS measurements and the model. The results show that the activation overpotential in the whole PEFC stack is dominated by low electrocatalytic activity in one of the cells. The results also show that oxygen transport limitations and PEM dehydration are attributed to variations in flow of the air through the open cathodes in the stack. The results also revealed adsorbed species during the ORR with increasing current density. At this point it

is not clear what exact adsorbed species are interfering with the ORR and limiting the performance of the PEFC stack. Further experiments to account for the exact intermediate species should be carried out. This newly established EIS knowledge will enable an assessment of the state of health of operational fuel cell stacks.

8.4 References

- [1] Mohtadi R., Lee W. -K., and Zee J. W. V., "Assessing Durability of Cathodes Exposed to Common Air Impurities", *J. Power Sources*, 138, (2004), pp. 216-225.
- [2] Moore J. M., Adcock P. L., Lakeman J. B., and Mepsted G. O., "The Effects of Battlefield Contaminants on PEMFC Performance", *J. Power Sources*, 85, (2000), pp. 254-260.
- [3] Dale N. V., Mann M. D., Salehfar H., Dhirde A. M., and Han T., "ac Impedance Study of a Proton Exchange Membrane Fuel Cell Stack Under Various Loading Conditions", *J. Fuel Cell Sci. Technol.*, 7, (2010), pp. 031010.
- [4] Yuan X., Sun J. C., Blanco M., Wang H., Zhang J., and Wilkinson D. P., "AC Impedance Diagnosis of a 500W PEM Fuel Cell Stack, Part I: Stack impedance", *J. Power Sources*, 161, (2006), pp. 920-928
- [5] Yuan X., Sun J. C., Wang H., and Zhang J., "AC Impedance Diagnosis of a 500W PEM Fuel Cell Stack Part II: Individual Cell Impedance", *J. Power Sources*, 161, (2006), pp. 929-937.
- [6] Cimenti M., Tam M., and Stumper J., "High Frequency Artifacts in Electrochemical Impedance Spectroscopy Measurements on PEM Fuel Cells", *Electrochem and Solid States Letter*, 12, (2009), pp. B131-B134.
- [7] Ciureanu M., and Roberge R., "Electrochemical Impedance Study of PEM Fuel Cells. Experimental Diagnostics and Modeling of Air Cathodes", *J. Phys. Chem. B*, 105, (2001), pp. 3531-3539.
- [8] Gode P., Jaouen F., Lindbergh G., Lundblad A., and Sundholm G., "Influence of the Composition on the Structure and Electrochemical Characteristics of the PEFC Cathode", *Electrochim. Acta*, 48, (2003), pp. 4175-4187.
- [9] Jaouen F., Lindbergh G., and Wiezell K., "Transient Techniques for Investigating Mass-Transport Limitations in Gas Diffusion Electrodes II. Experimental Characterization of the PEFC Cathode", *J. Electrochem. Soc.* 150, (2003), pp. A1711-A1717.
- [10] Paganin V. A., Oliveira C. L. F., Ticianelli E. A., Springer T. E., and Gonzalez E. R., "Modelistic Interpretation of the Impedance Response of a Polymer Electrolyte Fuel Cell", *Electrochim. Acta*, 43, (1998), pp. 3761-3766.
- [11] Makharia R., Mathias M. F. and Baker D. R., "Measurement of Catalyst Layer Electrolyte Resistance in PEFCs Using Electrochemical Impedance Spectroscopy", *J. Electrochem. Soc.*, 152, (2005), pp. A970-A977.
- [12] Antoine O., Bultel Y., and Durand R., "Oxygen reduction Reaction Kinetics and Mechanism on Platinum Nanoparticles inside Nafion", *J. Electroanal. Chem.*, 499, (2001), pp. 85-94.
- [13] Roy S. K., Orazem M. E., and Tribollet B., "Interpretation of Low-Frequency Inductive Loops in PEM Fuel Cells", *J. Electrochem. Soc.*, 154, (2007), pp. B1378-B1388.
- [14] Xie J., Wood III D. L., More K. L., Atanassov P., and Borup R. L., "Microstructural Changes of Membrane Electrode Assemblies during PEFC Durability Testing at High Humidity Conditions", *J. Electrochem. Soc.*, 152, (2005), pp. A1011-A1020.
- [15] Inaba M., Yamada H., Tokunaga J., and Tasaka A., "Effect of Agglomeration of Pt/C Catalyst on Hydrogen Peroxide Formation", *Electrochem. Solid-State Lett.*, 7, (2004), pp. A474-A476.
- [16] Fouquet N., Doulet C., Nouillant C., Dauphin-Tanguy, D., and Ould-Bouamama, B., "Model Based PEM Fuel Cell State-of-Health Monitoring via AC Impedance Measurements", *J. Power Sources*, 159, (2006), pp. 905-913.
- [17] Keddad M., Mottos O. R., and Takenouti H., "Reaction Model for Iron Dissolution Studied by Electrode Impedance I. Experimental Results and Reaction Model", *J. Electrochem. Soc.*, 128, (1981), pp. 257-266.

- [18] Ambrosi V., and Di Sarli A., "Development of a Mathematical Treatment for Electrochemical Impedance Data Obtained from Coated Metals: Part 1", *Anti-Corrosion Methods and Materials*, 40 (1993), pp. 4-9.
- [19] Ciureanu M., and Wang H., "Electrochemical Impedance Study of Electrode-Membrane Assemblies in PEM Fuel Cells I. Electro-oxidation of H₂ and H₂/CO Mixtures on Pt-Based Gas-Diffusion Electrodes", *J. Electrochem. Soc.*, 146, (1999), pp. 4031-4040.
- [20] A. J. Bard and L. R. Faulkner, *Electrochemical Methods*, John Wiley & Sons, Inc., New York, (2001).
- [21] Bai L., and Conway B. E., "Complex Behavior of Al Dissolution in Non-Aqueous Medium as Revealed by Impedance Spectroscopy", *J. Electrochem. Soc.*, 137, (1990), pp. 3737-3747.
- [22] Santa Rosa D.T., Pinto D.G., Silva V.S., Silva R.A., and Rangel C.M., "High Performance PEMFC Stack with Open-Cathode at Ambient Pressure and Temperature conditions", *Int. J. Hydrogen Energy*, 32, (2007), pp. 4350-4357.
- [23] Bleier F.P. *Fan handbook: selection, applications and design*. McGraw-Hill, New York (1998)
- [24] Sasmito A. P., Birgersson E., Lum K. W., and Mujumdar A. S., "Fan Selection and Stack Design for Open-Cathode Polymer Electrolyte Fuel Cell Stacks", *Renewable Energy*, 37 (2012), pp. 325-332.
- [25] Malevich D., Halliop E., Peppley B. A., Pharoah J. G., Karan K., "Investigation of Charge-Transfer and Mass-Transport Resistances in PEMFCs with Microporous Layer Using Electrochemical Impedance Spectroscopy", *J. Electrochem. Soc.*, 156, (2009), pp. B216-B224.

Chapter 9

Study of Current Distribution in the Fuel Cell Cathode Catalyst Layer through EIS

One of the main objectives for electrode performance in the polymer electrolyte fuel cell (PEFC) is the optimisation of spatio-temporal current distributions within the catalyst layer (CL). The electrode performance in a PEFC can be enhanced by knowing and optimising the current distribution within the cathode catalyst layer (CCL). Thompson *et al.* [1] reported that by knowing exactly how the current of the oxygen reduction reaction (ORR) is distributed through the CCL, it would be possible to develop cold start models that include the physics of product water uptake in the membrane and filling of electrode pores with water (ice). The ORR current distribution can be influenced by the mass transport resistance of oxygen reactant diffusion into the CCL and/or of oxygen permeation through the thin layer of ionomer covering the Pt catalyst sites. This emphasizes the need to estimate internal current distribution measurements on the electrode of the PEFC. To date, different experimental techniques to measure the current distribution through the electrode have been developed such as the printed circuit developed by Brown *et al.* [2] and Cleghorn *et al.* [3], the subcell approach in the membrane electrode assembly (MEA) and current mapping technique by Stumper *et al.* [4], the segmented subcells in conjunction with a multichannel potentiostatic system by Yang *et al.* [5], the segmented flow field approach by Nojonen *et al.* [6] and the current collector in segmented flow field by Mench *et al.* [7,8,9]. A spatially resolved in-situ diagnostic method for PEFC using electrochemical impedance spectroscopy (EIS) measurements was carried out in the study reported by Schneider *et al.* [10]. This method pinpoints in-homogeneities in the current distribution. The combination of locally resolved current density measurements and local EIS allows the identification of local in-homogeneities in the performance of a PEFC. Other works [11,12] have focused on the estimation of the current distribution through the CCL using mathematical models based on theories of porous composite structure, liquid water saturation, transport of reactants

and products, and electrochemical conversion in ORR. The models can predict potential loss and catalyst utilization in the CCL.

An impedance-based approach which allows a spatio-temporal current distribution analysis in the CCL has not been presented or validated in the fuel cell research to date. This Chapter considers an application of the validated model from Chapters 4 and 5 in order to reveal the transitory and steady-state response of the current as a function of the thickness of the CCL. The model was applied in the time domain to simulate the effects of ionic resistance and the double layer capacitance across the CCL on the transitory and steady-state current distribution. In this Chapter the effects of ionic resistance, the charge capacitance, equilibrium oxygen concentration and effective oxygen diffusion on the current distribution of the CCL are studied. The ionic resistance depends on the distribution of electrolyte within the CCL and its hydrated state. The charge capacitance is dependent upon the amount of charge stored between dissimilar materials, i.e., electrode-electrolyte interface. The equilibrium oxygen concentration and effective oxygen diffusion are parameters which can be influenced by operation and preparation of the PEFC.

9.1 CCL Low Current Distribution

The current distribution in the time domain defined in Chapter 4 (Eq. 4.23) is represented as:

$$\frac{d^2 \bar{j}}{dx^2} = R_p \left[\frac{\bar{j}}{R_c} + C_{dl} \frac{d\bar{j}}{dt} \right] \quad (9.1)$$

where R_p represents the resistance to the flow of ions in the electrolytic phase of the CCL, R_c is the charge transfer resistance presented in the ORR, and C_{dl} is the charge capacitance between the electrode-electrolyte interface. Its solution can be obtained in one dimension using the *pdepe* command in Matlab [13]. With the validated impedance spectrum of the CCL in Chapter 4 it is possible to extend the application of the theoretical modelling treatment by using the same parameters as given in Tab. 4.1 and applying them

to the key equation in the time domain, Eq. 9.1, in order to reveal the spatial and temporal current distributions for two test cases (30 °C and 60 °C). This provides a valuable insight into the actual performance of the CCL. Fig. 9.1 shows the simulated dynamic response of current through the CL at 30 °C and 60 °C. The current distribution increases from the $x = 0$ thickness fraction gas diffusion layer (GDL)-CCL interface to the $x = 1$ thickness fraction CCL-polymer electrolyte membrane (PEM) interface. This reflects the transfer of ions to the PEM from the anode catalyst layer, which results in maximum current at the interface between the CCL and the PEM and a minimum current at the interface between the CCL and GDL as ions are consumed due to the ORR through the thickness of the CCL. Thompson *et al.* [1] estimated the current distribution within the CCL operated at -20 °C using a mathematical model that considers only ionic resistance and kinetic resistance described by the Tafel slope. The results showed that for the lowest average current density, the initial current distribution is skewed heavily toward the membrane interface. Also as the average current density is increased, the current distribution is pushed closer to the membrane interface. The simulations suggest that the current distribution in the CCL reaches steady-state in the order of milliseconds.

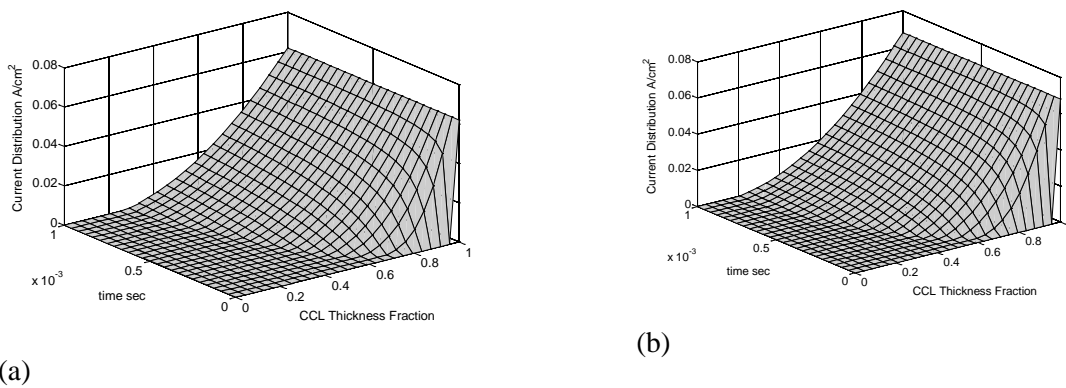


Figure 9.1 Simulated dynamic current response along the CCL at (a) 30 °C and (b) 60 °C

The steady-state current distribution along the CL can be observed more acutely in Fig. 9.2a for the two temperatures. At 60 °C, the distribution improves marginally between $x = 0.5$ and $x = 1.0$, yielding a higher local current at $x = 1.0$ than for the 30°C. This demonstrates that the ORR occurs to a greater degree in the half of the CCL closest to the PEM. Fig. 9.2b demonstrates the dynamic response of the CCL at a thickness fraction of

0.8. The thickness fraction of 0.8 is chosen because as Fig. 9.1 suggests it is a position where the dynamics of the CCL are well pronounced but also relatively close to the PEM-CCL boundary where electro-reduction will be correspondingly high. In general, Fig. 9.2b demonstrates that the time to steady-state improves with temperature. At 60°C, the current reaches 41 mA/cm² in 1 ms. At 30°C, the current reaches 38 mA/cm² in around 1.7 ms.

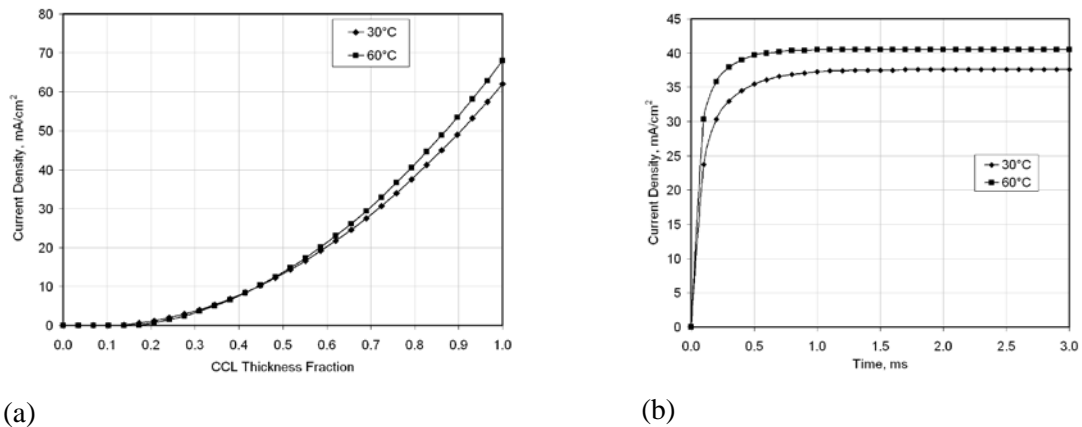


Figure 9.2 Current density profiles in the catalyst layer; (a) steady-state current distribution at $t = \infty$; (b) dynamic response of current at a thickness fraction of 0.8

9.1.1 Effect of Double-Layer Capacitance on CCL Low Current Distribution

The purpose of this section is to investigate the effects of double layer capacitance on the performance of the CCL. This is carried out by considering the 60 °C test case and altering the measured capacitance by - 50%, + 50% and + 120% while all other parameters are kept unchanged. In this current study, a constant phase element (CPE) parameter was used to correct the inhomogeneity in the charge distribution of the CCL. This can be observed in the non-perfect semicircle presented in the experimental impedance spectra. The CPE data can be converted to represent a capacitor (measured in Farads) through the following equation:

$$C_{dl} = Y(2\pi f_c)^{p-1} \tag{9.2}$$

noting that f_C is the frequency at which the imaginary part of the impedance reaches its minimum value. In this parametric study, three simulations are run where the capacitance is altered relative to its measured value in order to investigate the effect of double layer capacitance on current distribution and the dynamic response of the CCL. Fig. 9.3 demonstrates the effect of the magnitude of the double-layer capacitance on spatial and temporal current distributions in the CCL. From Fig. 9.3a, it is evident that the capacitance has no significant effect on the distribution of current through the CCL. However, Fig. 9.3b clearly demonstrates that by increasing the double layer capacitance, the time to steady-state is retarded. The steady-state current is approximately 40 mA/cm^2 ; for the measured baseline capacitance of 5.2 mF/cm^2 , the model demonstrates that the steady-state current is achieved in the CCL by 1.0 ms . If the capacitance is 50% less than the measured value (2.6 mF/cm^2), the steady-state current is achieved by 0.5 ms . By increasing the capacitance by 50% (7.8 mF/cm^2) and 120% (11.4 mF/cm^2) the time to steady-state is greater and increases to approximately 1.4 ms and 2.2 ms respectively.

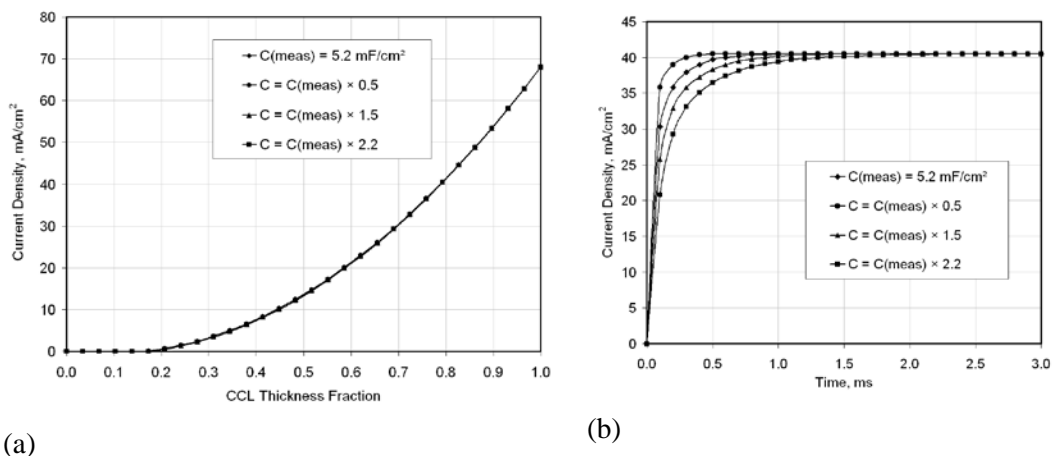


Figure 9.3 Effect of double-layer capacitance on CCL current profiles; (a) current distribution at steady-state; (b) dynamic response, $x = 0.8$ for different capacitances, 5.2, 2.6, 7.8 and 11.4 mF/cm^2

9.1.2 Simulated Effect of Ionic Resistance on CCL Low Current Distribution

It is possible to investigate the effect of ionic resistance in the CCL on the performance of the CCL in a similar manner to that carried out above. In the current study, two

simulations are run where the measured ionic resistance ($600 \text{ m}\Omega\text{cm}^2$) is decreased by 50% ($300 \text{ m}\Omega\text{cm}^2$) and increased by 50% ($900 \text{ m}\Omega\text{cm}^2$) to once again investigate the effect on current distribution and the dynamic response of the CCL.

Fig. 9.4 demonstrates that the ionic resistance has a primary effect on the current distribution and a secondary effect on the time to steady-state. Fig. 9.4a demonstrates that for low ionic resistance, the current distribution extends through the thickness of the CCL but can reduce to zero within the CCL if the ionic resistance is increased. This suggests that at low current operation when the oxygen distribution within the CL is assumed to be uniform, high ionic resistance can limit the extent of the ORR to regions closest to the PEM. The high ionic resistance limits the transfer of ions deeper through the electrolyte network towards the CCL-GDL interface, resulting in the curtailed current distribution. Fig. 9.4b demonstrates that while the ionic resistance reduces the maximum current achievable at the $x = 0.8$ position, the ionic resistance also has a secondary effect on the time to steady state. For the three cases considered, the simulated steady state current is approximately 47 mA/cm^2 , 41 mA/cm^2 and 34 mA/cm^2 for $300 \text{ m}\Omega\text{cm}^2$, $600 \text{ m}\Omega\text{cm}^2$ and $900 \text{ m}\Omega\text{cm}^2$ resistances respectively. At $300 \text{ m}\Omega\text{cm}^2$, the steady-state current is achieved in 0.6 ms . At $600 \text{ m}\Omega\text{cm}^2$, the steady-state current is achieved in 1 ms . At $900 \text{ m}\Omega\text{cm}^2$, it takes around 1.3 ms .

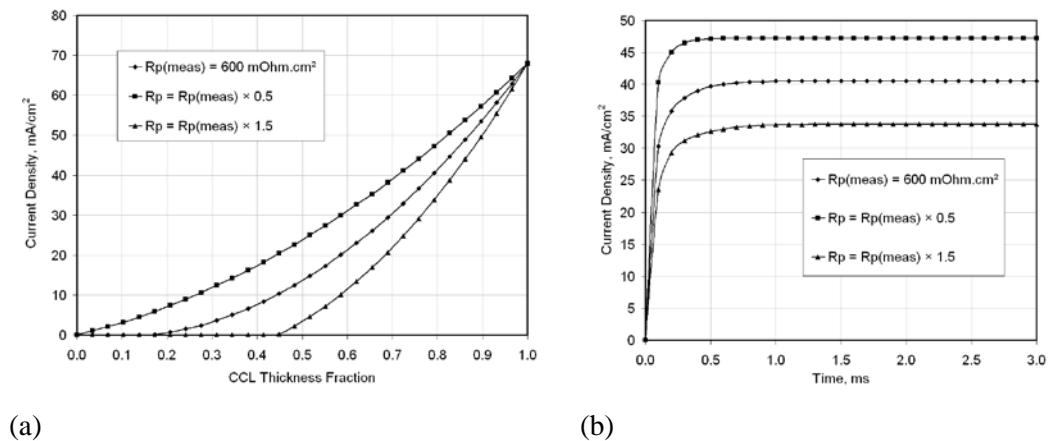


Figure 9.4 Effect of ionic resistance on CCL current profiles; (a) current distribution at steady-state; (b) dynamic response, $x=0.8$ for different proton resistances, 600, 300, 900 $\text{m}\Omega\text{cm}^2$

9.2 CCL High Current Distribution

In Chapter 4, it was considered that there is no change in oxygen concentration in the CCL at low currents. In this Chapter the change in oxygen concentration defined in the modelling considerations from section 5.1.2 Chapter 5 is taken into account at medium and high currents in the time domain, thereby addressing the assumption of no change in oxygen concentration at low current operation (Eq. 4.18), as such:

$$\frac{d\bar{j}}{dx} = \frac{c_o}{c_o^*} \frac{\bar{\eta}}{R_C} + C_{dl} \frac{d\bar{\eta}}{dt} \quad (9.3)$$

where \bar{j} is the current across the thickness of the CCL in the time domain, $\bar{\eta}$ is the potential difference between the electrode and electrolyte interface in the time domain, c_o^* is the equilibrium oxygen concentration at the GDL-CCL interface, c_o is the oxygen concentration at the CCL-PEM interface in the time domain, C_{dl} represents the capacitance between dissimilar materials, R_C represents the charge transfer resistance present in the ORR defined in Eq. 4.19, x represents the thickness (dimensionless) of the CCL from $x=0$ CCL-GDL interface to $x=1$ CCL-PEM interface.

The oxygen transport in the CCL in the Laplace domain defined in Chapter 5 (Eq. 5.12) can be arranged with $\beta_1 = \sqrt{s/D}$ as:

$$c_o(s) = c_o^*(s) - \frac{c_o(s)}{c_o^*(s)} \frac{\bar{\eta}_1(s)}{zFR_C \sqrt{D}} \frac{\sinh(\delta \sqrt{s/D})}{\sqrt{s} \cosh(\delta \sqrt{s/D})} \quad (9.4)$$

The solution of the inverse Laplace transform of Eq. 9.4 by the Heaviside's Expansion Theorem [14] is detailed in Appendix E and results in:

$$\frac{c_o}{c_o^*} \left[1 - \frac{\bar{\eta}_1 8\delta}{\pi^2 zFR_C D c_o^*} \exp\left(-\frac{\pi^2 D}{4\delta^2} t\right) \right] = 1 \quad (9.5)$$

The use of a small amplitude sinusoidal perturbation through the EIS technique allows the use of a linear model to represent the impedance of the CCL. Bard and Faulkner [15] reported that a linearized representation of the overpotential can be represented as $\bar{\eta}_1 = RT/zF$. The ratio between oxygen concentration at the CCL-PEM interface and CCL-GDL interface can be expressed as a function of mass transport resistance in the time domain and charge transfer resistance by considering $\bar{\eta}_1 = RT/zF$ and rearranging Eq. 9.5 as such:

$$\frac{c'_O}{c^*_O} = \left[\frac{R_C - R_M}{R_C} \right]^{-1} \quad (9.6)$$

where R_C is the charge transfer resistance (Eq. 4.19) and R_M is defined as the mass transport resistance in the time domain such that;

$$R_M = \frac{8R_W}{\pi^2} \exp\left(-\frac{\pi^2 D}{4\delta^2} t\right) \quad (9.7)$$

and R_W is defined as resistance for the diffusion process and is defined in Eq. 5.16.

In fuel cell theory the overpotential represented in a polarisation curve is expressed through the relation $E = E_o - \eta$, where E is the potential far from equilibrium (fuel cell voltage), E_o is the potential in equilibrium (open circuit voltage) and η represents the overpotential (activation, ohmic or mass transport) in the fuel cell. In section 2.2.4 the solution of the mass transport overpotential (Eq. 2.30) resulted in a negative sign. Therefore the equation of the mass transport overpotential was changed in sign (Eq. 2.31) to comply with the relation $E = E_o - \eta$ for polarisation curves. This change in sign in the mass transport overpotential equation has also been reported in the literature [16]. A change in the sign in mass transport resistance R_M in Eq. 9.6 has to be considered to comply with the theory of fuel cell mass transport overpotential, as such:

$$\frac{c_O}{c_O^*} = \frac{R_C}{R_C + R_M} \quad (9.8)$$

Substituting Eq. 9.8 into Eq. 9.3 yields:

$$\frac{d\bar{j}}{dx} = \frac{\bar{\eta}}{R_C + R_M} + C_{dl} \frac{d\bar{\eta}}{dt} \quad (9.9)$$

Substituting Eq. 9.9 into the electrolyte network $d\bar{\eta}/dx = \bar{j}R_p$ and neglecting the potential of the electrode, as discussed previously in section 4.1.2 Chapter 4, and considering η_{SS} in R_C as a constant due to $R_p/R_C \ll 1$ [17], as shown in Appendix B.3, yields:

$$\frac{d^2\bar{j}}{dx^2} = \frac{R_p\bar{j}}{R_C + R_M} + R_p C_{dl} \frac{d\bar{j}}{dt} \quad (9.10)$$

Eq. 9.10 represents the current distribution in the CCL in time domain and can be applied for any zone of the polarisation curve (low, mid, high current) and can be solved using mathematical software [18]. For the specific case where R_M is considered to be negligible either due to a high diffusion coefficient or high bulk oxygen concentration, Eq. 9.10 will represent the current distribution in the CCL with equilibrium boundary conditions in terms of oxygen concentration. These conditions can occur for low current operation and as such, Eq. 9.10 reduces to Eq. 9.1 for low current characterisation.

After validating the impedance spectrum of the CCL as shown in Chapter 5, it is possible to extend the application of the theoretical model by applying Eq. 9.10 to directly reveal the current distribution in the CCL for a PEFC operated at a high current. The data reported in the literature as shown in Tab. 5.1 Chapter 5 of a hydrogen-air PEFC operated at 700mA/cm² and 60°C have been used for the following analysis. Fig. 9.5 shows the simulated current distribution of the CCL in the time domain across the CCL, where $x=0$ represents the GDL-CCL interface and $x=1$ represents the PEM-CCL interface.

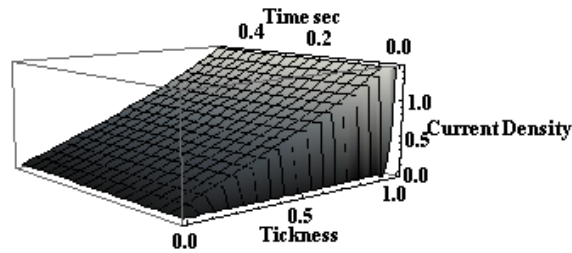


Figure 9.5 Simulated current distribution of the CCL in the time domain

In section 9.1, it was demonstrated that ionic resistance and capacitance can affect the transitory response of the CCL in the order of milliseconds and that only the ionic resistance has an effect on the steady state low current distribution. For this study, the effect of oxygen transport on the spatio-temporal current distribution of the CCL is considered. The effective diffusion coefficient $1.11 \times 10^{-4} \text{ cm}^2/\text{s}$ and the bulk concentration $4.2975 \times 10^{-6} \text{ mol}/\text{cm}^3$ of the oxygen were calculated from the parameters reported in Tab. 5.1, Chapter 5. Fig. 9.6 focuses on the transitory response of the current in CCL at three locations, $x=0.1$, $x=0.4$, and $x=0.7$ of CCL thickness fraction (dimensionless) through the thickness of the CCL. Figure 9.6a shows an initial transitory response in the current distribution due to the ionic resistance and the capacitance for all three locations up to 4 ms. This response is related to the interfacial area between the electrode and electrolyte networks and has been discussed in section 9.1. Figure 9.6b shows the response up to 0.25 s; the results show a decrease in current in the order of 10^{-1} s due to the non-stationary oxygen diffusion process in the CCL, and that the transitory effect is most noticeable closest to the PEM boundary.

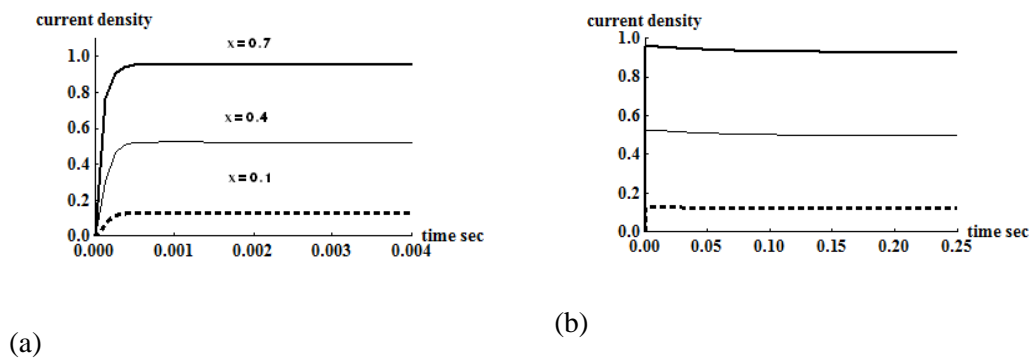


Figure 9.6 Simulated transitory current distribution through the CCL

Fig. 9.7 shows the oxygen concentration distribution through the CCL in a similar manner to the preceding sub-section. The concentration distribution is calculated using Eqs. 9.5, 9.10 and mathematical software [18]. Fig. 9.7a shows an initial depletion of oxygen concentration through the CCL, most severely closest to the PEM. This occurs due to the rapid reduction of oxygen as current is quickly established in the CCL as shown in Fig. 9.6a and process takes place in the order of 10 ms. Thereafter, the oxygen concentration recovers to the bulk concentration value throughout the CCL at steady-state, which occurs in the order of 1 s, as shown in Fig. 9.7b. Overall, therefore, Figs. 9.6 and 9.7 demonstrate that the increase in current density for the three cases is proportional to the decrease in oxygen concentration in the CCL.

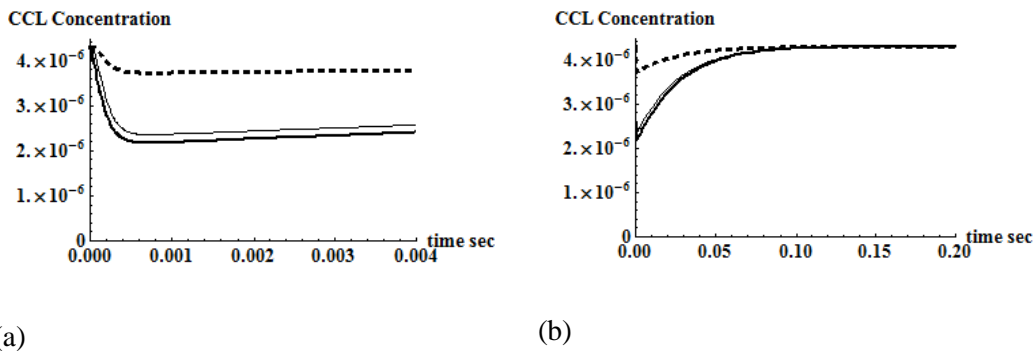


Figure 9.7 Simulated oxygen concentration distribution through the CCL

9.2.1 Effect of Oxygen Diffusion Coefficient and Oxygen Bulk Concentration on CCL High Current Distribution

It is possible to generate a broader understanding of the influence that the effective diffusion coefficient of oxygen in the CCL and the bulk oxygen concentration at the GDL boundary can have on the performance of the CCL. This therefore elucidates the effect of the mass transport resistance R_M on CCL performance. The effective diffusion coefficients depend in part upon the nature of the tortuous porous pathways in the CCL while the bulk oxygen concentration can depend upon the conditions of the reactant supply to the cell and the physical properties of adjacent porous transport layers such as the GDL and microporous layer (MPL). This part of the analysis considers the effect of

individually increasing the values of effective diffusion coefficient $1.11 \times 10^{-4} \text{ cm}^2/\text{s}$ and bulk concentration $4.2975 \times 10^{-6} \text{ mol/cm}^3$ as determined in Section 9.2 by one order of magnitude for effective diffusion coefficient and 500 % for bulk concentration. These values were chosen because the effective diffusion can change significantly when changing the operating conditions (flooding, drying), contact pressure in the MEA assembly, CCL structure (porosity, tortuosity), while the bulk concentration can change when increasing or reducing the operational gas pressure. Since the ORR occurs to a higher degree closest to the PEM as indicated by Fig. 9.6, the analysis is carried out at a thickness fraction of 0.7. Fig. 9.8 focuses on the effect of diffusion coefficient on oxygen concentration distribution in the CCL. Figure 9.8a shows the initial fall in concentration to support the current drawn, while Fig. 9.8b shows the time to steady-state. A higher diffusion coefficient reduces the time required for the oxygen concentration within the CCL to recover such that it is in equilibrium with the bulk oxygen concentration at the GDL boundary.

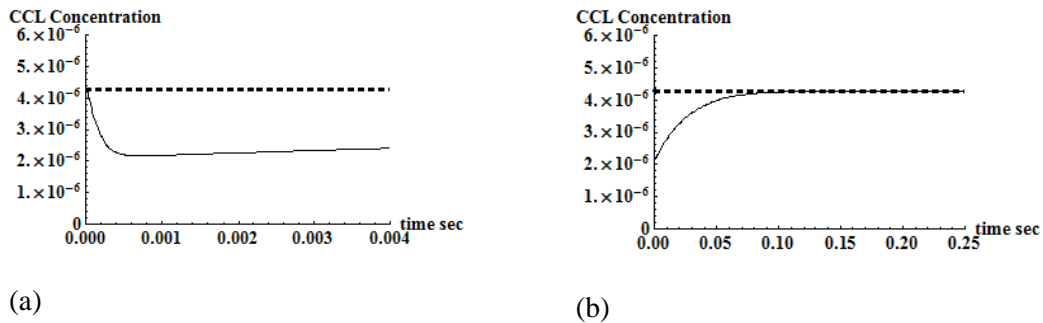


Figure 9.8 Effect of diffusion coefficient on the transient oxygen concentration distribution in the CCL, dashed increasing by one order of magnitude, thin represents the original value.

Fig. 9.9 shows the effect of diffusion coefficient on the transitory current density distribution in the CCL. Fig. 9.9a shows while the diffusion coefficient does not have a significant effect on the initial response, which is governed by C_{dl} and R_p , it does affect the maximum current achieved and as shown in Fig. 9.9b the time to steady-state. By increasing the diffusion coefficient, the maximum current decreases because the oxygen consumed at CCL surface to support the current drawn is quickly replenished by the high

diffusion and the time to steady-state decreases as the oxygen concentration quickly recovers to its bulk concentration value at GDL interface. The maximum current achieved represented in Fig. 9.9a reflects the rate at which oxygen can be brought to the electrode surface for a given set of mass-transfer conditions. A higher diffusion coefficient reduces R_M and approaches the current response at the equilibrium conditions.

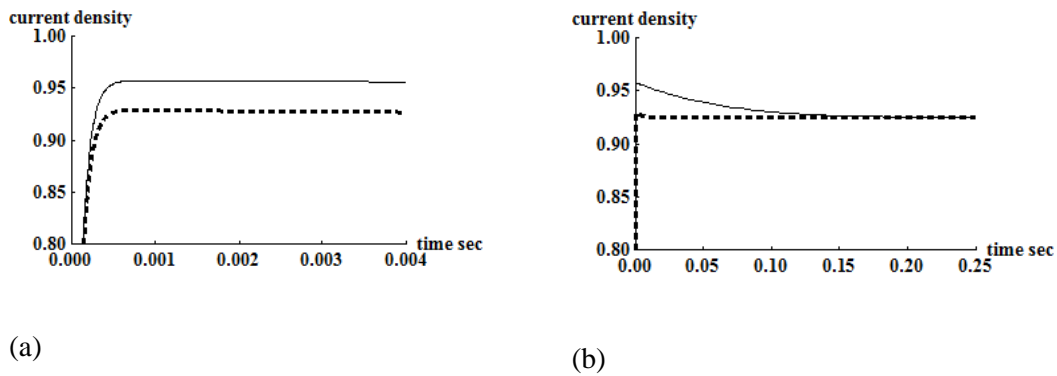


Figure 9.9 Effect of diffusion coefficient on the transient current density distribution in the CCL, dashed increasing by one order of magnitude, thin represents the original value.

The simulations in Figs. 9.10a and 9.10b show the time required for the oxygen concentration in the CCL to recover to the equilibrium within the bulk concentration at the GDL interface. The recovery occurs over the same order of magnitude in time for the two cases, and faster when increasing the bulk concentration.

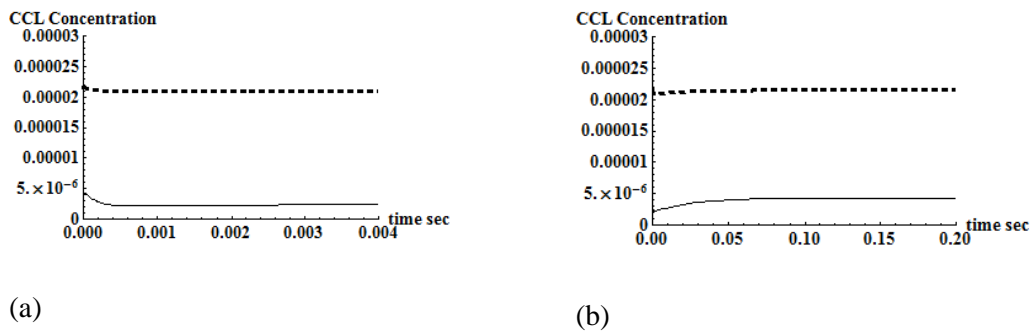
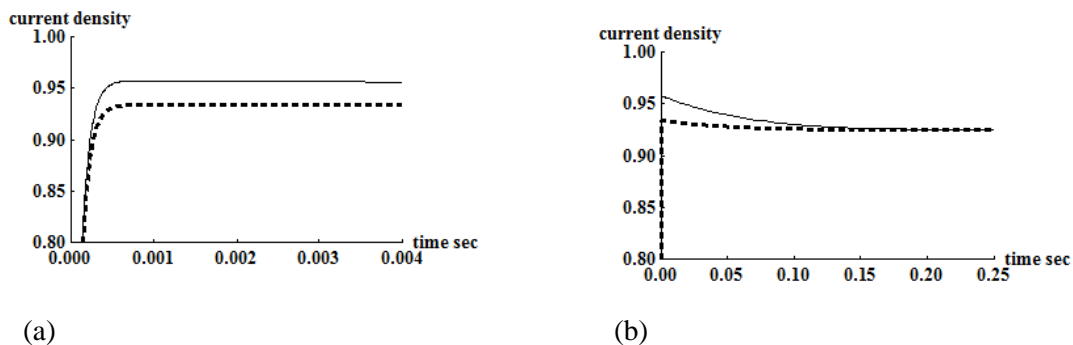


Figure 9.10 Effect of bulk oxygen concentration on the transient concentration distribution in the CCL; (a) initial response; (b) response to steady-state, dashed increasing 500 %, thin represents the original value

Fig. 9.11 considers the effect of bulk concentration on CCL performance; Fig. 9.11a demonstrates, as expected, when increasing bulk concentration there is a decrease in the maximum current and the transitory response of the current but over the same order of magnitude in time. The same applies to the response to steady-state shown in Fig. 9.11b compared to Fig. 9.9b, therefore indicating that the change in current to steady-state is more sensitive to a change of oxygen diffusion than bulk oxygen concentration.



(a) (b)
Figure 9.11 Effect of bulk oxygen concentration on the transient current density distribution in the CCL; (a) initial response; (b) response to steady-state, dashed increasing 500 %, thin represents the original value

9.2.2 CCL performance at Different Current Density Operation

The parameters from Tab. 7.1 reported in Chapter 7 at current densities of 0.12, 0.2 and 0.32 A/cm² were applied to Eq. 9.10 to simulate the current distribution through the CCL thickness. The current distribution through the CCL thickness occurs in a transitory manner due to the nonstationary oxygen diffusion process in the CCL, as discussed in section 9.2. The maximum current distribution in the CCL which reflects the maximum depletion of oxygen through the CCL and is a function of the ionic resistance, charge transfer resistance and mass transport resistance is considered. This point of the transitory current distribution was chosen as it reflects the polarisation curve with the three overpotentials (activation, ohmic, concentration). The ideal operating point of the current distribution would be where mass transport effect is negligible; however, this effect depends on the oxygen equilibrium concentration and diffusion constant, parameters which can be influenced by operation and preparation of the fuel cell. The equation for

the current distribution in Eq. 9.10 is defined by the ratio of the ionic resistance to the sum of the charge transfer resistance and the mass transport resistance in the time domain. Neyerling *et al.* [11] defined a similar relationship in the absence of the mass transport resistance, where the higher the non-dimensional ratio is, the more the current distribution will be skewed toward the membrane interface, while low values of this ratio predict a homogeneous current distribution. The ionic resistance, charge transfer resistance and mass transport resistance in the CCL can change for different operating conditions. In this study, if the ratio between ionic resistance and the sum of both the charge transfer resistance and mass transport resistance is increased, the ions may react only closer to the membrane. However, in the case when the ratio is reduced, the ions will react through the entire CCL thickness leading to a uniform current distribution.

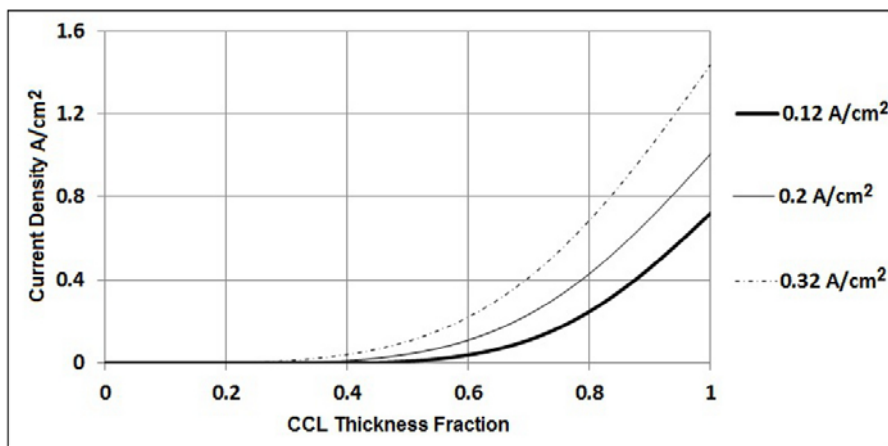


Figure 9.12 Simulated current distribution through the CCL thickness using parameters from table 7.1, Chapter 7.

The current distribution (area below the curve) through the CCL increases from the $x=0$ thickness fraction (GDL-CCL interface) to the $x=1$ thickness fraction (CCL-PEM interface), as shown in Fig. 9.12. This reflects the transfer of ions from the PEM and the anode catalyst layer, which results in a high value of current at the interface between the CCL and the PEM and a minimum current at the interface between the CCL and GDL as ions are consumed due to the ORR through the thickness of the CCL. A high ionic resistance within the CCL electrolyte tends to skew the current distribution towards the membrane interface, (0.12 A/cm^2). Therefore the same average current has to be provided

by fewer catalyst sites near the membrane. The increase in ionic resistance results in greater activation losses. Fig. 9.12 shows that the current density of 0.12 A/cm^2 is generated from $x=0.449$ to $x=1$, for 0.2 A/cm^2 is generated from $x=0.3265$ to $x=1$, and for 0.32 A/cm^2 from $x=0.2245$ to $x=1$ CCL thickness fraction. Therefore at high current densities there is an increase in the utilization of the catalytic particles through the CCL thickness because the ORR current distribution follows Tafel kinetics. This is also supported by the decrease in charge transfer resistance from Tab. 7.1, Chapter 7 when increasing current density. The ORR current distribution is further influenced by the mass transport resistance of oxygen reactant diffusion into the CCL. Tajiri *et al.* [19] studied the phenomenon of gas phase diffusion of oxygen at subfreezing conditions, and they concluded that the current distribution was dominated by the gas transport effect without estimating voltage losses in the CCL. Thompson *et al.* [1] studied the current distribution through the CCL without considering mass transport resistance of oxygen at sub-zero conditions of -20°C . This author concluded that the mass transport effect would skew the current distribution toward the diffusion medium interface (CCL-GDL). Overall, in Fig. 9.12 it is noticeable that the increase of mass transport resistance from Tab. 7.1 tends to skew the ORR current distribution towards the GDL interface. These valuable impedance-based results of ORR current distribution will help to develop cold-start models that include the physics of membrane uptake of product water and filling of electrode pores with water (ice) [20].

9.3 Discussion

Fundamentally, double layer capacitance and ionic resistance can be related to the electrode-electrolyte networks in the CL. The capacitance effect is induced by the build-up of charge between the electrode and electrolytic networks. If the interfacial area between the networks increases, the area between which the charge capacitance occurs will increase correspondingly. Therefore, while an increase in the interfacial area may assist in enhancing the utilisation of the full thickness of the CL, the increase in charge capacitance will have a slight retardation effect on its dynamic response, in the order of milliseconds at low currents (around 20 mA/cm^2). Initially the CCL at open circuit potential has an accumulated charge (capacitance), as the reaction takes place, water

produced increases the solution interface available and consequently the capacitance. This also enhances ionic conductivity.

The ionic resistance is directly affected by the uptake of water through the electrolytic network. This effect can be presented in the anode side by electrosmotic drag or in the cathode side by using a high flow rate for gas without no humidification. Nevertheless using a dead-end fuel cell configuration, the ionic resistance seems not to be affected due to the high water concentration present in the CCL. In the current work, while the ionic resistance is investigated independently of water transport, the results clearly demonstrate that high ionic resistance (as a result of a poor nafion distribution or due to a dehydration) in the CCL will limit the current distribution in the CCL and can also have a slight retardation effect on its dynamic response, again in the order of milliseconds. Since high ionic resistance inevitably reduces the rate of charge transfer for a given potential by Ohms law, it is evident that it will take longer for the charge to build up between the electrode-electrolyte interface than if the same potential was established with a lower ionic resistance and the rate of charge transfer was correspondingly greater. Therefore, the time to steady-state can be improved if the electrical charge is allowed to build up between the interface over a short space of time for a given potential, this can be achieved if the ionic resistance is minimised.

It is arguable that because the time to steady-state at low current is in the order of milliseconds, ionic resistance and charge capacitance may have a limited impact on the transient performance of the CCL. In terms of current distribution, however, it is evident from Figs. 9.3 and 9.4 that the ionic resistance has a significant effect on the utilisation of the CL and the total current in the CCL at the low current conditions currently simulated. The simulations suggest that by reducing the measured ionic resistance by 50% for the 60°C case, the total current in the CCL is increased by 15% and that current is generated over the full thickness of the CCL as opposed to the 83% of the CCL closest to the PEM. When the ionic resistance is increased by 50%, the total current in the CCL is reduced by 17% and current is generated over only 55% of the thickness of the CCL closest to the PEM.

The results give us an insight about how difficult the optimal design of the CCL can be. For one part, an excess amount of Nafion seems to improve the ion conductivity and the steady current distribution along the CCL but this may lead to mass transport limitations for oxygen. Furthermore the increase in nafion will create more interfacial area between the dissimilar materials, and as a consequence it will take more time for the charge to build up, and a retardation in the current distribution to achieve its steady state. The design of CLs requires further attention, as seems that improving one feature will worsen another one, for instance low ionic resistance will lead to high capacitance.

The utilisation of the CCL improves at higher loads due to the increase in the rate of charge transfer. The most important feature of the experimental and theoretical framework that has been developed, verified and applied in this study is that it clearly demonstrates the capability to elucidate the effects of charge capacitance and ionic resistance on cell performance.

The effective diffusion coefficient is related to the structure of the CL, which typically features a porosity of approximately 5-15% and pore diameters of roughly $1\mu\text{m}$ [21]. The void space in the CCL can be reduced during operation due to the accumulation of product water or through design by increasing the amount of ionic-conducting electrolyte impregnated within the CCL. Under these conditions, the effective diffusion coefficient can reduce correspondingly. This reduction affects the ability of oxygen to permeate into the CCL to the active sites and to recover to the bulk concentration. By maintaining the void space through design and operation, the corresponding increasing in effective diffusion coefficient can lead to diminished mass transport resistance. The bulk concentration of oxygen is largely dependant upon the operating conditions of the cell, particularly the reactant supply conditions. With a high bulk oxygen concentration, the availability of oxygen for the ORR inherently increases.

The simulations show that the concentration distribution of oxygen through the CCL occurs in a non-steady manner and recovers to the bulk concentration supplied in the GDL. The current distribution in the CCL achieves an initial maximum current as a function of the ionic resistance, charge transfer resistance and mass transport resistance,

as shown in Fig. 9.6 under potentiostatic conditions. After steady-state is established in the order of one second, the magnitude of the steady-state current depends only on the ionic resistance and charge transfer resistance. By increasing the effective diffusion coefficient and the bulk concentration the initial maximum current and the time to steady state decrease as shown in Figs. 9.9 and 9.11. Overall, therefore, the time to reach equilibrium with respect to oxygen concentration is minimised when the PEFC is operated at low currents, or by increasing the effective diffusion coefficient or the bulk concentration.

The results provide an insight about the effect of the effective diffusion and bulk concentration on the spatiotemporal distribution of the current for the CCL. The mathematical treatment developed in this study can be applied for the different zones of the polarisation curve and has demonstrated the capability of solving the spatiotemporal current distribution of the CCL based on the fundamental electrode theory and the measured frequency response of the PEFC.

The results of current distribution obtained can give an insight about the physics of product water uptake in the membrane and formation of ice in the CCL during subfreezing operation.

9.4 Conclusions

This study has demonstrated that it is possible to estimate the current density and oxygen concentration distributions in the CCL by coupling the fundamental electrochemistry and diffusion theory of the CCL to the experimental impedance technique. The theoretical formulation at low current reveals the spatial and temporal distributions of current in the CCL for the three conditions investigated for model validation. The results confirmed that by increasing the operating temperature, it is possible to marginally improve the current distribution through the CCL and the time to steady-state.

As a further extension to this investigation, the effect of double-layer capacitance and ionic resistance in the CCL were considered separately. With all other parameters

unchanged, a decrease in double-layer capacitance demonstrated a reduction in the time to steady-state, while a greater capacitance yielded an increase. The steady-state current distribution was largely unaffected by the double-layer capacitance. An increase in the ionic resistance resulted in a poorer current distribution across the CCL and a longer time to steady state. It is argued that the double layer capacitance is in part controlled by the total interfacial area between ion and electron-conducting networks in the CCL. By increasing the interfacial area in the CCL, the double-layer capacitance may also increase, thereby prolonging the time to steady-state. By increasing the ionic resistance in the CCL, the rate of charge transfer is reduced for a given potential which increases the time it takes for electrical charge to build up between the electrode-electrolyte interface.

The simulations in the time domain at high current showed that there is an initial dynamic response in the order of milliseconds due to the interfacial area between the electrode-electrolyte until a maximum current is achieved which is a function of the ionic resistance, charge transfer resistance and mass transport resistance. This maximum current decreases until steady-state is established in the order of one second. The steady-state current is a function of the ionic resistance and charge transfer resistance but not the mass transport resistance. The concentration distribution of oxygen was also simulated and the results revealed that the oxygen concentration consumed to support the current demand recovered to equilibrate with the bulk concentration GDL boundary in the order of 1 second. A further investigation on the effect of the effective diffusion coefficient and bulk concentration was considered by increasing the effective diffusion and bulk concentration by one order of magnitude and 500 % respectively. These increases resulted in the reduction of the initial maximum current and the time to steady state and were more noticeable for the effective diffusion coefficient. These results suggest that by increasing diffusion coefficient, it is possible to establish an equilibrium between the oxygen concentration in the CCL and the bulk of oxygen concentration supplied from the GDL and therefore to reduce the effect of the mass transport resistance in the current distribution of the CCL. The results also showed that at high current densities (low ionic resistance, high mass transport resistance) the ORR current distribution which follows Tafel kinetics is skewed towards the CCL-GDL interface improving the catalyst utilization through the CCL thickness. This newly established EIS knowledge will enable

an assessment of the state-of-health of operational fuel cells and enhance cell development in terms of physical changes within fuel cell materials and the critical operational factors through non-intrusive diagnostics.

9.5 References

- [1] Thompson E. L., Jorne J., Gu W., and Gasteiger H. A., "PEM Fuel Cell Operation at -20°C . II. Ice Formation Dynamics, Current Distribution, and Voltage Losses within Electrodes", *J. Electrochem. Soc.*, 155, (2008), pp. B887-B896.
- [2] Brown C. J., Pletcher D., Walsh F. C., Hammond J. K., and Robinson D., "Local Mass Transport Effects in the FMO1 Laboratory Electrolyser", *J. Appl. Electrochem.*, 22, (1992), pp. 613-619.
- [3] Cleghorn S. J. C., Derouin C. R., Wilson M. S., and Gottesfeld S., "A printed Circuit Board Approach to Measuring Current Distribution in a Fuel Cell", *J. Appl. Electrochem.*, 28, (1998), pp. 663-672.
- [4] Stumper J., Campbell S. A., Wilkinson D. P., Johnson M. C., and Davis M., "In-situ Methods for the Determination of Current Distributions in PEM Fuel Cells", *Electrochim. Acta*, 43, (1998), pp. 3773-3783.
- [5] Yang X. G., Burke N., Wang C. Y., Tajiri K., and Shinohara K., "Simultaneous Measurements of Species and Current Distributions in a PEFC under Low-Humidity Operation", *J. Electrochem. Soc.*, 152, (2005), pp. A759-A766.
- [6] Noponen M., Mennola T., Mikkola M., Hottinen T., and Lund P., "Measurement of Current Distribution in a Free-Breathing PEMFC", *J. Power Sources*, 106, (2002), pp. 304-312.
- [7] Mench M.M., Wang C. Y., and Ishikawa M., "In Situ Current Distribution Measurements in Polymer Electrolyte Fuel Cells", *J. Electrochem. Soc.*, 150, (2003), pp. A1052-A1059.
- [8] Mench M. M. and Wang C. Y., "An In Situ Method for Determination of Current Distribution in PEM Fuel Cells Applied to a Direct Methanol Fuel Cell", *J. Electrochem. Soc.*, 150, (2003), pp. A79-A85.
- [9] Mench M. M., Dong Q. L. and Wang C. Y., "In Situ Water Distribution Measurements in a Polymer Electrolyte Fuel Cell", *J. Power Sources*, 124, (2003), pp. 90-98.
- [10] Schneider I. A., Kuhn H., Wokaun A., and Scherer G. G., "Fast Locally Resolved Electrochemical Impedance Spectroscopy in Polymer Electrolyte Fuel Cells", *J. Electrochem. Soc.*, 152, (2005), pp. A2092-A2103.
- [11] Neyerlin K. C., Gu W., Jorne J., Clark A. Jr., and Gasteiger H. A., "Cathode Catalyst Utilization for the ORR in a PEMFC Analytical Model and Experimental Validation", *J. Electrochem. Soc.*, 154, (2007), pp. B279-B287.
- [12] Liu J. and Eikerling M., "Model of Cathode Catalyst Layers for Polymer Electrolyte Fuel Cells: The Role of Porous Structure and Water Accumulation", *Electrochim. Acta*, 53, (2008), pp. 4435-4446.
- [13] <http://www.mathworks.com/access/helpdesk/help/techdoc/ref/pdeval.html>, last accessed Jan 2010.
- [14] Lokenath D., Dambaru B., Integral Transforms and Their Applications, Chapman, New York (2007)
- [15] Bard A. J. and Faulkner L. R., Electrochemical Methods, John Wiley & Sons, Inc., New York, (2001).
- [16] Larminie J., Dicks A., Fuel Cell System Explained; Wiley, England (2003).
- [17] Makharia R., Mathias M. F. and Baker D. R., "Measurement of Catalyst Layer Electrolyte Resistance in PEFCs Using Electrochemical Impedance Spectroscopy", *J. Electrochem. Soc.*, 152, (2005), pp. A970-A977.
- [18] Wolfram Mathematica 7, <http://www.wolfram.com/products/mathematica/index.html>, last accessed May. 2010
- [19] Tajiri K., Tabuchi Y., Wang C.-Y., "Isothermal Cold Start of Polymer Electrolyte Fuel Cells", *J. Electrochem. Soc.*, 154, (2007), pp. B147-B152.
- [20] Lin G., He W. and Nguyen T. V., "Modeling Liquid Water Effects in the Gas Diffusion and Catalyst Layers of the Cathode of a PEM Fuel Cell", *J. Electrochem. Soc.*, 151, (2004), pp. A1999-A2006.
- [21] B. Sundén and M. Faghri, Transport Phenomena in Fuel Cells, WITPress, Southampton, UK (2005).

Chapter 10

Conclusions and Future Work

The aim of this doctoral thesis was to establish a backbone understanding of how the electrochemical and diffusion mechanisms relate to the electrochemical impedance spectra of polymer electrolyte fuel cells (PEFCs). A mathematical model based on the electrochemical and diffusion theories was developed to simulate the impedance response of the cathode catalyst layer (CCL) operated at low and high currents.

The theoretical treatment developed in the frequency domain was applied to electrochemical impedance spectroscopy (EIS) measurements in a single PEFC and a PEFC stack. The EIS results in a single PEFC demonstrated that the mathematical model can interpret and separate the electrochemical and diffusion mechanisms represented at different frequencies of the impedance complex plot. Simultaneous EIS measurements and the use of the impedance model have demonstrated that the factors that limit the performance in the PEFC stack can be assessed by relating the experimental EIS technique with the fundamental theory of PEFCs.

The mathematical model translated into the time domain allowed the interpretation of the spatio-temporal current distribution through the CCL.

10.1 Conclusions

The overall scientific contribution of this doctoral thesis was divided in two major sections: Modelling and Application.

10.1.1 Modelling

CCL Impedance Model

- The modelling work carried out in this thesis began in Chapter 4 with the development of a mathematical model to simulate the frequency response of the CCL at low currents considering that oxygen transport limitations are negligible.
- The theoretical treatment considered the following mechanisms: flux of chemical (reduced and oxidized) species, Arrhenius equation, exchange current under equilibrium conditions, potential between electrode-electrolyte interface, capacitance effect between dissimilar materials and ionic resistance in the CCL electrolyte. The theoretical treatment considered the following main assumptions: all processes proceed under isobaric and isothermal conditions, spatial gradients were only considered through the thickness of the CCL, the resistance to ion transfer in the electrolyte of CCL is much greater than the resistance to the electron transfer in the carbon of the catalyst layer. Therefore electronic ohmic loss in CCL was regarded as being negligible. The low current model was validated with EIS measurements in the frequency domain.
- In Chapter 5 the model which simulated the impedance response of the CCL at low currents was modified to include the change of oxygen concentration during the oxygen reduction reaction (ORR) in the frequency domain. The resulting model allowed the simulation of the CCL impedance response at high currents.
- The change in oxygen concentration in the CCL was estimated from the general theory of experimental controlled-currents methods which combines Fick's Law and Faraday's Law equations. The finite diffusion distance of oxygen transport was considered to be independent from the CCL thickness. This simplified the mathematical analysis and allowed the derivation of the Warburg impedance to reproduce the low frequency semicircle of EIS measurements in PEFCs. The mathematical treatment was successfully validated against EIS measurements reported in the literature.

10.1.2 Application

Inductive Effect on the Fuel Cell Cathode Impedance Spectrum at High Frequencies

- Chapter 6 demonstrated that the inductive effect of the electrical cables of the measurement system deforms the high frequency region of the cathode impedance spectrum and as such led to an erroneous interpretation of the electrochemical mechanisms in the CCL. The analysis of the inductive effect was divided into a theoretical analysis and an experimental analysis.
- In the theoretical analysis the impedance model developed in Chapter 5 that accounts for the impedance spectrum of the CCL was applied with experimental impedance data reported in the literature. The results showed that the ionic resistance of the CCL electrolyte which skews the ORR current distribution towards the membrane interface is masked in the CCL impedance spectrum by the inductive component.
- In the experimental analysis cathode experimental impedance spectra were obtained through a three-electrode configuration in the measurement system and with two different electrical cables connected between the Electronic Load and the PEFC. The results agreed with the theoretical analysis and also showed that the property of causality in the Kramers-Kronig (K-K) mathematical relations for EIS measurements is violated by the external inductance of the measurement cables. Therefore the experimental data presenting inductance at high frequencies do not represent the physics and chemistry of the PEFC.
- A further validation of the inductive effect was carried out by comparing the mathematical model derived in Chapter 5 with cathode experimental impedance data obtained with a three-electrode configuration and the use of conventional electrical cables (power flexible cable) and special low inductive cables (Low inductive cable with fusion Lug Technology, TDI POWER).
- This study demonstrates that the mathematical model derived in Chapter 5 can be applied reliably in order to correctly estimate the inductance effect and the electrochemical mechanisms of the CCL at high frequencies of the complex-plot.
- This study has demonstrated that the practice of using the real part Z' of the complex plot where the imaginary part Z'' is equal to zero or through a single

frequency as a reference to quantify the ohmic resistance in a PEFC can be subject to an erroneous interpretation due to the contribution of the size of the inductance.

- If there were a constant inductance in the electrical cables for every system when carrying out EIS measurements, the Ohmic resistance could be expressed where the real part Z' intercepts the real axes at high frequencies. Nevertheless, the inductance would mask the ionic resistance in the CCL represented in the Nyquist plot as discussed in Chapter 6.

Low Frequency Electrochemical Mechanisms in the Fuel Cell Cathode Impedance Spectrum

- In Chapter 7, EIS measurements that account for the cathodic side of a PEFC were compared with the simulated data obtained through the impedance model developed in Chapter 5.
- The use of a reference electrode in the measurement system ensured that the data accounting for the processes in the cathode were captured for analysis and interpretation. A comparison in the complex plot and bode format between measured EIS data at three different current densities and simulated data from the impedance model was carried out to account for the exact electrode process in the CCL EIS measurements.
- The model was applied to EIS measurements and allowed the estimation of the ionic resistance of the CCL electrolyte, charge transfer resistance of the ORR and mass transport resistance due to oxygen transport limitations in the CCL.
- The ionic resistance in the CCL decreased with increasing current density. This effect was attributed to the water produced during the ORR and the water transported from anode to cathode by electro-osmotic drag.
- The charge transfer resistance, whose dependence on electrode potential is given by the Tafel equation and reflects the increase in the driving force for the interfacial oxygen reduction process, decreased with increasing current density.

- The mass transport resistance, due to gaseous oxygen transport limitations and as a function of the gaseous oxygen equilibrium concentration in the CCL-gas diffusion layer (GDL) interface, increased with increasing current density.
- The semicircles that represent the charge transfer resistance and mass transport effect were overlapped in the measured EIS data. The mathematical model was able to separate the semicircles that represent charge transfer resistance and oxygen transport resistance by decreasing the magnitude of the effective diffusion coefficient for oxygen transport in the CCL.
- Low frequency EIS measurements commonly related to mass transport limitations are attributed to the low oxygen equilibrium concentration in the CCL-GDL interface and the low diffusivity of oxygen through the CCL.

Simultaneous Electrochemical Impedance Spectroscopy of Single Cells in an Open-Cathode Polymer Electrolyte Fuel Cell Stack

- In Chapter 8, the factors that limit the performance in a commercial 4-cell Open-Cathode PEFC stack were assessed using simultaneous EIS measurements and the impedance model developed in Chapter 5.
- Measured EIS data for each cell in the stack showed an inductive loop at low frequencies. The literature suggests that this effect is attributed to adsorbed intermediate species during the ORR.
- The impedance model derived in Chapter 5 which considered simple reaction kinetics in the ORR was modified to include adsorbed intermediate species which limit the performance of the PEFC stack. The comparison between measured data and simulated data from the model showed a good agreement.
- The results showed that there is a decrease of adsorbed species coverage in the CCL with increasing current density due to the reaction of the adsorbed species during the ORR. It could not be concluded what adsorbed intermediate species are interfering with the ORR and limiting the PEFC stack performance. Further experiments to account for the exact intermediate species have to be carried out.
- The charge transfer resistance, whose dependence on electrode potential is given by the Tafel equation and reflects the increase in the driving force during the

ORR, remained constant for three cells at the same current density. One of the cells in the stack showed a higher charge transfer resistance than the rest of the cells. This effect can be attributed to low electrocatalytic activity in the cell. A faulty membrane electrode assembly (MEA) at that particular cell could be a factor responsible for that behaviour.

- Oxygen transport limitations in this particular stack were attributed to variations in flow of the air through the open cathodes in the stack. In this study simultaneous EIS measurements have demonstrated that inhomogeneity of air flow rate in an Open-Cathode PEFC stack not only leads to an increase in ohmic resistance but also leads to an increase in oxygen transport limitations in the cells.
- The low air flow rate through the cells cannot expel excessive reaction generated heat which in turn leads to dehydration in the polymer electrolyte membrane (PEM), (high ohmic resistance). Ohmic resistance was found to be more sensitive than the charge transfer resistance to the temperature distribution through the stack.
- Chapter 8 has demonstrated that simultaneous EIS measurements combined with the theoretical analysis from Chapter 5 are a powerful tool for in-situ diagnosis of a PEFC stack.

CCL Current Distribution

- In the time domain the model revealed the spatial and temporal current distribution through the CCL. This provided a valuable insight into the actual performance of the CCL in terms of charge capacitance and ionic resistance.
- The capacitance effect in the CCL is induced by the buildup of charge between the electrode and electrolyte networks. If the interfacial area between the networks increases, the area between which the charge capacitance occurs increases correspondingly. The increase in charge capacitance has a slight retardation effect on the current dynamic response.
- The ionic resistance is directly affected by the uptake of water through the CCL electrolyte network. High ionic resistance in the CCL limits the current

distribution in the CCL and can also have a slight retardation effect on its dynamic response.

- The results gave us an important insight into the balance that has to be achieved between the ionic resistance and charge capacitance in the CCL, which both are related to the structure and composition of the CCL.
- Once validated in the frequency domain at high currents, the model was translated into the time domain by an Inverse Laplace method. In the time domain the model revealed the spatiotemporal current distribution and oxygen concentration along the thickness of the CCL.
- The results showed that the concentration distribution of oxygen through the CCL occurs in a nonsteady manner and recovers to the bulk concentration supplied in the GDL-CCL interface. This recovery of oxygen concentration to the equilibrium oxygen concentration will depend on CCL structure (porosity, tortuosity), the water removal characteristics of the adjacent porous layers (GDL, MPL), cell operating conditions, and contact pressure in the MEA.
- The simulations in the time domain showed that there is an initial dynamic response due to the interfacial area between the electrode-electrolyte, until a maximum current is achieved which is a function of the ionic resistance, charge transfer resistance, and mass transport resistance. This maximum current decreases in a transitory manner until a steady-state is established. The steady-state current is a function of the ionic resistance and charge transfer resistance but not the mass transport resistance.
- The effect of the effective diffusion coefficient and bulk concentration was considered in the current distribution. The increase in bulk concentration and diffusion coefficient resulted in the reduction of the maximum current and time to steady-state and the effect was more noticeable for the effective diffusion coefficient. It is possible to establish an equilibrium between oxygen concentration in the CCL surface and the bulk concentration supplied from the GDL and therefore to reduce the effect of mass transport resistance in the current distribution of the CCL.
- An analysis of the current distribution in a PEFC operated at three different current densities was also carried out. The results showed that high ionic

resistance within the CCL electrolyte skewed the current distribution towards the membrane interface. Therefore the current density has to be maintained by few catalyst sites near the membrane. High ionic resistance resulted in poor catalyst utilization through the CCL thickness.

10.2 Future Work

The fuel cell industry requires a fast-performing, non-intrusive and affordable diagnostics system based on frequency response tests which can determine degradation in the MEA, impurities in fuel and air, flooding and dehydration effects. The mathematical model developed in this doctoral thesis is capable of interoperating variations in PEFC impedance characteristics at different current densities. This new EIS understanding could be a powerful tool for in-situ diagnosis of a PEFC in terms of electrochemistry and degradation mechanisms. Three main tasks have to be considered to develop an in-field diagnosis system of a PEFC stack based on EIS measurements.

1. Development of software (MATLAB) based on complex non-linear regression method. The mathematical model developed in this doctoral thesis can be fitted to the frequency response of a PEFC using a complex nonlinear regression method e.g. Levenberg-Marquardt, Gauss-Newton and the resulting quality of the fit can be characterised by both chi-squared and weighted sum of square values [1]. However the model could become more complex by including other effects that affect the PEFC performance such as contaminants in the catalyst layer (CL). This would increase the number of parameters in the mathematical equation and could lead to greater errors in the fitted values. As a solution, some of the values of the parameters in the equation must be fixed during the fitting process to avoid possible errors in the values. The use of computational numerical methods such as computational fluid dynamics (CFD) and Lattice Boltzmann methods (LBM) could provide the input of some parameters (e.g. equilibrium oxygen concentration at the GDL-CCL interface) to be defined in the EIS model. Other experimental techniques such as Tafel slope can define other parameters in the EIS model (e.g. kinetic parameters during the charge transfer process). These experimental and computational methodologies could reduce the number of parameters to

be defined in the model to achieve a good agreement between the experimental and simulated data. At this point for a future application it cannot be defined the number of parameters in the model to be fixed during the fitting process and the number of rungs represented in its equivalent electrical circuit for data fitting purpose. The development of software to represent of the impedance spectrum of the PEFC at the full frequency range is one of the aims of a future work.

2. A new Frequency Response System. The frequency response tests are simple to carry out and can be easily tuned for greater accuracy by using readily-available sinusoidal generators and precise measuring equipment. However the elevate cost of commercial frequency response analysers, which increases with increasing the number of channels for a PEFC stack diagnosis, limits the development and application of EIS technology in PEFC stacks.

The recording time and the cost of a frequency response system to diagnosis a PEFC stack can be strongly reduced by selecting specific frequencies of interests. Based on the knowledge obtained in this doctoral thesis five frequencies in EIS measurements can be give an insight into the factors that limit a PEFC stack. The resulting experimental frequency response has to be consistent with K-K relations for EIS measurements.

High frequency. This region provides information about structural features in MEAs. Chapter 6 has demonstrated that if inductive effects of measurement cables are reduced which deform the high frequency region in the complex plot, a 45° straight line is apparent at high frequency end of the spectra. The magnitude and angle of the slope between two high frequency EIS values e.g. (10 kHz and 1 kHz) can provide information about the structure and composition of CLs. Interfacial contact resistance which depends on contact pressure and ionic conductivity in the PEM can be estimated through the highest frequency EIS value e.g. >10 kHz.

Medium frequency. A difference in change of charge capacitance between the electrode-electrolyte interface due to corrosion effect in MEAs of a PEFC can be estimated through an EIS value at a medium frequency, e.g. 50 Hz.

Low frequency. Mass transport effects and impurities effects can be estimated at two low frequency EIS values. In Chapter 7, it was demonstrated that the asymptotic value of EIS at low frequencies provides a qualitative value of the mass transport resistance which increases with increasing current density. The comparison between low frequency EIS values with negative imaginary components in cells of a stack can provide information about oxygen transport limitations along the stack. Chapter 8 demonstrated that EIS measurements at low frequencies with positive imaginary component are attributed to adsorbed intermediate species interfering during the ORR. EIS measurements at the lowest frequency value e.g. 0.1 Hz can provide information about non-desirable adsorbed species in the CL such as fuel impurities or air impurities which limit the life and performance in PEFC stacks.

3. In-Field Diagnosis of a PEFC Stack using a Newly Frequency Response System.

The combination of EIS model and the frequency response system will lead to a powerful tool for in-situ field diagnosis in PEFC stacks and will allow the identification of local inhomogeneities in the performance of a PEFC stack.

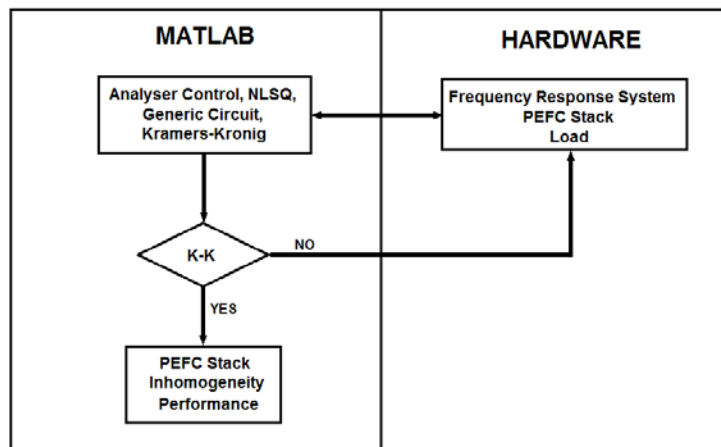


Figure 10.1 Frequency Response System Set-up

10.3 References

[1] Scribner Associates Inc., "ZView Version: 2.1b," 150E, NC 28387, USA, 1984

Appendix A (Chapter 2)

Kramers-Kronig Relations

The contour integral of the frequency domain for EIS measurements considering Cauchy's Theorem and a singularity in the right half plane is shown in Fig. A1.

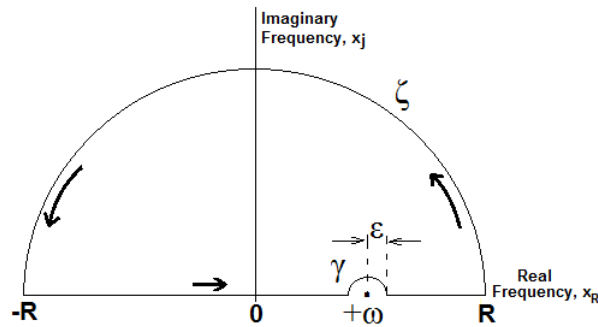


Figure A.1 Frequency domain integral contour for deriving K-K relations

Cauchy's Theorem states that if a function $Z(x)$ is analytic in a simple connected domain (in this case frequency domain), therefore the integral around the closed contour of the domain vanishes, as such:

$$\oint_C Z(x) dx = 0 \quad (\text{A.1})$$

Fig. A.1 shows that the function $Z(x)$ has a singularity on the real frequency axis x_R ; therefore in order for the function $Z(x)$ to be analytic at point ω on the boundary of the frequency domain it is necessary to apply Cauchy's Residue Theorem, as such:

$$\oint \frac{Z(x)}{x - \omega} dx = 0 \quad (\text{A.2})$$

Eq. A.2 can be expanded to define the close contour shown in Fig A.1, as:

$$\oint \frac{Z(x)}{x-\omega} dx = \int_{-\infty}^{\infty} \frac{Z(x)}{x-\omega} dx + \int_{\gamma} \frac{Z(x)}{x-\omega} dx + \int_{\zeta} \frac{Z(x)}{x-\omega} dx = 0 \quad (\text{A.3})$$

Integral around the pole ω , with $x = \omega + \varepsilon e^{j\theta}$; $dx = j\varepsilon e^{j\theta} d\theta$; $0 \leq \theta \leq \pi$

$$\int_{\gamma} \frac{Z(x)}{x-\omega} dx = \int_{\pi}^0 \frac{Z(x)}{x-\omega} dx \quad \text{therefore} \quad \int_{\pi}^0 \frac{[Z(\omega + \varepsilon e^{j\theta})]}{\omega + \varepsilon e^{j\theta} - \omega} j\varepsilon e^{j\theta} d\theta$$

$$\int_{\pi}^0 [Z(\omega + \varepsilon e^{j\theta})] j d\theta \quad \text{if } \omega \rightarrow \infty, \varepsilon \text{ shrinks to zero } \varepsilon \approx 0 \quad \text{therefore} \quad \int_{\pi}^0 j[Z(\omega)] d\theta \quad \text{evaluating}$$

the integral yields:

$$\int_{\gamma} \frac{Z(x)}{x-\omega} dx = -j\pi Z(\omega) \quad (\text{A.4})$$

Integration along the contour ζ , $x = R e^{j\theta}$, $dx = jR e^{j\theta} d\theta$, $0 \leq \theta \leq \pi$

$$\int_{\zeta} \frac{Z(x)}{x-\omega} dx = \int_0^{\pi} \frac{Z(x)}{x-\omega} dx \quad \text{therefore} \quad \int_0^{\pi} \frac{[Z(R e^{j\theta})]}{R e^{j\theta} - \omega} jR e^{j\theta} d\theta$$

$$2\omega \int_0^{\pi} \frac{[Z(R e^{j\theta})]}{R e^{j\theta} \left(1 - \frac{\omega}{R e^{j\theta}}\right)} jR e^{j\theta} d\theta = \int_0^{\pi} \frac{Z(R e^{j\theta})}{1 - \frac{\omega}{R e^{j\theta}}} j d\theta \quad \text{for large } R \rightarrow \infty \quad \text{therefore}$$

$$\int_0^{\pi} \frac{Z_{R,\infty}}{1 - \frac{\omega}{\infty}} j d\theta = 0 \quad \text{therefore} \quad \int_{\zeta} \frac{Z(x)}{x-\omega} dx = j\pi Z_{R,\infty} \quad (\text{A.5})$$

Substituting Eqs. A.4, A.5, into Eq. A.3 yields

$$\int_{-\infty}^{\infty} \frac{Z(x)}{x-\omega} dx - j\pi Z(\omega) + j\pi Z_{R,\infty} = 0 \quad \text{which can be arrange as:}$$

$$Z(\omega) = Z_{R,\infty} + \frac{1}{j\pi} \int_{-\infty}^{\infty} \frac{Z(x)}{x - \omega} dx \quad (\text{A.6})$$

To comply with the causality property, the residue expressed in Eq. A.6 of the singularity has to be zero. Therefore the function $Z(x)$ in the integrand of Eq. A.6 has to be combined with another function as such the result vanishes as ω tends to infinite. Eq. A.6 takes the form as:

$$Z(\omega) = Z_{R,\infty} + \frac{1}{j\pi} \int_{-\infty}^{\infty} \frac{Z(x) - Z^*(\omega)}{x - \omega} dx \quad (\text{A.7})$$

The term $Z^*(\omega)$ in Eq. A.7 indicates that the real and imaginary values of the complex number at frequency ω , are changed from real to imaginary and viceversa. Eq. A.7 can be split into its real and imaginary parts, as such:

$$\begin{aligned} Z(\omega) &= Z_{R,\infty} + \frac{1}{j\pi} \int_{-\infty}^{\infty} \frac{Z_R(x) + jZ_j(x) - Z_R(\omega) - jZ_j(\omega)}{x - \omega} dx \\ Z(\omega) &= Z_{R,\infty} + \frac{1}{j\pi} \int_{-\infty}^{\infty} \frac{Z_R(x) - Z_R(\omega)}{x - \omega} dx + \frac{1}{j\pi} \int_{-\infty}^{\infty} \frac{jZ_j(x) - jZ_j(\omega)}{x - \omega} dx \\ Z(\omega) &= Z_{R,\infty} + \frac{1}{\pi} \int_{-\infty}^{\infty} \frac{Z_j(x) - Z_j(\omega)}{x - \omega} dx - \frac{j}{\pi} \int_{-\infty}^{\infty} \frac{Z_R(x) - Z_R(\omega)}{x - \omega} dx \end{aligned} \quad (\text{A.8})$$

Transformation from Real to Imaginary Component

Transforming the integral of the imaginary part of Eq. A.8 into one of definite parity by multiplying the numerator and denominator of the integrand by $x + \omega$ and separating, yields:

$$\begin{aligned} Z_j(\omega) &= -\frac{1}{\pi} \int_{-\infty}^{\infty} \frac{Z_R(x) - Z_R(\omega)}{x - \omega} dx = -\frac{1}{\pi} \int_{-\infty}^{\infty} \frac{[Z_R(x) - Z_R(\omega)](x + \omega)}{(x - \omega)(x + \omega)} dx \\ Z_j(\omega) &= -\frac{1}{\pi} \int_{-\infty}^{\infty} \frac{xZ_R(x) + \omega Z_R(x) - xZ_R(\omega) - \omega Z_R(\omega)}{x^2 - \omega^2} dx \end{aligned} \quad (\text{A.9})$$

Applying the properties for even and odd functions to each term of the integrand in Eq. A.9, and using symmetry arguments $\int_{-a}^a \text{Even}(x)dx = 2\int_0^a \text{Even}(x)dx$ and $\int_{-a}^a \text{Odd}(x)dx = 0$ yields:

$$Z_j(\omega) = -\frac{2\omega}{\pi} \int_0^\infty \frac{Z_R(x) - Z_R(\omega)}{x^2 - \omega^2} dx \quad (\text{A.10})$$

Transformation from Imaginary to Real Component

Transforming the integral of the real part of Eq. A.8 into one of definite parity by multiplying the numerator and denominator of the integrand by $x+\omega$ and separating, yields:

$$Z_R(\omega) = Z_{R,\infty} + \frac{1}{\pi} \int_{-\infty}^\infty \frac{Z_j(x) - Z_j(\omega)}{x - \omega} dx = Z_{R,\infty} + \frac{1}{\pi} \int_{-\infty}^\infty \frac{[Z_j(x) - Z_j(\omega)](x + \omega)}{(x - \omega)(x + \omega)} dx$$

$$Z_R(\omega) = Z_{R,\infty} + \frac{1}{\pi} \int_{-\infty}^\infty \frac{xZ_j(x) + \omega Z_j(x) - xZ_j(\omega) - \omega Z_j(\omega)}{x^2 - \omega^2} dx$$

Applying the properties for even and odd functions to each term of the integrand in Eq. A.8, and using symmetry arguments $\int_{-a}^a \text{Even}(x)dx = 2\int_0^a \text{Even}(x)dx$ and $\int_{-a}^a \text{Odd}(x)dx = 0$ yields:

$$Z_R(\omega) = Z_{R,\infty} + \frac{2}{\pi} \int_0^\infty \frac{xZ_j(x) - \omega Z_j(\omega)}{x^2 - \omega^2} dx \quad (\text{A.11})$$

Appendix B (Chapter 4)

B.1 Arrhenius Equation

The temperature alters the rate of an electrochemical reaction. This can be expressed by Arrhenius equation:

$$k_{f,b} = A_a \exp\left(\frac{-G_{f,b}}{RT}\right) \quad (\text{B.1})$$

Where k is the reaction rate coefficient, G is Gibbs free energy of activation during the oxidation and reduction processes, R ideal gas constant, T is the temperature and A_a is the number of attempts to overcome the barrier (frequency factor).

If the equilibrium potential in the electrode is changed to a new potential value, the Gibbs free energy will be changed as well. This effect is shown in Fig. B.1.

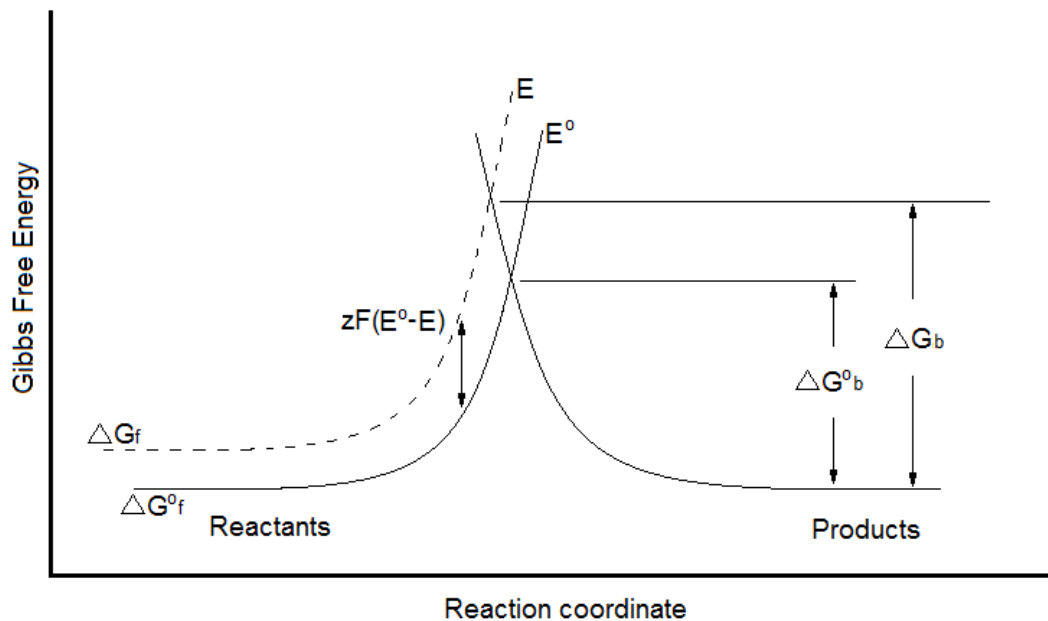


Figure B.1 Effect of the potential change on the free energy of activation

The change in equilibrium potential on the free energy of activation in Fig. B.1 can be defined as:

$$E^{\circ} - E = -\frac{\Delta G^{\circ} - \Delta G}{zF} \quad (\text{B.2})$$

It is possible to relate a parameter defined as charge transfer coefficient α which is a measure of the symmetry of the energy barrier during the electrochemical reaction in the change of potential.

$$E^{\circ} - E = (E^{\circ} - E)(1 - \alpha) + (E^{\circ} - E)\alpha \quad (\text{B.3})$$

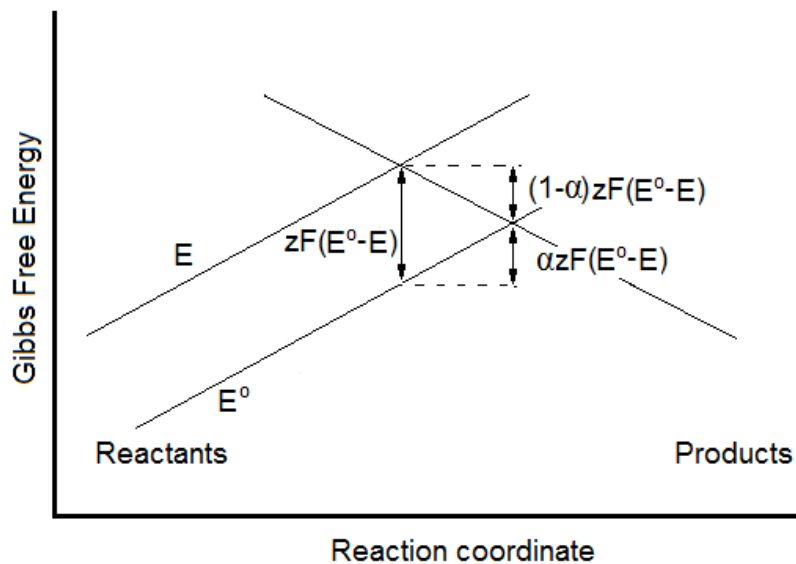


Figure B.2 Relationship between the angle of intersection and the transfer coefficient

Taking into account the change in potential represented in Fig. B.2, the change in Gibbs free Energy for forward and back reaction rates is:

$$\Delta G_f = \Delta G_f^{\circ} - zF\alpha(E^{\circ} - E) \quad (\text{B.4})$$

$$\Delta G_b = \Delta G_b^{\circ} + zF(1 - \alpha)(E^{\circ} - E) \quad (\text{B.5})$$

Substituting Eqs. B.4, B.5 into B.1 yields:

forward reaction coefficient

$$k_f = k^0 \exp\left(\frac{\alpha z F (E^o - E)}{RT}\right) \quad (\text{B.6})$$

backward reaction coefficient

$$k_b = k^0 \exp\left(\frac{-(1-\alpha)zF(E^o - E)}{RT}\right) \quad (\text{B.7})$$

where k^0 is called the standard rate constant^b

B.2 Linearisation

$$\frac{dj}{dx} = j_0 \exp\left(\frac{\alpha z F \eta}{RT}\right) + C_{dl} \frac{d\eta}{dt} \quad (\text{B.8})$$

Integrating and rearranging Eq. B.8 yields:

$$\frac{d\eta}{dt} = \frac{j - D}{C_{dl}x} - \frac{j_0}{C_{dl}} \exp\left(\frac{\eta}{b}\right) \quad (\text{B.9})$$

where $b = RT/[\alpha z F]$ is known as the Tafel slope

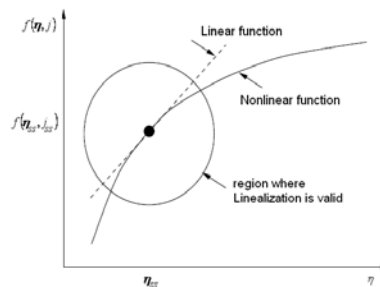


Figure B.3 Nonlinear response

^b In the electrochemical literature, sometimes it is also called the intrinsic rate constant.

$$\frac{d\eta}{dt} = f(\eta, j) \quad (\text{B.10})$$

Expanding the second term of Eq. B.10 which contains the nonlinear term in Taylor series up to its first derivative form, gives

$$f(\eta, j) \approx f(\eta_{SS}, j_{SS}) + \left(\frac{\partial f}{\partial \eta} \right)_{\eta_{SS}, j_{SS}} (\eta - \eta_{SS}) + \left(\frac{\partial f}{\partial j} \right)_{\eta_{SS}, j_{SS}} (j - j_{SS}) \quad (\text{B.11})$$

Given that the expansion is carried out around a steady state (η_{SS}, j_{SS}) , Eq. B.10 can be expressed as

$$\frac{d\eta_{SS}}{dt} = f(\eta_{SS}, j_{SS}) = 0 \quad (\text{B.12})$$

Because η_{SS} is a constant, the left side of Eq. B.10 can be expressed as:

$$\frac{d\eta}{dt} = \frac{d(\eta - \eta_{SS})}{dt} = \frac{d\bar{\eta}}{dt} \quad (\text{B.13})$$

where $\bar{\eta} = \eta - \eta_{SS}$ represents the deviation of variable η in the steady state η_{SS} . The linear equation can be defined as:

$$\frac{d\bar{\eta}}{dt} = \left(\frac{\partial f}{\partial \eta} \right)_{\eta_{SS}, j_{SS}} \bar{\eta} + \left(\frac{\partial f}{\partial j} \right)_{\eta_{SS}, j_{SS}} \bar{j} \quad (\text{B.14})$$

Eq. B.9 can be expressed as:

$$f(\eta, j) = \frac{j - D}{C_{dl} x} - \frac{j_0}{C_{dl}} \exp\left(\frac{\eta}{b}\right) \quad (\text{B.15})$$

Evaluating Eq. B.15 as partial derivatives yields:

$$\left(\frac{\partial f}{\partial \eta}\right)_{\eta_{SS}, j_{SS}} = -\frac{j_0}{C_{dl}b} \exp\left(\frac{\eta_{SS}}{b}\right) \quad \left(\frac{\partial f}{\partial j}\right)_{\eta_{SS}, j_{SS}} = \frac{1}{C_{dl}x} \quad (\text{B.16,17})$$

Substituting the partial derivatives Eqs. B.16,17 into Eq. B.14 yields:

$$\frac{d\bar{\eta}}{dt} = -\frac{j_0}{C_{dl}b} \exp\left(\frac{\eta_{SS}}{b}\right) \bar{\eta} + \frac{1}{C_{dl}x} \bar{j} \quad (\text{B.18})$$

Differentiating j with respect x in Eq. B.18 yields:

$$\frac{d\bar{j}}{dx} = \frac{j_0}{b} \exp\left(\frac{\eta_{SS}}{b}\right) \bar{\eta} + C_{dl} \frac{d\bar{\eta}}{dt} \quad (\text{B.19})$$

B.3 Evaluation of $\eta_{ss}(x)$ with R_P/R_C

Charge transfer resistance $R_C = b / j_0 \exp(\eta_{SS} / b)$, Potential in the electrolyte $\frac{d\eta_{SS}}{dx} = R_P j$

$$\frac{R_P}{R_C} = \frac{d\eta_{SS}}{dx} \frac{j_0 \exp(\eta_{SS} / b)}{bj} \quad \text{Separating variables} \quad \exp(\eta_{SS} / b) d\eta_{SS} = \frac{R_P}{R_C} \frac{bj}{j_0} dx$$

Integrating with limits at $x=0$ CCL-GDL interface $\eta_{SS} = \eta_{SS_0}$, and at $x=1$ CCL-PEM interface $\eta_{SS} = \eta_{SS_1}$

$$b \int_{\eta_{SS_0}}^{\eta_{SS_1}} \exp(\eta_{SS} / b) d\eta_{SS} = \frac{R_P}{R_C} \frac{bj}{j_0} \int_0^1 dx, \text{ yields } \exp(\eta_{SS_0} / b) = \exp(\eta_{SS_1} / b) - \frac{R_P}{R_C} \frac{j}{j_0} \quad \text{for } j > j_0$$

if $R_P / R_C \geq 1$ therefore $\eta_{SS_0} \neq \eta_{SS_1}$

but if $R_P / R_C \ll 1$ therefore the variation is small $\eta_{SS_0} \approx \eta_{SS_1}$ and η_{SS} can be considered constant along x .

B.4 Solution of the Frequency Response by the n^{th} -Order Homogeneous Equations with Constant Coefficients Method

$$\frac{d^2 \bar{j}(s)}{dx^2} = R_p \left[\frac{\bar{j}(s)}{R_C} + Ys^p \bar{j}(s) \right] \quad (\text{B.20})$$

Eq. B.20 can take the form of a homogeneous equation:

$$a \frac{d^2 \lambda}{dx^2} + b \frac{d\lambda}{dx} + c\lambda = 0 \quad (\text{B.21})$$

The homogeneous equation can be represented by:

$$\lambda^2 + \lambda + \alpha = 0 \quad (\text{B.22})$$

which has the following roots:

$$\lambda_{1,2} = \pm \sqrt{R_p \left[\frac{1}{R_C} + Ys^p \right]} \quad (\text{B.23})$$

The solution of a homogeneous equation with different roots can be obtained as follows:

$$\bar{j}(s) = A \exp(\lambda_1 x) + B \exp(\lambda_2 x) \quad (\text{B.24})$$

Appendix C (Chapter 5)

Solution of Fick's Second Law in the Laplace domain.

$$D \frac{\partial^2 c_o(y,t)}{\partial y^2} = \frac{\partial c_o(y,t)}{\partial t} \quad (\text{C.1})$$

Transforming Eq. C.1 in the Laplace domain and considering the initial condition at $t=0$ as $c_o(y,0) = c_o^*$ gives:

$$D \frac{\partial^2 c_o(y,s)}{\partial y^2} = s c_o(y,s) - c_o^* \quad (\text{C.2})$$

Eq. C.2 can be solved using the method of undetermined coefficients for a constant coefficient nonhomogeneous linear differential equation.

$$c_o(y,s) = c_{OH}(y,s) + c_{OP}(y,s) \quad (\text{C.3})$$

Where $c_{OH}(y,s)$ is the solution of the homogeneous equation expressed in Eq. C.2, and $c_{OP}(y,s)$ is a parameter associated to the method of the undetermined coefficients.

Solution.

1st Step. The characteristic equation for the homogeneous part in Eq. C.2 is $D\beta^2 - s = 0$ which has two distinct roots $\beta_{1,2} = \pm\sqrt{s/D}$. Hence the solution of the homogeneous equation is:

$$c_{OH}(y,s) = A \exp(\beta_1 y) + B \exp(\beta_2 y) \quad (\text{C.4})$$

2nd Step. The modification rule calls for $c_{OP}(y,s) = c_o(y,s) = K$ (C.5)

The first and second derivatives of Eq. C.5 yields:

$$\frac{dc_o(y,s)}{dy} = 0 \quad \frac{d^2c_o(y,s)}{dy^2} = 0 \quad (\text{C.6,7})$$

Substituting Eqs. C.5, C.6 and C.7 into C.2 yields:

$$s^* K - c_o^* = 0 \quad \text{hence} \quad K = \frac{c_o^*}{s} \quad \text{This gives} \quad c_{OP}(y,s) = \frac{c_o^*}{s} \quad (\text{C.8})$$

3rd Step. Substituting Eqs. C.4 and C.8 into C.3 yields:

$$c_o(y,s) = A \exp(\beta_1 y) + B \exp(\beta_2 y) + \frac{c_o^*}{s} \quad (\text{C.9})$$

Eq. C.9 can be expressed by considering the Laplace form $c_o^*(s) = c_o^*/s$ as:

$$c_o(y,s) - c_o^*(s) = A \exp(\beta_1 y) + B \exp(\beta_2 y) \quad \text{with} \quad \beta_{1,2} = \pm \sqrt{s/D} \quad (\text{C.10})$$

Appendix D (Chapter 6)

Graphical User Interface

A graphical user interface (GUI) was developed in MATLAB® as a front end for the numerical EIS model described in Chapters 4 and 5 which allows experimental impedance spectra to be compared to simulated impedance obtained through Eq. 5.24 in a user-friendly manner. To reach a good agreement between simulated and experimental data, the parameters in Eq. 5.24 have to be entered in to the GUI. Some commercial software fit experimental impedance data by using nonlinear regression strategies such as Levenberg-Marquardt, Gauss-Newton Method, etc., and with the use of equivalent electrical circuits. However this technique strongly requires some parameters of the

electrical circuit to be defined as initial values in order to achieve the best-fit. The graphic interface developed in this work relies on a mathematical model based on fundamental electrode and diffusion theory. The electrochemical and diffusion parameters defined in the model are related to one another in which counteracting interdependencies are accounted for, for instance, by changing the high ionic resistance at high frequency, the values of the impedance spectrum at low frequency will be changed. The least squares fitting method was used in order to find the best-fit between the model and the measured data. A good quality fit is obtained when the sum of the deviations squared (least square error) between the simulated and measured impedance data has a minimum value, for instance < 0.1 .

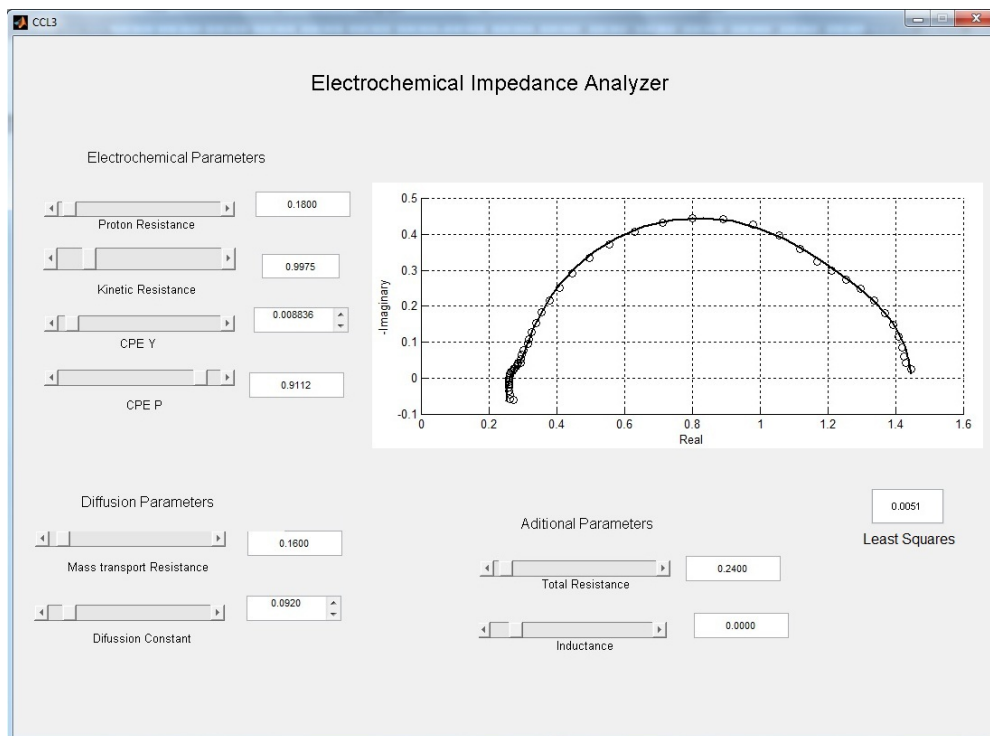


Figure D.1 Graphical user interface for the numerical electrochemical impedance spectroscopy modelling tool

The GUI requires the following parameters to be defined in order to achieve a good agreement between the experimental and simulated data; the following parameters have to be inputted to the mathematical model through the graphical interface;

- Ionic Resistance in CCL $\Omega.\text{cm}^2$,
- Charge Transfer Resistance $\Omega.\text{cm}^2$,
- (Y) Parameter related to CPE $s^p/\Omega.\text{cm}^2$,
- (P) Parameter to correct the inhomogeneity in the distribution of charge
- Resistance for the diffusion process $\Omega.\text{cm}^2$,
- Time constant for diffusion process, s
- Total Ohmic Resistance (PEM, GDL, Plate) $\Omega.\text{cm}^2$,

The comparison between the experimental data and the simulated data is presented in the GUI and also predicts the current distribution through the CCL thickness.

Appendix E (Chapter 9)

Solution of the inverse Laplace transform by the Heaviside's Expansion Theorem

$$\mathcal{L}^{-1}[c_o'(s)] = \mathcal{L}^{-1}[c_o^*(s)] - \mathcal{L}^{-1}\left[\frac{c_o'(s)}{c_o^*(s)} \frac{\bar{\eta}_1(s)}{zFR_c \sqrt{D}} \frac{\sinh(\delta\sqrt{s/D})}{(s)^{1/2} \cosh(\delta\sqrt{s/D})}\right] \quad (\text{E.1})$$

Expressing Eq. E.1 in terms of its Laplace form with $\bar{\eta}_1(s) = \bar{\eta}_1/s$, $c_o^*(s) = c_o^*/s$ and $c_o'(s) = c_o'/s$ yields:

$$c_o' \mathcal{L}^{-1}\left[\frac{1}{s}\right] = c_o^* \mathcal{L}^{-1}\left[\frac{1}{s}\right] - \frac{c_o'}{c_o^*} \frac{\bar{\eta}_1}{zFR_c \sqrt{D}} \mathcal{L}^{-1}\left[\frac{\sinh(\delta\sqrt{s/D})}{(s)^{3/2} \cosh(\delta\sqrt{s/D})}\right] \quad (\text{E.2})$$

Solving the inverse Laplace transform of the second term on the right-hand side of Eq. E.2 by the Heaviside's Expansion Theorem yields:

$$\mathcal{L}^{-1}\left[\frac{\sinh(\delta\sqrt{s/D})}{(s)^{3/2} \cosh(\delta\sqrt{s/D})}\right] = \mathcal{L}^{-1}\left[\frac{p(s)}{q(s)}\right] = \sum_{n=1}^k \frac{p(s_n)}{q'(s_n)} \exp(ts) \quad (\text{E.3})$$

Poles to consider: $(s_1)^{3/2} = 0$ $\cosh\left(\sqrt{\frac{s_2}{D}}\delta\right) = 0$ (E.4,5)

It is necessary to consider a trigonometric identity to find the pole in Eq. E.5:

$$\cosh\left(\sqrt{\frac{s_2}{D}}\delta\right) = \frac{\exp\left(\frac{\sqrt{s_2}}{\sqrt{D}}\delta\right) + \exp\left(-\frac{\sqrt{s_2}}{\sqrt{D}}\delta\right)}{2} = 0 \quad \therefore \quad \frac{\exp\left(\frac{2\sqrt{s_2}}{\sqrt{D}}\delta\right) + 1}{2\exp\left(\frac{\sqrt{s_2}}{\sqrt{D}}\delta\right)} = 0 \quad (\text{E.6,7})$$

Considering $\exp\left(\frac{\sqrt{s_2}}{\sqrt{D}}\delta\right) = x$ (E.8)

Substituting Eq. E8 into Eq. E.7 yields: $\frac{x^2 + 1}{2x} = 0$ which results in $x = \sqrt{-1}$ (E.9)

Substituting E.9 into E.8 yields:

$$\frac{\sqrt{s_2}}{\sqrt{D}}\delta = \ln(\sqrt{-1}) \quad (\text{E.10})$$

considering $\exp(i\pi) = -1$ and substituting into E.10 yields:

$$\frac{\sqrt{s_2}}{\sqrt{D}}\delta = \ln(\sqrt{\exp(i\pi)}) \quad (\text{E.11})$$

Eq. E.11 can be expressed as $s_2 = \frac{i^2 \pi^2 D}{4\delta^2}$ (E.12)

Once the poles, Eq. E.4, E.12, have been estimated it is possible to apply the Heaviside's Expansion Theorem defined in equation (E.3) to calculate the inverse Laplace transform. From Eq. E.3 it can be defined:

$$p(s) = \sinh\left(\frac{\sqrt{s}}{\sqrt{D}} \delta\right) \quad (\text{E.13})$$

$$q(s) = (s)^{3/2} \cosh\left(\frac{\sqrt{s}}{\sqrt{D}} \delta\right) \quad (\text{E.14})$$

$$q'(s) = \frac{3}{2}(s)^{1/2} \cosh\left(\frac{\sqrt{s}}{\sqrt{D}} \delta\right) + \frac{s\delta}{2\sqrt{D}} \sinh\left(\frac{\sqrt{s}}{\sqrt{D}} \delta\right) \quad (\text{E.15})$$

Substituting Eqs. E.13 and E.15 into Eq. E.3:

$$\mathcal{L}^{-1} \left[\frac{\sinh\left(\frac{\sqrt{s}}{\sqrt{D}} \delta\right)}{(s)^{3/2} \cosh\left(\frac{\sqrt{s}}{\sqrt{D}} \delta\right)} \right] = \sum_{n=1}^2 \frac{\sinh\left(\frac{\sqrt{s_n}}{\sqrt{D}} \delta\right) \exp(ts)}{\frac{3}{2}(s_n)^{1/2} \cosh\left(\frac{\sqrt{s_n}}{\sqrt{D}} \delta\right) + \frac{s_n \delta}{2\sqrt{D}} \sinh\left(\frac{\sqrt{s_n}}{\sqrt{D}} \delta\right)} \quad (\text{E.16})$$

Substituting pole $s_1=0$ into Eq. E.16 yields:

$$\frac{\sinh\left(\frac{\sqrt{0}}{\sqrt{D}} \delta\right) \exp(t0)}{\frac{3}{2}(0)^{1/2} \cosh\left(\frac{\sqrt{0}}{\sqrt{D}} \delta\right) + \frac{0\delta}{2\sqrt{D}} \sinh\left(\frac{\sqrt{0}}{\sqrt{D}} \delta\right)} \quad (\text{E.17})$$

Note that the solution of Eq. E.17 gives an indeterminate solution which can be 0 or ∞ . In order to simplify the mathematical treatment as a first approximation zero will be considered as a solution of Eq. E.17.

Substituting pole $s_2 = \frac{i^2 \pi^2 D}{4\delta^2}$ which can be represented as $\frac{\sqrt{s_2}}{\sqrt{D}} \delta = \frac{i\pi}{2}$ into Eq. E.16

yields:

$$\frac{\sinh\left(\frac{i\pi}{2}\right)\exp\left(t\frac{i^2\pi^2 D}{4\delta^2}\right)}{\frac{3\left(\frac{i^2\pi^2 D}{4\delta^2}\right)^{1/2}\cosh\left(\frac{i\pi}{2}\right)+\frac{i^2\pi^2 D}{2\sqrt{D}}\delta\sinh\left(\frac{i\pi}{2}\right)} = -\frac{8\delta\exp\left(-\frac{\pi^2 Dt}{4\delta^2}\right)}{\pi^2\sqrt{D}} \quad (\text{E.18})$$

Eq. E.16 is expressed as:

$$\mathcal{L}^{-1}\left[\frac{\sinh\left(\frac{\sqrt{s}}{\sqrt{D}}\delta\right)}{(s)^{3/2}\cosh\left(\frac{\sqrt{s}}{\sqrt{D}}\delta\right)}\right] = -\frac{8\delta}{\pi^2\sqrt{D}}\exp\left(-\frac{\pi^2 Dt}{4\delta^2}\right) \quad (\text{E.19})$$

The inverse Laplace Transform of Eq. E.2 yields:

$$c_o' = c_o^* + \frac{c_o'}{c_o^*} \frac{\bar{\eta}_1}{zFR_c D} \frac{8\delta}{\pi^2} \exp\left(-\frac{\pi^2 Dt}{4\delta^2}\right) \quad (\text{E.20})$$

Eq. E.20 can be arranged as:

$$\frac{c_o'}{c_o^*} \left[1 - \frac{\bar{\eta}_1 8\delta}{\pi^2 zFR_c D c_o^*} \exp\left(-\frac{\pi^2 D}{4\delta^2} t\right) \right] = 1 \quad (\text{E.21})$$

Publications

1. **S. Cruz-Manzo**, P. Rama, and R. Chen, "The Low Current Electrochemical Mechanisms of Fuel Cell Cathode Catalyst Layer Through an Impedance Study", *Journal of the Electrochemical Society*, 157 (3), B400-B408, (2010).
2. **S. Cruz-Manzo**, P. Rama, and R. Chen, "Impedance Study on Oxygen Diffusion Through Fuel Cell Cathode Catalyst Layer at High Current", *Journal of the Electrochemical Society*, 157 (12), B1865-B1871, (2010).
3. **S. Cruz-Manzo**, R. Chen and P. Rama, "Inductive Effect on the Fuel Cell Cathode Impedance Spectrum at High Frequencies", *Journal of Fuel Cell Science and Technology*, 9, 051002, (2012).
4. **S. Cruz-Manzo**, R. Chen and P. Rama, "Study of Current Distribution and Oxygen Diffusion in the Fuel Cell Cathode Catalyst Layer Through Electrochemical Impedance Spectroscopy", *International Journal of Hydrogen Energy*, 38, 1702-1713 (2013).
5. **S. Cruz-Manzo** and R. Chen, "A Generic Electrical Circuit for Performance Analysis of the Fuel Cell Cathode Catalyst Layer through Electrochemical Impedance Spectroscopy", *Journal of Electroanalytical Chemistry*, 694, 45-55 (2013).
6. **S. Cruz-Manzo**, R. Chen and P. Greenwood, "Analysis of the Performance of an Open-Cathode Polymer Electrolyte Fuel Cell Stack using Simultaneous Electrochemical Impedance Spectroscopy Measurements", *13th International Conference Advanced Batteries, Accumulators and Fuel Cells [ABAF 13th]*, August 27-30, 2012, Brno, Czech Republic, ISBN 978-80-214-4570-3.